der Bundeswehr
Universität München

Philipp Zilk

Isogeometric analysis on domains with corners: Numerical analysis and application to crack identification

Vollständiger Abdruck der von der Fakultät für Bauingenieurwesen und Umweltwissenschaften der Universität der Bundeswehr München zur Erlangung des akademischen Grades eines

Doktors der Naturwissenschaften (Dr. rer. nat.)

angenommenen Dissertation.

Gutachter:

1. Univ.-Prof. Dr. rer. nat. habil. Thomas Apel, Universität der Bundeswehr München
2. Prof. Serge Nicaise, Université Polytechnique Hauts-de-France
3. Prof. Giancarlo Sangalli, Università di Pavia

Vorsitzender:

Univ.-Prof. Dr.-Ing. Josef Kiendl, Universität der Bundeswehr München

Die Dissertation wurde am 30. März 2026 bei der Universität der Bundeswehr München eingereicht und durch die Fakultät für Bauingenieurwesen und Umweltwissenschaften am 17. Juni 2026 angenommen. Die mündliche Prüfung fand am 08. Juli 2026 statt.

Abstract

By employing non-uniform rational B-splines (NURBS) as ansatz functions, isogeometric analysis (IGA) combines exact geometry representation with high-order approximation spaces for the numerical solution of partial differential equations (PDEs). However, in geometrically challenging settings, such as in the presence of corners, cracks, or non-smooth domain parameterizations, the full potential of isogeometric methods has not yet been realized. A prominent example of the latter is given by polar parameterizations, which collapse one edge of the parametric domain to a single point. Although such mappings are widely used in computer-aided design, a comprehensive convergence theory remains unavailable. In addition, reduced solution regularity near corners fundamentally limits the convergence rates attainable with high-order splines.

This thesis addresses both challenges by focusing on polar parameterizations in which the polar point coincides with a corner of the physical domain. In this context, two key contributions are presented. First, a simple and effective mesh grading strategy toward the collapsed edge is introduced, yielding locally refined meshes near the polar corner that accurately capture singularities of the underlying PDE solutions. Second, a numerical analysis tailored to polar domains with corners is developed, establishing optimal convergence rates via error estimates in weighted Sobolev norms. Numerical experiments for the Poisson equation on benchmark domains confirm the theoretical findings and demonstrate the efficiency of the method. The grading concept is further transferred to the isogeometric collocation framework, where numerical results likewise confirm its effectiveness.

The excellent spectral approximation properties of IGA motivate its application to eigenvalue problems (EVPs). To this end, the Laplace EVP on circular sectors is considered as a model problem, since it admits analytical solutions with corner singularities and the geometry can be represented exactly by a polar NURBS parameterization. Optimal convergence of the eigenpairs is proven under graded mesh refinement and confirmed numerically. Furthermore, the computational results indicate that smooth spline spaces exhibit superior approximation constants compared to their C^0-continuous counterparts, a phenomenon previously established only for rectangular domains. Graded meshes prove particularly effective for accurately approximating a limited number of eigenvalues. To reduce redundant degrees of freedom, a hierarchical mesh structure is introduced, which can be combined with the gradual refinement scheme and leads to slightly different approximation behavior.

In the final part of this thesis, the spectral accuracy of the developed methods is leveraged in the context of inverse problems, with a particular focus on membranes containing cracks. Analytical results based on the short-time asymptotic expansion of the heat trace show that the existence and length of a crack and, under additional assumptions, also its angle can be recovered from the Laplace spectrum. Building on this analysis, a data-driven framework is proposed in which a neural network is trained on simulated spectral data, generated with guaranteed accuracy using graded IGA discretizations, to predict crack geometry parameters. Evaluation of the neural network on the test set demonstrates reliable and precise predictions.

Zusammenfassung

Die Methode der isogeometrischen Analyse (IGA) verbindet durch den Einsatz nicht-uniformer rationaler B-splines (NURBS) als Ansatzfunktionen die exakte computergestützte Darstellung von Rechengebieten mit Approximationsräumen höherer Ordnung zur numerischen Lösung partieller Differentialgleichungen. Das volle Potenzial isogeometrischer Methoden auf komplexeren Gebieten mit Ecken oder Rissen ist jedoch bislang nicht ausgeschöpft. Auch nicht glatte Gebietsparametrisierungen stellen weiterhin eine große Herausforderung dar. Ein zentrales Beispiel hierfür sind polare Parametrisierungen, die eine ganze Kante des parametrischen Definitionsbereichs auf einen einzigen Punkt abbilden. Obwohl solche Transformationen in der computergestützten Konstruktion weit verbreitet sind, ist eine umfassende Konvergenztheorie nach wie vor nicht vorhanden. Darüber hinaus schränkt die verminderte Regularität von Lösungen in der Nähe von Ecken die mit Approximationen höherer Ordnung erreichbaren Konvergenzraten grundlegend ein.

Diese Arbeit befasst sich mit beiden Herausforderungen zugleich, indem sie polare Parametrisierungen untersucht, deren Polpunkt eine Ecke des physikalischen Gebiets darstellt. In diesem Zusammenhang werden zwei zentrale Forschungsthemen behandelt. Zum einen wird eine einfache und effektive Netzverfeinerungsstrategie in Richtung der kollabierten Kante des Referenzgebiets vorgestellt. Dadurch entsteht im Rechengebiet ein Netz, das zur polaren Ecke hin lokal verfeinert ist und eine genaue Approximation singularer Lösungen partieller Differentialgleichungen ermöglicht. Zum anderen wird eine speziell auf polare Gebiete mit Ecken zugeschnittene numerische Analyse entwickelt, welche mittels Fehlerabschätzungen in gewichteten Sobolev-Normen optimale Konvergenzraten nachweist. Numerische Experimente zur Poisson-Gleichung auf Benchmark-Gebieten bestätigen die theoretischen Ergebnisse und belegen die Effizienz des Ansatzes. Zudem wird das Konzept der graduellen Verfeinerung auf isogeometrische Kollokationsverfahren übertragen, wobei numerische Ergebnisse zeigen, dass es sich auch in diesem Kontext erfolgreich anwenden lässt.

Darüber hinaus motivieren die hervorragenden spektralen Approximationseigenschaften der IGA ihre Anwendung auf Eigenwertprobleme. Dazu wird das Laplace-Eigenwertproblem auf Kreissektoren als Modellproblem betrachtet, da sich die kreisförmige Geometrie exakt durch eine polare NURBS-Parametrisierung beschreiben lässt und die analytisch bekannten Eigenfunktionen klassische Eckensingularitäten aufweisen. Für die Approximation der Eigenpaare mittels gradueller Netzverfeinerung werden optimale Konvergenzraten bewiesen, die sich auch in numerischen Experimenten widerspiegeln. Ferner deuten die numerischen Ergebnisse darauf hin, dass glatte Spline-Räume bessere Approximationskonstanten aufweisen als C^0-stetige Ansatzräume – ein Phänomen, das bislang nur für rechteckige Gebiete festgestellt wurde. Graduell verfeinerte Netze erweisen sich insbesondere dann als vorteilhaft, wenn eine feste Anzahl von Eigenwerten präzise berechnet werden soll. Zur Vermeidung redundanter Freiheitsgrade wird außerdem eine hierarchische Gitterstruktur eingeführt, die sich gut mit dem graduellen Verfeinerungsschema kombinieren lässt und leicht veränderte Approximationseigenschaften aufweist.

Schließlich wird die spektrale Genauigkeit der entwickelten Methoden für das inverse Problem der Risserkennung in Membranen genutzt. Analytische Ergebnisse, die auf der kurzzeitigen asymptotischen Entwicklung der Wärmespur basieren, zeigen, dass die Existenz, die Länge und, unter zusätzlichen Annahmen, auch der Winkel eines Risses aus dem Laplace-Spektrum des zugehörigen Gebiets ermittelt werden können. Darauf aufbauend wird ein datengetriebener Ansatz vorgestellt, bei dem ein neuronales Netz auf simulierten Daten trainiert wird, um aus den zugehörigen Eigenwerten einer Membran auf die Geometrie des vorliegenden Risses zu schließen. Der Datensatz besteht aus Simulationsergebnissen, die mittels graduell verfeinerter IGA-Diskretisierungen mit garantierter Genauigkeit generiert werden. Die Auswertung auf dem Testdatensatz zeigt, dass das trainierte Netz geometrische Rissparameter zuverlässig und präzise rekonstruieren kann.

Acknowledgments

This dissertation contains the results of my work as a research associate at the Institute for Mathematics and Computer-Based Simulation at the Universität der Bundeswehr München since March 2021. As it marks the end of an important period in my professional life, I take this opportunity to express my sincere gratitude to all those who have accompanied and supported me along this journey.

First and foremost, I would like to thank my supervisor, Prof. Thomas Apel, for giving me the opportunity to pursue my ambition of earning a doctoral degree. To me, he is an outstanding example not only of a PhD supervisor, but also of a human being. His supervision, encouragement, and support, as well as the values he stands for, have been exemplary throughout these years. I am especially grateful for his patience, his many valuable ideas, and his advice whenever I encountered difficulties in my research. He created a warm and approachable work environment and granted me the freedom to explore my own ideas while at the same time setting ambitious yet realistic goals. Moreover, I am very thankful for the opportunity to attend several conferences and, more generally, for the space and trust to shape my own academic path.

I am also sincerely grateful to Prof. Serge Nicaise, who mentored me during a short research stay at the University of Valenciennes in early 2023 and kindly agreed to serve as a reviewer of this thesis. I greatly benefited from his valuable input on the topic of crack identification, which he encouraged me to pursue further and believe in through his energetic and motivating manner. Furthermore, I am thankful to Prof. Giancarlo Sangalli for agreeing to review this dissertation and for many motivating discussions at various conferences.

In this context, I wish to acknowledge all the people I met during conferences and research visits for the many inspiring scientific discussions and valuable exchanges along the way. In particular, I would like to thank the senior academics Thomas Takacs, Alessandro Reali, Hendrik Speleers, Lloyd Nicholas Trefethen, Fleurianne Bertrand, and Max Winkler, who generously dedicated some of their valuable time to sharing their knowledge and insights with me. I also look back with gratitude on the many encounters with Reymart, Luigi, Michele, Nils, Henrik, Tom-Christian, Marius, Yannis, and many others, which included not only interesting discussions, but also a great deal of fun.

Furthermore, I am very thankful for the support of my colleagues at our university. In particular, I would like to thank Max, with whom I had the pleasure of sharing an office, as well as Volker, Tarik, Katharina, Johannes, Christof, Gabriela, and Aysun, who all contributed to the success of this thesis in one way or another, whether in matters of a theoretical, computational, or administrative nature. More broadly, my thanks go to all colleagues at IMCS and UniBw whom I met along the way, many of whom became friends and brought joy to everyday work, which is crucial for sustaining motivation in such a long-term project.

Finally, I would like to thank my family, especially my parents and grandparents, for their unconditional support, without which this achievement would not have been possible. My deepest

thanks also go to my girlfriend, Luisa, for being by my side throughout this journey, for cheering me up even during the most difficult times, and for always supporting my ambitions with patience and understanding for the dedication and sacrifices that come with them. Last but not least, I would like to thank all my friends for making my life outside academia joyful and fulfilling. Their presence and friendship have been a constant source of motivation throughout my PhD and have provided a valuable counterbalance to academic life.

Contents

1 Introduction **1**

2 Preliminaries and introduction to isogeometric analysis **7**
2.1 Fundamental notation and concepts . . . 7
2.1.1 Classical and weighted function spaces . . . 7
2.1.2 Corner singularities in solutions of the Poisson equation . . . 9
2.1.3 Numerical methods for the solution of partial differential equations . . . 11
2.2 B-splines, NURBS and quasi-interpolants . . . 13
2.2.1 Univariate B-splines, NURBS, and Refinement Algorithms . . . 14
2.2.2 Bivariate B-splines, NURBS, and Bézier meshes . . . 18

3 Numerical analysis of IGA on polar domains with corners **21**
3.1 Motivation and novelties . . . 21
3.2 Graded mesh refinement in the vicinity of polar corners . . . 24
3.2.1 Polar parameterizations and polar corners . . . 24
3.2.2 Mesh grading toward polar corners . . . 30
3.3 Function spaces and projectors for polar parameterizations . . . 36
3.3.1 The polar approximation space and a suitable projection . . . 36
3.3.2 Polar Sobolev spaces on the parametric domain . . . 40
3.3.3 Bent polar Sobolev spaces . . . 46
3.3.4 Polar transformation of the projection error . . . 48
3.4 Error estimates for graded refinement in the vicinity of polar corners . . . 49
3.4.1 Main results . . . 49
3.4.2 Proof of Theorem 3.21 . . . 51
3.4.3 Properties of the modified quasi-interpolant . . . 65
3.5 Numerical Examples for graded Galerkin IGA . . . 68
3.6 Graded collocation toward polar corners . . . 77
3.6.1 Construction of graded collocation points . . . 77
3.6.2 Numerical tests . . . 79
3.6.3 Scope, limitations and outlook . . . 84

4 IGA of the Laplace eigenvalue problem on circular sectors **85**
4.1 Motivation and novelties . . . 85
4.2 The Laplace eigenvalue problem on circular sectors . . . 87
4.2.1 Analytical solutions . . . 87

4.2.2 Regularity of the eigenfunctions . . . 90
4.2.3 Eigenfunctions of the unit disk with crack . . . 94
4.3 Isogeometric discretization and numerical analysis . . . 95
4.3.1 Variational formulation . . . 95
4.3.2 Mesh grading and error estimates . . . 97
4.4 Numerical experiments . . . 101
4.4.1 Optimal convergence and grading parameter . . . 101
4.4.2 Spectral approximation properties of smooth splines on circular sectors . . . 105
4.4.3 Hierarchical meshes in combination with graded refinement . . . 107

5 Can one hear the shape of a crack in a drum? 113
5.1 Motivation and novelties . . . 113
5.2 Short-time asymptotic expansion of the heat trace . . . 117
5.3 Spectral fingerprints of a crack in the heat trace . . . 119
5.3.1 Modeling of a crack . . . 119
5.3.2 Can one hear the length of a crack? . . . 120
5.3.3 Can one hear the angle of a crack? . . . 122
5.4 Hearing the shape of a crack - A data-driven perspective . . . 128
5.4.1 Solving the forward problem via IGA and graded mesh refinement . . . 129
5.4.2 Regularity of the eigenfunctions . . . 137
5.4.3 Solving the inverse problem via neural networks . . . 139

6 Conclusion and Outlook 149

References 155

List of Figures

1.1 Polar parameterization of a circular sector with inner angle $\omega = 2\pi$, i.e., a unit disk with a crack. Equally colored boundary edges are mapped onto each other. The left edge of the parametric domain (cyan) is mapped to the center of the disk, corresponding to the crack tip. (a): Uniform coarse mesh. (b): Gradually refined mesh. (c): Gradually refined hierarchical mesh. 2

1.2 Schematic illustration of the isospectral problem for cracks. 3

2.1 Curvilinear polygonal domain with a single corner $\boldsymbol{V}$. A zoomed view of the corner region highlights the relevant geometric quantities introduced in Definition 2.2. . . 10

2.2 Examples of cubic B-spline functions constructed from different knot vectors Ξ. (a): $\Xi = \{0,0,0,0,\frac{1}{4},\frac{1}{2},\frac{3}{4},1,1,1,1\}$. (b): $\Xi = \{0,0,0,0,\frac{1}{4},\frac{1}{4},\frac{1}{4},\frac{1}{2},\frac{1}{2},\frac{3}{4},1,1,1,1\}$. 15

2.3 Illustration of the support extensions $\widetilde{Q}_{\boldsymbol{j}}$ and $\widetilde{K}_{\boldsymbol{j}} = \boldsymbol{F}(\widetilde{Q}_{\boldsymbol{j}})$ of a parametric and physical Bézier mesh element $Q_{\boldsymbol{j}} \in \widehat{\mathcal{M}}$ and $K_{\boldsymbol{j}} = \boldsymbol{F}(Q_{\boldsymbol{j}}) \in \mathcal{M}$, respectively. Here, $\boldsymbol{i} = (i_1, i_2) \in \boldsymbol{I}$ is such that $Q_{\boldsymbol{j}} = I_{1,j_1} \times I_{2,j_2} = (\zeta_{1,j_1}, \zeta_{1,j_1+1}) \times (\zeta_{2,j_2}, \zeta_{2,j_2+1}) = (\xi_{1,i_1}, \xi_{1,i_1+1}) \times (\xi_{2,i_2}, \xi_{2,i_2+1})$, and hence, $\widetilde{Q}_{\boldsymbol{j}} = \widetilde{I}_{1,j_1} \times \widetilde{I}_{2,j_2} = (\xi_{1,i_1-p_1}, \xi_{1,i_1+p_1+1}) \times (\xi_{2,i_2-p_2}, \xi_{2,i_2+p_2+1})$, see (2.32) and (2.17). In this example, we choose $\boldsymbol{p} = (p_1, p_2) = (2,1)$ and assume that the knots ξ_{l,k_l}, $k_l \in \{i_l - p_l, i_l + p_l + 1\}$, $l = 1,2$, are pairwise distinct. 19

3.1 Polar parameterizations of exemplary domains with corners and corresponding boundary notation. (a): Circular sector with angle $\omega = \frac{2}{3}\pi$ (b): Circular sector with angle $\omega = \frac{5}{3}\pi$, also known as Pacman domain. (c): Triangle. (d): L-shaped domain. 27

3.2 (a): Illustration of the mapping $\zeta_2 \mapsto \boldsymbol{G}(\zeta_2) = (G_1(\zeta_2), G_2(\zeta_2))$ in (3.3) for the polar parameterization of a unit disk with crack together with the classical angular transformation $\zeta_2 \mapsto (\cos(2\pi\zeta_2), \sin(2\pi\zeta_2))$. (b): Difference between the corresponding functions. 28

3.3 Parametric and physical Bézier meshes. First row: Uniform refinement ($\mu = 1$). Second row: Graded refinement ($\mu < 1$). (a): Circular sector. (b): L-shaped domain. 32

3.4 Sketch of multipatch parameterizations for complex domains based on polar mappings. (a): U-shaped domain parameterized by eight polar triangles with graded meshes toward the two corners. (b): Scaled boundary parameterization of a segment of a flower-shaped domain, where a circular sector with a graded mesh is employed locally near the corner. 33

3.5 Illustration of the mesh size quantities in the parametric Bézier mesh: (a): Uniform mesh ($\mu = 1$). (b): Graded mesh ($\mu < 1$). 34

3.6 Illustration of the function Θ for $\alpha \in \{2, 3, \ldots, 6\}$. 35
3.7 Basis functions for a coarse discretization of a circular sector sector with angle $\omega = \frac{5}{3}\pi$. Some mesh lines that do not correspond to the coarse discretization are inserted for better visualization. (a): Standard singular basis functions (3.18). (b): Modified basis function (3.20). 38
3.8 Splitting of the parametric and physical domain and the corresponding meshes. (a): Circular sector. (b): L-shaped domain. 53
3.9 Illustration of the scaling transformation $\mathring{\mathbf{\Phi}}$ with the reference domains $\mathring{\Omega}$ and $\mathring{\Omega}_C$ and the corresponding parametric domains $\widehat{\Omega}$ and $\widehat{\Omega}_C$, respectively. 58
3.10 First row: Illustration of the parametric scaling transformation (3.63), with the extended parametric strip $\widetilde{\widehat{\Omega}}_C$ and the corresponding reference domain $\widetilde{\mathring{\Omega}}_C$ being hatched in green. Second row: Illustration of the physical scaling transformation (3.64), with the extended small polar domain $\widetilde{\Omega}_C$ and the corresponding reference domain $\widetilde{\mathring{\Omega}}_C$ being hatched in green. 59
3.11 Solving the Poisson equation on a quarter of the unit disk: (a): Plot of a numerical solution on a uniform mesh with 16 subdivisions for bicubic NURBS ($p = 3$). (b): $H^1(\Omega)$-error of the approximation. (c): $L^2(\Omega)$-error of the approximation. 70
3.12 Solving the Poisson equation on a circular sector with inner angle $\omega = \frac{2}{3}\pi$: (a): Plot of a numerical solution on a graded mesh with 16 subdivisions using bicubic NURBS. (b): $H^1(\Omega)$-error of the approximation. (c): $L^2(\Omega)$-error of the approximation. . . . 70
3.13 Solving the Poisson equation on the Quasi-Pacman domain: (a): Plot of a numerical solution on a graded mesh for biquadratic NURBS. (b): $H^1(\Omega)$-error of the approximation. (c): $L^2(\Omega)$-error of the approximation. 71
3.14 Solving the Poisson equation on the Pacman domain: (a): Surface plot of an approximation on a graded mesh for bicubic NURBS. (b): $H^1(\Omega)$-error of the approximation. (c): $L^2(\Omega)$-error of the approximation. 74
3.15 Solving the Poisson equation on the Pacman domain with smoothness $k = 0$ and $k = p-1$: (a): $H^1(\Omega)$-error of the approximation. (b): $L^2(\Omega)$-error of the approximation. 74
3.16 Solving the Poisson equation with a weak singular exponent on the L-shaped domain with graded and adaptive hierarchical refinement: (a): Plot of the numerical solution on a graded mesh for biquadratic NURBS. (b): $H^1(\Omega)$-error of the approximation. (c): $L^2(\Omega)$-error of the approximation. 75
3.17 Solving the Poisson equation with a strong singular exponent on the L-shaped domain with graded and adaptive hierarchical refinement: (a): Plot of the exact solution, where some mesh lines are inserted for visualization purposes. (b): $H^1(\Omega)$-error of the approximation. (c): $L^2(\Omega)$-error of the approximation. 75
3.18 Solving the Poisson equation on a circular sector with a jumping material coefficient: (a): Exact solution, with selected mesh lines added for visualization. (b): $H^1(\Omega)$-error of the approximation. (c): $L^2(\Omega)$-error of the approximation. 77
3.19 Bézier meshes and associated interior GA collocation points (3.75), shown as asterisks, for quartic NURBS defined by the knot vectors Ξ_1 and $\Xi_2 = \{0, 0, 0, 0, 0, \frac{1}{4}, \frac{1}{2}, \frac{3}{4}, 1, 1, 1, 1, 1\}$. (a): Uniform GA ($\mu = 1$): $\Xi_1 = \{0, 0, 0, 0, 0, \frac{1}{4}, \frac{1}{2}, \frac{3}{4}, 1, 1, 1, 1, 1\}$. (b): Graded GA ($\mu < 1$): $\Xi_1 = \{0, 0, 0, 0, 0, \frac{1}{16}, \frac{1}{4}, \frac{9}{16}, 1, 1, 1, 1, 1\}$. The 28 collocation points on the boundary are not shown. 79
3.20 Solving Example 3.44 using uniform and graded collocation with GA: (a): Plot of a numerical solution on a graded mesh with 16 subdivisions for bicubic NURBS. (b): $H^1(\Omega)$-error of the approximation. (c): $L^2(\Omega)$-error of the approximation. 80

3.21 Solving Example 3.44 using uniform and graded collocation with CSP: (a): $H^1(\Omega)$-error of the approximation. (b): $L^2(\Omega)$-error of the approximation. 81
3.22 Solving Example 3.45 using graded collocation with GA: (a): Plot of a numerical solution on a graded mesh with 16 subdivisions for bicubic NURBS. (b): $H^1(\Omega)$-error of the approximation. (c): $L^2(\Omega)$-error of the approximation. 83
3.23 Solving Example 3.45 using graded collocation with CSP: (a): $H^1(\Omega)$-error of the approximation. (b): $L^2(\Omega)$-error of the approximation. 83

4.1 Circular sectors Ω with angle ω and the corresponding Dirichlet and Neumann boundaries. (a): $\omega = \frac{3}{2}\pi$. (b): $\omega = 2\pi$. 87
4.2 Illustration of 12 Laplace eigenfunctions $u_{\nu_\ell,m}$ of the unit disk with crack. Columns from left to right: $\nu_\ell = 0, \frac{1}{2}, 1, \frac{3}{2}$. Rows from top to bottom: $m = 1, 2, 3$. 94
4.3 Visualization of the Bessel functions J_{ν_ℓ} to the orders $\nu_\ell \in \{0, 0.5, 1, \ldots, 5.5, 6\}$ in the interval $[0, 10]$. 95
4.4 Approximation of the eigenfunction $u_{\nu_1,1}$ using NURBS of lowest possible degree $\boldsymbol{p} = (p_1, p_2) = (1, 2)$ and regularity $\boldsymbol{k} = (0, 1)$ while gradually refining the coarse mesh $2, 4, 8, 16$ times with the grading parameter $\mu = 0.9 \cdot \frac{\nu_1}{p_1} = 0.45$, recall (4.32). 102
4.5 Approximation errors for the eigenfunction $u = u_{\nu_1,1}$ and its corresponding eigenvalue $\lambda = \lambda_{\nu_1,1}$ using gradually and uniformly refined NURBS of degree $\boldsymbol{p} = (p, p)$, $p \in \{2, 3, 4\}$, and regularity $\boldsymbol{k} = (p-1, p-1)$. We set $\mu = 0.9\frac{\nu_1}{p} = \frac{0.9}{2p}$ for graded meshes and $\mu = 1$ corresponds to uniform refinement. 102
4.6 Approximation errors for the eigenfunction $u = u_{\nu_2,1}$ and its corresponding eigenvalue $\lambda = \lambda_{\nu_2,1}$ using gradually and uniformly refined NURBS of degree $\boldsymbol{p} = (p, p)$, $p \in \{2, 3, 4\}$, and regularity $\boldsymbol{k} = (p-1, p-1)$. We set $\mu = 0.9\frac{\nu_2}{p} = \frac{0.9}{p}$ for graded meshes and $\mu = 1$ corresponds to uniform refinement. 104
4.7 Relative eigenvalue errors, ordered by discrete eigenvalue size, using gradually and uniformly refined NURBS of degree $\boldsymbol{p} = (p, p)$ and regularity $\boldsymbol{k} = (k, k)$. A total of 916 degrees of freedom are used in all computations. For graded meshes, we set $\mu = 0.9\frac{\nu_1}{p} = \frac{0.9}{2p}$, while $\mu = 1$ corresponds to uniform refinement. 106
4.8 Relative errors of the first 100 eigenvalues, ordered by the size of the discrete eigenvalues, computed using graded and uniform NURBS discretizations of degree $\boldsymbol{p} = (p, p)$ and regularity $\boldsymbol{k} = (k, k)$. A total of 67731 degrees of freedom are used in all computations. For graded meshes, we set $\mu = 0.9\frac{\nu_1}{p} = \frac{0.9}{2p}$, while $\mu = 1$ corresponds to uniform refinement. 107
4.9 Illustration of hierarchical refinement scheme. Solid black lines are used for new subdivisions and dashed black lines for the initial coarse meshes $\widehat{\mathcal{M}_0}$ and $\mathcal{M}_0$. (a) Uniform refinement ($\mu = 1$). (b) Graded refinement ($\mu < 1$). 109
4.10 Sketch of the physical mesh elements near the conical point during refinement. (a): Tensor product meshes. (b): Hierarchical meshes. The scaling between refinement steps is manipulated for better visibility. 109
4.11 Approximation errors for the eigenfunction $u = u_{\nu_1,1}$ and its corresponding eigenvalue $\lambda = \lambda_{\nu_1,1}$ using gradually and uniformly refined hierarchical NURBS of degree $\boldsymbol{p} = (p, p)$, $p \in \{2, 3, 4\}$, and regularity $\boldsymbol{k} = (p-1, p-1)$. We set $\mu = 0.9\frac{\nu_1}{p} = \frac{0.9}{2p}$ for graded meshes and $\mu = 1$ corresponds to uniform refinement. 110
4.12 Approximation errors for the eigenfunction $u = u_{\nu_1,1}$ and its corresponding eigenvalue $\lambda = \lambda_{\nu_1,1}$ using NURBS of degree $\boldsymbol{p} = (4, 4)$ and regularity $\boldsymbol{k} = (3, 3)$ on tensor product and hierarchical meshes. We set $\mu = 0.9\frac{\nu_1}{4} = 0.1125$ for graded meshes and $\mu = 1$ corresponds to uniform refinement. 110

4.13 Approximation errors for the eigenfunction $u = u_{\nu_2,1}$ and its corresponding eigenvalue $\lambda = \lambda_{\nu_2,1}$ using gradually and uniformly refined hierarchical NURBS of degree $\boldsymbol{p} = (p, p)$, $p \in \{2, 3, 4\}$, and regularity $\boldsymbol{k} = (p-1, p-1)$. We set $\mu = 0.9\frac{\nu_2}{p} = \frac{0.9}{p}$ for graded meshes and $\mu = 1$ corresponds to uniform refinement. 111
4.14 Approximation errors for the eigenfunction $u = u_{\nu_2,1}$ and its corresponding eigenvalue $\lambda = \lambda_{\nu_2,1}$ using NURBS of degree $\boldsymbol{p} = (4, 4)$ and regularity $\boldsymbol{k} = (3, 3)$ on tensor product and hierarchical meshes. We set $\mu = 0.9\frac{\nu_2}{4} = 0.225$ for graded meshes and $\mu = 1$ corresponds to uniform refinement. 111

5.1 Experimental setup to measure the frequencies of a plate with piezoelectric sensors. (a): One sensor. (b): Three sensors. [Photos: P. Zilk] 114
5.2 Functionality of scanning vibrometer. 114
5.3 Experimental setup to measure the eigenfrequencies of a small plate. (a): Laser. (b): Plate clamped on one side and connected to a vibration stimulator. (c): Complete setup. (d): Animation of the eigenmodes and eigenfrequencies. [Photos: P. Zilk] . . 115
5.4 Illustration of domains with cracks of different shapes, together with the corresponding notation. (a): Curved inner crack, where the two sides of the crack are indicated. (b): Two straight outer cracks. (c): Polygonal outer crack. 120
5.5 (a): Domain with three cracks. (b): Corresponding domain without cracks. (c): Domain with a straight crack, whose starting point and the tangential vector are known. 122
5.6 Sketch of all the corners and corresponding inner angles of different domains. (a): Domain with straight outer crack. (b): Domain with straight outer crack starting at a corner. (c): Corresponding domain without crack. 123
5.7 Crack corner contribution (5.12) of a straight crack for the four types of adjacent boundary conditions. (a): $1, 3 \in I_{=}$. (b): $1, 3 \in I_{\neq}$. (c): $1 \in I_{=}, 3 \in I_{\neq}$. (d): $1 \in I_{\neq}, 3 \in I_{=}$. 124
5.8 (a): Schematic representation of a domain with a straight outer crack and known starting point, including the unit tangent vectors of both the crack and the adjacent boundary. (b): Corresponding domain with inner crack of same length. 127
5.9 Schematic overview of our data-driven approach. The forward problem (top row) is solved via numerical simulation to generate eigenvalue data from domains with known crack geometries. This data is used to train a neural network that approximates the inverse mapping (bottom row). 129
5.10 Discretization of a unit square with a symmetric crack. (a): Illustration of the polar parameterization. (b): Graded mesh refinement toward the crack tip. 131
5.11 Illustration of the eigenfunctions corresponding to the first ten Laplace eigenvalues of the unit square with a horizontal crack of length $l = 0.5$. 135
5.12 Approximation errors for the eigenfunction $u = u_2$ and its associated eigenvalue $\lambda = \lambda_2$ using gradually and uniformly refined B-splines of degree $\boldsymbol{p} = (p, p)$, $p \in \{1, 2, 3, 4\}$, and regularity $\boldsymbol{k} = (p-1, p-1)$. We set $\mu = \frac{0.9}{2p}$ for graded meshes and $\mu = 1$ corresponds to uniform refinement. 135
5.13 Development of the first ten eigenvalues of a unit square with horizontal crack of varying length $l \in (0, 1)$. 136
5.14 Illustration of the eigenfunctions corresponding to the first ten Laplace eigenvalues for a unit square with a horizontal crack of length $l = 0.1$. 137
5.15 Illustration of the eigenfunctions corresponding to the first ten Laplace eigenvalues for a unit square with a horizontal crack of length $l = 0.9$. 137

5.16 Multipatch discretization of a domain with an inner crack using ten patches of polar triangles. (a): Polar parameterization of triangle I. (b): Composition of all patches. The dashed lines indicate inner patch interfaces that must be coupled. 138
5.17 Examples of horizontal cracks in the unit square with varying length. 140
5.18 Neural network architecture used for predicting the crack length l from the first n_{eig} eigenvalues. 141
5.19 Training loss of the neural network for predicting crack length from different numbers of input eigenvalues n_{eig}. 142
5.20 Prediction performance of the neural network based on n_{eig} input eigenvalues. The horizontal axis shows the true crack length, and the vertical axis shows the predicted value. The diagonal indicates perfect prediction. 143
5.21 Examples of cracks in the unit square with fixed starting point and variable end point in the lower half. 144
5.22 Neural network architecture used for predicting the crack endpoint. 145
5.23 Training loss of the neural network for predicting the crack endpoint from different numbers of input eigenvalues n_{eig}. 145
5.24 Prediction performance of the neural network for the x-coordinate of the crack endpoint based on n_{eig} input eigenvalues. The horizontal axis shows the true value, and the vertical axis shows the predicted value. The diagonal indicates perfect prediction. 146
5.25 Predicted versus true y-coordinates of crack endpoints for varying values of n_{eig}. The diagonal indicates perfect prediction. In addition, the points are color-coded by the corresponding absolute x-coordinate prediction error. 147
5.26 Predicted and true crack endpoints in the (x, y)-plane for varying values of n_{eig}. Predictions (blue) are connected to ground truth (red) by black lines indicating the magnitude of the error. 148

List of Tables

3.1 Definition of control points $\boldsymbol{c_i}, \boldsymbol{i} \in \boldsymbol{I}$, for a polar parameterization of a circular sector with inner angle $\omega \in (0, \pi)$, starting angle $\varphi_0 \in [0, 2\pi)$ and radius 1. 28

3.2 Definition of control points $\boldsymbol{c_i}$ and weights $w_{\boldsymbol{i}}$, $\boldsymbol{i} \in \boldsymbol{I}$, for a polar parameterization of an L-shaped domain. 29

3.3 Approximation errors $\|u - u_h\|_{H^1(\Omega)}$ (and corresponding EOC) for Example 3.39 using graded refinement for NURBS of degree $p = 3$ and different grading parameters μ. 72

3.4 Approximation errors $\|u - u_h\|_{L^2(\Omega)}$ (and corresponding EOC) for Example 3.39 using graded refinement for NURBS of degree $p = 3$ and different grading parameters μ. 72

3.5 Approximation errors $\|u - u_h\|_{L^2(\Omega)}$ (and corresponding EOC) for Example 3.39 using graded refinement for NURBS of degree $p = 3$ and different grading parameters μ. 72

3.6 Definition of control points $\boldsymbol{c_i}$, $\boldsymbol{i} \in \boldsymbol{I}$, for a polar parameterization of the Quasi-Pacman domain. 73

3.7 Definition of weights $w_{\boldsymbol{i}}$, $\boldsymbol{i} \in \boldsymbol{I}$, for a polar parameterization of the Quasi-Pacman domain. 73

3.8 Convergence rates for the approximation of smooth PDE solutions with isogeometric collocation methods [MST17]. 79

3.9 Approximation errors $\|u - u_h\|_{H^1(\Omega)}$ (and corresponding EOC) for Example 3.44 using graded collocation with GA, NURBS degree $p = 4$ and different grading parameters μ. 82

3.10 Approximation errors $\|u - u_h\|_{H^1(\Omega)}$ (and corresponding EOC) for Example 3.44 using graded collocation with GA, NURBS degree $p = 5$ and different grading parameters μ. 82

3.11 Approximation errors $\|u - u_h\|_{H^1(\Omega)}$ (and corresponding EOC) for Example 3.44 using graded collocation with CSP, NURBS degree $p = 3$ and different grading parameters μ. 82

4.1 The eigenfrequencies (4.7) of the unit disk with crack are listed in ascending order within the interval $[0, 10]$. As per equation (4.6), each eigenfrequency corresponds to the m-th root of a Bessel function J_{ν_ℓ}, denoted by $\bar{\omega}_n = \eta_{\nu_\ell,m}$ for some $\nu_\ell \in \{0, \frac{1}{2}, 1, \frac{3}{2}, \dots\}$ and $m \in \mathbb{N}$. Additionally, the corresponding eigenfunctions and their regularity are provided, where $\varepsilon > 0$ is an arbitrarily small constant. Rows containing eigenfunctions with the strongest and second strongest singularity are highlighted in dark orange and light orange, respectively. 96
4.2 Approximation errors $\|u - u_h\|_{H^1(\Omega)}$ (and corresponding EOC with respect to n_{dof}) for the eigenfunction $u = u_{\nu_1,1}$ using gradually refined NURBS of degree $\boldsymbol{p} = (2, 2)$ and regularity $\boldsymbol{k} = (1, 1)$ with different grading parameters μ. 103
4.3 Approximation errors $|\lambda - \lambda_h|$ (and corresponding EOC with respect to n_{dof}) for the eigenvalue $\lambda = \lambda_{\nu_1,1}$ using gradually refined NURBS of degree $\boldsymbol{p} = (2, 2)$ and regularity $\boldsymbol{k} = (1, 1)$ with different grading parameters μ. 103
4.4 Approximation errors $\|u - u_h\|_{H^1(\Omega)}$ (and corresponding EOC with respect to n_{dof}) for the eigenfunction $u = u_{\nu_1,1}$ using gradually refined NURBS of degree $\boldsymbol{p} = (2, 2)$ and regularity $\boldsymbol{k} = (0, 0)$ with different grading parameters μ. 103
4.5 Approximation errors $|\lambda - \lambda_h|$ (and corresponding EOC with respect to n_{dof}) for the eigenvalue $\lambda = \lambda_{\nu_1,1}$ using gradually refined NURBS of degree $\boldsymbol{p} = (2, 2)$ and regularity $\boldsymbol{k} = (0, 0)$ with different grading parameters μ. 104
4.6 Approximation errors $\|u - u_h\|_{H^1(\Omega)}$ (and corresponding EOC with respect to n_{dof}) for the eigenfunction $u = u_{\nu_2,1}$ using gradually refined hierarchical NURBS of degree $\boldsymbol{p} = (2, 2)$ and regularity $\boldsymbol{k} = (1, 1)$ with different grading parameters μ. 112
4.7 Approximation errors $|\lambda - \lambda_h|$ (and corresponding EOC with respect to n_{dof}) for the eigenvalue $\lambda = \lambda_{\nu_2,1}$ using gradually refined hierarchical NURBS of degree $\boldsymbol{p} = (2, 2)$ and regularity $\boldsymbol{k} = (1, 1)$ with different grading parameters μ. 112

5.1 Definition of control points $\boldsymbol{c_i}$, $\boldsymbol{i} \in \boldsymbol{I}$, for a polar parameterization of the unit square with symmetric crack. 132
5.2 Definition of accuracy metrics for the prediction of a crack parameter θ. 140
5.3 Accuracy metrics for predicting the crack length using a neural network trained on n_{eig} input eigenvalues. 141
5.4 Accuracy metrics for predicting the x- and y-coordinate of crack endpoints using a neural network trained on n_{eig} input eigenvalues. 147

List of Symbols

$\sim$, 7

$\widehat{B}_{\boldsymbol{i},\boldsymbol{p}}$, 18

$\boldsymbol{c_i}$, 19
C, 7
$C^s(\Omega)$, 7
$C^s(\overline{\Omega})$, 8

$D^{\boldsymbol{\alpha}}$, 8, 40
$D^{\boldsymbol{\alpha}}_{\boldsymbol{F}}$, 41
$\widehat{D}^{\boldsymbol{\alpha}}$, 41
$\mathring{D}^{\boldsymbol{\alpha}}$, 57
$\mathcal{D}'(\Omega)$, 8

$\boldsymbol{F}$, 19

$\boldsymbol{\gamma}_c$, 119
$\gamma_{j,p}$, 17
$\boldsymbol{G}$, 26
Γ_c, 119
$\Gamma_c^{\pm}$, 119
Γ_0, 119
Γ_0^N, 119

h, 36
h_l, 31
h_{l,j_l}, 33
$h_{1,\widehat{\Omega}_C}$, 56
$\boldsymbol{\theta}$, 34
H, 117
$H^s(\Omega)$, 8
$H^s_\beta(\Omega)$, 8
$\widehat{H}^s_\beta(Q)$, 43
$\widehat{H}^s_{\odot,\beta}(Q)$, 45
$\mathcal{H}^s_\beta(\widehat{E})$, 46
$\mathcal{H}^s_{\odot,\beta}(\widehat{E})$, 47

$\boldsymbol{I}$, 18
$\boldsymbol{I}_\odot$, 25

$\boldsymbol{J}$, 18
J_{ν_ℓ}, 88

$K_{\boldsymbol{j}}$, 20

$\lambda_{\nu_\ell,m}$, 89
$L^q(\Omega)$, 8
$L^2_\beta(\Omega)$, 9
$\widehat{L}^2_\beta(Q)$, 44
$\mathcal{L}^2_\beta(E)$, 46

μ, 31
$\mathcal{M}$, 20
$\widehat{\mathcal{M}}$, 18

$\mathcal{M}^{\mu}$, 31
$\widehat{\mathcal{M}}^{\mu}$, 31

ν, 10
ν_{ℓ}, 89
$\mathbb{N}$, 7
$\mathbb{N}_0$, 7
$N_{\boldsymbol{i},\boldsymbol{p}}$, 36
$\widehat{N}_{\boldsymbol{i},\boldsymbol{p}}$, 19
$N_{\odot,\boldsymbol{p}}$, 37
$\widehat{N}_{\odot,\boldsymbol{p}}$, 37
$N_{\boldsymbol{p}}(\boldsymbol{\Xi}, W)$, 19

$\widehat{\Omega}$, 18
$\mathring{\Omega}$, 57
Ω_C, 52
$\widetilde{\Omega}_C$, 52
$\widehat{\Omega}_C$, 52
$\widetilde{\widehat{\Omega}}_C$, 52
$\mathring{\Omega}_C$, 57
$\widetilde{\mathring{\Omega}}_C$, 57
Ω_R, 52
$\widetilde{\Omega}_R$, 52
$\widehat{\Omega}_R$, 52
$\widetilde{\widehat{\Omega}}_R$, 52

p, 49
p_l, 18
$\boldsymbol{p}$, 18
$\boldsymbol{P}$, 24
$\Pi_{\boldsymbol{p},\boldsymbol{\Xi}}$, 20
$\Pi^{\widehat{\Gamma}}_{\boldsymbol{p},\boldsymbol{\Xi}}$, 20
$\Pi_{V_h^{\odot}}$, 39

$Q_{\boldsymbol{j}}$, 18
$\widetilde{Q}_{\boldsymbol{j}}$, 18

r, 8

$S_{\boldsymbol{p}}(\boldsymbol{\Xi})$, 19

$u_{\nu_{\ell},m}$, 89

$\widehat{v}$, 41
$\mathring{v}$, 57
V, 11
V_0, 11
$V_h^{\odot}$, 38
$V_{0h}^{\odot}$, 38
$V_{\beta}^{s}(\Omega)$, 8
$V_{\beta,0}^{s}(\Omega)$, 132
$\widehat{V}_{\beta}^{s}(Q)$, 43
$\widehat{V}_{\odot,\beta}^{s}(Q)$, 45
$\mathcal{V}_{\beta}^{s}(\widehat{E})$, 46
$\mathcal{V}_{\odot,\beta}^{s}(\widehat{E})$, 47

$w_{\boldsymbol{i}}$, 19
ω, 9
W, 19

ξ_i, 14
Ξ, 14
Ξ^0, 16

ζ, 14
$\boldsymbol{\zeta}$, 18

List of Abbreviations

BC Boundary condition

CAD Computer-aided design

CSP Clustered superconvergent points

EOC Experimental order of convergence

EVP Eigenvalue problem

FEA Finite element analysis

FEM Finite element method

GA Greville abscissae

IGA Isogeometric analysis

MAE Mean absolute error

MaxE Maximum error

MSE Mean squared error

NURBS Non-uniform rational B-splines

PDE Partial differential equation

ReLU Rectified linear unit

CHAPTER 1

Introduction

Isogeometric analysis was introduced as a unifying framework that bridges numerical simulation and computer-aided design by employing spline-based functions for both geometry representation and the approximation of PDEs. Since its inception, IGA has demonstrated several strengths, including exact discretization of curved domains, high-order accuracy, and excellent spectral approximation properties. Classical approximation theory for h-refinement in Galerkin-based IGA [Baz+06; BBSV14; BCS12; HS17] shows that, on a smoothly parameterized domain Ω, for every $v \in H^s(\Omega)$ with $s \in \mathbb{N}$ and $s \geq 2$, there exists an isogeometric approximation v_h on a uniform mesh, where h denotes the global mesh size, such that

$$\|v - v_h\|_{H^1(\Omega)} \leq Ch^{s-1}\|v\|_{H^s(\Omega)}. \tag{1.1}$$

Hence, high convergence rates can be achieved under uniform mesh refinement, provided that the geometry mapping is smooth and the PDE solution possesses sufficient Sobolev regularity.

In many practically relevant situations, however, these assumptions are not satisfied. In the presence of corners, cracks, or other non-smooth geometric features, solutions of elliptic boundary value problems typically exhibit reduced regularity and therefore do not belong to the Sobolev space $H^s(\Omega)$, as required by estimate (1.1), for large s. Consequently, standard IGA discretizations may fail to achieve optimal higher-order convergence rates.

A further difficulty is that geometry parameterizations are not globally smooth in many CAD applications. An important example is given by polar parameterizations, which collapse one edge of the parametric domain to a single point in the physical domain. Such mappings occur naturally in the description of rotationally symmetric geometries and allow for exact representations of conic sections. For instance, circular sectors, as illustrated in Figure 1.1a for an interior angle of $\omega = 2\pi$, corresponding to a unit disk with a crack, can be parameterized in this way. From a numerical analysis perspective, the singularity of the parameterization at the polar point violates the smoothness assumptions underlying classical IGA theory. In particular, error bounds of the form (1.1) are no longer available in this setting.

Understanding and overcoming these limitations, both by designing adapted numerical discretizations and by developing an approximation theory that relaxes the classical smoothness assumptions on solutions and parameterizations, is essential for extending the reliable use of IGA to realistic computational geometries. The first part of this thesis addresses these challenges by exploiting polar

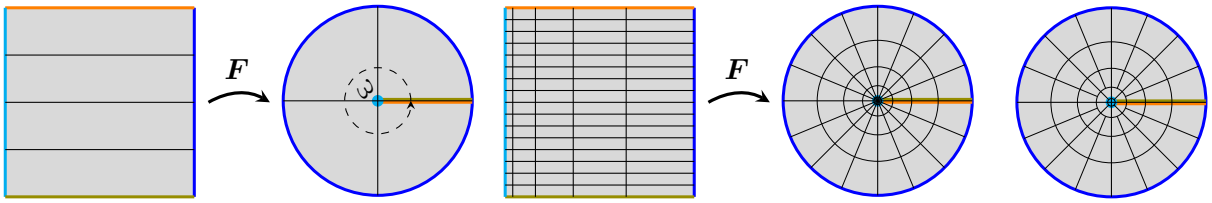

Figure 1.1: Polar parameterization of a circular sector with inner angle $\omega = 2\pi$, i.e., a unit disk with a crack. Equally colored boundary edges are mapped onto each other. The left edge of the parametric domain (cyan) is mapped to the center of the disk, corresponding to the crack tip. (a): Uniform coarse mesh. (b): Gradually refined mesh. (c): Gradually refined hierarchical mesh.

parameterizations in which the collapsed edge coincides with a physical corner of the domain. Corner singularities in solutions of elliptic boundary value problems are well understood and can often be characterized a priori, which motivates the use of mesh grading. While local refinement in IGA is often achieved by sophisticated adaptive spline techniques that increase implementation complexity, the combination of polar parameterizations and mesh grading offers a comparatively simple and effective alternative. Grading the parametric mesh toward the collapsed edge concentrates degrees of freedom near the singularity in the physical domain, while preserving the global tensor product mesh structure; see Figure 1.1b.

Building on this idea, a numerical analysis framework tailored to polar domains with corners is developed in Chapter 3. The key ingredient is the introduction of polar function spaces that reflect the singular behavior of both the geometry mapping and the PDE solution. Within this setting, an analogue of the error estimate (1.1) is derived for polar parameterizations and solutions in weighted Sobolev spaces $V^s_\beta(\Omega)$, which can capture characteristic corner singularities. More precisely, under appropriate conditions on s, β, and the grading parameter, we prove that for every $v \in V^s_\beta(\Omega)$ there exists $v_h \in V^\odot_h$, where $V^\odot_h$ denotes a polar isogeometric approximation space commonly used in the literature, such that

$$\|v - v_h\|_{H^1(\Omega)} \leq C h^{s-1} \|v\|_{V^s_\beta(\Omega)}. \tag{1.2}$$

Thus, optimal convergence is obtained for a suitable choice of the grading parameter, and the required conditions are explicitly derived. Numerical experiments for benchmark Poisson problems confirm the theoretical results and illustrate the efficiency of the graded refinement strategy. Moreover, the grading concept is extended to the isogeometric collocation framework, and the computational results demonstrate that the approach is not restricted to Galerkin formulations.

Beyond boundary value problems, isogeometric analysis is well known for its excellent spectral approximation properties. In particular, on rectangular domains, highly accurate approximations of the Laplace spectrum can be achieved, and smooth spline spaces exhibit remarkably small approximation constants for eigenvalues and eigenfunctions [HRS08; HER14; MSS22; SMS19; SMS20]. Extending these observations to domains with corner singularities, however, is far from trivial, as the reduced regularity of eigenfunctions may severely affect spectral convergence.

To investigate this setting, Chapter 4 considers the Laplace eigenvalue problem on circular sectors, which provides a natural model problem for several reasons: the isogeometric framework permits an exact geometric representation, as visualized in Figure 1.1; the eigenpairs are analytically known;

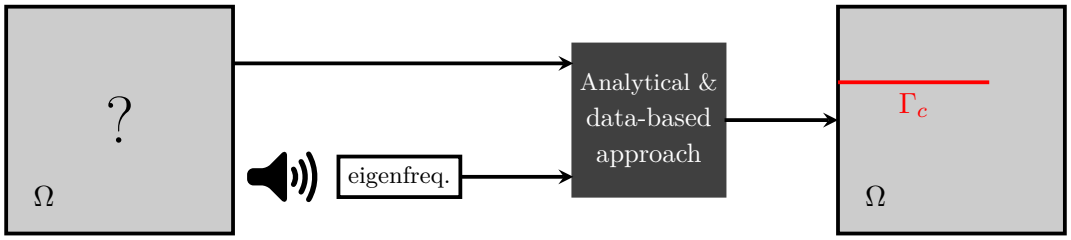

Figure 1.2: Schematic illustration of the isospectral problem for cracks.

and the eigenfunctions exhibit a canonical corner singularity while satisfying the weighted Sobolev regularity required for the estimate (1.2). Owing to the symmetry of the domain, the spectrum also contains smooth eigenfunctions, enabling a differentiated study of smooth and singular modes within a unified framework.

Using the proposed mesh grading strategy toward the polar corner, optimal convergence rates are obtained for both eigenvalues and eigenfunctions. In addition, uniform meshes on polar parameterizations perform equally well for smooth eigenfunctions. The numerical results further demonstrate that smooth spline spaces yield superior approximation constants compared to their C^0-continuous counterparts for the lower part of the spectrum, extending earlier observations from rectangular geometries. In this context, a hierarchical mesh structure, illustrated in Figure 1.1c, is introduced. It can be combined with mesh grading and improves computational efficiency by avoiding anisotropic elements and eliminating redundant degrees of freedom near the singularity, while yielding slightly different approximation behavior.

Building on the excellent spectral properties of IGA, the final part of the thesis is devoted to inverse spectral problems on domains with cracks. Cracks manifest themselves through changes in the vibrational behavior of a structure, and hence geometric information about a crack is encoded in the Laplace spectrum. The high accuracy of the isogeometric discretizations developed in this thesis makes such spectral information accessible in a reliable computational manner. Consequently, the question arises whether geometric crack parameters can be reconstructed from the eigenfrequencies of the underlying domain, a problem closely related to the classical question of "hearing the shape of a drum" [Kac66] and illustrated in Figure 1.2.

In Chapter 5, we investigate this inverse problem by combining analytical and data-driven approaches. Analytical results based on the short-time asymptotic expansion of the heat trace identify which geometric features of a crack are encoded in the Laplace spectrum and under which conditions they can be recovered. In particular, it is shown that the existence and length of a crack and, under additional assumptions, also the angle between the crack and the tangential direction of the boundary are spectrally detectable. These results ensure the well-posedness of the inverse problem for a class of crack geometries.

Complementing the analytical investigation, a data-driven framework is presented in which neural networks are trained on simulated spectral data to infer crack parameters. The required eigenvalues of the sampled domains are computed using the graded isogeometric discretizations developed earlier in the thesis, which allow for local refinement near the crack tip. Accompanying error estimates guarantee the accuracy of the computational data. Numerical experiments demonstrate that the proposed approach enables robust reconstruction of crack parameters from spectral input.

Overall, this thesis advances the numerical analysis of isogeometric methods on domains with corners. It introduces a local refinement strategy based on mesh grading toward polar points, derives parameterization-aware error estimates in weighted function spaces, extends spectral approximation

theory to non-smooth geometries, and demonstrates the applicability of these techniques to the inverse problem of crack identification. These results strengthen the mathematical foundations of IGA on polar domains, which arise naturally in CAD and engineering applications. Detailed comparisons of the main contributions with the state of the art are provided in the corresponding chapters.

Outline of the thesis

The outline of this dissertation is as follows. Chapter 2 introduces the relevant mathematical preliminaries, including weighted Sobolev spaces, corner singularities in PDE solutions, and fundamental concepts of B-splines, NURBS, and isogeometric methods. Chapter 3 develops a numerical analysis of IGA on polar domains with corners for boundary value problems. We introduce graded mesh refinement and graded collocation strategies toward polar corners, establish parameterization-aware approximation spaces and projection operators, and derive error estimates that prove optimal convergence of the graded Galerkin approach for solutions with reduced regularity. The chapter is largely based on [AZ26], while the extension to the collocation setting and some additional numerical experiments constitute novel contributions of this thesis. Chapter 4 then builds on [AZ24a] and extends the numerical analysis to a suitable model eigenvalue problem, namely the Laplace eigenvalue problem on circular sectors. In this context, we further study the spectral approximation properties of splines on graded meshes and introduce a possible combination of the grading scheme with a hierarchical mesh structure. Chapter 5 applies the developed methods to inverse spectral problems for crack identification. It combines analytical results based on heat trace asymptotics with a data-driven reconstruction approach and draws on the work presented in [ANZ25]. Finally, Chapter 6 summarizes the main contributions of the thesis and suggests directions for future research.

Related Publications

As mentioned above, this thesis is partly based on research that has already been published in journal articles and preprints. The publications and their abstracts are listed below, together with a brief note on their relevance to the thesis.

Publication I

[AZ24] T. Apel and P. Zilk. “Isogeometric analysis of the Laplace eigenvalue problem on circular sectors: Regularity properties and graded meshes”. *Comput. Math. Appl.* 175 (2024), 236–254. DOI: 10.1016/j.camwa.2024.09.018.

Abstract: The Laplace eigenvalue problem on circular sectors has eigenfunctions with corner singularities. Standard methods may produce suboptimal approximation results. To address this issue, a novel numerical algorithm that enhances standard isogeometric analysis is proposed in this paper by using a single-patch graded mesh refinement scheme. Numerical tests demonstrate optimal convergence rates for both the eigenvalues and eigenfunctions. Furthermore, the results show that smooth splines possess a superior approximation constant compared to their C^0-continuous counterparts for the lower part of the Laplace spectrum. This is an extension of previous findings about excellent spectral approximation properties of smooth splines on rectangular domains to circular sectors. In addition, graded meshes prove to be particularly advantageous for an accurate approximation of a limited number of eigenvalues. Finally, a hierarchical mesh structure is presented

to avoid anisotropic elements in the physical domain and to omit redundant degrees of freedom in the vicinity of the singularity. Numerical results validate the effectiveness of hierarchical mesh grading for simulating eigenfunctions of low and high regularity.

Relevance for the thesis: In this paper, we analyze the central model problem to assess spectral accuracy of our novel approach. The study demonstrates that graded isogeometric mesh refinement based on polar parameterizations enables optimal approximation of eigenvalues and eigenfunctions, while exploiting exact geometric representations of circular domains. The results provide a proof of concept for the use of graded polar meshes in IGA and motivate the subsequent theoretical analysis and extensions developed in the thesis.

Publication II

[AZ26] T. Apel and P. Zilk. "Error estimates and graded mesh refinement for isogeometric analysis in the vicinity of polar corners". *Comput. Methods Appl. Mech. Engrg.* 452 (2026), 118695. DOI: 10.1016/j.cma.2025.118695.

Abstract: Isogeometric analysis (IGA) combines exact geometric representations with higher-order accuracy for the numerical solution of partial differential equations. However, in geometrically complex settings – such as domains with corner singularities or non-standard parameterizations – these advantages may not be fully realized by standard IGA techniques. In particular, commonly used NURBS parameterizations can result in polar mappings, where one edge of the parametric domain is collapsed onto a single point, known as the polar point. Although widely used in computer-aided design, such configurations lack a full convergence theory. Additionally, reduced solution regularity near corners can significantly limit the performance of standard IGA, as higher-order convergence is no longer attainable. In this work, both challenges are addressed by analyzing parameterizations in which the polar point coincides with a corner of the physical domain. To tackle the resulting singularity, a simple and effective local refinement strategy is proposed based on mesh grading toward the collapsed edge. This produces a locally refined mesh in the vicinity of the polar corner that accurately captures the singular behavior of the PDE solution. To support this strategy, a numerical analysis tailored to polar domains with corners is developed. The framework includes the definition of polar function spaces on the parametric domain, a quasi-interpolant for polar splines, and the derivation of error estimates in weighted Sobolev norms. Optimal convergence is proven for smooth solutions under uniform refinement and for singular solutions using appropriately graded meshes. Numerical experiments on benchmark domains confirm the theoretical predictions and demonstrate the practical efficiency of the proposed method.

Relevance for the thesis: This publication forms the theoretical core of the thesis. It generalizes the computational algorithms introduced in Publication I and, above all, provides a rigorous numerical analysis for isogeometric discretizations based on polar parameterizations. Central to this analysis are parameterization-aware function spaces and error estimates in weighted Sobolev norms that prove optimal convergence rates under graded refinement. These results provide the mathematical foundation for the concept of mesh grading toward polar corners and subsequent extensions developed throughout the thesis.

Publication III

[ANZ25] T. Apel, S. Nicaise, and P. Zilk. *Can one hear the shape of a crack in a drum? Spectral fingerprints and a data-driven perspective*. Preprint. 2025. HAL: https://hal.science/hal-05415870.

Abstract: This paper investigates whether the shape of a crack in a membrane can be identified from the corresponding Laplace spectrum. To this end, analytical results are derived using the short-time asymptotic expansion of the heat trace, a fundamental spectral invariant. The analysis reveals that the existence, length and, under additional conditions, also the angle of a crack can be recovered, which allows for the reconstruction of certain crack shapes.

Determining geometric parameters from the eigenfrequencies of a domain is a classical inverse problem, commonly referred to as the inverse spectral problem. In the second part of this work, a data-driven framework is presented, where a neural network is trained on simulated spectral data to approximate the inverse mapping. The simulations are carried out using isogeometric analysis, and the singularities at crack tips are resolved through graded mesh refinement. Error estimates are provided to ensure accurate simulation results. Numerical experiments confirm that the neural network reliably reconstructs crack parameters from spectral input.

Relevance for the thesis: In this preprint, the methods developed in Publications I and II are applied to an inverse spectral problem involving domains with cracks. The approximation framework previously introduced for boundary value problems is extended to the Laplace eigenvalue problem on cracked domains. The resulting high-accuracy spectral data are used to train a neural network that solves the associated inverse problem, whose well-posedness is established through analytical insights from heat trace asymptotics. The work demonstrates that the graded isogeometric discretizations developed in this thesis provide sufficiently accurate data to train machine learning models to reliably identify crack parameters from the spectrum, thereby illustrating the applicability of the proposed approach for data-driven solutions of inverse problems.

CHAPTER 2

Preliminaries and introduction to isogeometric analysis

This chapter introduces the mathematical foundations of numerical methods for partial differential equations and establishes the relevant notation. In Section 2.1, we recall basic concepts, including classical and weighted function spaces, and discuss corner singularities in solutions of the Poisson equation on domains with corners, which play a central role throughout the thesis. Building on these analytical foundations, we provide an overview of the numerical methods considered in this work, namely Galerkin and collocation approaches.

The second part of the chapter, presented in Section 2.2, is devoted to the fundamentals of isogeometric analysis. We review B-splines and NURBS, beginning with the univariate setting and subsequently extending to the multivariate case. Key definitions and properties are introduced, followed by a discussion of refinement techniques, Greville abscissae, and projection and quasi-interpolation operators. The chapter concludes with an overview of multivariate NURBS geometries and Bézier meshes.

2.1 Fundamental notation and concepts

Throughout this thesis, the symbol C denotes a generic positive constant, which may be different at each occurrence. Moreover, for $a, b > 0$ we write $a \sim b$ if there exist positive constants C_1 and C_2 such that $C_1 b \leq a \leq C_2 b$. The mentioned constants are independent of the mesh parameter h and the function under consideration. Further, we denote by $\mathbb{N}$ the positive integers starting from 1, and by $\mathbb{N}_0$ the non-negative integers starting from 0.

2.1.1 Classical and weighted function spaces

Various function spaces arise naturally in the study of PDEs. We introduce the required standard notation below and refer to [AF03, Chapter 1] for further details and proofs. Let $\Omega \subset \mathbb{R}^d$, $d \in \mathbb{N}$, be an open domain. For any nonnegative integer $s \in \mathbb{N}_0$, we denote by $C^s(\Omega)$ the space of all continuous functions f on Ω whose partial derivatives $D^{\boldsymbol{\alpha}} f$ of order $|\boldsymbol{\alpha}| \leq s$ are also continuous on

Ω. Here, $\boldsymbol{\alpha} = (\alpha_1, \alpha_2, \ldots, \alpha_d)^T \in \mathbb{N}^d$ is a multi-index, and we write

$$|\boldsymbol{\alpha}| := \sum_{i=1}^{d} \alpha_i \quad \text{and} \quad D^{\boldsymbol{\alpha}} := \frac{\partial^{|\boldsymbol{\alpha}|}}{\partial x_1^{\alpha_1} \cdots \partial x_d^{\alpha_d}}. \tag{2.1}$$

For two multi-indices $\boldsymbol{\alpha}, \boldsymbol{\gamma} \in \mathbb{N}^d$, the relations $\boldsymbol{\alpha} \geq \boldsymbol{\gamma}$ and $\boldsymbol{\alpha} \leq \boldsymbol{\gamma}$ are understood componentwise. Moreover, we write $C(\Omega) := C^0(\Omega)$ and define $C^\infty(\Omega) := \bigcap_{s=0}^{\infty} C^s(\Omega)$. While functions in $C^s(\Omega)$ are continuous, they need not be bounded on Ω, a property that is commonly required in analysis. For this reason, we also introduce the space

$$C^s(\overline{\Omega}) := \{f \in C^s(\Omega) : D^{\boldsymbol{\alpha}} f \text{ is bounded and uniformly continuous on } \Omega \text{ for } |\boldsymbol{\alpha}| \leq s\},$$

where the notation indicates that these functions admit a continuous extension to the closure $\overline{\Omega}$ of Ω. The spaces $C^s(\overline{\Omega})$ are Banach spaces equipped with the norm

$$\|f\|_{C^s(\overline{\Omega})} := \max_{0 \leq |\boldsymbol{\alpha}| \leq s} \sup_{\boldsymbol{x} \in \Omega} |D^{\boldsymbol{\alpha}} f(\boldsymbol{x})|.$$

Furthermore, we denote the standard Lebesgue spaces by $L^q(\Omega)$, $1 \leq q \leq \infty$, with the corresponding norms

$$\|f\|_{L^q(\Omega)} = \left(\int_\Omega |f(\boldsymbol{x})|^q \mathrm{d}\boldsymbol{x} \right)^{1/q}, \quad 1 \leq q < \infty,$$
$$\|f\|_{L^\infty(\Omega)} = \operatorname{ess\,sup}_{\boldsymbol{x} \in \Omega} |f(\boldsymbol{x})|.$$

In particular, $L^2(\Omega)$ is a Hilbert space. Based on this definition and the concept of weak derivatives [AF03, Chapter 1], we introduce the standard Sobolev spaces

$$H^s(\Omega) = \left\{ v \in L^2(\Omega) : \|v\|_{H^s(\Omega)} < \infty \right\},$$

for $s \in \mathbb{N}_0$, equipped with the norm

$$\|v\|_{H^s(\Omega)} := \left(\sum_{|\boldsymbol{\alpha}| \leq s} \|D^{\boldsymbol{\alpha}} v\|_{L^2(\Omega)}^2 \right)^{1/2}.$$

The Sobolev spaces $H^s(\Omega)$ are Hilbert spaces, with $H^0(\Omega) = L^2(\Omega)$. For general $s \geq 0$ with $s \notin \mathbb{N}_0$, the notation $H^s(\Omega)$ is used for the Sobolev–Slobodeckij spaces.

Solutions of PDEs posed on non-smooth domains typically exhibit singularities. In such situations, weighted Sobolev spaces provide a convenient framework to describe the regularity of the solution. To this end, let $\mathcal{D}'(\Omega)$ be the space of distributions on Ω.

Definition 2.1. Let $\Omega \subset \mathbb{R}^2$ be a bounded domain and let $r = r(\boldsymbol{x}) = |\boldsymbol{x}| = \sqrt{x^2 + y^2}$ be the distance of every point $\boldsymbol{x} = (x, y) \in \Omega$ to $\mathbf{0}$. We define the *weighted Sobolev spaces* $H^s_\beta(\Omega)$ and $V^s_\beta(\Omega)$ for $s \in \mathbb{N}_0$ and $\beta \in \mathbb{R}$ by

$$H^s_\beta(\Omega) := \left\{ v \in \mathcal{D}'(\Omega) : \|v\|_{H^s_\beta(\Omega)} < \infty \right\} \quad \text{and} \quad V^s_\beta(\Omega) := \left\{ v \in \mathcal{D}'(\Omega) : \|v\|_{V^s_\beta(\Omega)} < \infty \right\},$$

respectively, where

$$\|v\|_{H^s_\beta(\Omega)} := \left(\sum_{|\boldsymbol{\alpha}|\leq s} \left\| r^\beta D^{\boldsymbol{\alpha}} v \right\|^2_{L^2(\Omega)} \right)^{1/2} = \left(\sum_{|\boldsymbol{\alpha}|\leq s} \int_\Omega \left| r(\boldsymbol{x})^\beta D^{\boldsymbol{\alpha}} v(\boldsymbol{x}) \right|^2 \mathrm{d}\boldsymbol{x} \right)^{1/2},$$

$$\|v\|_{V^s_\beta(\Omega)} := \left(\sum_{|\boldsymbol{\alpha}|\leq s} \left\| r^{\beta-s+|\boldsymbol{\alpha}|} D^{\boldsymbol{\alpha}} v \right\|^2_{L^2(\Omega)} \right)^{1/2} = \left(\sum_{|\boldsymbol{\alpha}|\leq s} \int_\Omega \left| r(\boldsymbol{x})^{\beta-s+|\boldsymbol{\alpha}|} D^{\boldsymbol{\alpha}} v(\boldsymbol{x}) \right|^2 \mathrm{d}\boldsymbol{x} \right)^{1/2}.$$

Corresponding seminorms are defined by

$$|v|_{H^s_\beta(\Omega)} := |v|_{V^s_\beta(\Omega)} := \left(\sum_{|\boldsymbol{\alpha}|=s} \left\| r^\beta D^{\boldsymbol{\alpha}} v \right\|^2_{L^2(\Omega)} \right)^{1/2}.$$

Besides, we have $H^s(\Omega) = H^s_0(\Omega)$ and we write $V^s(\Omega) = V^s_0(\Omega)$ and $L^2_\beta(\Omega) = H^0_\beta(\Omega) = V^0_\beta(\Omega)$.

Such spaces have been studied both in the analytic setting [Dau88; Gri85; MP78] and in the context of finite element methods [ASW96; MR82]. It is well-known that they form Hilbert spaces and corresponding embedding theorems have been derived. In particular, for all $s \in \mathbb{N}$ and $\beta \in \mathbb{R}$, the embedding

$$V^s_\beta(\Omega) \hookrightarrow H^s_\beta(\Omega). \tag{2.2}$$

follows directly.

2.1.2 Corner singularities in solutions of the Poisson equation

Subsequently, we introduce the main model problem and investigate reduced regularity properties of its solutions, which may lead to inaccurate approximations when standard numerical methods are employed. We begin by defining the class of domains under consideration.

Definition 2.2. A domain $\Omega \subset \mathbb{R}^2$ is called a bounded *curvilinear polygonal domain* if its boundary Γ is piecewise smooth and has a vertex at each non-smooth point. A *vertex* is a point $\boldsymbol{V} \in \Gamma$ that satisfies the following conditions:

1. The boundary in a neighborhood of $\boldsymbol{V}$ is defined by a continuous curve $\boldsymbol{\gamma} : (-a, a) \to \Gamma$ for $a > 0$ with $\boldsymbol{\gamma}(0) = \boldsymbol{V}$. Moreover, $\boldsymbol{\gamma}$ is required to be smooth on $(-a, 0]$ and $[0, a)$ with $\|\boldsymbol{\gamma}'(t)\| = 1$ for all $t \in (-a, a) \setminus \{0\}$ and

   $$\lim_{t \nearrow 0} \boldsymbol{\gamma}'(t) = \boldsymbol{v}_1, \quad \lim_{t \searrow 0} \boldsymbol{\gamma}'(t) = \boldsymbol{v}_2$$

   for some unit vectors $\boldsymbol{v}_1, \boldsymbol{v}_2 \in \mathbb{R}^2$.

2. The *interior angle* ω at the vertex $\boldsymbol{V}$, defined as the counterclockwise angle between $-\boldsymbol{v}_1$ and $\boldsymbol{v}_2$, satisfies $\omega \in (0, 2\pi]$. Here, the interior angle is characterized by the property that, for every vector $\boldsymbol{w}$ forming an angle $\tilde{\omega} \in (0, \omega)$ with $-\boldsymbol{v}_1$, we assume that there exists $\epsilon > 0$ such that $\boldsymbol{V} + t\boldsymbol{w} \in \Omega$ for all $t \in (0, \epsilon)$.

Figure 2.1 illustrates a curvilinear polygonal domain with a single corner and visualizes the geometric quantities introduced in Definition 2.2.

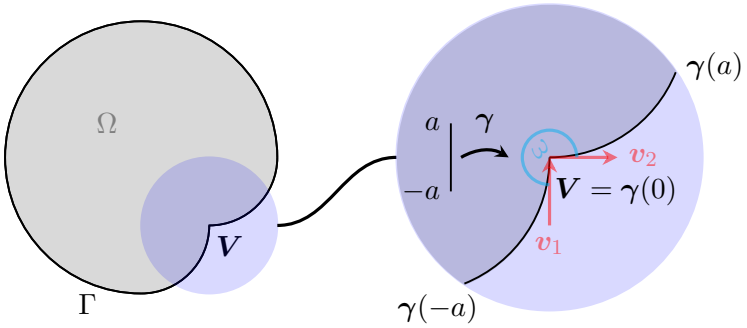

Figure 2.1: Curvilinear polygonal domain with a single corner $\boldsymbol{V}$. A zoomed view of the corner region highlights the relevant geometric quantities introduced in Definition 2.2.

Remark 2.3. Definition 2.2 follows the formulation of Definition 1.1 in [NRS24], restricted to the planar case and with a slight modification. The condition $\boldsymbol{v}_1 \neq \boldsymbol{v}_2$ for the tangential vectors at a vertex is omitted, and instead the interior angle is assumed to satisfy $\omega \in (0, 2\pi]$. Thus, inward-pointing cracks and cusps are admitted, whereas outward-pointing cusps remain excluded.

Now, let $\Omega \subset \mathbb{R}^2$ be a bounded curvilinear polygonal domain with boundary $\Gamma = \partial\Omega$. Let Γ_D and Γ_N be two open subsets of Γ such that $\Gamma = \overline{\Gamma_D} \cup \overline{\Gamma_N}$ and $\Gamma_D \cap \Gamma_N = \emptyset$. We consider the Poisson equation

$$\begin{aligned} -\Delta u &= f \quad && \text{in } \Omega, \\ u &= 0 \quad && \text{on } \Gamma_D, \\ \frac{\partial u}{\partial n} &= 0 \quad && \text{on } \Gamma_N, \end{aligned} \tag{2.3}$$

where Γ_D and Γ_N are referred to as the Dirichlet and Neumann boundaries of Ω, respectively. For the sake of simplicity, we usually assume a non-empty Dirichlet boundary, $\Gamma_D \neq \emptyset$, and homogeneous boundary conditions (BCs). The numerical analysis of inhomogeneous boundary data leads to additional technical difficulties which are beyond the scope of this dissertation.

Throughout our work, we focus on problems posed on non-smooth domains, that is, domains with at least one vertex in the sense of Definition 2.2. Of particular interest is the behavior and approximation of solutions in the vicinity of the vertices, where corner singularities typically arise.

Remark 2.4. Numerical analysis on such domains is usually carried out locally in the neighborhoods of each corner and then combined to obtain global results. We therefore restrict our attention to the analysis near a single corner, which, without loss of generality, is located at $\boldsymbol{V} = \boldsymbol{0}$. This assumption is consistent with the weighted Sobolev spaces introduced in Definition 2.1, where the weight r is defined as the distance to $\boldsymbol{0}$. Furthermore, we assume that the solution is sufficiently smooth away from this vertex so as not to affect our local analysis around the corner.

In general, at the vertex $\boldsymbol{V} = \boldsymbol{0}$, the solution u of the Poisson equation (2.3) exhibits a singularity of type r^ν, where the singular exponent $\nu \in \mathbb{R}$ depends on the corner angle ω and the boundary conditions imposed on the adjacent edges. The strongest possible singular exponent is given by $\nu = \frac{\pi}{\omega}$ for Dirichlet or Neumann BCs on both adjacent edges, and by $\nu = \frac{\pi}{2\omega}$ in the case of mixed

BCs. This reduced regularity can be described conveniently in terms of weighted Sobolev spaces. In weighted H-spaces, we have

$$u \in H^s_\beta(\Omega) \quad \text{for all } \beta \in \mathbb{R} \text{ with } s-1-\nu < \beta < s-1+\nu,$$

under the assumption that the right-hand side satisfies $f \in H^{s-2}_\beta(\Omega)$ for $s \in \mathbb{N}, s \geq 2$, see, for example, [CDN12, Theorem 7.2]. In weighted V-spaces, and only for Dirichlet and mixed BCs at the corner, the regularity result reads

$$u \in V^s_\beta(\Omega) \quad \text{for all } \beta \in \mathbb{R} \text{ with } s-1-\nu < \beta < s-1+\nu, \tag{2.4}$$

provided that $f \in V^{s-2}_\beta(\Omega)$ for $s \in \mathbb{N}, s \geq 2$. In addition, the a priori estimate

$$\|u\|_{V^s_\beta(\Omega)} \leq C\|f\|_{V^{s-2}_\beta(\Omega)} \tag{2.5}$$

holds [NP94, Chapter 2, Theorem 3.1]. For Neumann BCs, additional restrictions are required due to the presence of constants in the solution. For instance, assuming that u vanishes at the polar corner restores the regularity (2.4) at least for $s = 2$. For further details on these regularity results, we refer to [Dau88; Pfe14; Win15].

2.1.3 Numerical methods for the solution of partial differential equations

A variety of approaches exist for the numerical solution of PDEs. In this work, we focus on two main classes: Galerkin and collocation methods.

Galerkin methods

The approach is based on Galerkin's principle, which we illustrate below using our model problem. To this end, we introduce the Hilbert spaces

$$V := H^1(\Omega) \quad \text{and} \quad V_0 := \{v \in V : v = 0 \text{ on } \Gamma_D\}. \tag{2.6}$$

Multiplying the Poisson equation with test functions $v \in V_0$ on both sides and integrating by parts over Ω leads to the corresponding variational formulation, also known as weak form, of problem (2.3): find $u \in V_0$ such that

$$a(u,v) = b(v) \quad \forall v \in V_0, \tag{2.7}$$

where the bilinear and linear forms are defined by

$$\begin{aligned} a : V \times V \to \mathbb{R}, \quad a(u,v) &:= \int_\Omega \nabla u \cdot \nabla v \, \mathrm{d}\boldsymbol{x}, \\ b : V \to \mathbb{R}, \quad b(v) &:= \int_\Omega f v \, \mathrm{d}\boldsymbol{x}. \end{aligned}$$

Both forms are bounded on V, that is,

$$\begin{aligned} a(u,v) &\leq C\|u\|_V\|v\|_V \quad \forall u, v \in V, \\ b(v) &\leq C\|v\|_V \quad \forall u, v \in V, \end{aligned} \tag{2.8}$$

and, in particular on V_0. Moreover, the bilinear form is coercive on V_0,

$$a(u,u) \geq C\|u\|_V^2 \quad \forall u \in V_0,$$

where we recall that $\Gamma_D \neq \emptyset$ is assumed. Hence, by the Lax-Milgram theorem, the variational problem (2.7) admits a unique solution $u \in V_0$. Note that the Dirichlet boundary condition is enforced through the definition of the function space V_0, whereas the Neumann BC is naturally incorporated into the weak formulation through the vanishing of the associated boundary terms. In this context, homogeneous Neumann BC are often referred to as natural boundary conditions. Related variational formulations can be built by choosing different spaces for the test functions. For more details, we refer, for example, to [Bra97; BS08; SF08].

In the next step, let $V_{0h} \subset V_0$ be a finite-dimensional subspace. The corresponding discrete problem then reads: find $u_h \in V_{0h}$ such that

$$a(u_h, v_h) = b(v_h) \quad \forall v_h \in V_{0h}. \tag{2.9}$$

Again, owing to the boundedness of both forms and the coercivity of a on V_{0h}, the Lax–Milgram theorem guarantees the existence of a unique discrete solution $u_h \in V_{0h}$. Moreover, let $\{\phi_1, \phi_2 \ldots, \phi_l\}$ be a basis of V_{0h}. Then, the discrete solution u_h can be represented as a linear combination of the basis functions,

$$u_h = \sum_{j=1}^{l} u_h^j \, \phi_j, \tag{2.10}$$

with coefficients $u_h^j \in \mathbb{R}$, $j = 1, 2, \ldots, l$. Inserting this ansatz into the discrete weak formulation (2.9) leads to the matrix system

$$A\,\vec{u}_h = B, \tag{2.11}$$

where

$$A = (a(\phi_j, \phi_i))_{i,j\in\{1,2,\ldots,l\}}\,, \quad \vec{u}_h = \left(u_h^j\right)_{j\in\{1,2,\ldots,l\}}\,, \quad B = (b(\phi_j))_{j\in\{1,2,\ldots,l\}}\,.$$

Under appropriate assumptions on the family of approximation spaces V_{0h}, which depend on a discretization parameter $h > 0$, the discrete solution u_h converges to the exact solution u as $h \to 0$. For instance, piecewise polynomial approximation spaces of degree p are said to converge with optimal order with respect to h if, for all $v \in V_0$,

$$\inf_{v_h \in V_{0h}} \|v - v_h\|_V \leq Ch^p, \tag{2.12}$$

where $\|\cdot\|_V$ denotes a norm in V. The precise definition of the parameter h relevant for this dissertation is specified later in (3.15). Estimates of type (2.12) form the basis of a priori error analysis and require approximation bounds such as (1.1) or (1.2), depending on the regularity of the exact solution and the underlying discretization. If (2.12) holds, Céa's lemma yields optimal convergence of the Galerkin approximation,

$$\|u - u_h\|_V \leq C \inf_{v_h \in V_{0h}} \|u - v_h\|_V \leq Ch^p\,.$$

Various numerical methods arise from different choices of the approximation spaces V_{0h} and the associated basis functions. A common strategy is to employ piecewise polynomial basis functions with small support, leading to sparse system matrices in (2.11). While finite element methods typically employ piecewise polynomials that are globally C^0-continuous, IGA makes use of B-splines and NURBS, which will be introduced in Section 2.2 and achieve a higher order of global differentiability.

Collocation methods

In contrast to Galerkin's principle, collocation is based on the strong form of the PDE. The idea is to enforce the differential equation and the boundary conditions pointwise at a prescribed set of collocation points. More precisely, let $\psi_j \in C^2(\overline{\Omega})$, $j = 1, 2, \dots, l$ be basis functions with $\psi_j = 0$ on Γ_D. We then represent the discrete solution as a linear combination of these functions,

$$u_h = \sum_{j=1}^{l} u_h^j \, \psi_j, \tag{2.13}$$

and determine the coefficients $u_h^j \in \mathbb{R}$ such that u_h satisfies the model problem at l collocation points $\boldsymbol{\tau}_j \in \overline{\Omega}$, $j = 1, 2 \dots, l$, namely,

$$\begin{aligned} -\Delta u_h(\boldsymbol{\tau}_j) &= f(\boldsymbol{\tau}_j) \qquad \text{for } j = 1, 2, \dots, l_\Omega, \\ \frac{\partial u_h}{\partial n}(\boldsymbol{\tau}_j) &= 0 \qquad\quad \text{for } j = l_\Omega + 1, l_\Omega + 2, \dots, l. \end{aligned} \tag{2.14}$$

Note that the points $\boldsymbol{\tau}_j \in \Omega$, $j = 1, 2, \dots, l_\Omega$ lie in the interior of the domain, while the points $\boldsymbol{\tau}_j \in \Gamma_N$, $j = l_\Omega+1, l_\Omega+2, \dots, l$, are collocation points on the Neumann boundary. The homogeneous Dirichlet BC is automatically satisfied by the choice of basis functions, and therefore no collocation points are required on Γ_D. Inserting the ansatz (2.13) into these conditions yields the matrix system

$$A_c \, \vec{u}_h = B_c \,, \tag{2.15}$$

with the coefficient vector $\vec{u}_h = \left(u_h^j\right)_{j \in \{1,2,\dots,l\}}$ and the matrices

$$A_c = \begin{pmatrix} -\Delta\psi_1(\boldsymbol{\tau}_1) & -\Delta\psi_2(\boldsymbol{\tau}_1) & \dots & -\Delta\psi_l(\boldsymbol{\tau}_1) \\ \vdots & \vdots & \vdots & \vdots \\ -\Delta\psi_1(\boldsymbol{\tau}_{l_\Omega}) & -\Delta\psi_2(\boldsymbol{\tau}_{l_\Omega}) & \dots & -\Delta\psi_l(\boldsymbol{\tau}_{l_\Omega}) \\ \frac{\partial\psi_1}{\partial n}(\boldsymbol{\tau}_{l_\Omega+1}) & \frac{\partial\psi_2}{\partial n}(\boldsymbol{\tau}_{l_\Omega+1}) & \dots & \frac{\partial\psi_l}{\partial n}(\boldsymbol{\tau}_{l_\Omega+1}) \\ \vdots & \vdots & \vdots & \vdots \\ \frac{\partial\psi_1}{\partial n}(\boldsymbol{\tau}_l) & \frac{\partial\psi_2}{\partial n}(\boldsymbol{\tau}_l) & \dots & \frac{\partial\psi_l}{\partial n}(\boldsymbol{\tau}_l) \end{pmatrix}, \quad B_c = \begin{pmatrix} f(\boldsymbol{\tau}_1) \\ \vdots \\ f(\boldsymbol{\tau}_{l_\Omega}) \\ 0 \\ \vdots \\ 0 \end{pmatrix}, \tag{2.16}$$

where the first l_Ω rows correspond to the interior collocation points and the remaining rows to the collocation points on the Neumann boundary. A crucial consequence of this formulation is that the basis functions must be twice continuously differentiable in the entire computational domain, which excludes classical C^0-continuous finite elements. This restriction is naturally overcome within the isogeometric spline framework introduced below, which provides the required level of smoothness.

While several theoretical results are available for isogeometric collocation methods in one dimension, see, for instance, [Aur+10], the numerical analysis and convergence theory for spline-based collocation methods in higher dimensions is still incomplete. Results are known only for particular cases; see, for example, [AS84; Pre89]. A further delicate issue is the choice of the collocation points, which can significantly influence the convergence order [MST17].

2.2 B-splines, NURBS and quasi-interpolants

This section contains an introduction to the basic concepts of B-splines, NURBS, and related quasi-interpolation operators that are used throughout this thesis. The main purpose is to fix notation

and to collect the definitions and properties required for the numerical analysis of isogeometric methods. The presentation follows standard references in the literature [Baz+06; BBSV14; BCS12], but is tailored to the needs of this dissertation. Further background can be found in the books [CHB09; LMS18; Sch07].

2.2.1 Univariate B-splines, NURBS, and Refinement Algorithms

We begin with the description of univariate B-splines and NURBS, including their basic properties, refinement algorithms, and the construction of a corresponding quasi-interpolant.

Definition and properties

Let $p \in \mathbb{N}_0$ and $n \in \mathbb{N}$. We call $\Xi := \{\xi_1, \xi_2, \dots, \xi_{n+p+1}\}$ a *p-open knot vector* if

$$\xi_1 = \xi_2 = \cdots = \xi_{p+1} < \xi_{p+2} \leq \xi_{p+3} \leq \cdots \leq \xi_{n-1} \leq \xi_n < \xi_{n+1} = \xi_{n+2} = \cdots = \xi_{n+p+1},$$

where $\xi_i \in \mathbb{R}$, $i = 1, \dots, n+p+1$, is called the i-th knot which is allowed to occur repeatedly. Without loss of generality, we assume $\xi_1 = 0$ and $\xi_{n+p+1} = 1$. Furthermore, we define the vector $Z = \{\zeta_1, \zeta_2, \dots, \zeta_N\}$ of knots without repetitions, also called breakpoints, by

$$\Xi = \{\underbrace{\zeta_1, \dots, \zeta_1}_{m_1 \text{ times}}, \underbrace{\zeta_2, \dots, \zeta_2}_{m_2 \text{ times}}, \dots, \underbrace{\zeta_N, \dots, \zeta_N}_{m_N \text{ times}}\},$$

where $N \in \mathbb{N}$ is the total number of pairwise distinct knots and $m_j \in \mathbb{N}$ denotes the multiplicity of the breakpoint ζ_j such that $\sum_{j=1}^{N} m_j = n + p + 1$. For p-open knot vectors, $m_1 = m_N = p + 1$ always holds, and we assume $m_j \leq p + 1$ for the internal knot multiplicities. The entries of Z thereby induce a mesh on the unit interval $[0, 1]$.

B-splines of degree p are denoted by

$$\widehat{B}_{i,p} \colon [0,1] \to \mathbb{R}, \quad \zeta \mapsto \widehat{B}_{i,p}(\zeta), \quad i = 1, 2, \dots, n,$$

and can be constructed recursively from the knot vector Ξ using the Cox–de Boor formula. For $p = 0$, we define

$$\widehat{B}_{i,0}(\zeta) = \begin{cases} 1 & \text{if } \xi_i \leq \zeta < \xi_{i+1}\,, \\ 0 & \text{else}\,, \end{cases}$$

and for $p \geq 1$,

$$\widehat{B}_{i,p}(\zeta) = \frac{\zeta - \xi_i}{\xi_{i+p} - \xi_i} \widehat{B}_{i,p-1}(\zeta) + \frac{\xi_{i+p+1} - \zeta}{\xi_{i+p+1} - \xi_{i+1}} \widehat{B}_{i+1,p-1}(\zeta)\,,$$

with the convention $0/0 := 0$. These functions form a basis of the space of splines on the subdivision Z, that is, piecewise polynomials of degree p with $p - m_j$ continuous derivatives at the internal breakpoints ζ_j, $j = 2, \dots, N-1$, where $p - m_j = -1$ stands for a discontinuity at ζ_j. Among other characteristics, the B-spline basis functions are non-negative and form a partition of unity. We denote the corresponding *univariate spline space* by

$$S_p(\Xi) = \operatorname{span}\left\{\widehat{B}_{i,p} : i = 1, 2, \dots, n\right\}.$$

In Figure 2.2, we illustrate two cubic B-spline ensembles to showcase the varying smoothness at internal knots. The functions visualized in Figure 2.2a are constructed from the open knot vector $\Xi =$

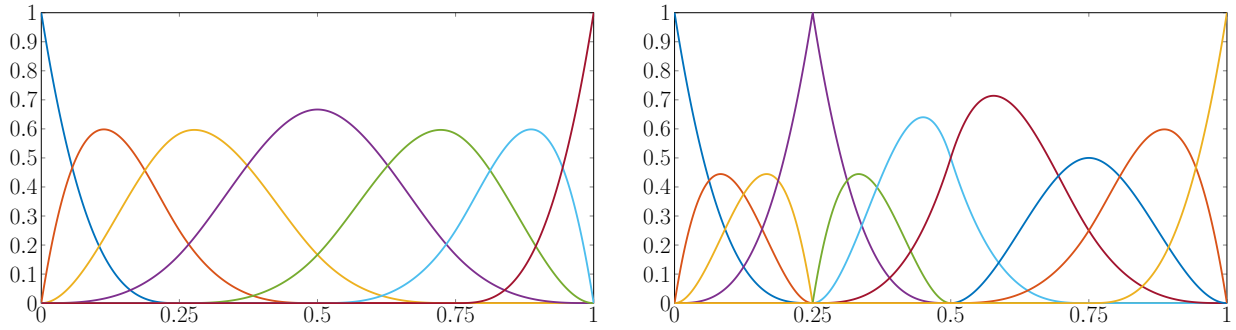

(a) (b)

Figure 2.2: Examples of cubic B-spline functions constructed from different knot vectors Ξ. (a): $\Xi = \{0,0,0,0,\frac{1}{4},\frac{1}{2},\frac{3}{4},1,1,1,1\}$. (b): $\Xi = \{0,0,0,0,\frac{1}{4},\frac{1}{4},\frac{1}{4},\frac{1}{2},\frac{1}{2},\frac{3}{4},1,1,1,1\}$.

$\{0,0,0,0,\frac{1}{4},\frac{1}{2},\frac{3}{4},1,1,1,1\}$ and are C^2-continuous at the breakpoints $\frac{1}{4}$, $\frac{1}{2}$ and $\frac{3}{4}$. In contrast, Figure 2.2b displays B-splines defined by the open knot vector $\Xi = \{0,0,0,0,\frac{1}{4},\frac{1}{4},\frac{1}{4},\frac{1}{2},\frac{1}{2},\frac{3}{4},1,1,1,1\}$, where repeated interior knot values lead to C^0, C^1 and C^2-regularity at the breakpoints $\frac{1}{4}$, $\frac{1}{2}$ and $\frac{3}{4}$, respectively.

The support of each basis function is given by $\operatorname{supp}(\widehat{B}_{i,p}) = [\xi_i, \xi_{i+p+1}]$. For each interval $I_j = (\zeta_j, \zeta_{j+1})$, which can equivalently be written as $I_j = (\xi_i, \xi_{i+1})$ for a unique index i, we define the support extension $\widetilde{I}_j$ by

$$\widetilde{I}_j = (\xi_{i-p}, \xi_{i+p+1}), \tag{2.17}$$

which represents the interior of the union of the supports of all basis functions whose support intersects I_j. That is, we have

$$\overline{\widetilde{I}_j} = \bigcup_{\{k\,:\,\operatorname{supp}(\widehat{B}_{k,p})\cap I_j \neq \emptyset\}} \operatorname{supp}(\widehat{B}_{k,p}) = [\xi_{i-p}, \xi_{i+p+1}].$$

Spline and NURBS curves

By associating each basis function $\widehat{B}_{i,p}$, $i = 1,\dots,n$ with a control point $\boldsymbol{c}_i \in \mathbb{R}^m$, $m = 2,3$, we define a *spline curve* as the linear combination

$$\boldsymbol{C}(\zeta) = \sum_{i=1}^{n} \boldsymbol{c}_i\, \widehat{B}_{i,p}(\zeta)\,.$$

However, classical splines face restrictions in representing essential geometries like conic sections. To overcome this limitation, *non-uniform rational B-splines* (NURBS) are introduced, see [PT95] for more details. Therefore, the *weight function*

$$W(\zeta) = \sum_{l=1}^{n} w_l\, \widehat{B}_{l,p}(\zeta)$$

is determined by choosing positive constants $w_l > 0$, $l = 1,\dots,n$, which are called weights. The NURBS basis functions are then defined by

$$\widehat{N}_{i,p}(\zeta) = \frac{w_i \widehat{B}_{i,p}(\zeta)}{\sum_{l=1}^{n} w_l\, \widehat{B}_{l,p}(\zeta)} = \frac{w_i \widehat{B}_{i,p}(\zeta)}{W(\zeta)}, \quad i = 1,\dots,n,$$

and we denote the corresponding NURBS space by

$$N_p(\Xi, W) = \operatorname{span}\left\{\widehat{N}_{i,p} : i = 1, \dots, n\right\}.$$

A NURBS curve can now be introduced in the same way as a spline curve,

$$\boldsymbol{C}(\zeta) = \sum_{i=1}^{n} \boldsymbol{c}_i \, \widehat{N}_{i,p}(\zeta)\,,$$

where again $\{\boldsymbol{c}_i\}_{i=1,\dots,n}$ is the set of control points $\boldsymbol{c}_i \in \mathbb{R}^m$, $m = 2, 3$, that are chosen depending on the geometry to be parameterized.

Refinement algorithms

Refinement in geometric modelling consists in enriching a spline or NURBS curve with additional control points without altering its parametrization $\boldsymbol{C}(\zeta)$. Accordingly, the refined function space must contain the original space of the parameterization. In the case of NURBS, this additionally requires the weight function $W(\zeta)$ to remain unchanged. More precisely, the spline and NURBS spaces $S_p(\Xi)$ and $N_p(\Xi, W)$ are said to be *refinements* of given coarse spaces $S_{p^0}(\Xi^0)$ and $N_{p^0}(\Xi^0, W)$ if

$$S_{p^0}(\Xi^0) \subset S_p(\Xi) \quad \text{and} \quad N_{p^0}(\Xi^0, W) \subset N_p(\Xi, W), \tag{2.18}$$

respectively. Such refinements are realized through two fundamental algorithms, namely knot insertion and degree elevation, whose combination gives rise to three distinct refinement strategies [HCB05].

Knot insertion, also known as *h-refinement*, is the analogue of classical mesh refinement in finite element analysis. Let $\bar{\Xi} := \Xi \cup \bar{\xi}$ denote the knot vector obtained by inserting the knot $\bar{\xi}$ into Ξ, where $\xi_j \le \bar{\xi} \le \xi_{j+1}$. Denoting the knots of $\bar{\Xi}$ by $\bar{\xi}_i$ and the associated B-spline basis functions by $\bar{B}_{i,p}$, the original basis functions $\widehat{B}_{i,p}$ can be expressed as linear combinations of the refined basis functions,

$$\widehat{B}_{i,p}(\zeta) = \alpha_i \bar{B}_{i,p}(\zeta) + (1 - \alpha_{i+1})\, \bar{B}_{i+1,p}(\zeta), \tag{2.19}$$

with coefficients

$$\alpha_i = \begin{cases} 1, & i = 1, \dots, j-p, \\ \dfrac{\bar{\xi} - \bar{\xi}_i}{\bar{\xi}_{i+p+1} - \bar{\xi}_i}, & i = j-p+1, \dots, j, \\ 0, & i = j+1, \dots, n+1. \end{cases} \tag{2.20}$$

If the inserted knot $\bar{\xi}$ coincides with ξ_j or ξ_{j+1}, knot insertion reduces the inter-element continuity of the spline space at $\bar{\xi}$. Since this thesis focuses on convergence theory with respect to the mesh size h, knot insertion is the primary refinement mechanism under consideration. In particular, in Section 3.2.2, we introduce a variant referred to as *graded h-refinement*, which enables the construction of locally refined spline spaces.

The second fundamental refinement mechanism for B-splines is *order elevation*, also referred to as degree elevation or *p-refinement*. It consists of increasing the polynomial degree while maintaining the inter-element continuity, that is, the multiplicity of all breakpoints. Finally, combining degree elevation with knot insertion gives rise to a third refinement strategy, known as *k-refinement*. In this approach, degree elevation is first applied to the spline curve in the coarse space $N_{p_0}(\Xi_0, W)$, followed by knot insertion. This procedure preserves the continuity at the knots of Ξ_0 while simultaneously increasing both the degree and the regularity at newly introduced knots, a feature that has no direct analogue in FEA.

The Greville abscissa

In the context of isogeometric collocation methods, an additional construction is often employed. To each B-spline basis function $\widehat{B}_{j,p}$ we associate the *Greville abscissa*, also known as the knot average, defined by

$$\gamma_{j,p} = \frac{1}{p}\left(\xi_{j+1} + \cdots + \xi_{j+p}\right), \qquad j = 1, \ldots, n, \tag{2.21}$$

where we recall that $\operatorname{supp}(\widehat{B}_{j,p}) = [\xi_j, \xi_{j+p+1}]$ holds. The Greville abscissae naturally arise as the coefficients of the identity function in its expansion with respect to the B-spline basis, namely,

$$\zeta = \sum_{j=1}^{n} \gamma_{j,p}\, \widehat{B}_{j,p}(\zeta).$$

If the multiplicities of the internal knots satisfy $m_j \leq p$ for $j = 2, \ldots, n-1$, the Greville points $\gamma_{j,p}$ are pairwise distinct and form a partition of the interval $[0, 1]$, which we refer to as the Greville mesh.

A univariate quasi-interpolant

We next introduce a projection operator onto the univariate spline space, which is standard in isogeometric approximation theory [Baz+06; BBSV14; BCS12]. Specifically, we define

$$\Pi_{p,\Xi} : L^1([0,1]) \to S_p(\Xi), \quad \Pi_{p,\Xi}(v) := \sum_{i=1}^{n} \lambda_{i,p}(v)\, \widehat{B}_{i,p}, \tag{2.22}$$

where $\lambda_{j,p}$ are dual functionals satisfying

$$\lambda_{i,p}(\widehat{B}_{k,p}) = \delta_{ik}, \tag{2.23}$$

and δ_{ik} is the Kronecker symbol. In general, $\Pi_{p,\Xi}$ is not an interpolation operator, but it is typically called a *quasi-interpolant* in the literature. It is straightforward to verify that $\Pi_{p,\Xi}$ preserves splines,

$$\Pi_{p,\Xi}(v) = v \quad \text{for all } v \in S_p(\Xi),$$

The dual basis $\{\lambda_{i,p}\}_{i=1,\ldots,n}$ can be chosen in several ways [LLM01]. Here, we adopt the classical construction developed in [Sch07, Section 4.6],

$$\lambda_{i,p}(v) = \int_{\xi_j}^{\xi_{j+p+1}} v(s)\, D^{p+1}\psi_i(s)\, \mathrm{d}s, \tag{2.24}$$

where $\psi_i(\zeta) = G_i(\zeta)\Psi_i(\zeta)$ with

$$\Psi_i(\zeta) = \frac{(\zeta - \xi_{i+1}) \cdots (\zeta - \xi_{i+p})}{p!} \tag{2.25}$$

and

$$G_i(\zeta) = g\left(\frac{2\zeta - \xi_i - \xi_{i+p+1}}{\xi_{i+p+1} - \xi_i}\right), \tag{2.26}$$

where g denotes the transition function described in [Sch07, Theorem 4.37]. Note that the dual functionals (2.24) are well-defined for all $v \in L^1([0,1])$, see [Sch07, Theorem 4.41].

The presented quasi-interpolant is commonly adapted further to be interpolatory at the boundary $\widehat{\Gamma} = \{0,1\}$, see [BBSV14],

$$\Pi^{\widehat{\Gamma}}_{p,\Xi} : C([0,1]) \to S_p(\Xi), \quad \Pi^{\widehat{\Gamma}}_{p,\Xi}(v) := \sum_{i=1}^{n} \lambda^{\widehat{\Gamma}}_{i,p}(v)\, \widehat{B}_{i,p} \quad \text{with} \tag{2.27}$$

$$\lambda^{\widehat{\Gamma}}_{1,p}(v) = v(0), \quad \lambda^{\widehat{\Gamma}}_{n,p}(v) = v(1), \quad \lambda^{\widehat{\Gamma}}_{i,p}(v) = \lambda_{i,p}(v),\ i = 2,\dots,n-1. \tag{2.28}$$

Since we only consider open knot vectors, the first and last B-spline basis function are interpolatory, that is,

$$\lambda^{\widehat{\Gamma}}_{1,p}(B_{1,p}) = B_{1,p}(0) = 1 \quad \text{and} \quad \lambda^{\widehat{\Gamma}}_{n,p}(B_{n,p}) = B_{n,p}(1) = 1. \tag{2.29}$$

Moreover, we have

$$\lambda^{\widehat{\Gamma}}_{1,p}(B_{i,p}) = B_{i,p}(0) = 0 \quad \text{and} \quad \lambda^{\widehat{\Gamma}}_{n,p}(B_{i,p}) = B_{i,p}(1) = 0 \quad \text{for } i = 2,3,\dots,n-1, \tag{2.30}$$

hence, the modified functionals $\lambda^{\widehat{\Gamma}}_{i,p}(v)$ also satisfy the dual functional property (2.23).

2.2.2 Bivariate B-splines, NURBS, and Bézier meshes

Subsequently, the univariate concepts are extended to the bivariate setting by means of tensor product constructions. Moreover, we introduce bivariate NURBS geometries together with the associated Bézier meshes, and conclude this section with the definition of a bivariate quasi-interpolant that is fundamental to the numerical analysis developed in this thesis.

NURBS geometries and Bézier meshes

For $l = 1,2$, let $n_l \in \mathbb{N}$, degrees $p_l \in \mathbb{N}$, and p_l-open knot vectors $\Xi_l = \{\xi_{l,1}, \xi_{l,2} \dots, \xi_{l,n_l+p+1}\}$ be given. We define the polynomial degree vector $\boldsymbol{p} = (p_1, p_2)$ and the bivariate knot vector $\boldsymbol{\Xi} = (\Xi_1, \Xi_2)$. In addition, let $N_l \in \mathbb{N}$ denote the number of knots without repetition in the l-th direction, and let the corresponding univariate knot vectors of breakpoints be given by $Z_l = \{\zeta_{l,1}, \zeta_{l,2} \dots, \zeta_{l,N_l}\}$, $l = 1,2$. The vectors Z_1 and Z_2 induce a Cartesian grid in the *parametric domain* $\widehat{\Omega} = (0,1)^2$, which defines the *parametric Bézier mesh* $\widehat{\mathcal{M}}$,

$$\widehat{\mathcal{M}} := \left\{ Q_{\boldsymbol{j}} \subset \widehat{\Omega} : Q_{\boldsymbol{j}} = Q_{(j_1,j_2)} = (\zeta_{1,j_1}, \zeta_{1,j_1+1}) \times (\zeta_{2,j_2}, \zeta_{2,j_2+1}),\ \boldsymbol{j} \in \boldsymbol{J} \right\}, \tag{2.31}$$

where we introduce the set of multi-indices $\boldsymbol{J} = \{\boldsymbol{j} = (j_1, j_2) : 1 \le j_l \le N_l - 1,\ l = 1,2\}$. The diameter of an element $Q_{\boldsymbol{j}} \in \widehat{\mathcal{M}}$ is denoted by $h_{Q_{\boldsymbol{j}}}$. Moreover, we introduce the support extension of a Bézier element $Q_{\boldsymbol{j}} \in \widehat{\mathcal{M}}$,

$$\widetilde{Q}_{\boldsymbol{j}} := \widetilde{I}_{1,j_1} \times \widetilde{I}_{2,j_2}, \tag{2.32}$$

where $\widetilde{I}_{l,j_l}$ is the univariate support extension of $I_{l,j_l} = (\zeta_{l,j_l}, \zeta_{l,j_l+1})$ from (2.17) for $l = 1,2$. The concept is illustrated for polynomial degree $\boldsymbol{p} = (2,1)$ in the left half of Figure 2.3.

For each $\boldsymbol{i} \in \boldsymbol{I} = \{\boldsymbol{i} = (i_1, i_2) : 1 \le i_l \le n_l,\ l = 1,2\}$, bivariate B-spline functions are defined by

$$\widehat{B}_{\boldsymbol{i},\boldsymbol{p}} : [0,1]^2 \to \mathbb{R}, \quad \widehat{B}_{\boldsymbol{i},\boldsymbol{p}}(\boldsymbol{\zeta}) = \widehat{B}_{i_1,p_1}(\zeta_1)\, \widehat{B}_{i_2,p_2}(\zeta_2),$$

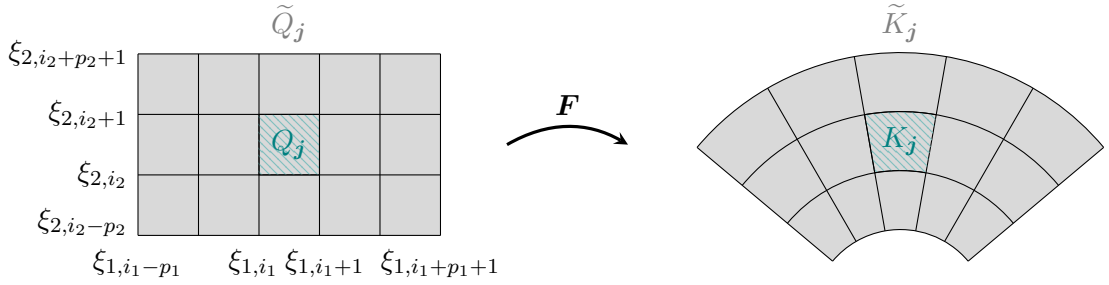

Figure 2.3: Illustration of the support extensions $\widetilde{Q}_{\boldsymbol{j}}$ and $\widetilde{K}_{\boldsymbol{j}} = \boldsymbol{F}(\widetilde{Q}_{\boldsymbol{j}})$ of a parametric and physical Bézier mesh element $Q_{\boldsymbol{j}} \in \widehat{\mathcal{M}}$ and $K_{\boldsymbol{j}} = \boldsymbol{F}(Q_{\boldsymbol{j}}) \in \mathcal{M}$, respectively. Here, $\boldsymbol{i} = (i_1, i_2) \in \boldsymbol{I}$ is such that $Q_{\boldsymbol{j}} = I_{1,j_1} \times I_{2,j_2} = (\zeta_{1,j_1}, \zeta_{1,j_1+1}) \times (\zeta_{2,j_2}, \zeta_{2,j_2+1}) = (\xi_{1,i_1}, \xi_{1,i_1+1}) \times (\xi_{2,i_2}, \xi_{2,i_2+1})$, and hence, $\widetilde{Q}_{\boldsymbol{j}} = \widetilde{I}_{1,j_1} \times \widetilde{I}_{2,j_2} = (\xi_{1,i_1-p_1}, \xi_{1,i_1+p_1+1}) \times (\xi_{2,i_2-p_2}, \xi_{2,i_2+p_2+1})$, see (2.32) and (2.17). In this example, we choose $\boldsymbol{p} = (p_1, p_2) = (2, 1)$ and assume that the knots ξ_{l,k_l}, $k_l \in \{i_l - p_l, i_l + p_l + 1\}$, $l = 1, 2$, are pairwise distinct.

and the spline space on the parametric domain $\widehat{\Omega}$ is given by

$$S_{\boldsymbol{p}}(\boldsymbol{\Xi}) = \operatorname{span}\left\{ \widehat{B}_{\boldsymbol{i},\boldsymbol{p}} : \boldsymbol{i} \in \boldsymbol{I} \right\}.$$

The corresponding bivariate NURBS basis functions then read

$$\widehat{N}_{\boldsymbol{i},\boldsymbol{p}}(\boldsymbol{\zeta}) = \frac{w_{\boldsymbol{i}}\, \widehat{B}_{\boldsymbol{i},\boldsymbol{p}}(\boldsymbol{\zeta})}{W(\boldsymbol{\zeta})},$$

with the weight function

$$W(\boldsymbol{\zeta}) = \sum_{\boldsymbol{l} \in \boldsymbol{I}} w_{\boldsymbol{l}}\, \widehat{B}_{\boldsymbol{l},\boldsymbol{p}}(\boldsymbol{\zeta}), \tag{2.33}$$

where we choose weights $w_{\boldsymbol{i}} > 0$ for all $\boldsymbol{i} \in \boldsymbol{I}$. The space of NURBS on the parametric domain is denoted by

$$N_{\boldsymbol{p}}(\boldsymbol{\Xi}, W) = \operatorname{span}\left\{ \widehat{N}_{\boldsymbol{i},\boldsymbol{p}} : \boldsymbol{i} \in \boldsymbol{I} \right\}.$$

Bivariate NURBS parameterizations of planar geometries are defined as linear combinations of the tensor product functions introduced above,

$$\boldsymbol{F}(\boldsymbol{\zeta}) = \sum_{\boldsymbol{i} \in \boldsymbol{I}} \boldsymbol{c}_{\boldsymbol{i}} \widehat{N}_{\boldsymbol{i},\boldsymbol{p}}(\boldsymbol{\zeta}), \tag{2.34}$$

where each basis function is associated with a control point $\boldsymbol{c}_{\boldsymbol{i}} \in \mathbb{R}^2$, $\boldsymbol{i} \in \boldsymbol{I}$. The $\boldsymbol{F}$-image $\Omega = \boldsymbol{F}(\widehat{\Omega})$ of the parametric domain $\widehat{\Omega} = (0, 1)^2$ is commonly referred to as the *physical domain*. This construction yields exact parameterizations $\boldsymbol{F} \colon \widehat{\Omega} \to \Omega$ of various types of domains, including geometric primitives such as conic sections [Boo01; CHB09; Far95; PT95].

Refinements of bivariate spline and NURBS spaces can be defined similar to (2.18), and the univariate refinement algorithms presented above extend naturally to the bivariate setting. To define a mesh on the physical domain Ω, we consider the image under $\boldsymbol{F}$ of the parametric Bézier

mesh (2.31). More precisely, each parametric mesh element $Q_{\boldsymbol{j}} \in \widehat{\mathcal{M}}$ is mapped to a physical mesh element $K_{\boldsymbol{j}} = \boldsymbol{F}(Q_{\boldsymbol{j}})$, and we set

$$\mathcal{M} := \left\{ K_{\boldsymbol{j}} \subset \Omega : K_{\boldsymbol{j}} = \boldsymbol{F}(Q_{\boldsymbol{j}}),\ Q_{\boldsymbol{j}} \in \widehat{\mathcal{M}} \right\},$$

which is commonly known as the *physical Bézier mesh*, or simply Bézier mesh. The meshes resulting from the coarsest knot vector $\boldsymbol{\Xi}^0 = (\Xi_1^0, \Xi_2^0)$ will be denoted by $\widehat{\mathcal{M}}_0$ and $\mathcal{M}_0$. Moreover, we define the support extension $\widetilde{K}_{\boldsymbol{j}} = \boldsymbol{F}(\widetilde{Q}_{\boldsymbol{j}})$ of a physical Bézier mesh element $K_{\boldsymbol{j}} = \boldsymbol{F}(Q_{\boldsymbol{j}}) \in \mathcal{M}$, where $\widetilde{Q}_{\boldsymbol{j}}$ denotes the support extension (2.32) of $Q_{\boldsymbol{j}} \in \widehat{\mathcal{M}}$; see Figure 2.3 for an illustration.

A bivariate quasi-interpolant

The univariate quasi-interpolant (2.27) can be generalized to the bivariate setting using the tensor product construction described in [BBSV14],

$$\Pi_{\boldsymbol{p},\boldsymbol{\Xi}}(v) = (\Pi_{p_1,\Xi_1} \otimes \Pi_{p_2,\Xi_2})\, .$$

Equivalently, the bivariate quasi-interpolant can be expressed in terms of a dual basis [Boo01, Chapter XVII],

$$\Pi_{\boldsymbol{p},\boldsymbol{\Xi}} : L^1([0,1]^2) \to S_{\boldsymbol{p}}(\boldsymbol{\Xi}), \quad \Pi_{\boldsymbol{p},\boldsymbol{\Xi}}(v) = \sum_{\boldsymbol{i} \in \boldsymbol{I}} \lambda_{\boldsymbol{i},\boldsymbol{p}}(v) \widehat{B}_{\boldsymbol{i},\boldsymbol{p}}, \tag{2.35}$$

where the dual functionals are given by tensor products of (2.24),

$$\lambda_{\boldsymbol{i},\boldsymbol{p}} = \lambda_{i_1,p_1} \otimes \lambda_{i_2,p_2},$$

and satisfy

$$\lambda_{\boldsymbol{i},\boldsymbol{p}}(\widehat{B}_{\boldsymbol{k},\boldsymbol{p}}) = \delta_{\boldsymbol{i}\boldsymbol{k}}. \tag{2.36}$$

Here, $\delta_{\boldsymbol{i}\boldsymbol{k}}$ stands for the multi-index Kronecker symbol, i.e.,

$$\delta_{\boldsymbol{i}\boldsymbol{k}} = \begin{cases} 1 & \text{if } \boldsymbol{i} = (i_1, i_2) = (k_1, k_2) = \boldsymbol{k}, \\ 0 & \text{else.} \end{cases}$$

This operator is typically modified further to account for boundary conditions imposed on the boundary $\widehat{\Gamma} = \partial\widehat{\Omega}$ of the parametric domain $\widehat{\Omega}$. Using the univariate construction (2.27), we define

$$\Pi^{\widehat{\Gamma}}_{\boldsymbol{p},\boldsymbol{\Xi}} = \left(\Pi^{\widehat{\Gamma}}_{p_1,\Xi_1} \otimes \Pi^{\widehat{\Gamma}}_{p_2,\Xi_2} \right) : C([0,1]^2) \to S_{\boldsymbol{p}}(\boldsymbol{\Xi}). \tag{2.37}$$

Due to the properties (2.29) and (2.30), the modified projector satisfies a strong locality property on $\widehat{\Gamma}$: the restriction $(\Pi^{\widehat{\Gamma}}_{\boldsymbol{p},\boldsymbol{\Xi}} v)\big|_{\widehat{\Gamma}_i}$ depends only on $v\big|_{\widehat{\Gamma}_i}$ for each face $\widehat{\Gamma}_i$ of $\widehat{\Gamma}$. Moreover, the operator admits the representation

$$\Pi^{\widehat{\Gamma}}_{\boldsymbol{p},\boldsymbol{\Xi}}(v) = \sum_{\boldsymbol{i} \in \boldsymbol{I}} \lambda^{\widehat{\Gamma}}_{\boldsymbol{i},\boldsymbol{p}}(v) \widehat{B}_{\boldsymbol{i},\boldsymbol{p}}, \tag{2.38}$$

with the modified dual functionals $\lambda^{\widehat{\Gamma}}_{\boldsymbol{i},\boldsymbol{p}} = \lambda^{\widehat{\Gamma}}_{i_1,p_1} \otimes \lambda^{\widehat{\Gamma}}_{i_2,p_2}$, $\boldsymbol{i} \in \boldsymbol{I}$, that is, tensor products of (2.28). These functionals also satisfy the usual duality property (2.36), since all knot vectors under consideration are open. Finally, we point out that the notation $\widehat{\Gamma}$ is used both for the univariate boundary $\widehat{\Gamma} = \{0, 1\}$ and for the bivariate boundary $\widehat{\Gamma} = \partial\widehat{\Omega}$; the intended meaning is always clear from the context.

CHAPTER 3

Numerical analysis of IGA on polar domains with corners

This chapter develops a numerical analysis of isogeometric methods on polar domains in which the polar point coincides with a corner and the associated singularity is taken into account by mesh grading. We largely follow [AZ26] and include some additional examples and an extension to the collocation setting. Section 3.1 motivates the approach, reviews related literature, and highlights the novelties of our analysis. Section 3.2 introduces polar parameterizations and the concept of graded mesh refinement toward polar corners. In Section 3.3, we establish the mathematical framework by introducing polar approximation spaces, suitable projection operators, and weighted polar Sobolev spaces on the parametric domain, together with a detailed study of the transformation of derivatives and norms under polar mappings. Building on this, Section 3.4 is devoted to the derivation of error estimates for graded h-refinement near polar corners that establish optimal convergence of the approximation. After stating the main results, we outline a proof strategy based on a decomposition of the polar domain and show estimates both away from the corner and in its vicinity, which are then combined to obtain error bounds on the full domain. Section 3.5 presents numerical examples in which the proposed mesh grading scheme is employed for Galerkin-based IGA, and the computational results verify our theoretical findings. Finally, in Section 3.6, we introduce an extension of the polar grading concept to the isogeometric collocation framework. Although a corresponding theoretical analysis is not yet available, optimal convergence rates are observed numerically and illustrate the practical effectiveness of graded collocation points.

3.1 Motivation and novelties

The motivation for our approach is largely based on Section 1 of [AZ26] and complemented by an extension of the methodology to the isogeometric collocation framework.

Efficient higher-order approximation and enhanced smoothness of basis functions are central advantages of isogeometric analysis. However, when applied to non-smooth domains with geometric singularities such as corners, standard Galerkin-based IGA encounters significant difficulties. The reduced regularity of PDE solutions near such singularities prevents higher-order convergence and substantially limits the achievable accuracy.

To address these drawbacks, a wide range of refinement and enrichment strategies has been

proposed. From a broader perspective, numerical methods for handling corner singularities can be classified into two main categories: approaches based on local mesh refinement and approaches based on enrichment of the approximation space with singular functions [LL00], with some methods combining both ideas. Within the framework of IGA, a method of the first category has been developed where the parametric mapping is modified to obtain a grading of the mesh [JOKK13]. In a related work, which belongs to both categories, this idea has been combined with an enrichment of the basis by singular functions [OKJ14]. Another representative method is graded CutIGA, where singularities are resolved using arbitrarily cut background meshes while retaining optimal approximation properties [JLL19].

Beyond these approaches, trimmed methods and adaptive refinement techniques have attracted considerable attention in recent years; see, for example, the overview articles [Buf+22; MH18]. Adaptive approaches are typically based on advanced spline technologies such as T-splines, LR-splines, PHT-splines, and hierarchical constructions, which enable flexible local refinement. However, this flexibility usually comes at the cost of increased implementation complexity and higher computational overhead.

The reduced regularity associated with corner singularities is well understood and can often be characterized a priori, which motivates simpler yet equally effective local refinement schemes. In classical finite element methods, graded mesh refinement is a well-established tool for efficiently resolving such singularities and recovering optimal convergence rates [AN98; ASW96; Bab70; MR82; OR68]. In the context of isogeometric analysis, however, grading tensor-product meshes on smoothly parameterized domains leads to the propagation of mesh lines along mapped edges of the parametric domain, resulting in a non-local refinement pattern; see, for example, [BCS12; LMMT15].

The only setting in which mapped graded tensor-product meshes achieve genuinely local refinement toward a point singularity is when one edge of the parametric domain is collapsed into the corner. Such parameterizations closely resemble transformations from polar to Cartesian coordinates; consequently, these geometries are naturally referred to as *polar domains with corners*, the associated mappings as *polar parameterizations* and the considered corner as *polar corner*. By grading the parametric mesh toward the collapsed edge, refinement of the Bézier mesh can be effectively concentrated around the singularity, while maintaining the tensor-product structure of the mesh.

Polar parameterizations emerge naturally within CAD and IGA applications, especially for rotationally symmetric domains. Representative examples include the analysis of cylindrical sector shapes in electromagnetics [Wie+24], arterial geometries in biomechanics [CHB09; Zha+07], and a range of applications in structural mechanics such as the modeling of cylindrical continuum rods [LZ11], vibration analysis of circular plates [CHB09; Zho+20] or acoustic analysis of reactive mufflers [Xue+20]. Furthermore, polar parameterizations appear prominently in scaled boundary parameterizations within IGA [ASKS19], which have recently been extended to simulate plates and shells [ARKS23; RASK23; RKLK24]. The widely known Pacman domain also serves as a singularly mapped benchmark for evaluating adaptive refinement strategies in isogeometric boundary element methods [Fal+19; FGHP16].

Nonetheless, polar mappings suffer from a lack of regularity, and standard isogeometric approximation spaces – defined as push-forwards of the parametric spaces – are not suitable [TJ11; TJ12]. The development of suitable spline spaces for polar domains has become the subject of substantial recent interest [ST21; TSHH17]. Although polar parameterizations are extensively employed in practical engineering applications of IGA, their mathematical foundations, in particular the availability of corresponding approximation estimates, remain underdeveloped. A primary reason for this gap is the inherent singularity introduced at the polar point [TJ11; TJ12], which conflicts with the smoothness assumptions underlying classical IGA approximation theory [Baz+06; BBSV14]. Consequently, such singular configurations are typically excluded. To date, approximation properties in the presence of

polar singularities have only been established for specialized cases, such as singularly parameterized triangular domains [Tak15a] and, more recently, within subdivision-based IGA frameworks [Tak25].

This chapter of the dissertation aims to bridge the described gap in the literature by providing a detailed numerical analysis and deriving error estimates that account for the specific structure of polar parameterizations, thereby addressing the challenges associated with the presence of a polar point. Within this analysis, we allow for the use of graded meshes and establish a theoretical foundation for the choice of the mesh grading parameter required to handle characteristic singularities of the PDE solution at the polar corner. The theoretical findings are validated through numerical experiments. Finally, we apply the grading concept to construct collocation points that are concentrated near polar corners and assess the resulting graded isogeometric collocation method numerically.

The main contributions of this chapter to the state of the art are as follows:

- **A numerical analysis framework tailored to polar parameterizations:** We develop a numerical analysis framework for isogeometric mappings that collapse one edge of the parametric domain onto a physical corner. This includes the definition of a quasi-interpolant for polar splines on the parametric square, the construction of a corresponding projection operator in the physical domain, and the introduction of a new class of polar function spaces. These spaces are built upon weighted Sobolev norms and are naturally suited for pull-backs of functions defined on polar domains with corners.
- **Error estimates for smooth solutions:** Within this framework, we derive error estimates in polar function spaces and transfer them to the physical domain. For a class of sufficiently smooth solutions, our analysis confirms optimal convergence rates that have been previously observed numerically for uniformly refined meshes mapped via a polar parameterization; see, for example, the recent study [Tak25].
- **Error estimates for singular solutions:** We extend our analysis to functions exhibiting classical corner singularities at the polar point. These singularities are captured within appropriately defined weighted Sobolev spaces, enabling a systematic convergence analysis in the non-smooth setting.
- **A graded mesh refinement scheme toward the polar corner:** To approximate the singularity at the polar corner, we introduce a boundary-fitted graded mesh refinement strategy based on a grading parameter, which is prescribed a priori. This approach effectively concentrates degrees of freedom near the polar corner and restores optimal approximation accuracy for non-smooth solutions.
- **Analysis of the optimal grading parameter:** By combining the singular behavior of PDE solutions with the structure of the polar function spaces, we derive explicit conditions on the grading parameter that ensure optimal convergence rates. This provides practical guidance for the construction of effective graded meshes.
- **Numerical implementation and illustrative examples:** We show how to integrate the proposed method into existing IGA codes with minimal effort. A series of benchmark Poisson problems on various polar domains with corners confirms the computational efficiency of the approach and validates the theoretical error estimates.
- **Extension to graded collocation:** We transfer the grading strategy toward polar corners to the isogeometric collocation framework and describe its practical implementation. Numerical experiments indicate optimal convergence rates in the collocation setting, thereby demonstrating the effectiveness of grading concepts beyond Galerkin-based formulations.

In particular, this chapter of the thesis contributes to several active research directions in the IGA community:

- **Alignment with CAD representations:** Rotationally symmetric geometries are naturally described in CAD using polar coordinates, as noted in the seminal IGA textbook [CHB09]. Our analysis strengthens the mathematical foundation for incorporating such parameterizations within IGA. This addresses one of the original goals of IGA, seamless integration with CAD, and highlights a key advantage over classical FEM, which cannot exactly represent circular geometries.
- **Parameterization-sensitive error analysis:** Classical approximation theory in IGA assumes globally smooth parameterizations. In contrast, our framework explicitly accommodates one of the most common geometric singularities, namely the presence of a polar point [BBSV14; HS17; TJ12]. Embedding the mapping properties directly into the analysis represents a first step toward parameterization-aware error estimates in IGA.
- **Simple local refinement strategies for corner singularities:** Many local refinement techniques in IGA rely on advanced spline technologies that require substantial implementation effort and additional libraries, see, e.g., [GV18]. In contrast, the grading approach proposed in this thesis – together with its extension to the collocation framework – can be incorporated into existing IGA codes with only minimal modifications, typically as a post-processing step of standard refinement procedures. It therefore provides a simple and flexible tool for the accurate treatment of corner singularities in both Galerkin and collocation settings, and serves as an accessible framework for studying the interplay between singularities and local refinement in research and teaching contexts.

3.2 Graded mesh refinement in the vicinity of polar corners

In this section, we introduce the main ingredients of our numerical approach, including polar parameterizations of domains with corners and graded mesh refinement. The presentation largely follows Sections 3.1, 3.3, 3.5 and Appendix C of [AZ26].

3.2.1 Polar parameterizations and polar corners

Polar parameterizations in IGA have been extensively studied in multiple research works [ST21; TJ11; TJ12; TSHH17]. The terminology originates from the analogy with the classical transformation from polar to Cartesian coordinates. To establish notation and highlight essential properties, we introduce the following definition, which aligns closely with standard configurations in the literature.

Definition 3.1 (Polar parameterization, polar point, polar domain)**.** An isogeometric mapping $\boldsymbol{F}\colon \widehat{\Omega} \to \Omega$ of the form (2.34), constructed as described in Section 2.2.2, is called a *polar parameterization* if it collapses the left edge of the parametric domain into a single point,

$$\boldsymbol{F}(0, \zeta_2) = \boldsymbol{P} = \boldsymbol{0} \quad \text{for all } \zeta_2 \in [0, 1], \tag{3.1}$$

where $\boldsymbol{P} \in \mathbb{R}^2$ is termed the *polar point* and, without loss of generality, is always chosen as $\boldsymbol{P} = \boldsymbol{0}$. The corresponding image $\Omega = \boldsymbol{F}(\widehat{\Omega})$ is referred to as a *polar domain*.

Next, we specify the considered class of polar domains further with respect to the location of the polar point within the domain.

Definition 3.2 (Polar domain with corner, polar corner)**.** Let $\Omega \subset \mathbb{R}^2$ be a polar domain such that the polar point $\boldsymbol{P}$ lies on the boundary of the domain, i.e., $\boldsymbol{P} \in \Gamma = \partial\Omega$. Then, $\boldsymbol{P}$ represents a vertex of the domain, and Ω is called a *polar domain with corner*. The corresponding interior angle at $\boldsymbol{P}$ is denoted by $\omega \in (0, 2\pi]$. In this context, $\boldsymbol{P}$ is also called the *polar corner* of the domain. Strictly speaking, the case $\omega = \pi$ does not constitute a corner in the geometric sense, but we still regard $\boldsymbol{P}$ as a corner of the parameterization for the purposes of the subsequent analysis.

Definition 3.2 is typically not required in the available literature on polar domains [ST21; TJ11; TJ12; TSHH17], and we point out the background of this choice in the following Remark.

Remark 3.3. The condition $\boldsymbol{P} \in \Gamma$ excludes parameterizations in which the polar point is located inside the domain. A well-known example of such an excluded scenario is the polar parameterization of a unit disk, which additionally requires prescribing periodic boundary conditions on the two boundary edges adjacent to the polar point. In most related publications, a periodicity condition is imposed explicitly [ST21; TSHH17]. Here, we instead require that the boundary of the parametric domain is mapped onto the boundary of the polar domain. The mathematical convergence analysis of the periodic case introduces additional challenges, which go beyond the scope of this thesis. Nonetheless, the mathematical framework developed here may serve as a foundation for future investigations on polar domains without corners like the unit disk - in particular, since numerical results are very promising, see for instance [BCS12, Remark 6.12].

In Figure 3.1, we illustrate exemplary parameterizations of polar domains with corners, which will be discussed in more detail in Examples 3.6, 3.7 and 3.8 at the end of this section. Beforehand, we explain how such isogeometric mappings can be constructed and point out some central properties. We denote the four boundary edges of the parametric domain by $\widehat{\Gamma}_i$, $i = 1, \dots, 4$, following the ordering proposed in [Váz16], see also Figure 3.1. The left edge of the parametric domain collapses as required in (3.1) if all the control points associated to $\widehat{\Gamma}_1$ are located at the polar point [TJ11; TJ12],

$$\boldsymbol{c}_{\boldsymbol{i}_\odot} = \boldsymbol{P} = \boldsymbol{0} \quad \text{for all } \boldsymbol{i}_\odot \in \boldsymbol{I}_\odot := \{\boldsymbol{i} = (i_1, i_2) \in \boldsymbol{I} : i_1 = 1\}, \tag{3.2}$$

where $\boldsymbol{I}_\odot \subset \boldsymbol{I}$ is called the polar index set and $\boldsymbol{I}$ is defined as in Section 2.2.2. Moreover, the coarse linear knot vector

$$\Xi_1^0 = \{0, 0, 1, 1\}$$

is typically employed in the first parametric direction; see Examples 3.6, 3.7 and 3.8. Formula (2.34) and the partition of unity property of NURBS then yield that $\boldsymbol{F}$ is of the form

$$\boldsymbol{F}(\zeta_1, \zeta_2) = \sum_{i_2=1}^{n_2} \widehat{N}_{2,1}(\zeta_1)\widehat{N}_{i_2,p_2}(\zeta_2)\, \boldsymbol{c}_{(2,i_2)} = \zeta_1 \sum_{i_2=1}^{n_2} \widehat{N}_{i_2,p_2}(\zeta_2)\, \boldsymbol{c}_{(2,i_2)} = \zeta_1\, \boldsymbol{G}(\zeta_2),$$

where $\boldsymbol{G} = (G_1, G_2)^T : [0, 1] \to \Gamma_2$ is a NURBS curve that depends only on ζ_2 and parameterizes the part of the boundary away from the polar point, namely, $\Gamma_2 := \boldsymbol{F}(\widehat{\Gamma}_2) = \boldsymbol{G}([0, 1]) \subset \partial\Omega$. The remaining parametric boundary edges are mapped onto the edges adjacent to the corner, $\Gamma_3 := \boldsymbol{F}(\widehat{\Gamma}_3)$, and $\Gamma_4 := \boldsymbol{F}(\widehat{\Gamma}_4)$. This motivates the following assumption which will be useful for the proofs in this chapter.

Assumption 3.4. We assume that the polar parameterization $\boldsymbol{F}$ is of the form

$$\boldsymbol{F}(\zeta_1, \zeta_2) = \zeta_1\, \boldsymbol{G}(\zeta_2) \tag{3.3}$$

with a NURBS curve $\boldsymbol{G} = (G_1, G_2)^T : [0,1] \to \mathbb{R}^2$ such that

$$|\boldsymbol{G}(\zeta_2)| \sim 1.$$

Moreover, we assume that G_1 and G_2 have bounded derivatives at all points where $\boldsymbol{F}$ is differentiable with respect to the second component, and that

$$\left|\boldsymbol{G}(\zeta_2) \times \boldsymbol{G}'(\zeta_2)\right| = \left|G_1(\zeta_2)\, G_2'(\zeta_2) - G_2(\zeta_2)\, G_1'(\zeta_2)\right| \sim 1.$$

Intuitively, Assumption 3.4 guarantees that the curve $\boldsymbol{G}$ parameterizing the boundary part Γ_2 remains bounded and separated from the polar point $\boldsymbol{P} = 0$; see again Figure 3.1 for illustrations. Moreover, its tangent is never parallel to its position vector, meaning that the curve genuinely moves around the polar point and can never move directly toward or away from it. For completeness, we further remind the reader that the isogeometric mapping $\boldsymbol{F}$ generally does not change during the refinement process.

The Jacobian of a polar parameterization of the form (3.3) is given by

$$J_{\boldsymbol{F}}(\zeta_1, \zeta_2) = \begin{pmatrix} G_1(\zeta_2) & \zeta_1\, G_1'(\zeta_2) \\ G_2(\zeta_2) & \zeta_1\, G_2'(\zeta_2) \end{pmatrix} \tag{3.4}$$

at all points $\boldsymbol{\zeta} = (\zeta_1, \zeta_2) \in \widehat{\Omega}$ where $\boldsymbol{F}$ is differentiable with respect to ζ_2. Consequently, under Assumption 3.4, we obtain

$$|\det(J_{\boldsymbol{F}}(\zeta_1, \zeta_2))| = \left|\zeta_1 \left(G_1(\zeta_2)\, G_2'(\zeta_2) - G_2(\zeta_2)\, G_1'(\zeta_2)\right)\right| \sim \zeta_1. \tag{3.5}$$

The parameterization (3.3) contains a polar singularity in the sense that

$$\frac{\partial \boldsymbol{F}}{\partial \zeta_2}(0, \zeta_2) = (0,0)^T \quad \text{and} \quad \det(J_{\boldsymbol{F}}(0, \zeta_2)) = 0.$$

In this regard, the collapsing edge $\widehat{\Gamma}_1$ will sometimes also be called the singular edge. Furthermore, we set $\boldsymbol{\zeta}(\boldsymbol{x}) = (\zeta_1(\boldsymbol{x}), \zeta_2(\boldsymbol{x})) = \boldsymbol{F}^{-1}(\boldsymbol{x})$ for all $\boldsymbol{x} \neq \boldsymbol{0}$ and by the inverse function theorem, we have

$$J_{\boldsymbol{F}^{-1}}(\boldsymbol{x}) = J_{\boldsymbol{F}}^{-1}(\zeta_1(\boldsymbol{x}), \zeta_2(\boldsymbol{x})) = \frac{1}{\det(J_{\boldsymbol{F}}(\zeta_1(\boldsymbol{x}), \zeta_2(\boldsymbol{x})))} \begin{pmatrix} \zeta_1(\boldsymbol{x}) G_2'(\zeta_2(\boldsymbol{x})) & -\zeta_1(\boldsymbol{x}) G_1'(\zeta_2(\boldsymbol{x})) \\ -G_2(\zeta_2(\boldsymbol{x})) & G_1(\zeta_2(\boldsymbol{x})) \end{pmatrix}. \tag{3.6}$$

Due to Assumption 3.4 and (3.5), the determinant of the Jacobian of the inverse transformation is given by

$$|\det\left(J_{\boldsymbol{F}^{-1}}(\boldsymbol{x})\right)| \sim \frac{1}{\zeta_1(\boldsymbol{x})} \tag{3.7}$$

and blows up near the polar point. In this context, we further note another property. Let $r(\boldsymbol{x}) = |\boldsymbol{x}|$ be the distance of every point $\boldsymbol{x} \in \mathbb{R}^2$ to $\boldsymbol{0}$. Then, for all $\boldsymbol{x} \neq \boldsymbol{0}$, it follows from Assumption 3.4 that

$$r(\boldsymbol{x}) = r(\boldsymbol{F}(\boldsymbol{\zeta}(\boldsymbol{x}))) = r(\zeta_1(\boldsymbol{x})\, \boldsymbol{G}(\zeta_2(\boldsymbol{x}))) = \zeta_1(\boldsymbol{x}) |\boldsymbol{G}(\zeta_2(\boldsymbol{x}))| \sim \zeta_1(\boldsymbol{x}), \tag{3.8}$$

while $r(\boldsymbol{0}) = 0$ trivially holds.

Lastly, we comment on the weight function (2.33) introduced in Section 2.2.2. Typically, as in the considered Examples 3.6, 3.7 and 3.8, the weights associated with the same i_2-index are chosen identically,

$$w_{(1,i_2)} = w_{(2,i_2)} = \cdots = w_{(n_1,i_2)}, \quad i_2 = 1, 2, \ldots, n_2.$$

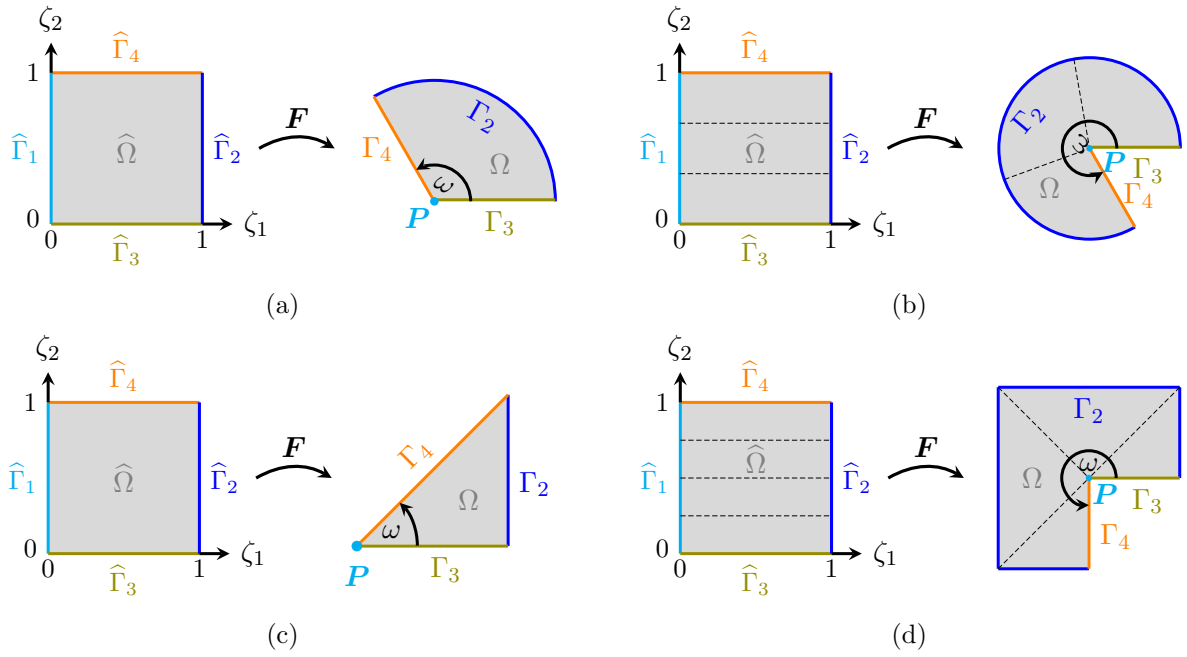

Figure 3.1: Polar parameterizations of exemplary domains with corners and corresponding boundary notation. (a): Circular sector with angle $\omega = \frac{2}{3}\pi$ (b): Circular sector with angle $\omega = \frac{5}{3}\pi$, also known as Pacman domain. (c): Triangle. (d): L-shaped domain.

Using the partition of unity formed by univariate B-splines, it follows that the weight function has the form

$$W(\boldsymbol{\zeta}) = \sum_{\boldsymbol{i}\in\boldsymbol{I}} w_{\boldsymbol{i}} \widehat{B}_{\boldsymbol{i},\boldsymbol{p}}(\boldsymbol{\zeta}) = \sum_{i_1=1}^{n_1} \widehat{B}_{i_1,p_1}(\zeta_1) \sum_{i_2=1}^{n_2} w_{(1,i_2)} \widehat{B}_{i_2,p_2}(\zeta_2) = \sum_{i_2=1}^{n_2} w_{(1,i_2)} \widehat{B}_{i_2,p_2}(\zeta_2)$$

and thus depends only on ζ_2. This leads to the following assumption:

Assumption 3.5. The weight function (2.33) depends solely on ζ_2, that is, there exists a function $w : [0,1] \to \mathbb{R}$ such that

$$W(\boldsymbol{\zeta}) = w(\zeta_2) \quad \text{for all } \boldsymbol{\zeta} = (\zeta_1, \zeta_2) \in \widehat{\Omega}. \tag{3.9}$$

In the following, we investigate in more detail the polar domains with corners depicted in Figure 3.1. Assumptions 3.4 and 3.5 hold for all considered parameterizations, confirming their practical relevance.

Example 3.6 (Circular sector). Consider a circular sector Ω with interior angle $\omega \in (0, \pi)$ and starting angle $\varphi_0 \in [0, 2\pi)$. Without loss of generality, we assume the sector is centered at $\boldsymbol{P} = (0,0)$ and has radius 1, that is, $\Omega = \{(r\cos\varphi, r\sin\varphi) : 0 < r < 1,\ \varphi_0 < \varphi < \varphi_0 + \omega\}$. Such a sector can be parameterized using the knot vectors $\Xi_1^0 = \{0,0,1,1\}$ and $\Xi_2^0 = \{0,0,0,1,1,1\}$, along with the control points provided in Table 3.1 and weights given by $w_{(i_1,i_2)} = \cos\left(\frac{\omega}{2}\right)$ for $i_2 = 2$ and $w_{(i_1,i_2)} = 1$ otherwise, see also [CHB09; Lu09]. An example that illustrates this parameterization for an interior angle of $\omega = \frac{2}{3}\pi$ is displayed in Figure 3.1a. The resulting isogeometric mapping is smooth throughout the interior of the domain, in more detail, it holds $\boldsymbol{F} \in \left(C^2(\widehat{\Omega})\right)^2$, see [BCS12, p.10]. In contrast, a polar parameterization for a circular sector with angle $\omega \in (\pi, 2\pi]$

$\boldsymbol{c}_{(i_1,i_2)}$	$i_2 = 1$	$i_2 = 2$	$i_2 = 3$
$i_1 = 1$	$(0,0)^T$	$(0,0)^T$	$(0,0)^T$
$i_1 = 2$	$(\cos(\varphi_0), \sin(\varphi_0))^T$	$\left(\frac{\cos(\varphi_0+\frac{\omega}{2})}{\cos(\frac{\omega}{2})}, \frac{\sin(\varphi_0+\frac{\omega}{2})}{\cos(\frac{\omega}{2})}\right)^T$	$(\cos(\varphi_0+\omega), \sin(\varphi_0+\omega))^T$

Table 3.1: Definition of control points $\boldsymbol{c_i}, \boldsymbol{i} \in \boldsymbol{I}$, for a polar parameterization of a circular sector with inner angle $\omega \in (0, \pi)$, starting angle $\varphi_0 \in [0, 2\pi)$ and radius 1.

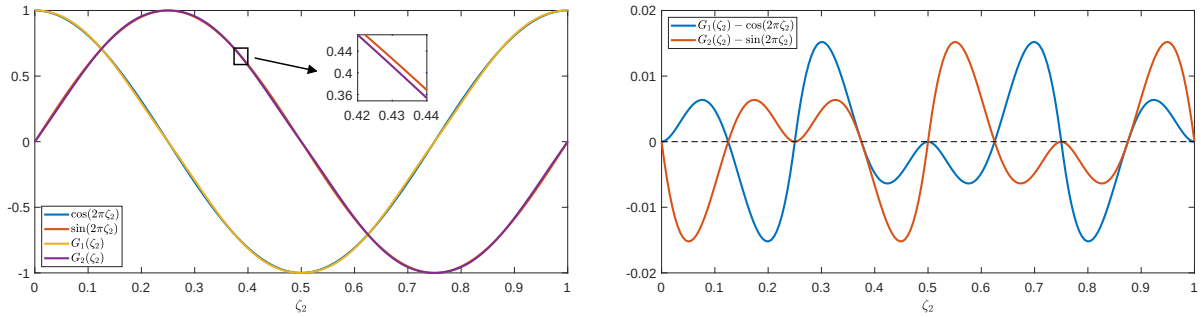

(a) (b)

Figure 3.2: (a): Illustration of the mapping $\zeta_2 \mapsto \boldsymbol{G}(\zeta_2) = (G_1(\zeta_2), G_2(\zeta_2))$ in (3.3) for the polar parameterization of a unit disk with crack together with the classical angular transformation $\zeta_2 \mapsto (\cos(2\pi\zeta_2), \sin(2\pi\zeta_2))$. (b): Difference between the corresponding functions.

can be constructed by combining multiple small sectors. To this end, repeated knot values are inserted into the knot vector Ξ_2^0. For example, a circular sector of angle $\omega = \frac{5}{3}\pi$ can be composed of three smaller sectors, each having an angle of $\frac{5}{9}\pi$, using the knot vectors $\Xi_1^0 = \{0,0,1,1\}$ and $\Xi_2^0 = \{0,0,0,\frac{1}{3},\frac{1}{3},\frac{2}{3},\frac{2}{3},1,1,1\}$. The seven control points and corresponding weights are derived by combining those of the three smaller sectors as listed in in Table 3.1, where repetitions are omitted. The resulting geometry mapping is visualized in Figure 3.1b. However, inserting repeated knot values reduces the inter-element smoothness to C^0, thus yielding a parameterization $\boldsymbol{F} \in \left(C^0(\widehat{\Omega})\right)^2$. Finally, a circular sector with angle $\omega = 2\pi$, corresponding to a unit disk with crack as shown in Figure 1.1a, can be constructed from four quarter disks using the knot vectors $\Xi_1^0 = \{0,0,1,1\}$ and $\Xi_2^0 = \{0,0,0,\frac{1}{4},\frac{1}{4},\frac{1}{2},\frac{1}{2},\frac{3}{4},\frac{3}{4},1,1,1\}$. Based on the study in [AZ24a], an explicit representation of the angular function $\boldsymbol{G} = (G_1, G_2)$ appearing in the isogeometric mapping (3.3) is displayed in Figure 3.2a, together with a detailed comparison to the angular functions in the classical transformation from polar to Cartesian coordinates, namely $\zeta_2 \mapsto \cos(2\pi\zeta_2)$ and $\zeta_2 \mapsto \sin(2\pi\zeta_2)$. Moreover, Figure 3.2b illustrates the marginal differences between the two parameterizations, which coincide at the points $\zeta_2 = \frac{i}{8}$, $i = 0, 1, \ldots, 8$. This comparison further justifies the terminology *polar parameterization* used for the considered isogeometric mappings and confirms that Assumption 3.4 is indeed satisfied.

Example 3.7 (**Triangle**)**.** Another domain that can be represented by a polar parameterization is a triangle, using the knot vectors $\Xi_1^0 = \Xi_2^0 = [0,0,1,1]$. For instance, choosing the control points as $\boldsymbol{c}_{(1,1)} = \boldsymbol{c}_{(1,2)} = (0,0)$, $\boldsymbol{c}_{(2,1)} = (1,0)$ and $\boldsymbol{c}_{(2,2)} = (0,1)$ and weights $w_{\boldsymbol{i}} = 1$, $\boldsymbol{i} \in \boldsymbol{I}$, generates a triangular domain defined by the three distinct control points. In this construction, the polar

$\boldsymbol{c}_{(i_1,i_2)}$	$i_2 = 1$	$i_2 = 2$	$i_2 = 3$	$i_2 = 4$	$i_2 = 5$
$i_1 = 1$	$(0,0)^T$	$(0,0)^T$	$(0,0)^T$	$(0,0)^T$	$(0,0)^T$
$i_1 = 2$	$(1,0)^T$	$(1,1)^T$	$(-1,1)^T$	$(-1,-1)^T$	$(0,-1)^T$

Table 3.2: Definition of control points $\boldsymbol{c_i}$ and weights $w_{\boldsymbol{i}}$, $\boldsymbol{i} \in \boldsymbol{I}$, for a polar parameterization of an L-shaped domain.

singularity is located at the vertex $\boldsymbol{P} = (0,0)$. Such triangular configurations have been extensively studied in previous works [Tak15a; Tak15b]. The resulting parameterization is given by

$$\boldsymbol{F} : \widehat{\Omega} \to \Omega, \quad (\zeta_1, \zeta_2) \mapsto (\zeta_1, \zeta_1\zeta_2),$$

which is smooth at all inner points of the domain, i.e., $\boldsymbol{F} \in \left(C^\infty(\widehat{\Omega})\right)^2$.

Example 3.8 (**L-Shape**)**.** More complex geometries can be constructed by combining multiple polar triangles. For instance, an L-shaped domain can be represented by connecting four polar triangles, each parameterized from the unit square via a polar mapping. Precisely, we can use the knot vectors $\Xi_1^0 = \{0,0,1,1\}$ and $\Xi_2^0 = \{0,0,\frac{1}{4},\frac{1}{2},\frac{3}{4},1,1\}$, the control points listed in Table 3.2 and the constant weights $w_{\boldsymbol{i}} = 1$, $\boldsymbol{i} \in \boldsymbol{I}$. The resulting isogeometric mapping is depicted in Figure 3.1d. Due to the repeated knot values in Ξ_2^0, the global mapping is only C^0-continuous, that is, $\boldsymbol{F} \in \left(C^0(\widehat{\Omega})\right)^2$.

Remark 3.9. Lastly, we discuss limitations of the polar parameterizations considered in this work and compare them with alternative strategies available in the literature.

- Generally, the polar domains considered in this chapter possess multiple corners, not only the polar corner. More specifically, at least two further corners usually occur at the intersections of the boundary edge Γ_2 with its adjacent edges Γ_3 and Γ_4, as illustrated in all examples shown in Figure 3.1. Additional corners may also appear along the boundary segment Γ_2, as seen in the L-shaped domain discussed in Example 3.8. However, these corners do not correspond to polar points of the parameterization, and the approximation properties near such corners are well understood. In accordance with the focus of this dissertation, we therefore restrict our analysis to the local behavior near polar corners and do not further investigate the remaining ones.
- The continuity of the polar parameterizations depends strongly on the interior angle at the corner and leads to trade-offs determined by the chosen refinement strategy and the underlying geometry representation.
  - For corner angles $\omega < \pi$, the polar parameterization remains smooth throughout the interior of the domain, preserving all advantages of higher-order smooth spline spaces, see Examples 3.6 and 3.7.
  - For domains with interior angles $\omega > \pi$, repeated knot insertion is required, which reduces inter-element continuity, as demonstrated in Examples 3.6 and 3.8. This phenomenon can be explained via the geometric interpretation of NURBS parameterizations as projective transformations of piecewise quadratic curves and has been investigated in the literature, see, for instance, the discussion of circular arcs in the seminal IGA book [Baz+06, Section 2.2.1]. While C^0-continuity remains sufficient for second-order PDEs, higher

smoothness can be achieved using more advanced parameterization techniques instead. These include multipatch constructions, unstructured spline methods such as splines on triangulations, D-patch constructions, subdivision-based discretizations, almost-C^1 schemes, and trimming; see for instance [JLL19; NKP14; ST21; Tak25; TT23; TSHH17]. Given the range of available approaches, the list is not exhaustive. However, these methods typically require careful patch layout, interface compatibility, or specialized basis functions. In addition, trimming-based techniques may struggle with corner angles of 2π, as encountered in domains with cracks. In this work, we focus on the standard polar parameterization and intentionally keep the geometric complexity to a minimum in order to facilitate analysis and maintain compatibility with standard IGA frameworks.

  - The number and placement of C^0-lines are fixed by the coarse parameterization and remain unchanged under refinement. Between these isolated mesh lines, higher continuity of the shape functions can be enforced using classical isogeometric k-refinement. Accordingly, throughout this thesis, the term B-spline regularity refers to smoothness away from isolated C^0-interfaces. Numerical evidence, provided in Example 3.41, indicates that increasing the continuity of the discrete function space in this manner leads to improved approximation accuracy for the second-order model problem (2.3).

- For the sake of simplicity, this work is confined to single-patch polar parameterizations. Extending the approach to multipatch configurations with potentially smooth coupling could overcome the continuity deficits and remains a topic for future research.

3.2.2 Mesh grading toward polar corners

Let $\Omega \subset \mathbb{R}^2$ be a polar domain with corner as introduced in Section 3.2.1 and $\partial\Omega = \Gamma = \Gamma_N \cup \Gamma_D$ its boundary, where the Dirichlet and Neumann boundary are denoted by Γ_D and Γ_N, respectively, with $\Gamma_N \cap \Gamma_D = \emptyset$. We assume non-empty Dirichlet boundary, $\Gamma_D \neq \emptyset$, and require each boundary edge to be completely contained in either the Dirichlet or the Neumann boundary, that is, $\Gamma_\gamma \subset \Gamma_D$ or $\Gamma_\gamma \subset \Gamma_N$ for $\gamma = 2, 3, 4$. We consider the Poisson equation (2.3). Due to the corner singularity, we need to refine locally toward the corner.

Remark 3.10. Consistent with the title and focus of this chapter, we do not analyze solution regularity at the non-polar corners of the domain, see also Remark 3.9. At those vertices, we assume the solution is sufficiently smooth so as not to affect our local analysis around the polar corner.

Definition of graded h-refinement

Next, we describe how isogeometric meshes can be refined in a graded way to tackle the corner singularities numerically. The idea of mesh grading toward corners is inspired by comparable approaches for finite elements [AN98; ASW96; Bab70; OR68]. Similar concepts have also been proposed in isogeometric literature [BCS12; LMMT15], but only for smoothly parameterized domains, leading to non-local refinement along the mapped edges of a patch. In our recent work [AZ24a], we introduced the grading scheme for polar parameterizations of circular sectors, which will be generalized in the following. To simplify notation and without loss of generality, we assume that the coarse parametric Bézier mesh defined by the coarse knot vector $\boldsymbol{\Xi}^0 = (\Xi_1^0, \Xi_2^0)$ is uniform. That is, we have the coarse vectors of breakpoints

$$Z_l^0 = \left\{ \zeta_{l,j_l} := (j_l - 1)h_l^0 : 1 \leq j_l \leq N_l^0 \right\}, \quad l = 1, 2,$$

with the uniform coarse mesh sizes $h_l^0 = \frac{1}{N_l^0 - 1}$ for some $N_l^0 \in \mathbb{N}$. The construction extends analogously to non-uniform coarse meshes.

The central idea of our method is to modify the typical uniform refinement procedure for the coarse radial knot vector Ξ_1^0. In this way, we achieve a grading of the resulting Bézier mesh toward the corner of the polar domain. In more detail, let $\Xi_1^{\mathrm{u}} = \{\xi_{1,1}^{\mathrm{u}}, \xi_{1,2}^{\mathrm{u}} \dots, \xi_{1,n_1+p_1+1}^{\mathrm{u}}\}$ be a uniform refinement of Ξ_1^0, obtained by standard knot insertion and degree elevation up to degree p_1, and let $Z_1^{\mathrm{u}} = \{\zeta_{1,j_1}^{\mathrm{u}} := (j_1-1)h_1 : 1 \leq j_l \leq N_1\}$ be the corresponding uniform vector of knots without repetitions, where $h_1 = \frac{1}{N_1-1}$ for some $N_1 \in \mathbb{N}$ with $\frac{N_1-1}{N_1^0-1} \in \mathbb{N}$. We choose a *grading parameter* $\mu \in (0,1]$ and define the graded knot vector Ξ_1 by taking all the entries of the uniform vector Ξ_1^{u} to the power of $\frac{1}{\mu}$,

$$\Xi_1 = \left\{\xi_{1,i_1} := (\xi_{1,i_1}^{\mathrm{u}})^{\frac{1}{\mu}} : 1 \leq i_1 \leq n_1 + p_1 + 1\right\} = \left\{(\xi_{1,1}^{\mathrm{u}})^{\frac{1}{\mu}}, (\xi_{1,2}^{\mathrm{u}})^{\frac{1}{\mu}}, \dots, (\xi_{1,n_1+p_1+1}^{\mathrm{u}})^{\frac{1}{\mu}}\right\}. \tag{3.10}$$

Hence, the corresponding graded vector of knots without repetitions is also given by taking all the entries of Z_1 to the power of $\frac{1}{\mu}$,

$$Z_1 = \left\{\zeta_{1,j_1} := (\zeta_{1,j_1}^{\mathrm{u}})^{\frac{1}{\mu}} = ((j_1-1)h_1)^{\frac{1}{\mu}} : 1 \leq j_1 \leq N_1\right\}, \tag{3.11}$$

which we refer to as graded mesh refinement. Note that choosing $\mu = 1$ leads to standard uniform refinement, making the proposed scheme a generalization of classical refinement. In this sense, mesh grading may be interpreted as a post-processing of the uniform mesh. Throughout the thesis, we work exclusively with graded refinement in the first parametric direction, allowing any $\mu \in (0,1]$.

In ζ_2-direction, no adjustments are needed, and we employ a standard uniform refinement $\Xi_2 = \Xi_2^{\mathrm{u}}$ of Ξ_2^0 and its corresponding uniform vector of breakpoints

$$Z_2 = Z_2^{\mathrm{u}} = \left\{\zeta_{2,j_2} = \zeta_{2,j_2}^{\mathrm{u}} = (j_2-1)h_2 : 1 \leq j_2 \leq N_2\right\}, \tag{3.12}$$

with $h_2 = \frac{1}{N_2-1}$ for $N_2 \in \mathbb{N}$ with $\frac{N_2-1}{N_2^0-1} \in \mathbb{N}$. Consequently, we obtain a graded parametric Bézier mesh

$$\widehat{\mathcal{M}}^{\mu} := \left\{Q_{\boldsymbol{j}} \subset \widehat{\Omega} : Q_{\boldsymbol{j}} = (\zeta_{1,j_1}, \zeta_{1,j_1+1}) \times (\zeta_{2,j_2}, \zeta_{2,j_2+1}),\ \boldsymbol{j} \in \boldsymbol{J}\right\},$$

which is locally refined towards the singular edge. The corresponding physical Bézier mesh

$$\mathcal{M}^{\mu} := \{K_{\boldsymbol{j}} \subset \Omega : K_{\boldsymbol{j}} = \boldsymbol{F}(Q_{\boldsymbol{j}}),\ \boldsymbol{j} \in \boldsymbol{J}\}$$

is locally refined towards the polar corner of the domain. In Figure 3.3a and 3.3b, we illustrate the graded meshes in comparison with their uniform counterparts exemplarily for a circular sector and an L-shaped domain.

Remark 3.11. Finally, we collect several observations on the proposed a priori grading scheme.

- Grading the mesh toward the polar corner enables resolution of the singularity through a better distribution of degrees of freedom, without increasing the total number compared to uniform refinement.
- Previous mesh grading strategies in IGA either restricted refinement to mapped edges of smoothly parameterized domains [BCS12; LMMT15], or relied on trimming techniques that can fail when the corner angle equals 2π, see for instance [JLL19]. In contrast, our approach enables mesh grading directly toward the polar point singularity and remains robust even for domains exhibiting cracks.

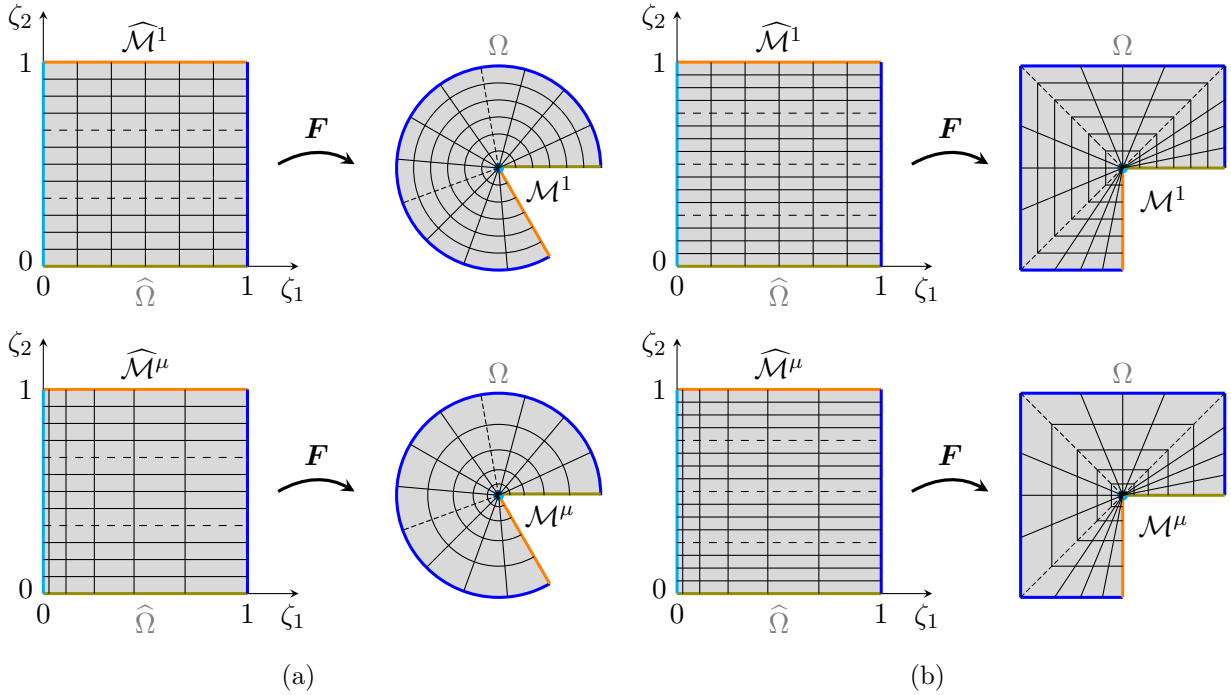

Figure 3.3: Parametric and physical Bézier meshes. First row: Uniform refinement ($\mu = 1$). Second row: Graded refinement ($\mu < 1$). (a): Circular sector. (b): L-shaped domain.

- Our analysis focuses on the local approximation behavior in the vicinity of the polar corner. This setting is particularly challenging due to the singularity of the isogeometric mapping. Therefore, the solution is assumed to be sufficiently smooth elsewhere, and the treatment of other corners is omitted; see also Remarks 3.9 and 3.10.
- Since corner singularities are local phenomena, the grading construction around the polar corner can be applied repeatedly to treat domains with multiple singularities, connected through a multipatch framework. An example is shown in Figure 3.4a, where several polar triangles are combined to form a U-shaped geometry. Alternatively, a discontinuous multipatch approach may be employed, as demonstrated in [JLL19, Section 3.3]. For more general domains with one single corner singularity, scaled boundary parameterizations provide an effective alternative, as illustrated exemplarily in Figure 3.4b. A detailed investigation of these multipatch strategies lies beyond the scope of the present work.
- **A priori graded versus adaptive hierarchical refinement:** When the singular behavior at a corner is known or can be estimated a priori, graded refinement offers a conceptually simple and computationally efficient alternative to adaptive methods. In particular, it is sufficient to have a lower bound for the singular exponent ν, which is available for many PDE problems. Graded meshes achieve optimal convergence without requiring refinement indicators or major changes to solver infrastructure. Due to their simplicity, they enable highly accurate approximations on fine meshes, particularly when combined with higher-order basis functions. In this context, a priori mesh grading also provides a benchmark for the optimal convergence rates that adaptive methods based on a posteriori error estimators are expected to achieve. In contrast, fully adaptive methods offer significantly greater flexibility. The proposed grading approach cannot automatically detect and resolve unexpected singular behaviors – capabilities

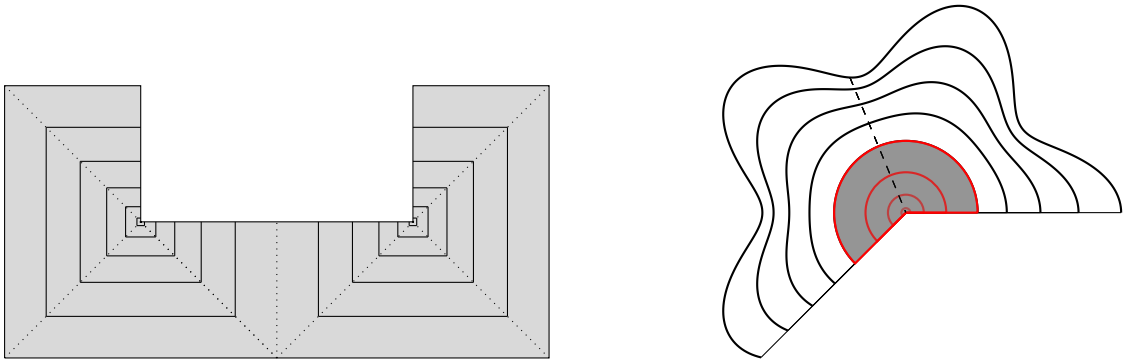

(a) (b)

Figure 3.4: Sketch of multipatch parameterizations for complex domains based on polar mappings. (a): U-shaped domain parameterized by eight polar triangles with graded meshes toward the two corners. (b): Scaled boundary parameterization of a segment of a flower-shaped domain, where a circular sector with a graded mesh is employed locally near the corner.

that adaptive hierarchical methods are specifically designed to address. Finally, we note that mesh grading preserves the global tensor-product structure of the underlying Bézier mesh. However, the resulting polar spline space (3.19) generally no longer possesses a tensor-product form, as can be seen from its basis representation (3.23), except for specific constellations of boundary conditions, see Remark 3.15. Conversely, hierarchical refinement breaks the global tensor-product structure but retains locally structured tensor-product meshes and spline spaces.

Properties of graded meshes

In this paragraph, we deduce essential properties of the constructed graded isogeometric meshes. The parametric and physical Bézier mesh both contain anisotropic elements [AZ24a]. Therefore, instead of using the seminal approximation framework described in [Baz+06], which is restricted to uniform meshes, we orientate ourselves on the anisotropic theory from [BBSV14; BCS12].

To begin with, we summarize the mesh size quantities and illustrate them in Figure 3.5. Recall that h_1 and h_2 denote the refinement parameters in each direction, as introduced in Section 3.2.2. They characterize the edge lengths of the elements of the uniform mesh $\widehat{\mathcal{M}}^1$, shown in Figure 3.5a, and the corresponding support extensions have edge lengths that are integer multiples of these quantities. For a general graded element $Q_{\boldsymbol{j}} \in \widehat{\mathcal{M}}^\mu$, illustrated in Figure 3.5b, this property no longer holds in the first parametric direction. We therefore denote the edge lengths of $Q_{\boldsymbol{j}} \in \widehat{\mathcal{M}}^\mu$ by h_{1,j_1} and h_{2,j_2}. Similarly, the edge lengths of the graded support extension $\widetilde{Q}_{\boldsymbol{j}}$ are denoted by $\widetilde{h}_{1,j_1}$ and $\widetilde{h}_{2,j_2}$.

Nevertheless, we can show that graded parametric meshes satisfy a local quasi-uniformity assumption, as required in [BBSV14, Assumption 4.10].

Lemma 3.12. *The graded parametric Bézier mesh $\widehat{\mathcal{M}}^\mu$ is locally quasi-uniform for all $\mu \in (0, 1]$, i.e., there are constants $\theta_l \geq 1$, $l = 1, 2$, such that*

$$\theta_l^{-1} \leq h_{l,j_l}/h_{l,j_l+1} \leq \theta_l, \quad j_l = 1, 2, \dots, N_l - 2, \tag{3.13}$$

in particular, $\theta_1 = 2^{1/\mu} - 1$ and $\theta_2 = 1$.

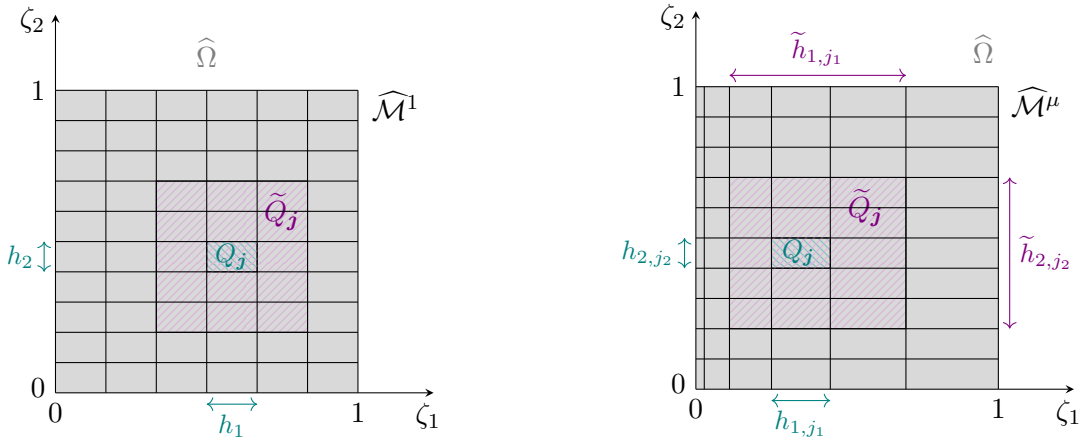

Figure 3.5: Illustration of the mesh size quantities in the parametric Bézier mesh: (a): Uniform mesh ($\mu = 1$). (b): Graded mesh ($\mu < 1$).

Proof. In ζ_2-direction, the uniform vector of breakpoints (3.12) leads to a constant edge length,

$$h_{2,j_2} = \zeta_{2,j_2+1} - \zeta_{2,j_2} = (j_2\, h_2) - ((j_2 - 1)\, h_2) = h_2, \quad j_2 = 1, 2, \dots, N_2 - 1,$$

and thus condition (3.13) is fulfilled for $l = 2$ with $\theta_2 = 1$. In ζ_1-direction, the graded vector of knots without repetition (3.11) yields

$$h_{1,j_1} = \zeta_{1,j_1+1} - \zeta_{1,j_1} = \left(j_1^{1/\mu} - (j_1 - 1)^{1/\mu}\right) h_1^{1/\mu}, \quad j_1 = 1, \dots, N_1 - 1,$$

and we define

$$\Theta_1(j_1) := \frac{h_{1,j_1}}{h_{1,j_1+1}} = \frac{\left(j_1^{1/\mu} - (j_1 - 1)^{1/\mu}\right) h_1^{1/\mu}}{\left((j_1 + 1)^{1/\mu} - j_1^{1/\mu}\right) h_1^{1/\mu}} = \frac{j_1^{1/\mu} - (j_1 - 1)^{1/\mu}}{(j_1 + 1)^{1/\mu} - j_1^{1/\mu}}.$$

In the subsequent Lemma 3.13, we show that the sequence $(\Theta_1(j_1))_{j_1=1}^{\infty}$ is monotonously increasing and satisfies $\lim_{j_1\to\infty} \Theta_1(j_1) = 1$. Furthermore, we have $\Theta_1(1) = \frac{1}{2^{1/\mu}-1} \in (0, 1]$, and we obtain the desired local quasi-uniformity property (3.13) for $l = 1$ with $\theta_1 = 2^{1/\mu} - 1$. □

Throughout this dissertation, we will refer to the parameter $\boldsymbol{\theta} = (\theta_1, \theta_2)$ in the sense of Lemma 3.12. Next, we show an auxiliary result mentioned in the proof of Lemma 3.12.

Lemma 3.13. *Let $\alpha \geq 1$. The sequence $(\Theta(j))_{j=1}^{\infty}$ with*

$$\Theta(j) := \frac{j^\alpha - (j-1)^\alpha}{(j+1)^\alpha - j^\alpha}$$

is monotonously increasing and satisfies $\lim_{j\to\infty} \Theta(j) = 1$.

Proof. For $\alpha = 1$, it holds $\Theta(j) = 1$ for all $j \in \mathbb{N}$ and the assertion follows directly. For $\alpha > 1$, we consider the function

$$\Theta : [1, \infty) \to \mathbb{R}, \quad \Theta(x) := \frac{x^\alpha - (x-1)^\alpha}{(x+1)^\alpha - x^\alpha},$$

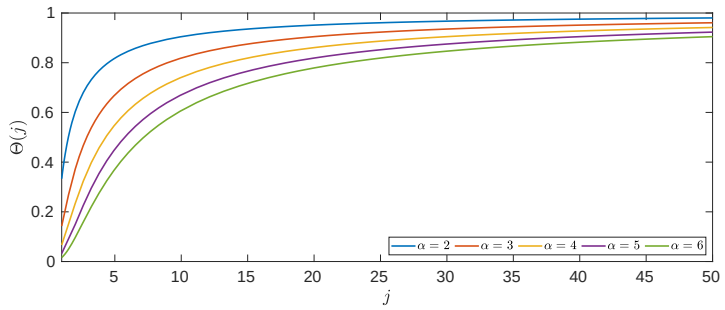

Figure 3.6: Illustration of the function Θ for $\alpha \in \{2, 3, \dots, 6\}$.

which is illustrated exemplarily for $\alpha \in \{2, 3, \dots, 6\}$ in Figure 3.6, where the claimed properties can be anticipated visually. In more detail, we define the functions $f : [1, \infty) \to \mathbb{R},\ f(x) := x^\alpha$ and $g : [1, \infty) \to \mathbb{R},\ g(x) := (x+1)^\alpha$. Then, by the generalized mean value theorem, for every $j \in \mathbb{N}$ there exists $x \in (j-1, j)$ such that

$$\Theta(j) = \frac{f(j) - f(j-1)}{g(j) - g(j-1)} = \frac{f'(x)}{g'(x)} = \left(\frac{x}{x+1}\right)^{\alpha-1} =: \widetilde{\Theta}(x).$$

The derivative of the new function $\widetilde{\Theta}$ is given by

$$\widetilde{\Theta}'(x) = (\alpha - 1)\left(\frac{x}{x+1}\right)^{\alpha-2} \frac{1}{(x+1)^2} = (\alpha - 1)\, x^{\alpha-2}(x+1)^{-\alpha},$$

and, since $\alpha > 1$ and $x > j - 1 \geq 0$, it always holds $\widetilde{\Theta}'(x) > 0$. Thus, the function $\widetilde{\Theta}$ and consequently also the sequence $(\Theta(j))_{j=1}^\infty$ are monotonously increasing. Moreover, we have

$$\lim_{j\to\infty} \Theta(j) = \lim_{x\to\infty} \widetilde{\Theta}(x) = \lim_{x\to\infty} \left(\frac{x}{x+1}\right)^{\alpha-1} = 1$$

and the proof is concluded. □

In the following, we compute further quantities to describe the graded meshes in more detail. Due to property (3.13), it holds

$$h_{1,j_1} \leq \theta_1 h_{1,j_1-1} \leq \cdots \leq \theta_1^{j_1-1} h_{1,1}.$$

Hence, for elements $Q_{\boldsymbol{j}} \in \widehat{\mathcal{M}}^\mu$ that are located close to the singular edge, e.g., for $j_1 \leq p_1 + 1$, we have

$$h_{1,j_1} \leq C h_{1,1} = C h_1^{1/\mu}.$$

If $Q_{\boldsymbol{j}} \in \widehat{\mathcal{M}}^\mu$ is not adjacent to the singular edge, e.g., $j_1 \geq 2$, the mean value theorem yields the existence of $x_0 \in ((j_1 - 1)h_1, j_1 h_1)$ such that

$$h_{1,j_1} = \zeta_{1,j_1+1} - \zeta_{1,j_1} = (j_1 h_1)^{\frac{1}{\mu}} - ((j_1 - 1)h_1)^{\frac{1}{\mu}} = \left(\frac{1}{\mu} - 1\right) h_1 (x_0)^{\frac{1}{\mu}-1}.$$

As the function $x \mapsto x^{1/\mu}$ is monotonously increasing, it follows by definition (3.11) and Lemma 3.12 that

$$h_{1,j_1} = Ch_1(x_0)^{\frac{1}{\mu}-1} \leq Ch_1(j_1 h_1)^{\frac{1}{\mu}(1-\mu)} = Ch_1(\zeta_{1,j_1+1})^{1-\mu} \leq Ch_1(\zeta_{1,j_1})^{1-\mu} \quad \text{for } j_1 \geq 2.$$

A similar way to prove this property is demonstrated in [Ape99, page 143].

Due to the local quasi-uniformity of the mesh, we obtain similar relations the edge lengths of the support extension,

$$\begin{aligned} &\widetilde{h}_{1,j_1} \leq C\, h_1^{1/\mu} && \text{for elements close to the singular edge, e.g., } j_1 \leq p_1 + 1, \\ &\widetilde{h}_{1,j_1} \leq C\, h_1\, (\zeta_{1,j_1})^{1-\mu} && \text{for elements away from the singular edge, e.g., } j_1 > p_1 + 1, \\ &\widetilde{h}_{2,j_2} \leq C\, h_2 && \text{for all elements.} \end{aligned} \tag{3.14}$$

A more precise characterization of the support extensions is also given in Section 3.4.2.

For simplicity, throughout this work, we assume that $h_1 \sim h_2$. Recall that $h_{Q_{\boldsymbol{j}}}$ denotes the diameter of a parametric Bézier element $Q_{\boldsymbol{j}}$. We define the mesh size h, also referred to as the mesh or discretization parameter, by

$$h := \max_{Q_{\boldsymbol{j}} \in \widehat{\mathcal{M}}^1} h_{Q_{\boldsymbol{j}}} \sim \max\{h_1, h_2\} \sim h_1 \sim h_2. \tag{3.15}$$

By definition, h denotes the mesh size associated with the uniform parametric mesh $\widehat{\mathcal{M}}^1$, rather than the graded mesh $\widehat{\mathcal{M}}^\mu$. Nevertheless, the mesh sizes of the uniform and graded meshes are equivalent. As demonstrated above, the edge lengths of the graded elements satisfy $h_{l,j_l} \leq Ch$, $\boldsymbol{j} = (j_1, j_2) \in \boldsymbol{J}$, $l = 1, 2$, which implies $h_{Q_{\boldsymbol{j}}} \leq Ch$ for all $Q_{\boldsymbol{j}} \in \widehat{\mathcal{M}}^\mu$. Moreover, graded elements away from the singularity are larger than their uniform counterparts, see Figure 3.5 for a visualization, and it follows

$$\max_{Q_{\boldsymbol{j}} \in \widehat{\mathcal{M}}^\mu} h_{Q_{\boldsymbol{j}}} \sim h = \max_{Q_{\boldsymbol{j}} \in \widehat{\mathcal{M}}^1} h_{Q_{\boldsymbol{j}}}. \tag{3.16}$$

3.3 Function spaces and projectors for polar parameterizations

In this section, we describe suitable approximation spaces for Galerkin IGA on polar domains with corners and introduce a corresponding projector. Furthermore, we present the concept of polar Sobolev spaces on the parametric domain, which are defined as pull-backs of classical Sobolev spaces on the physical domain. The content presented here is adapted from Section 4 and Appendix A of [AZ26].

3.3.1 The polar approximation space and a suitable projection

We start by recalling polar spline and NURBS spaces, which have been studied extensively in isogeometric literature [ST21; TJ11; TJ12; TSHH17], and define a suitable projector into these spaces. Let Ω be a polar domain with corner and let $\widehat{V}_h = N_{\boldsymbol{p}}(\boldsymbol{\Xi}, W)$ be a standard NURBS space on $\widehat{\Omega}$, which has been obtained by graded refinement of the initial polar discretization, following an isoparametric approach. Throughout the remainder of the chapter, we work under Assumptions 3.4 and 3.5. The lack of regularity in the polar parameterization results in a variational crime when standard isogeometric approximation spaces

$$V_h = \left\{ f \circ \boldsymbol{F}^{-1} : f \in N_{\boldsymbol{p}}(\boldsymbol{\Xi}, W) \right\} = \operatorname{span} \left\{ N_{\boldsymbol{i},\boldsymbol{p}}(\boldsymbol{x}) := \widehat{N}_{\boldsymbol{i},\boldsymbol{p}} \circ \boldsymbol{F}^{-1}(\boldsymbol{x}) : \boldsymbol{i} \in \boldsymbol{I} \right\} \tag{3.17}$$

are used since the basis functions associated to the control points collapsing in the polar point,

$$\left\{ N_{\boldsymbol{i}_\odot,\boldsymbol{p}} = \widehat{N}_{\boldsymbol{i}_\odot,\boldsymbol{p}} \circ \boldsymbol{F}^{-1} : \boldsymbol{i}_\odot \in \boldsymbol{I}_\odot \right\}, \quad \text{with } \boldsymbol{I}_\odot \text{ from (3.2)}, \tag{3.18}$$

are not in $H^1(\Omega)$ and thus $V_h \not\subset V = H^1(\Omega)$, see [TJ11; TJ12]. Besides, the functions (3.18) are not well-defined at the polar point since the corresponding parametric functions are not constant on the singular edge $\widehat{\Gamma}_1$, which also implies that $V_h \not\subset C^0(\overline{\Omega})$. Instead, the modified polar approximation space

$$V_h^\odot := V_h \cap H^1(\Omega), \tag{3.19}$$

which was initially proposed in [TJ11], see also [TSHH17], is employed. Note that the space also depends on the grading parameter $\mu \in (0, 1]$ and the polynomial degree $\boldsymbol{p}$, although this dependence is not indicated explicitly in the notation. It is well-known that (3.19) yields a space of NURBS that are C^0-continuous at the polar point $\boldsymbol{P}$. Advanced approaches have been proposed in the literature to generate higher continuity at the polar point [ST21; TSHH17]. Since our main focus lies on deriving error estimates for the second-order model problem (2.3), we only consider the simple construction (3.19), which satisfies the minimum regularity requirements for a standard Galerkin IGA approach and keeps the complexity of the polar spline space as low as possible.

A basis of the polar spline space (3.19) can be constructed by replacing all the basis functions (3.18) with a single function consisting of their sum [TJ11; TJ12],

$$N_{\odot,\boldsymbol{p}} := \sum_{\boldsymbol{i}_\odot \in \boldsymbol{I}_\odot} N_{\boldsymbol{i}_\odot,\boldsymbol{p}} = \sum_{i_2=1}^{n_2} N_{(1,i_2),\boldsymbol{p}}, \tag{3.20}$$

which satisfies $N_{\odot,\boldsymbol{p}} \in H^1(\Omega)$. In Figure 3.7a and 3.7b, we exemplarily display the excluded basis functions (3.18) and the modified basis function (3.20) for a coarse discretization of a circular sector with angle $\frac{5}{3}\pi$. The parametric B-spline and NURBS functions corresponding to the modified physical basis function (3.20) are given by

$$\begin{aligned} \widehat{B}_{\odot,\boldsymbol{p}} &\colon [0,1]^2 \to \mathbb{R}, \ \widehat{B}_{\odot,\boldsymbol{p}}(\boldsymbol{\zeta}) := \sum_{\boldsymbol{i}_\odot \in \boldsymbol{I}_\odot} \widehat{B}_{\boldsymbol{i}_\odot,\boldsymbol{p}}(\boldsymbol{\zeta}), \\ \widehat{N}_{\odot,\boldsymbol{p}} &\colon [0,1]^2 \to \mathbb{R}, \ \widehat{N}_{\odot,\boldsymbol{p}}(\boldsymbol{\zeta}) := \sum_{\boldsymbol{i}_\odot \in \boldsymbol{I}_\odot} \widehat{N}_{\boldsymbol{i}_\odot,\boldsymbol{p}}(\boldsymbol{\zeta}). \end{aligned} \tag{3.21}$$

In fact, due to the specific form (3.9) of the weight function required in Assumption 3.5, both functions reduce to the first univariate B-spline basis function in ζ_1-direction,

$$\begin{aligned} \widehat{B}_{\odot,\boldsymbol{p}}(\boldsymbol{\zeta}) &= \sum_{i_2=1}^{n_2} \widehat{B}_{(1,i_2),\boldsymbol{p}}(\boldsymbol{\zeta}) = \widehat{B}_{1,p_1}(\zeta_1) \sum_{i_2=1}^{n_2} \widehat{B}_{i_2,p_2}(\zeta_2) = \widehat{B}_{1,p_1}(\zeta_1), \\ \widehat{N}_{\odot,\boldsymbol{p}}(\boldsymbol{\zeta}) &= \frac{\sum_{i_2=1}^{n_2} w_{(1,i_2)} \widehat{B}_{(1,i_2),\boldsymbol{p}}(\boldsymbol{\zeta})}{W} = \frac{\widehat{B}_{1,p_1}(\zeta_1) \sum_{i_2=1}^{n_2} w_{(1,i_2)} \widehat{B}_{i_2,p_2}(\zeta_2)}{\sum_{i_2=1}^{n_2} w_{(1,i_2)} \widehat{B}_{i_2,p_2}(\zeta_2)} = \widehat{B}_{1,p_1}(\zeta_1). \end{aligned}$$

Since univariate B-splines constructed from open knot vectors are interpolatory at the boundary, $\widehat{N}_{\odot,\boldsymbol{p}}$ is constant on $\widehat{\Gamma}_1$, with $\widehat{N}_{\odot,\boldsymbol{p}}(0,\cdot) = \widehat{B}_{1,p_1}(0) = 1$. Hence, the push-forward of $\widehat{N}_{\odot,\boldsymbol{p}}$ is well-defined and yields the modified NURBS basis function (3.20),

$$N_{\odot,\boldsymbol{p}} = \sum_{\boldsymbol{i}_\odot \in \boldsymbol{I}_\odot} N_{\boldsymbol{i}_\odot,\boldsymbol{p}} = \sum_{\boldsymbol{i}_\odot \in \boldsymbol{I}_\odot} \widehat{N}_{\boldsymbol{i}_\odot,\boldsymbol{p}} \circ \boldsymbol{F}^{-1} = \widehat{N}_{\odot,\boldsymbol{p}} \circ \boldsymbol{F}^{-1}. \tag{3.22}$$

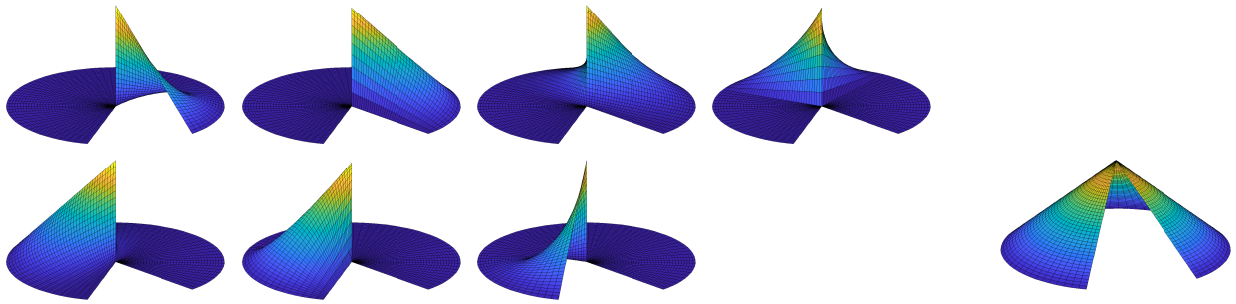

(a) (b)

Figure 3.7: Basis functions for a coarse discretization of a circular sector sector with angle $\omega = \frac{5}{3}\pi$. Some mesh lines that do not correspond to the coarse discretization are inserted for better visualization. (a): Standard singular basis functions (3.18). (b): Modified basis function (3.20).

Thus, we will write the basis of our approximation space throughout the thesis as

$$V_h^{\odot} = \operatorname{span}\left(\{N_{\odot,\boldsymbol{p}}\} \cup \left\{N_{\boldsymbol{i},\boldsymbol{p}} = \widehat{N}_{\boldsymbol{i},p_1} \circ \boldsymbol{F}^{-1} : \boldsymbol{i} \in \boldsymbol{I} \setminus \boldsymbol{I}_{\odot}\right\}\right), \tag{3.23}$$

noting that all basis functions are continuous in $\boldsymbol{P}$ with $N_{\odot,\boldsymbol{p}}(\boldsymbol{P}) = 1$ and $N_{\boldsymbol{i},\boldsymbol{p}}(\boldsymbol{P}) = 0$ for all $\boldsymbol{i} \in \boldsymbol{I} \setminus \boldsymbol{I}_{\odot}$.

Lastly, we define the space

$$V_{0h}^{\odot} = V_h^{\odot} \cap V_0 = \left\{v \in V_h^{\odot} : v = 0 \text{ on } \Gamma_D\right\}$$

with V_0 from (2.6), which also takes homogeneous Dirichlet boundary conditions into account. In this context, we comment on the numerical treatment of mixed boundary conditions.

Remark 3.14. The solutions of our model problem (2.3) are globally continuous, since the classical Sobolev embedding $H^s(\Omega) \hookrightarrow C^0(\overline{\Omega})$ holds for all $s > 1$. This implies that the Dirichlet boundary condition is satisfied on the closed boundary segment $\overline{\Gamma_D}$. In the case of mixed BC on two adjacent boundary edges, it follows that the corresponding degree of freedom at the corner is naturally treated as part of the homogeneous Dirichlet boundary.

Moreover, we observe the following property of the approximation space.

Remark 3.15. The structure of the modified approximation space with boundary conditions depends crucially on whether the polar corner is included in the homogeneous Dirichlet boundary. If this is the case, i.e., when Dirichlet or mixed BCs are prescribed on the adjacent edges, the basis functions associated with the polar point are not active. Hence, the modified space with BCs coincides with the standard space,

$$V_{0h}^{\odot} = V_h^{\odot} \cap V_0 = V_h \cap V_0 = V_{0h},$$

and the tensor-product structure is preserved. Only for Neumann BCs at the corner is the modified space a proper subspace, $V_{0h}^{\odot} \subsetneq V_{0h}$. In this context, we comment on the numerical treatment of mixed boundary conditions.

In the next step, we define a projector onto the modified isogeometric approximation space $V_h^{\odot}$. In standard literature [Baz+06; BBSV14; BCS12], a projection onto the usual approximation space

V_h is constructed based on the multivariate quasi-interpolant for the parametric spline space (2.35), the parameterization $\boldsymbol{F}$ and the weight function W,

$$\Pi_{V_h} : L^1(\Omega) \to V_h, \quad \Pi_{V_h} v := \frac{\Pi_{\boldsymbol{p},\boldsymbol{\Xi}}(W(v \circ \boldsymbol{F}))}{W} \circ \boldsymbol{F}^{-1}. \tag{3.24}$$

However, the isogeometric mapping $\boldsymbol{F}$ is typically assumed to satisfy certain regularity properties, which are not fulfilled by polar parameterizations. In what follows, we propose a slightly modified projector that is adapted to the polar setting and maps into the subspace $V_h^{\odot} \subset V_h$.

The standard projection (3.24) is generally not well-defined at the polar point $\boldsymbol{P}$ due to the collapsing edge effect (3.1). This can be remedied by using a spline projector on the parametric domain that takes Dirichlet boundary conditions into account – in particular, on the singular edge $\widehat{\Gamma}_1$. For simplicity, we employ the modified quasi-interpolant (2.37), which is interpolatory at the complete parametric boundary [BBSV14; BCS12], and requires functions from $C([0,1]^2)$. We then define a projector onto the polar approximation space (3.19) by

$$\Pi_{V_h^{\odot}} : C(\overline{\Omega}) \to V_h^{\odot}, \quad \Pi_{V_h^{\odot}} v = \frac{\Pi^{\widehat{\Gamma}}_{\boldsymbol{p},\boldsymbol{\Xi}}(W(v \circ \boldsymbol{F}))}{W} \circ \boldsymbol{F}^{-1}. \tag{3.25}$$

Due to the regularity property (2.4) of the considered PDE solution and the embeddings $V^s_\beta(\Omega) \hookrightarrow H^s_\beta(\Omega) \hookrightarrow H^{s-\beta}(\Omega) \hookrightarrow C(\overline{\Omega})$, which hold for $\beta < s - 1$, see (2.2) and [Ros92], it is justified to work with a projector that requires functions from $C(\overline{\Omega})$. The following Lemma establishes the expected properties of this projection.

Lemma 3.16. *The operator $\Pi_{V_h^{\odot}}$ is a well-defined projector onto $V_h^{\odot}$, that is, $\Pi_{V_h^{\odot}} v \in V_h^{\odot}$ for all $v \in C(\overline{\Omega})$ and $\Pi_{V_h^{\odot}} v = v$ for all $v \in V_h^{\odot}$. Moreover, we have $\Pi_{V_h^{\odot}} v \in V_{0h}^{\odot}$ for all $v \in C(\overline{\Omega})$ with $v = 0$ on Γ_D.*

Proof. Let $v \in C(\overline{\Omega})$ and $\widehat{v} = v \circ \boldsymbol{F}$. Then, $\widehat{v}$ is constant on $\widehat{\Gamma}_1$, and we set $c = v(\boldsymbol{P}) = \widehat{v}(0,\cdot)$. The first univariate dual functional defined in (2.27) satisfies

$$\lambda^{\widehat{\Gamma}}_{1,p_1}(W\widehat{v}(\cdot,\zeta_2)) = W\widehat{v}(0,\zeta_2) = c\,W(0,\zeta_2)$$

for all $\zeta_2 \in [0,1]$. Hence, the bivariate dual functionals corresponding to the collapsed edge reduce to

$$\lambda^{\widehat{\Gamma}}_{\boldsymbol{i}_\odot,\boldsymbol{p}}(W\widehat{v}) = (\lambda^{\widehat{\Gamma}}_{1,p_1} \otimes \lambda^{\widehat{\Gamma}}_{i_2,p_2})(W\widehat{v}) = \lambda^{\widehat{\Gamma}}_{i_2,p_2}(c\,W(0,\cdot)) = c\,\lambda^{\widehat{\Gamma}}_{i_2,p_2}(W(0,\cdot)). \tag{3.26}$$

Besides, most of the B-spline basis functions vanish on the collapsing edge $\widehat{\Gamma}_1$, the univariate quasi-interpolant $\Pi^{\widehat{\Gamma}}_{p_2,\Xi_2}$ defined in (2.27) is a projector onto $S_{p_2}(\Xi_2)$, and we have $W(0,\cdot) \in S_{p_2}(\Xi_2)$. Therefore, the modified bivariate quasi-interpolant (2.37), which is also given in the form (2.38), can be computed explicitly on the collapsed edge,

$$\begin{aligned}\left(\Pi^{\widehat{\Gamma}}_{\boldsymbol{p},\boldsymbol{\Xi}}(W(v \circ \boldsymbol{F}))\right)(0,\cdot) = \left(\Pi^{\widehat{\Gamma}}_{\boldsymbol{p},\boldsymbol{\Xi}}(W\widehat{v})\right)(0,\cdot) &= \sum_{\boldsymbol{i} \in \boldsymbol{I}} \lambda^{\widehat{\Gamma}}_{\boldsymbol{i},\boldsymbol{p}}(W\widehat{v})\widehat{B}_{\boldsymbol{i},\boldsymbol{p}}(0,\cdot) = \sum_{\boldsymbol{i}_\odot \in \boldsymbol{I}_\odot} \lambda^{\widehat{\Gamma}}_{\boldsymbol{i}_\odot,\boldsymbol{p}}(W\widehat{v})\widehat{B}_{\boldsymbol{i}_\odot,\boldsymbol{p}}(0,\cdot) \\ &= c\,\widehat{B}_{1,p_1}(0) \sum_{i_2=1}^{n_2} \lambda^{\widehat{\Gamma}}_{i_2,p_2}(W(0,\cdot))\widehat{B}_{i_2,p_2}(\cdot) = c\,\Pi^{\widehat{\Gamma}}_{p_2,\Xi_2}(W(0,\cdot)) = c\,W(0,\cdot).\end{aligned}$$

As a consequence, the projection $\Pi_{V_h^\odot} v$ is well-defined and continuous in $\boldsymbol{P}$, with $\left(\Pi_{V_h^\odot} v\right)(\boldsymbol{P}) = c$, and it holds $\Pi_{V_h^\odot} v \in H^1(\Omega)$, see [TJ11; TJ12]. By definition of the spaces (3.17) and (3.19), we further obtain $\Pi_{V_h^\odot} v \in V_h$ and also $\Pi_{V_h^\odot} v \in V_h^\odot$, and thus the operator (3.25) is well-defined.

Next, we show that $\Pi_{V_h^\odot}$ is indeed a projector. Therefore, let $v \in V_h^\odot$, that is, with (3.22) and (3.23),

$$v = c\, N_{\odot,\boldsymbol{p}} + \sum_{\boldsymbol{i}\in\boldsymbol{I}\setminus\boldsymbol{I}_\odot} \alpha_{\boldsymbol{i}} N_{\boldsymbol{i},\boldsymbol{p}} = c \sum_{\boldsymbol{i}_\odot\in\boldsymbol{I}_\odot} N_{\boldsymbol{i}_\odot,\boldsymbol{p}} + \sum_{\boldsymbol{i}\in\boldsymbol{I}\setminus\boldsymbol{I}_\odot} \alpha_{\boldsymbol{i}} N_{\boldsymbol{i},\boldsymbol{p}},$$

where $c = v(\boldsymbol{P})$ and $\alpha_{\boldsymbol{i}} \in \mathbb{R}, \boldsymbol{i} \in \boldsymbol{I} \setminus \boldsymbol{I}_\odot$. Then, it is $v = \widehat{v} \circ \boldsymbol{F}^{-1}$ with

$$\widehat{v} = c\, \widehat{N}_{\odot,\boldsymbol{p}} + \sum_{\boldsymbol{i}\in\boldsymbol{I}\setminus\boldsymbol{I}_\odot} \alpha_{\boldsymbol{i}} \widehat{N}_{\boldsymbol{i},\boldsymbol{p}} = c \sum_{\boldsymbol{i}_\odot\in\boldsymbol{I}_\odot} \widehat{N}_{\boldsymbol{i}_\odot,\boldsymbol{p}} + \sum_{\boldsymbol{i}\in\boldsymbol{I}\setminus\boldsymbol{I}_\odot} \alpha_{\boldsymbol{i}} \widehat{N}_{\boldsymbol{i},\boldsymbol{p}} \in N_{\boldsymbol{p}}(\Xi),$$

see (3.21). Further, we have $\widehat{v} = \widehat{u}/W$ with

$$\widehat{u} = c \sum_{\boldsymbol{i}\in\boldsymbol{I}_\odot} w_{\boldsymbol{i}_\odot} \widehat{B}_{\boldsymbol{i}_\odot,\boldsymbol{p}} + \sum_{\boldsymbol{i}\in\boldsymbol{I}\setminus\boldsymbol{I}_\odot} \alpha_{\boldsymbol{i}} w_{\boldsymbol{i}} \widehat{B}_{\boldsymbol{i},\boldsymbol{p}} \in S_{\boldsymbol{p}}(\Xi).$$

Since $\Pi^{\widehat{\Gamma}}_{\boldsymbol{p},\boldsymbol{\Xi}}$ is a projector onto $S_{\boldsymbol{p}}(\Xi)$, it follows

$$\Pi_{V_h^\odot} v = \frac{\Pi^{\widehat{\Gamma}}_{\boldsymbol{p},\boldsymbol{\Xi}}(W(v\circ\boldsymbol{F}))}{W} = \frac{\Pi^{\widehat{\Gamma}}_{\boldsymbol{p},\boldsymbol{\Xi}}(W\widehat{v})}{W} = \frac{\Pi^{\widehat{\Gamma}}_{\boldsymbol{p},\boldsymbol{\Xi}}(W\widehat{u}/W)}{W} = \frac{\Pi^{\widehat{\Gamma}}_{\boldsymbol{p},\boldsymbol{\Xi}}(\widehat{u})}{W} = \frac{\widehat{u}}{W}\circ\boldsymbol{F}^{-1} = \widehat{v}\circ\boldsymbol{F}^{-1} = v$$

and the proof is complete. The result for the functions satisfying Dirichlet boundary conditions follows directly from the construction of the quasi-interpolant $\Pi^{\widehat{\Gamma}}_{\boldsymbol{p},\boldsymbol{\Xi}}$. □

Remark 3.17. Note that all the constructions of Section 3.3.1 can be extended to a non-isoparametric approach by simply setting $W = 1$.

3.3.2 Polar Sobolev spaces on the parametric domain

In standard isogeometric approximation theory, error estimates are typically derived on the parametric domain and then transferred to the physical domain, where the Jacobian of the geometry mapping $\boldsymbol{F}$ and its inverse are assumed to be bounded [Baz+06; BBSV14; BCS12]. This condition, however, is not satisfied by polar parameterizations, see equations (3.5) and (3.7). Therefore, the corresponding transformations of derivatives and norms must be treated more carefully, as demonstrated in this section. Consequently, we introduce a novel class of Sobolev spaces on the parametric domain to characterize pull-backs of functions on polar domains with corners.

Polar transformation of derivatives

We start by analyzing the transformation between derivatives on the physical domain and their corresponding pull-back derivatives. To this end, we first introduce some notation. Let $\boldsymbol{\alpha} = (\alpha_1, \alpha_2) \in \mathbb{N}_0^2$ be a multi-index. Simplifying the notation (2.1) to the two-dimensional setting, we denote derivatives of functions $v : \Omega \to \mathbb{R}$ defined on the physical domain by

$$D^{\boldsymbol{\alpha}} v := \frac{\partial^{\alpha_1}}{\partial x^{\alpha_1}} \frac{\partial^{\alpha_2} v}{\partial y^{\alpha_2}} \quad \text{and} \quad \partial_x v = \frac{\partial v}{\partial x},\ \partial_y v = \frac{\partial v}{\partial y},\ \partial_{xx} v = \frac{\partial^2 v}{\partial x^2},\ \ldots.$$

In contrast, for a function $\widehat{v} : \widehat{\Omega} \to \mathbb{R}$ acting on the parametric domain, we write

$$\widehat{D}^{\boldsymbol{\alpha}}\widehat{v} := \frac{\partial^{\alpha_1}}{\partial\zeta_1^{\alpha_1}}\frac{\partial^{\alpha_2}\widehat{v}}{\partial\zeta_2^{\alpha_2}} \quad \text{and} \quad \widehat{\partial}_1\widehat{v} = \frac{\partial\widehat{v}}{\partial\zeta_1},\ \widehat{\partial}_2\widehat{v} = \frac{\partial\widehat{v}}{\partial\zeta_2},\ \widehat{\partial}_{11}\widehat{v} = \frac{\partial^2\widehat{v}}{\partial\zeta_1^2},\ \dots.$$

Moreover, following the framework in [BBSV14; BCS12], we define the coordinate system naturally induced by $\boldsymbol{F}$, referred to as the $\boldsymbol{F}$-coordinate system, whose tangent base vectors $\boldsymbol{g}_1$ and $\boldsymbol{g}_2$ are given by

$$\boldsymbol{g}_i = \boldsymbol{g}_i(\boldsymbol{x}) = \frac{\partial \boldsymbol{F}}{\partial\zeta_i}(\boldsymbol{F}^{-1}(\boldsymbol{x})), \quad i = 1, 2.$$

As computed in (3.4), we have

$$\boldsymbol{g}_1(\boldsymbol{x}) = \begin{pmatrix} G_1(\zeta_2(\boldsymbol{x})) \\ G_2(\zeta_2(\boldsymbol{x})) \end{pmatrix} \quad \text{and} \quad \boldsymbol{g}_2(\boldsymbol{x}) = \begin{pmatrix} \zeta_1(\boldsymbol{x})\, G_1'(\zeta_2(\boldsymbol{x})) \\ \zeta_1(\boldsymbol{x})\, G_2'(\zeta_2(\boldsymbol{x})) \end{pmatrix}, \tag{3.27}$$

where we set $\boldsymbol{\zeta}(\boldsymbol{x}) = (\zeta_1(\boldsymbol{x}), \zeta_2(\boldsymbol{x})) = \boldsymbol{F}^{-1}(\boldsymbol{x})$ for all $\boldsymbol{x} \neq \boldsymbol{P}$. We also consider derivatives with respect to the $\boldsymbol{F}$-coordinates,

$$\begin{aligned}
&\frac{\partial v}{\partial \boldsymbol{g}_i}(\boldsymbol{x}) = \nabla v(\boldsymbol{x}) \cdot \boldsymbol{g}_i(\boldsymbol{x}) = \lim_{t\to 0} \frac{v(\boldsymbol{x} + t\boldsymbol{g}_i(\boldsymbol{x})) - v(\boldsymbol{x})}{t}, \quad i = 1, 2, \\
&\frac{\partial^{\alpha_i} v}{\partial \boldsymbol{g}_i^{\alpha_i}} = \frac{\partial}{\partial \boldsymbol{g}_i}\left(\frac{\partial^{\alpha_i - 1} v}{\partial \boldsymbol{g}_i^{\alpha_i - 1}}\right) = \frac{\partial}{\partial \boldsymbol{g}_i}\left(\cdots\left(\frac{\partial}{\partial \boldsymbol{g}_i}\left(\frac{\partial v}{\partial \boldsymbol{g}_i}\right)\right)\right), \quad \alpha_i \in \mathbb{N},\ i = 1, 2, \\
&D_{\boldsymbol{F}}^{\boldsymbol{\alpha}} v = \frac{\partial^{\alpha_1}}{\partial \boldsymbol{g}_1^{\alpha_1}}\frac{\partial^{\alpha_2} v}{\partial \boldsymbol{g}_2^{\alpha_2}}, \quad \boldsymbol{\alpha} = (\alpha_1, \alpha_2) \in \mathbb{N}^2.
\end{aligned}$$

Now, let $\widehat{v} = v \circ \boldsymbol{F}$ be the pull-back of a sufficiently smooth function $v : \Omega \to \mathbb{R}$. As shown in [BCS12, Proposition 5.1], we have

$$\mathrm{D}_{\boldsymbol{F}}^{\boldsymbol{\alpha}} v = (\widehat{D}^{\boldsymbol{\alpha}}\widehat{v}) \circ \boldsymbol{F}^{-1} = \left(\frac{\partial^{\alpha_1}}{\partial\zeta_1}\frac{\partial^{\alpha_2}\widehat{v}}{\partial\zeta_2}\right) \circ \boldsymbol{F}^{-1}, \tag{3.28}$$

i.e., in particular, $\mathrm{D}_{\boldsymbol{F}}^{(1,0)} v = \widehat{\partial}_1\widehat{v} \circ \boldsymbol{F}^{-1}$ and $\mathrm{D}_{\boldsymbol{F}}^{(0,1)} v = \widehat{\partial}_2\widehat{v} \circ \boldsymbol{F}^{-1}$. By inserting the polar tangent base vectors (3.27), we obtain the first directional derivatives at all points $\boldsymbol{x} \neq \boldsymbol{0}$ by

$$\mathrm{D}_{\boldsymbol{F}}^{(1,0)} v(\boldsymbol{x}) = G_1(\zeta_2(\boldsymbol{x}))\, \partial_x v(\boldsymbol{x}) + G_2(\zeta_2(\boldsymbol{x}))\, \partial_y v(\boldsymbol{x}), \tag{3.29}$$

$$\mathrm{D}_{\boldsymbol{F}}^{(0,1)} v(\boldsymbol{x}) = \zeta_1(\boldsymbol{x})\, G_1'(\zeta_2(\boldsymbol{x}))\, \partial_x v(\boldsymbol{x}) + \zeta_1(\boldsymbol{x})\, G_2'(\zeta_2(\boldsymbol{x}))\, \partial_y v(\boldsymbol{x}). \tag{3.30}$$

Vice versa, equations (3.5), (3.6) and (3.28) yield

$$\partial_x v(\boldsymbol{x}) = G_2(\zeta_2(\boldsymbol{x}))\, \mathrm{D}_{\boldsymbol{F}}^{(1,0)} v(\boldsymbol{x}) - \frac{1}{\zeta_1(\boldsymbol{x})} G_2'(\zeta_2(\boldsymbol{x}))\, \mathrm{D}_{\boldsymbol{F}}^{(0,1)} v(\boldsymbol{x}), \tag{3.31}$$

$$\partial_y v(\boldsymbol{x}) = -G_1'(\zeta_2(\boldsymbol{x}))\, \mathrm{D}_{\boldsymbol{F}}^{(1,0)} v(\boldsymbol{x}) + \frac{1}{\zeta_1(\boldsymbol{x})} G_1(\zeta_2(\boldsymbol{x}))\, \mathrm{D}_{\boldsymbol{F}}^{(0,1)} v(\boldsymbol{x}). \tag{3.32}$$

In the following Lemmata 3.18 and 3.19, we derive precise representations for the polar transformation of derivatives of arbitrary orders, thereby extending the formulas presented here.

Lemma 3.18. *For each multi-index $\boldsymbol{\alpha}$, there exist bounded functions $G_{\boldsymbol{\gamma}} : [0,1] \to \mathbb{R}$, $1 \leq |\boldsymbol{\gamma}| \leq |\boldsymbol{\alpha}|$, such that*

$$D_{\boldsymbol{F}}^{\boldsymbol{\alpha}} v = \sum_{1 \leq |\boldsymbol{\gamma}| \leq |\boldsymbol{\alpha}|} \zeta_1^{-\alpha_1 + |\boldsymbol{\gamma}|} G_{\boldsymbol{\gamma}} D^{\boldsymbol{\gamma}} v, \tag{3.33}$$

where we write $\boldsymbol{\zeta} = (\zeta_1, \zeta_2) = (\zeta_1(\boldsymbol{x}), \zeta_2(\boldsymbol{x})) = \boldsymbol{F}^{-1}(\boldsymbol{x})$ and $G_{\boldsymbol{\gamma}} = G_{\boldsymbol{\gamma}}(\zeta_2(\boldsymbol{x}))$ for all $\boldsymbol{x} \neq \boldsymbol{0}$.

Proof. We prove the assertion by induction over $|\boldsymbol{\alpha}|$. For $|\boldsymbol{\alpha}| = 1$, the result follows from (3.29) and (3.30), which serve as the induction base. We now demonstrate the induction step. Assume that the identity (3.33) holds for all multi-indices $\boldsymbol{\alpha}$ with $|\boldsymbol{\alpha}| = s \in \mathbb{N}$. From now on, $G_{\boldsymbol{\gamma}}$ denotes generic bounded coefficient functions depending only on ζ_2, and their precise form may change from line to line. By using (3.29), the product rule, the fact that $G_{\boldsymbol{\gamma}}$ only depends on ζ_2 and an index shift, we compute

$$\begin{aligned}
D_{\boldsymbol{F}}^{(\alpha_1+1,\alpha_2)} v &= D_{\boldsymbol{F}}^{(1,0)} \left(D_{\boldsymbol{F}}^{\boldsymbol{\alpha}} v\right) = D_{\boldsymbol{F}}^{(1,0)} \left(\sum_{1 \leq |\boldsymbol{\gamma}| \leq |\boldsymbol{\alpha}|} \zeta_1^{-\alpha_1 + |\boldsymbol{\gamma}|} G_{\boldsymbol{\gamma}} D^{\boldsymbol{\gamma}} v \right) \\
&= \sum_{1 \leq |\boldsymbol{\gamma}| \leq |\boldsymbol{\alpha}|} \left[D_{\boldsymbol{F}}^{(1,0)} \left(\zeta_1^{-\alpha_1 + |\boldsymbol{\gamma}|} \right) G_{\boldsymbol{\gamma}} D^{\boldsymbol{\gamma}} v + \zeta_1^{-\alpha_1 + |\boldsymbol{\gamma}|} G_{\boldsymbol{\gamma}} D_{\boldsymbol{F}}^{(1,0)} \left(D^{\boldsymbol{\gamma}} v \right) \right] \\
&= \sum_{1 \leq |\boldsymbol{\gamma}| \leq |\boldsymbol{\alpha}|} \left[(-\alpha_1 + |\boldsymbol{\gamma}|) \zeta_1^{-(\alpha_1+1) + |\boldsymbol{\gamma}|} G_{\boldsymbol{\gamma}} D^{\boldsymbol{\gamma}} v + \zeta_1^{-\alpha_1 + |\boldsymbol{\gamma}|} G_{\boldsymbol{\gamma}} \left(G_1 \, \partial_x (D^{\boldsymbol{\gamma}} v) + G_2 \, \partial_y (D^{\boldsymbol{\gamma}} v) \right) \right] \\
&= \sum_{1 \leq |\boldsymbol{\gamma}| \leq |\boldsymbol{\alpha}|} (-\alpha_1 + |\boldsymbol{\gamma}|) \zeta_1^{-(\alpha_1+1) + |\boldsymbol{\gamma}|} G_{\boldsymbol{\gamma}} D^{\boldsymbol{\gamma}} v + \sum_{1 \leq |\boldsymbol{\gamma}'| \leq |\boldsymbol{\alpha}|+1} \zeta_1^{-(\alpha_1+1) + |\boldsymbol{\gamma}'|} G_{\boldsymbol{\gamma}'} D^{\boldsymbol{\gamma}'} v \\
&= \sum_{1 \leq |\boldsymbol{\gamma}| \leq |\boldsymbol{\alpha}|+1} \zeta_1^{-(\alpha_1+1) + |\boldsymbol{\gamma}|} G_{\boldsymbol{\gamma}} D^{\boldsymbol{\gamma}} v.
\end{aligned}$$

Similarly, we obtain with (3.30) that

$$\begin{aligned}
D_{\boldsymbol{F}}^{(\alpha_1,\alpha_2+1)} v &= D_{\boldsymbol{F}}^{(0,1)} \left(D_{\boldsymbol{F}}^{\boldsymbol{\alpha}} v\right) = D_{\boldsymbol{F}}^{(0,1)} \left(\sum_{1 \leq |\boldsymbol{\gamma}| \leq |\boldsymbol{\alpha}|} \zeta_1^{-\alpha_1 + |\boldsymbol{\gamma}|} G_{\boldsymbol{\gamma}} D^{\boldsymbol{\gamma}} v \right) \\
&= \sum_{1 \leq |\boldsymbol{\gamma}| \leq |\boldsymbol{\alpha}|} \zeta_1^{-\alpha_1 + |\boldsymbol{\gamma}|} D_{\boldsymbol{F}}^{(0,1)} \left(G_{\boldsymbol{\gamma}} D^{\boldsymbol{\gamma}} v \right) \\
&= \sum_{1 \leq |\boldsymbol{\gamma}| \leq |\boldsymbol{\alpha}|} \zeta_1^{-\alpha_1 + |\boldsymbol{\gamma}|} \left(G'_{\boldsymbol{\gamma}} D^{\boldsymbol{\gamma}} v + G_{\boldsymbol{\gamma}} \left(\zeta_1 G'_1 \partial_x (D^{\boldsymbol{\gamma}} v) + \zeta_1 G'_2 \partial_y (D^{\boldsymbol{\gamma}} v) \right) \right) \\
&= \sum_{1 \leq |\boldsymbol{\gamma}| \leq |\boldsymbol{\alpha}|+1} \zeta_1^{-\alpha_1 + |\boldsymbol{\gamma}|} G_{\boldsymbol{\gamma}} D^{\boldsymbol{\gamma}} v.
\end{aligned}$$

Thus, equation (3.33) holds for all $\boldsymbol{\alpha}'$ with $|\boldsymbol{\alpha}'| = s + 1$, completing the induction. □

Now we show the converse direction, i.e., how standard physical derivatives can be expressed through directional derivatives.

Lemma 3.19. *For each multi-index $\boldsymbol{\alpha}$, there exist bounded functions $G_{\boldsymbol{\gamma}} : [0,1] \to \mathbb{R}$, $1 \leq |\boldsymbol{\gamma}| \leq |\boldsymbol{\alpha}|$, such that*

$$D^{\boldsymbol{\alpha}} v = \sum_{1 \leq |\boldsymbol{\gamma}| \leq |\boldsymbol{\alpha}|} \zeta_1^{-|\boldsymbol{\alpha}| + \gamma_1} G_{\boldsymbol{\gamma}} D_{\boldsymbol{F}}^{\boldsymbol{\gamma}} v, \tag{3.34}$$

where we write $\boldsymbol{\zeta} = (\zeta_1, \zeta_2) = (\zeta_1(\boldsymbol{x}), \zeta_2(\boldsymbol{x})) = \boldsymbol{F}^{-1}(\boldsymbol{x})$ and $G_{\boldsymbol{\gamma}} = G_{\boldsymbol{\gamma}}(\zeta_2(\boldsymbol{x}))$ for all $\boldsymbol{x} \neq \boldsymbol{0}$.

Proof. We proceed by induction on $|\boldsymbol{\alpha}|$, in analogy to the proof of Lemma 3.18. For $|\boldsymbol{\alpha}| = 1$, the statement follows from (3.31) and (3.32). Assume that the formula (3.34) holds for all multi-indices $\boldsymbol{\alpha}$ with $|\boldsymbol{\alpha}| = s \in \mathbb{N}$ and let again $G_{\boldsymbol{\gamma}}$ denote generic bounded coefficient functions depending only on ζ_2. Then, we find from (3.31) that

$$\begin{aligned}\partial_x \zeta_1 &= G_2 \, \mathrm{D}_{\boldsymbol{F}}^{(1,0)} \zeta_1 - \zeta_1^{-1} G_2' \, \mathrm{D}_{\boldsymbol{F}}^{(0,1)} \zeta_1 = G_2, \\ \partial_x (G_{\boldsymbol{\gamma}}) &= G_2 \, \mathrm{D}_{\boldsymbol{F}}^{(1,0)} G_{\boldsymbol{\gamma}} - \zeta_1^{-1} G_2' \, \mathrm{D}_{\boldsymbol{F}}^{(0,1)} G_{\boldsymbol{\gamma}} = -\zeta_1^{-1} G_2' G_{\boldsymbol{\gamma}}',\end{aligned}$$

and thus

$$\begin{aligned}D^{(\alpha_1+1,\alpha_2)} v = D^{(1,0)} \left(D^{\boldsymbol{\alpha}} v \right) &= \partial_x \left(\sum_{1 \le |\boldsymbol{\gamma}| \le |\boldsymbol{\alpha}|} \zeta_1^{-|\boldsymbol{\alpha}|+\gamma_1} G_{\boldsymbol{\gamma}} D_{\boldsymbol{F}}^{\boldsymbol{\gamma}} v \right) \\ &= \sum_{1 \le |\boldsymbol{\gamma}| \le |\boldsymbol{\alpha}|} \left[\partial_x \left(\zeta_1^{-|\boldsymbol{\alpha}|+\gamma_1} \right) G_{\boldsymbol{\gamma}} D_{\boldsymbol{F}}^{\boldsymbol{\gamma}} v + \zeta_1^{-|\boldsymbol{\alpha}|+\gamma_1} \partial_x \left(G_{\boldsymbol{\gamma}} D_{\boldsymbol{F}}^{\boldsymbol{\gamma}} v \right) \right] \\ &= \sum_{1 \le |\boldsymbol{\gamma}| \le |\boldsymbol{\alpha}|} (-|\boldsymbol{\alpha}| + \gamma_1) \zeta_1^{-(|\boldsymbol{\alpha}|+1)+\gamma_1} \partial_x \zeta_1 \, G_{\boldsymbol{\gamma}} D_{\boldsymbol{F}}^{\boldsymbol{\gamma}} v \\ &\quad + \sum_{1 \le |\boldsymbol{\gamma}| \le |\boldsymbol{\alpha}|} \zeta_1^{-|\boldsymbol{\alpha}|+\gamma_1} \left(\partial_x (G_{\boldsymbol{\gamma}}) D_{\boldsymbol{F}}^{\boldsymbol{\gamma}} v + G_{\boldsymbol{\gamma}} \left(G_2 D_{\boldsymbol{F}}^{\boldsymbol{\gamma}+(1,0)} v - \zeta_1^{-1} G_2' D_{\boldsymbol{F}}^{\boldsymbol{\gamma}+(0,1)} v \right) \right) \\ &= \sum_{1 \le |\boldsymbol{\gamma}| \le |\boldsymbol{\alpha}|+1} \zeta_1^{-(|\boldsymbol{\alpha}|+1)+\gamma_1} G_{\boldsymbol{\gamma}} D_{\boldsymbol{F}}^{\boldsymbol{\gamma}} v.\end{aligned}$$

A similar formula can be derived for $D^{(\alpha_1,\alpha_2+1)} v$. Hence, (3.34) holds for all $\boldsymbol{\alpha}'$ with $|\boldsymbol{\alpha}'| = s + 1$ and the Lemma is proven. □

Polar transformation of norms and polar Sobolev spaces

With that, we now consider the transformation of Sobolev norms on the physical domain to the parametric domain. To this end, we first define weighted function spaces on the parametric domain, which differ from the ones in Definition 2.1 in the sense that the distance of a point to the edge $\widehat{\Gamma}_1$, that is, the first coordinate ζ_1, is weighted and not the distance to $\mathbf{0}$. However, since those quantities correspond to each other, recall (3.8), this is a natural choice. That is, for $Q \subset \widehat{\Omega}$, we set

$$\widehat{H}^s_\beta(Q) := \left\{ \widehat{v} \in \mathcal{D}'(Q) : \|\widehat{v}\|_{\widehat{H}^s_\beta(Q)} < \infty \right\} \quad \text{and} \quad \widehat{V}^s_\beta(Q) := \left\{ \widehat{v} \in \mathcal{D}'(Q) : \|\widehat{v}\|_{\widehat{V}^s_\beta(Q)} < \infty \right\},$$

with the norms

$$\begin{aligned}\|\widehat{v}\|^2_{\widehat{H}^s_\beta(Q)} &:= \sum_{|\boldsymbol{\alpha}| \le s} \left\| \zeta_1^\beta \widehat{D}^{\boldsymbol{\alpha}} \widehat{v} \right\|^2_{\widehat{L}^2(Q)} := \sum_{|\boldsymbol{\alpha}| \le s} \int_Q \left| \zeta_1^\beta \widehat{D}^{\boldsymbol{\alpha}} \widehat{v}(\boldsymbol{\zeta}) \right|^2 \mathrm{d}\boldsymbol{\zeta}, \\ \|\widehat{v}\|^2_{\widehat{V}^s_\beta(Q)} &:= \sum_{|\boldsymbol{\alpha}| \le s} \left\| \zeta_1^{\beta-s+|\alpha|} \widehat{D}^{\boldsymbol{\alpha}} \widehat{v} \right\|^2_{\widehat{L}^2(Q)} := \sum_{|\boldsymbol{\alpha}| \le s} \int_Q \left| \zeta_1^{\beta-s+|\alpha|} \widehat{D}^{\boldsymbol{\alpha}} \widehat{v}(\boldsymbol{\zeta}) \right|^2 \mathrm{d}\boldsymbol{\zeta}\end{aligned}$$

and seminorms

$$|\widehat{v}|^2_{\widehat{H}^s_\beta(Q)} := |\widehat{v}|^2_{\widehat{V}^s_\beta(Q)} := \sum_{|\boldsymbol{\alpha}| = s} \left\| \zeta_1^\beta \widehat{D}^{\boldsymbol{\alpha}} \widehat{v} \right\|^2_{\widehat{L}^2(Q)}.$$

The Sobolev spaces on Q without weight are denoted by $\widehat{H}^s(Q) = \widehat{H}^s_0(Q)$ and $\widehat{V}^s(Q) = \widehat{V}^s_0(Q)$ and we write $\widehat{L}^2_\beta(Q) = \widehat{H}^0_\beta(Q) = \widehat{V}^0_\beta(Q)$ and $\widehat{L}^2(Q) = \widehat{H}^0(Q) = \widehat{V}^0(Q)$. Similar to (2.2), for all $s \in \mathbb{N}$ and $\beta \in \mathbb{R}$, we have an embedding of the V-spaces into the H-spaces,

$$\widehat{V}^s_\beta(Q) \hookrightarrow \widehat{H}^s_\beta(Q). \tag{3.35}$$

In the following, let $K \in \mathcal{M}$ be an element of the Bézier mesh, $Q = \boldsymbol{F}^{-1}(K) \in \widehat{\mathcal{M}}$ its corresponding parametric element and let $\widehat{v} = v \circ \boldsymbol{F}$ be the pull-back of a function $v : \Omega \to \mathbb{R}$. When working with smooth parameterizations as considered in [Baz+06; BBSV14; BCS12], it can be shown that a function belongs to $H^s_\beta(K)$ if and only if its pull-back lies in $\widehat{H}^s_\beta(Q)$. However, the same does not hold for pull-backs based on polar parameterizations. To demonstrate this, we first consider the pull-back of a function $v \in L^2(K)$. By a simple integral transformation, taking into account the Jacobian (3.5), we obtain the relation

$$\|v\|^2_{L^2(K)} = \int_Q |\widehat{v}||\det(J_{\boldsymbol{F}})| \,\mathrm{d}\boldsymbol{\zeta} \sim \int_Q |\widehat{v}|^2 \zeta_1 \,\mathrm{d}\zeta_1 \,\mathrm{d}\zeta_2 = \|\widehat{v}\|^2_{\widehat{L}^2_{1/2}(Q)}, \tag{3.36}$$

that is, we have $v \in L^2(K)$ if and only if $\widehat{v} \in \widehat{L}^2_{1/2}(Q)$. In the next steps, we compute the transformation of Sobolev norms. By combining equations (3.31), (3.32) and (3.28), the Jacobian determinant (3.5), a transformation of integrals and Assumption 3.4, we obtain

$$\begin{aligned}
|v|^2_{V^1(K)} = |v|^2_{H^1(K)} &= \int_K |\partial_x v|^2 + |\partial_y v|^2 \,\mathrm{d}\boldsymbol{x} \\
&= \int_Q \left(\left(G_2 \,\widehat{\partial}_1 \widehat{v} - \frac{1}{\zeta_1} G_2' \,\widehat{\partial}_2 \widehat{v} \right)^2 + \left(-G_1' \,\widehat{\partial}_1 \widehat{v} + \frac{1}{\zeta_1} G_1 \,\widehat{\partial}_2 \widehat{v} \right)^2 \right) |\det(J_{\boldsymbol{F}})| \,\mathrm{d}\boldsymbol{\zeta} \\
&\leq C \int_Q \left(\left(\widehat{\partial}_1 \,\widehat{v} \right)^2 + \left(\frac{1}{\zeta_1} \widehat{\partial}_2 \widehat{v} \right)^2 \right) \zeta_1 \,\mathrm{d}\boldsymbol{\zeta} = C \left(\left\| \widehat{\partial}_1 \widehat{v} \right\|^2_{\widehat{L}^2_{1/2}(Q)} + \left\| \zeta_1^{-1} \widehat{\partial}_2 \widehat{v} \right\|^2_{\widehat{L}^2_{1/2}(Q)} \right).
\end{aligned}$$

By using (3.8) and again (3.5), it further follows

$$\left\| r^{-1} v \right\|^2_{L^2(K)} \sim \int_Q |\zeta_1^{-1} \widehat{v}| \zeta_1 \,\mathrm{d}\boldsymbol{\zeta} = \left\| \zeta_1^{-1} \widehat{v} \right\|^2_{\widehat{L}^2_{1/2}(Q)}.$$

Thus, we have an estimate for the V^1-norm,

$$\|v\|^2_{V^1(K)} = \left\| r^{-1} v \right\|^2_{L^2(K)} + |v|^2_{V^1(K)} \leq C \|\widehat{v}\|^2_{\widehat{V}^1_\odot(Q)}, \tag{3.37}$$

with $\|\widehat{v}\|^2_{\widehat{V}^1_\odot(Q)} := \left\| \zeta_1^{-1} \widehat{v} \right\|_{\widehat{L}^2_{1/2}(Q)} + \left\| \widehat{\partial}_1 \widehat{v} \right\|^2_{\widehat{L}^2_{1/2}(Q)} + \left\| \zeta_1^{-1} \widehat{\partial}_2 \widehat{v} \right\|^2_{\widehat{L}^2_{1/2}(Q)}$. In the other direction, it follows with relations (3.7), (3.8), (3.28), (3.29), and Assumption 3.4 that

$$\begin{aligned}
\left\| \widehat{\partial}_1 \widehat{v} \right\|^2_{\widehat{L}^2_{1/2}(Q)} &= \int_Q \left(\widehat{\partial}_1 \widehat{v} \right)^2 \zeta_1 \,\mathrm{d}\boldsymbol{\zeta} = \int_K \left(\widehat{\partial}_1 \widehat{v} \circ \boldsymbol{F}^{-1} \right)^2 \zeta_1(\boldsymbol{x}) |\det(J_{\boldsymbol{F}^{-1}})| \,\mathrm{d}\boldsymbol{x} \\
&\sim \int_K \left(\mathrm{D}^{(1,0)}_{\boldsymbol{F}} v \right)^2 \,\mathrm{d}\boldsymbol{x} = \int_K \left(G_1(\zeta_2(\boldsymbol{x})) \partial_x v + G_2(\zeta_2(\boldsymbol{x})) \partial_y v \right)^2 \,\mathrm{d}\boldsymbol{x} \\
&\leq C \int_K |\partial_x v|^2 + |\partial_y v|^2 \,\mathrm{d}\boldsymbol{x} = C |v|^2_{V^1(K)}.
\end{aligned}$$

By using similar arguments and (3.30), we compute

$$\begin{aligned}\left\|\zeta_1^{-1}\widehat{\partial}_2\widehat{v}\right\|^2_{\widehat{L}^2_{1/2}(Q)} &= \int_Q \left(\zeta_1^{-1}\widehat{\partial}_2\widehat{v}\right)^2 \zeta_1 \,\mathrm{d}\boldsymbol{\zeta} \sim \int_K \left(\zeta_1^{-1}(\boldsymbol{x})\,\mathrm{D}_{\boldsymbol{F}}^{(0,1)}v\right)^2 \mathrm{d}\boldsymbol{x}\\ &= \int_K \left(G_1'(\zeta_2(\boldsymbol{x}))\partial_x v + G_2'(\zeta_2(\boldsymbol{x}))\partial_y v\right)^2 \mathrm{d}\boldsymbol{x}\\ &\le C\int_K |\partial_x v|^2 + |\partial_y v|^2 \,\mathrm{d}\boldsymbol{x} = C|v|^2_{V^1(K)}.\end{aligned}$$

Hence, we have not only the one-way estimate (3.37), but the equivalence relation

$$\|v\|^2_{V^1(K)} \sim \|\widehat{v}\|^2_{\widehat{V}^1_\odot(Q)}. \tag{3.38}$$

To generalize this pattern, we introduce *weighted polar Sobolev spaces* of order $s \in \mathbb{N}_0$ with weight $\beta \in \mathbb{R}$ on any subset $Q \subset \widehat{\Omega}$ of the parametric domain,

$$\widehat{H}^s_{\odot,\beta}(Q) := \left\{\widehat{v} \in \mathcal{D}'(Q)\colon \|\widehat{v}\|_{\widehat{H}^s_{\odot,\beta}(Q)} < \infty\right\} \quad \text{and} \quad \widehat{V}^s_{\odot,\beta}(Q) := \left\{\widehat{v} \in \mathcal{D}'(Q)\colon \|\widehat{v}\|_{\widehat{V}^s_{\odot,\beta}(Q)} < \infty\right\},$$

with the norms

$$\begin{aligned}\|\widehat{v}\|^2_{\widehat{H}^s_{\odot,\beta}(Q)} &:= \sum_{|\boldsymbol{\alpha}|\le s} \left\|\zeta_1^{\beta-\alpha_2}\widehat{D}^{\boldsymbol{\alpha}}\widehat{v}\right\|^2_{\widehat{L}^2_{1/2}(Q)} = \sum_{|\boldsymbol{\alpha}|\le s}\int_Q \left|\zeta_1^{\beta-\alpha_2}\widehat{D}^{\boldsymbol{\alpha}}\widehat{v}(\boldsymbol{\zeta})\right|^2 \zeta_1 \,\mathrm{d}\boldsymbol{\zeta},\\ \|\widehat{v}\|^2_{\widehat{V}^s_{\odot,\beta}(Q)} &:= \sum_{|\boldsymbol{\alpha}|\le s} \left\|\zeta_1^{\beta-s+\alpha_1}\widehat{D}^{\boldsymbol{\alpha}}\widehat{v}\right\|^2_{\widehat{L}^2_{1/2}(Q)} = \sum_{|\boldsymbol{\alpha}|\le s}\int_Q \left|\zeta_1^{\beta-s+\alpha_1}\widehat{D}^{\boldsymbol{\alpha}}\widehat{v}(\boldsymbol{\zeta})\right|^2 \zeta_1 \,\mathrm{d}\boldsymbol{\zeta}\end{aligned}$$

and seminorms

$$|\widehat{v}|^2_{\widehat{H}^s_{\odot,\beta}(Q)} := |\widehat{v}|^2_{\widehat{V}^s_{\odot,\beta}(Q)} := \sum_{|\boldsymbol{\alpha}|=s} \left\|\zeta_1^{\beta-\alpha_2}\widehat{D}^{\boldsymbol{\alpha}}\widehat{v}\right\|^2_{\widehat{L}^2_{1/2}(Q)}.$$

Polar Sobolev spaces without weight will be denoted by $\widehat{H}^s_\odot(Q) = \widehat{H}^s_{\odot,0}(Q)$ and $\widehat{V}^s_\odot(Q) = \widehat{V}^s_{\odot,0}(Q)$. Furthermore, it holds $\widehat{H}^0_\odot(Q) = \widehat{V}^0_\odot(Q) = \widehat{L}^2_{1/2}(Q)$ and $\widehat{H}^0_{\odot,\beta}(Q) = \widehat{V}^0_{\odot,\beta}(Q) = \widehat{L}^2_{1/2+\beta}(Q)$. We emphasize that the definition of the polar Sobolev spaces intrinsically includes the weight $\frac{1}{2}$, although this is not explicitly indicated in the notation.

It is easy to see that

$$\|\widehat{v}\|_{\widehat{H}^s_{1/2+\beta}(Q)} \le C\|\widehat{v}\|_{\widehat{H}^s_{\odot,\beta}(Q)} \le C\|\widehat{v}\|_{\widehat{V}^s_{\odot,\beta}(Q)} \quad \text{for all } \widehat{v} \in V^s_{\odot,\beta}(Q), \tag{3.39}$$

recall also (3.35), and thus the embeddings $\widehat{V}^s_{\odot,\beta}(Q) \subset \widehat{H}^s_{\odot,\beta}(Q) \subset \widehat{H}^s_{1/2+\beta}(Q)$ hold.

Most importantly, the key property of the polar V-spaces is their natural correspondence to the standard V-spaces on the physical domain, which we establish in detail in the following lemma.

Lemma 3.20. *Let $v \in V^s_\beta(K)$, $K \in \mathcal{M}^\mu$, $s \in \mathbb{N}_0$ and $\beta \in \mathbb{R}$. Then, with $Q = \boldsymbol{F}^{-1}(K)$ and $\widehat{v} = v \circ \boldsymbol{F}$, it holds*

$$\|v\|_{V^s_\beta(K)} \sim \|\widehat{v}\|_{\widehat{V}^s_{\odot,\beta}(Q)}. \tag{3.40}$$

Proof. We verified this property for $\beta = 0$ and $s = 0, 1$ in (3.36) and (3.38). Now, let $s \in \mathbb{N}$ and $\beta \in \mathbb{R}$ be arbitrary. Consider one term in $\|v\|_{V^s_\beta(K)}$ as defined in Definition 2.1. By relation (3.8) and Lemma 3.19, we have

$$r^{\beta-s+|\boldsymbol{\alpha}|}|D^{\boldsymbol{\alpha}}v| \sim \zeta_1^{\beta-s+|\boldsymbol{\alpha}|}|D^{\boldsymbol{\alpha}}v| \leq \sum_{|\boldsymbol{\gamma}|\leq|\boldsymbol{\alpha}|} \zeta_1^{\beta-s+\gamma_1}|G_{\boldsymbol{\gamma}}|\,|D^{\boldsymbol{\gamma}}_{\boldsymbol{F}}v|.$$

After squaring and summing over $|\boldsymbol{\alpha}| \leq s$ and applying the Cauchy-Schwarz inequality, the boundedness of all $G_{\boldsymbol{\gamma}}$ and the Jacobian determinant (3.5), we obtain

$$\|v\|^2_{V^s_\beta(K)} = \sum_{|\boldsymbol{\alpha}|\leq s}\int_K r^{2(\beta-s+|\boldsymbol{\alpha}|)}|D^{\boldsymbol{\alpha}}v|^2\,d\boldsymbol{x} \leq C\sum_{|\boldsymbol{\gamma}|\leq s}\int_Q \zeta_1^{2(\beta-s+\gamma_1)}|D^{\boldsymbol{\gamma}}_{\boldsymbol{F}}v|^2\,\zeta_1\,d\boldsymbol{\zeta} = C\,\|\widehat{v}\|^2_{\widehat{V}^s_{\odot,\beta}(Q)}.$$

Vice versa, as demonstrated in Lemma 3.18, a single term of $\|\widehat{v}\|_{\widehat{V}^s_{\odot,\beta}(Q)}$ can be estimated by

$$\zeta_1^{\beta-s+\alpha_1}|D^{\boldsymbol{\alpha}}_{\boldsymbol{F}}v| \leq \sum_{|\boldsymbol{\gamma}|\leq|\boldsymbol{\alpha}|} \zeta_1^{\beta-s+|\boldsymbol{\gamma}|}|G_{\boldsymbol{\gamma}}|\,|D^{\boldsymbol{\gamma}}v|,$$

which leads, by similar arguments, to

$$\|\widehat{v}\|^2_{\widehat{V}^s_{\odot,\beta}(Q)} \leq C\sum_{|\boldsymbol{\alpha}|\leq s}\int_K \zeta_1^{2(\beta-s+\alpha_1)}|D^{\boldsymbol{\alpha}}_{\boldsymbol{F}}v|^2\,d\boldsymbol{x} \leq C\sum_{|\boldsymbol{\gamma}|\leq s}\int_K r^{2(\beta-s+|\boldsymbol{\gamma}|)}|D^{\boldsymbol{\gamma}}v|^2\,d\boldsymbol{x} = C\,\|v\|^2_{V^s_\beta(K)}.$$

Combining the two inequalities yields the desired equivalence. □

3.3.3 Bent polar Sobolev spaces

In general, the Sobolev regularity of a pull-back function is affected not only by the polar singularity, but also by the reduced continuity of the isogeometric parameterization across element interfaces. In particular, polar parameterizations as defined in Section 3.2.1 are only C^0-continuous along coarse mesh lines if the associated knot values in the coarse knot vector Ξ^0_2 are repeated, see for instance Examples 3.6 and 3.8. Therefore, bent Sobolev spaces, as introduced in [Baz+06], must be taken into account.

Throughout this section, let $E \subset \Omega$ be a union of elements $K \in \mathcal{M}$ and let $\widehat{E} = \boldsymbol{F}^{-1}(E) \subset \widehat{\Omega}$ be the corresponding union of parametric elements. First, we note that some of the derivatives (3.28) with respect to the $\boldsymbol{F}$-coordinates may be in $L^2(K)$ for all $K \in E$, but not necessarily in $L^2(E)$. Therefore, we introduce the broken norms

$$\|\mathrm{D}^{\boldsymbol{\alpha}}_{\boldsymbol{F}}v\|^2_{\mathcal{L}^2(E)} = \sum_{K\in E}\|\mathrm{D}^{\boldsymbol{\alpha}}_{\boldsymbol{F}}v\|_{L^2(K)} \quad\text{and}\quad \|\mathrm{D}^{\boldsymbol{\alpha}}_{\boldsymbol{F}}v\|^2_{\mathcal{L}^2_\beta(E)} = \sum_{K\in E}\|\mathrm{D}^{\boldsymbol{\alpha}}_{\boldsymbol{F}}v\|_{L^2_\beta(K)},$$

which is useful for distributions that are not in $L^2_\beta(E)$, with $\beta \in \mathbb{R}$. This definition enables us to generalize the computations from Section 3.3.2 to unions of mesh elements. Even though we have the element-wise relation (3.40) for all $K \in E$, the pull-back $\widehat{v} = v \circ \boldsymbol{F}$ of a function $v \in V^s_\beta(E)$ is not necessarily in $\widehat{V}^s_{\odot,\beta}(\widehat{E})$. For two adjacent parametric elements $Q_1, Q_2 \in \widehat{\mathcal{M}}$, let m_{Q_1,Q_2} denote the maximal order of continuous derivatives of $\boldsymbol{F}$ across their common edge $\partial Q_1 \cap \partial Q_2$. Then, we define *weighted bent Sobolev spaces* $\mathcal{X}^s_\beta(\widehat{E}) = \mathcal{H}^s_\beta(\widehat{E})$ and $\mathcal{X}^s_\beta(\widehat{E}) = \mathcal{V}^s_\beta(\widehat{E})$ of order $s \in \mathbb{N}$, $s \geq 1$

with weight $\beta > 0$ by

$$\mathcal{X}^s_\beta(\widehat{E}) := \left\{ \widehat{v} \in \widehat{L}^2(\widehat{E}) \colon \left\{ \begin{aligned} &\widehat{v}_{|Q} \in \widehat{X}^s_\beta(Q) && \text{for all } Q \in \widehat{E} \text{ and} \\ &\widehat{\nabla}^q(\widehat{v}_{|Q_1}) = \widehat{\nabla}^q(\widehat{v}_{|Q_2}) && \text{on } \partial Q_1 \cap \partial Q_2 \text{ for } q = 0, 1, \dots, \\ &&& \min\{m_{Q_1,Q_2}, s-1\} \text{ for all} \\ &&& Q_1, Q_2 \text{ with } \partial Q_1 \cap \partial Q_2 \neq \emptyset \end{aligned} \right\} \right\},$$

where we insert $\widehat{X}^s_\beta(Q) = \widehat{H}^s_\beta(Q)$ and $\widehat{X}^s_\beta(Q) = \widehat{V}^s_\beta(Q)$, respectively, and $\widehat{\nabla}^q$ denotes the q-th order partial derivative operator, with $\widehat{\nabla}^0 v = v$. This definition yields well-defined Hilbert spaces endowed with the broken norm and seminorm

$$\|\widehat{v}\|^2_{\mathcal{X}^s_\beta(\widehat{E})} := \sum_{Q \in \widehat{E}} \|\widehat{v}\|^2_{\widehat{X}^s_\beta(Q)}, \quad |\widehat{v}|^2_{\mathcal{X}^s_\beta(\widehat{E})} := \sum_{Q \in \widehat{E}} |\widehat{v}|^2_{\widehat{X}^s_\beta(Q)}.$$

The standard bent Sobolev spaces without weight are denoted by $\mathcal{H}^s(\widehat{E}) = \mathcal{H}^s_0(\widehat{E})$ and $\mathcal{V}^s(\widehat{E}) = \mathcal{V}^s_0(\widehat{E})$.

In the next step, we combine the concepts of polar and bent function spaces and introduce *weighted bent polar Sobolev spaces* $\mathcal{X}^s_{\odot,\beta}(\widehat{E}) = \mathcal{H}^s_{\odot,\beta}(\widehat{E})$ and $\mathcal{X}^s_{\odot,\beta}(\widehat{E}) = \mathcal{V}^s_{\odot,\beta}(\widehat{E})$ of order $s \in \mathbb{N}$, $s \geq 1$ with weight $\beta > 0$,

$$\mathcal{X}^s_{\odot,\beta}(\widehat{E}) := \left\{ \widehat{v} \in \widehat{L}^2(\widehat{E}) \colon \left\{ \begin{aligned} &\widehat{v}_{|Q} \in \widehat{X}^s_{\odot,\beta}(Q) && \text{for all } Q \in \widehat{E} \text{ and} \\ &\widehat{\nabla}^q(\widehat{v}_{|Q_1}) = \widehat{\nabla}^q(\widehat{v}_{|Q_2}) && \text{on } \partial Q_1 \cap \partial Q_2 \text{ for } q = 0, 1, \dots, \\ &&& \min\{m_{Q_1,Q_2}, s-1\} \text{ for all} \\ &&& Q_1, Q_2 \text{ with } \partial Q_1 \cap \partial Q_2 \neq \emptyset \end{aligned} \right\} \right\},$$

where we insert $\widehat{X}^s_{\odot,\beta}(Q) = \widehat{H}^s_{\odot,\beta}(Q)$ and $\widehat{X}^s_{\odot,\beta}(Q) = \widehat{V}^s_{\odot,\beta}(Q)$, respectively, endowed with the broken norm and seminorm

$$\|\widehat{v}\|^2_{\mathcal{X}^s_{\odot,\beta}(\widehat{E})} := \sum_{Q \in \widehat{E}} \|\widehat{v}\|^2_{\widehat{X}^s_{\odot,\beta}(Q)}, \quad |\widehat{v}|^2_{\mathcal{X}^s_{\odot,\beta}(\widehat{E})} := \sum_{Q \in \widehat{E}} |\widehat{v}|^2_{\widehat{X}^s_{\odot,\beta}(Q)}.$$

Bent polar Sobolev spaces without weight are denoted by $\mathcal{H}^s_\odot(\widehat{E}) = \mathcal{H}^s_{\odot,0}(\widehat{E})$ and $\mathcal{V}^s_\odot(\widehat{E}) = \mathcal{V}^s_{\odot,0}(\widehat{E})$. From (3.40), we immediately obtain the characteristic relation

$$\|v\|_{V^s_\beta(E)} \sim \|\widehat{v}\|_{\mathcal{V}^s_{\odot,\beta}(\widehat{E})} \quad \text{for all } v \in V^s_\beta(E), \tag{3.41}$$

with $s \in \mathbb{N}_0$ and $\beta \in \mathbb{R}$, and (3.39) yields the estimate

$$\|\widehat{v}\|_{\mathcal{H}^s_{1/2+\beta}(\widehat{E})} \leq C\|\widehat{v}\|_{\mathcal{H}^s_{\odot,\beta}(\widehat{E})} \leq C\|\widehat{v}\|_{\mathcal{V}^s_{\odot,\beta}(\widehat{E})} \quad \text{for all } \widehat{v} \in \mathcal{V}^s_{\odot,\beta}(\widehat{E}). \tag{3.42}$$

Thus, the embeddings $\mathcal{V}^s_{\odot,\beta}(\widehat{E}) \subset \mathcal{H}^s_{\odot,\beta}(\widehat{E}) \subset \mathcal{H}^s_{1/2+\beta}(\widehat{E})$ hold.

In this context, suitable projectors $\Pi : \mathcal{X}^s_{\odot,\beta}(\widehat{\Omega}) \to S_{(s-1,s-1)}(\boldsymbol{\Xi})$ are required that map from weighted bent polar Sobolev spaces of order s into the spline spaces of degree $s-1$ and satisfy the crucial property

$$\widehat{v} - \Pi(\widehat{v}) \in \widehat{X}^s_{\odot,\beta}(\widehat{\Omega}) \quad \text{for all } \widehat{v} \in \mathcal{X}^s_{\odot,\beta}(\widehat{\Omega}). \tag{3.43}$$

The existence of such projectors can be shown by analogy to similar results from the literature [BBSV14].

3.3.4 Polar transformation of the projection error

Ultimately, we perform a transformation of the projection error, which will be needed to prove Theorem 3.21. Therefore, in addition to the computations above, the weight function has to be taken into account. For $q = 0$, we obtain

$$\begin{aligned}\left\|v - \Pi_{V_h^\odot} v\right\|_{L^2(K)}^2 &= \int_K \left|v - \Pi_{V_h^\odot} v\right|^2 \mathrm{d}\boldsymbol{x} \sim \int_Q \left|v \circ \boldsymbol{F} - \Pi_{V_h^\odot} v \circ \boldsymbol{F}\right|^2 \zeta_1 \,\mathrm{d}\boldsymbol{\zeta} \\ &= \int_Q \left|\frac{W(v \circ \boldsymbol{F}) - \Pi^{\widehat{\Gamma}}_{\boldsymbol{p},\boldsymbol{\Xi}}(W(v \circ \boldsymbol{F}))}{W}\right|^2 \zeta_1 \,\mathrm{d}\boldsymbol{\zeta} \leq C \int_Q \left|W\widehat{v} - \Pi^{\widehat{\Gamma}}_{\boldsymbol{p},\boldsymbol{\Xi}}(W\widehat{v})\right|^2 \zeta_1 \,\mathrm{d}\boldsymbol{\zeta} \\ &= C\left\|W\widehat{v} - \Pi^{\widehat{\Gamma}}_{\boldsymbol{p},\boldsymbol{\Xi}}(W\widehat{v})\right\|_{\widehat{L}^2_{1/2}(Q)}^2, \end{aligned} \tag{3.44}$$

where we use the boundedness of W and its inverse W^{-1}, see [BBSV14], and set $\widehat{v} = v \circ \boldsymbol{F}$. For $q = 1$, we compute

$$\begin{aligned}\left|v - \Pi_{V_h^\odot} v\right|_{H^1(K)}^2 &= \int_K \left|\partial_x \left(v - \Pi_{V_h^\odot} v\right)\right|^2 + \left|\partial_y \left(v - \Pi_{V_h^\odot} v\right)\right|^2 \mathrm{d}\boldsymbol{x} \\ &\sim \int_Q \left(\left|\widehat{\partial}_1 \left(v \circ \boldsymbol{F} - \Pi_{V_h^\odot} v \circ \boldsymbol{F}\right)\right|^2 + \left|\frac{1}{\zeta_1}\widehat{\partial}_2 \left(v \circ \boldsymbol{F} - \Pi_{V_h^\odot} v \circ \boldsymbol{F}\right)\right|^2\right) \zeta_1 \,\mathrm{d}\boldsymbol{\zeta} \\ &= \int_Q \left(\left|\widehat{\partial}_1 \left(\frac{W\widehat{v} - \Pi^{\widehat{\Gamma}}_{\boldsymbol{p},\boldsymbol{\Xi}}(W\widehat{v})}{W}\right)\right|^2 + \left|\frac{1}{\zeta_1}\widehat{\partial}_2 \left(\frac{W\widehat{v} - \Pi^{\widehat{\Gamma}}_{\boldsymbol{p},\boldsymbol{\Xi}}(W\widehat{v})}{W}\right)\right|^2\right) \zeta_1 \,\mathrm{d}\boldsymbol{\zeta} \\ &\leq C\Bigg(\left\|\widehat{\partial}_1 \left(W\widehat{v} - \Pi^{\widehat{\Gamma}}_{\boldsymbol{p},\boldsymbol{\Xi}}(W\widehat{v})\right)\right\|_{\widehat{L}^2_{1/2}(Q)}^2 + \left\|W\widehat{v} - \Pi^{\widehat{\Gamma}}_{\boldsymbol{p},\boldsymbol{\Xi}}(W\widehat{v})\right\|_{\widehat{L}^2_{1/2}(Q)}^2 \\ &\quad + \left\|\widehat{\partial}_2 \left(W\widehat{v} - \Pi^{\widehat{\Gamma}}_{\boldsymbol{p},\boldsymbol{\Xi}}(W\widehat{v})\right)\right\|_{\widehat{L}^2_{-1/2}(Q)}^2 + \left\|W\widehat{v} - \Pi^{\widehat{\Gamma}}_{\boldsymbol{p},\boldsymbol{\Xi}}(W\widehat{v})\right\|_{\widehat{L}^2_{-1/2}(Q)}^2\Bigg), \end{aligned} \tag{3.45}$$

where we use the Leibniz formula

$$\partial^{\boldsymbol{\alpha}} \left(\frac{g}{W}\right) = \sum_{\{\boldsymbol{\beta}:\boldsymbol{\beta}\leq\boldsymbol{\alpha}\}} \binom{\boldsymbol{\alpha}}{\boldsymbol{\beta}} \left(\partial^{\boldsymbol{\beta}} g\right) \left(\partial^{\boldsymbol{\alpha}-\boldsymbol{\beta}} W^{-1}\right) \tag{3.46}$$

with $g = \widehat{v} - \Pi^{\widehat{\Gamma}}_{\boldsymbol{p},\boldsymbol{\Xi}}\widehat{v}$ and Young's formula. Here, we remark again that the weight function W and its inverse W^{-1} as well as their derivatives are bounded [BBSV14]. Throughout the chapter, the latter will be used multiple times, and the Leibniz formula will be applied in combination with the weight function without further explication.

Finally, let $E \subset \Omega$ be given by a union of elements $K \in \mathcal{M}$ and let $\widehat{E} = \boldsymbol{F}^{-1}(E) \subset \widehat{\Omega}$. Then, we have analogous results to (3.44) and (3.45), but with bent Sobolev spaces,

$$\left\|v - \Pi_{V_h^\odot} v\right\|_{L^2(E)}^2 \leq \left\|W\widehat{v} - \Pi^{\widehat{\Gamma}}_{\boldsymbol{p},\boldsymbol{\Xi}}(W\widehat{v})\right\|_{\mathcal{L}^2_{1/2}(\widehat{E})}^2$$

and

$$\begin{aligned}\left|v - \Pi_{V_h^\odot} v\right|_{H^1(E)}^2 \leq C\Bigg(&\left\|\widehat{\partial}_1 \left(W\widehat{v} - \Pi^{\widehat{\Gamma}}_{\boldsymbol{p},\boldsymbol{\Xi}}(W\widehat{v})\right)\right\|_{\mathcal{L}^2_{1/2}(\widehat{E})}^2 + \left\|W\widehat{v} - \Pi^{\widehat{\Gamma}}_{\boldsymbol{p},\boldsymbol{\Xi}}(W\widehat{v})\right\|_{\mathcal{L}^2_{1/2}(\widehat{E})}^2 \\ &+ \left\|\widehat{\partial}_2 \left(W\widehat{v} - \Pi^{\widehat{\Gamma}}_{\boldsymbol{p},\boldsymbol{\Xi}}(W\widehat{v})\right)\right\|_{\mathcal{L}^2_{-1/2}(\widehat{E})}^2 + \left\|W\widehat{v} - \Pi^{\widehat{\Gamma}}_{\boldsymbol{p},\boldsymbol{\Xi}}(W\widehat{v})\right\|_{\mathcal{L}^2_{-1/2}(\widehat{E})}^2\Bigg).\end{aligned}$$

3.4 Error estimates for graded refinement in the vicinity of polar corners

In this section, largely based on Sections 3.4, 5, and Appendix B of [AZ26], we develop an approximation theory for graded Galerkin IGA on polar domains with corners and identify a condition on the grading parameter that ensures optimal convergence rates.

3.4.1 Main results

We begin by stating the central theorem. It establishes optimal approximation power of the space $V_h^{\odot}$ introduced in (3.19) with respect to the mesh parameter h. We recall that Assumptions 3.4 and 3.5 are in force, and $h \sim h_1 \sim h_2$ is a suitable mesh parameter of both the uniform and graded mesh, see equations (3.15) and (3.16). Note that the the grading parameter $\mu \in (0, 1]$ and the polynomial degrees $\boldsymbol{p} = (p_1, p_2)$, where we set $p = \min\{p_1, p_2\}$, are implicitly contained in the definition of $V_h^{\odot}$, although not stated explicitly in the notation. The theorem applies to functions in a suitable weighted Sobolev space on Ω, characterized in Section 2.1.2, provided that the grading parameter μ is chosen appropriately. The proof requires a detailed analysis and is thus presented subsequently in Section 3.4.2.

Theorem 3.21. *Let $q \in \{0, 1\}$ and $s \in \mathbb{N}$ with $2 \leq s \leq p+1$. Further, let $\nu \in \mathbb{R}$ such that $v \in V_\beta^s(\Omega)$ for all $\beta \in \mathbb{R}$ with $s - 1 - \nu < \beta < s - 1$. If the mesh grading parameter $\mu \in (0, 1]$ satisfies the condition*

$$\mu < \frac{\nu - q + 1}{s - q}, \tag{3.47}$$

then, for every $h > 0$, there is a NURBS function $v_h \in V_h^{\odot}$ on the corresponding graded mesh $\mathcal{M}^\mu$ such that

$$\|v - v_h\|_{H^q(\Omega)} \leq C h^{s-q} \|v\|_{V_\beta^s(\Omega)}.$$

In particular, we derive an error estimate for sufficiently smooth functions on uniform meshes.

Corollary 3.22. *Let $q \in \{0, 1\}$ and $s \in \mathbb{N}$ with $2 \leq s \leq p + 1$. Moreover, let $\nu > s - 1$ and $v \in V_\beta^s(\Omega)$ for all $\beta \in \mathbb{R}$ with $s - 1 - \nu < \beta < s - 1$. Then, for every $h > 0$, there exists a NURBS function $v_h \in V_h^{\odot}$ on the corresponding uniform mesh $\mathcal{M}^1$ such that*

$$\|v - v_h\|_{H^q(\Omega)} \leq C h^{s-q} \|v\|_{V^s(\Omega)}.$$

Proof. Since $\nu > s - 1$ is equivalent to $\nu - q + 1 > s - q$, condition (3.47) is satisfied for $\mu = 1$, and the assertion follows directly from Theorem 3.21. □

Remark 3.23. In general, functions belonging to the standard Sobolev spaces $H^s(\Omega)$ do not satisfy the regularity assumptions of Corollary 3.22 for any s, since the definition of the weighted spaces $V_\beta^s(\Omega)$ involves stronger integrability conditions on lower-order derivatives, see Definition 2.1. Nevertheless, the numerical experiments indicate that uniform meshes still yield optimal approximation rates, see Example 3.38. Hence, the present result may not be sharp for functions with quadratically integrable derivatives, but it constitutes a first step toward a comprehensive analysis.

Since the approximation error in the H^1-norm decreases with the same order as the projection error, we can immediately deduce approximation error estimates for the model problem (2.3) by requiring the grading parameter to satisfy (3.47) for $q = 1$.

Corollary 3.24. *Let u be the solution of the variational model problem (2.7) such that the regularity property (2.4) is satisfied. Further, let $u_h \in V_h^{\odot}$ be the solution of the discrete weak problem (2.9), where the discretization is based on the graded mesh refinement scheme presented in Section 3.2.2 for NURBS degree $p = s - 1$. If the mesh grading parameter $\mu \in (0, 1]$ satisfies*

$$\mu < \frac{\nu}{p}, \tag{3.48}$$

we obtain optimal convergence with respect to the mesh size h in the energy norm and the L^2-norm,

$$\|u - u_h\|_{H^q(\Omega)} \leq Ch^{p+1-q}\|u\|_{V_\beta^s(\Omega)} \quad \text{for } q \in \{0, 1\}.$$

Proof. For $q = 1$, the assertion follows directly from Céa's lemma and Theorem 3.21. For $q = 0$, we apply a duality argument for weighted Sobolev spaces. Without loss of generality, let $\nu < 1$, since otherwise, we have the higher regularity $u \in H^2(\Omega)$ and a standard duality argument can be used. Now, let w be the solution of the dual problem

$$a(v, w) = (u - u_h, v) \quad \forall v \in H_0^1(\Omega), \tag{3.49}$$

where $(\cdot, \cdot)$ denotes the standard scalar product in $L^2(\Omega)$. For all $\varepsilon \in (0, 2\nu)$, we have $u - u_h \in V^0_{1-\nu+\varepsilon}(\Omega)$, and the regularity result (2.4) yields that $w \in V^2_{1-\nu+\varepsilon}(\Omega)$. Moreover, the a priori estimate (2.5) and the embedding $L^2(\Omega) = V_0^0(\Omega) \hookrightarrow V^0_{1-\nu+\varepsilon}(\Omega)$, which holds for all $\epsilon > 0$ and $\nu \leq 1$, imply that

$$\|w\|_{V^2_{1-\nu+\varepsilon}(\Omega)} \leq C\|u - u_h\|^2_{V^0_{1-\nu+\varepsilon}(\Omega)} \leq C\|u - u_h\|^2_{L^2(\Omega)}. \tag{3.50}$$

By applying equation (3.49) and the Galerkin orthogonality, we further obtain

$$\begin{aligned}\|u - u_h\|^2_{L^2(\Omega)} &= (u - u_h, u - u_h) = a(u - u_h, w) = a(u - u_h, w - w_h) \\ &\leq \|u - u_h\|_{H^1(\Omega)}\|w - w_h\|_{H^1(\Omega)},\end{aligned}$$

where $w_h \in V_h^{\odot}$ is the NURBS approximation of w from Theorem 3.21. Since the grading parameter satisfies $\mu < \frac{\nu}{p} \leq \frac{\nu}{1}$, it follows with (3.49) and (3.50) that

$$\|u - u_h\|^2_{L^2(\Omega)} \leq \left(Ch^p\|u\|_{V_\beta^{p+1}(\Omega)}\right)\left(Ch\|w\|_{V^2_{1-\nu+\varepsilon}(\Omega)}\right) \leq Ch^{p+1}\|u\|_{V_\beta^{p+1}(\Omega)}\|u - u_h\|^2_{L^2(\Omega)}.$$

Dividing by $\|u - u_h\|_{L^2(\Omega)}$ completes the proof. □

In particular, we obtain an approximation result for smooth solutions, corresponding to the projection error estimate in Corollary 3.22.

Corollary 3.25. *Let u be the solution of the variational model problem (2.7) such that the regularity property (2.4) is satisfied for $\nu > s - 1$. Further, let $u_h \in V_h^{\odot}$ be the solution of the discrete weak problem (2.9) on the corresponding uniform mesh $\mathcal{M}^1$ for NURBS degree $p = s - 1$. Then, it holds*

$$\|u - u_h\|_{H^q(\Omega)} \leq Ch^{p+1-q}\|u\|_{V^{p+1}(\Omega)} \quad \text{for } q \in \{0, 1\}.$$

Proof. Since $\nu > s - 1 = p$, condition (3.48) is satisfied for $\mu = 1$, and the assertion follows directly from Corollary 3.24. □

We finish this chapter with a remark on the explicit choice of grading parameter μ. Equation (3.47) in Theorem 3.21 only states a necessary condition for optimal convergence, but for an actual computation it arises the question how to choose μ precisely. This has been discussed several times in the literature, see for instance [AM17]. Based on the numerical studies in [AZ24a], where the Laplace eigenfunctions of circular sectors, which possess comparable regularities as the solutions of our model problem (2.3), are approximated using different grading parameters, we choose

$$\mu = \min\left\{0.9 \cdot \frac{\nu}{p}, 1\right\}. \tag{3.51}$$

3.4.2 Proof of Theorem 3.21

Subsequently, we derive several error estimates for the proposed modified projector under graded h-refinement on polar domains with corners. The error is analyzed separately in the neighborhood of the polar point and in the remainder of the domain, which is not affected by the corner singularity. Both are then combined to prove Theorem 3.21.

Splitting of the polar domain

First, we explain in more detail how the model domain and the underlying meshes can be split suitably. Let $\widehat{\mathcal{M}}^\mu$ and $\mathcal{M}^\mu$ be graded parametric and physical meshes, respectively, resulting from the knot vectors Ξ_1 and Ξ_2 for some grading parameter $\mu \in (0,1]$ and polynomial degrees $\boldsymbol{p} = (p_1, p_2)$, recall Section 3.2.2. To describe a region surrounding the corner $\boldsymbol{P}$, we consider the physical Bézier elements $K_{\boldsymbol{j}} = \boldsymbol{F}(Q_{\boldsymbol{j}}) \in \mathcal{M}^\mu$ whose support extensions satisfy

$$\boldsymbol{P} \in \overline{\widetilde{K}_{\boldsymbol{j}}} = \overline{\boldsymbol{F}(\widetilde{Q}_{\boldsymbol{j}})} = \boldsymbol{F}(\overline{\widetilde{Q}_{\boldsymbol{j}}}),$$

that is, the closure of the support extension $\widetilde{K}_{\boldsymbol{j}}$ contains the singularity. The corresponding parametric mesh elements $Q_{\boldsymbol{j}}$ are characterized by the condition

$$\Gamma_1 \cap \overline{\widetilde{Q}_{\boldsymbol{j}}} = (\{0\} \times [0,1]) \cap \left(\overline{\widetilde{I}_{1,j_1}} \times \overline{\widetilde{I}_{2,j_2}}\right) = \left(\{0\} \cap \overline{\widetilde{I}_{1,j_1}}\right) \times \overline{\widetilde{I}_{2,j_2}} \neq \emptyset,$$

i.e., the singular edge Γ_1 touches the closure of the support extension $\widetilde{Q}_{\boldsymbol{j}}$, which, by equation (2.32), is equivalent to $0 \in \overline{\widetilde{I}_{1,j_1}}$. The refined knot vector in ζ_1-direction can be expressed in terms of the breakpoints (3.11)

$$\Xi_1 = \{\xi_{1,1}, \xi_{1,2}, \dots, \xi_{1,n_1+p_1+1}\} = \{\underbrace{\zeta_{1,1}, \dots, \zeta_{1,1}}_{p_1+1 \text{ times}}, \zeta_{1,2}, \zeta_{1,3}, \dots, \zeta_{1,N_1-2}, \zeta_{1,N_1-1}, \underbrace{\zeta_{1,N_1}, \dots, \zeta_{1,N_1}}_{p_1+1 \text{ times}}\}. \tag{3.52}$$

Thus, it holds $n_1 + p_1 + 1 = N_1 + 2p_1$ and

$$I_{1,j_1} = (\zeta_{1,j_1}, \zeta_{1,j_1+1}) = (\xi_{1,j_1+p_1}, \xi_{1,j_1+p_1+1}), \quad j_1 = 1, 2, \dots, N_1 - 1.$$

With definition (2.17), we obtain

$$\widetilde{I}_{1,j_1} = (\xi_{1,j_1+p_1-p_1}, \xi_{1,j_1+p_1+p_1+1}) = (\xi_{1,j_1}, \xi_{1,j_1+2p_1+1}), \quad j_1 = 1, 2, \dots, N_1 - 1.$$

By construction (3.52), we further have $\xi_{1,j_1} = 0$ and hence, it is $0 \in \overline{\widetilde{I}_{1,j_1}}$ if and only if $j_1 \leq p_1 + 1$. Therefore, we divide the graded parametric and physical Bézier mesh $\widehat{\mathcal{M}}^\mu$ and $\mathcal{M}^\mu$ into two submeshes,

$$\widehat{\mathcal{M}}^\mu = \widehat{\mathcal{M}}^\mu_C \cup \widehat{\mathcal{M}}^\mu_R \quad \text{and} \quad \mathcal{M}^\mu = \mathcal{M}^\mu_C \cup \mathcal{M}^\mu_R,$$

respectively, with

$$\begin{aligned} \widehat{\mathcal{M}}^\mu_C &:= \{Q_{\boldsymbol{j}}\}_{j_1 \in \{1,2,\dots,p_1+1\}, j_2 \in \{1,2,\dots,N_2\}}, & \widehat{\mathcal{M}}^\mu_R &:= \{Q_{\boldsymbol{j}}\}_{j_1 \in \{p_1+2,p_1+3,\dots,N_1\}, j_2 \in \{1,2,\dots,N_2\}}, \\ \mathcal{M}^\mu_C &:= \{K_{\boldsymbol{j}}\}_{j_1 \in \{1,2,\dots,p_1+1\}, j_2 \in \{1,2,\dots,N_2\}}, & \mathcal{M}^\mu_R &:= \{K_{\boldsymbol{j}}\}_{j_1 \in \{p_1+2,p_1+3,\dots,N_1\}, j_2 \in \{1,2,\dots,N_2\}}. \end{aligned}$$

Induced by these partitions, we also divide the parametric domain into two subdomains,

$$\widehat{\Omega} = \widehat{\Omega}_C \cup \widehat{\Omega}_R, \text{ with } \widehat{\Omega}_C := (0, \zeta_{1,p_1+2}] \times (0,1) \text{ and } \widehat{\Omega}_R := [\zeta_{1,p_1+2}, 1) \times (0,1). \tag{3.53}$$

In this way, we obtain the desired partition of the physical domain,

$$\Omega = \Omega_C \cup \Omega_R,$$

into a small polar domain surrounding the corner,

$$\Omega_C := \boldsymbol{F}(\widehat{\Omega}_C) = \boldsymbol{G}(\widehat{\Omega}_C) = \left\{ \zeta_1 \boldsymbol{G}(\zeta_2) \in \mathbb{R}^2 : 0 < \zeta_1 \leq \zeta_{1,p_1+2},\ 0 < \zeta_2 < 1 \right\},$$

and the remaining ring-type domain

$$\Omega_R := \boldsymbol{F}(\widehat{\Omega}_R) = \left\{ \zeta_1 \boldsymbol{G}(\zeta_2) \in \mathbb{R}^2 : \zeta_{1,p_1+2} \leq \zeta_1 < 1,\ 0 < \zeta_2 < 1 \right\},$$

where we used the representation of the polar parameterization $\boldsymbol{F}$ from Assumption 3.4. In Figure 3.8, we provide an illustration of the partitioned domains and meshes for a circular sector and an L-shaped domain. Note that the splitting depends on the mesh size h_1 and the polynomial degree p_1 of the first univariate direction, which is not pointed out explicitly in the notation. Lastly, we define the overlapping domains consisting of the union of the support extensions of all elements in $\mathcal{M}^\mu_C$ and $\mathcal{M}^\mu_R$, respectively,

$$\widetilde{\widehat{\Omega}}_C := \bigcup_{Q_{\boldsymbol{j}} \in \widehat{\mathcal{M}}^\mu_C} \widetilde{Q}_{\boldsymbol{j}}, \quad \widetilde{\widehat{\Omega}}_R := \bigcup_{Q_{\boldsymbol{j}} \in \widehat{\mathcal{M}}^\mu_R} \widetilde{Q}_{\boldsymbol{j}}, \quad \widetilde{\Omega}_C := \bigcup_{K_{\boldsymbol{j}} \in \mathcal{M}^\mu_C} \widetilde{K}_{\boldsymbol{j}}, \quad \widetilde{\Omega}_R := \bigcup_{K_{\boldsymbol{j}} \in \mathcal{M}^\mu_R} \widetilde{K}_{\boldsymbol{j}}. \tag{3.54}$$

Estimates on Ω_R

We begin by deriving error estimates on Ω_R, where the distance to the singularity is strictly positive. In this setting, a similar strategy to that used in standard anisotropic approximation theory can be applied [BBSV14; BCS12], in which element-wise estimates on the parametric domain are mapped to the physical domain via a change of variables. However, in contrast to the literature, the transformed quantities depend on the distance between each element and the singularity, and thus, by construction of Ω_R, also on the mesh size.

The following element-wise error estimate on the parametric domain from the literature serves as the starting point for our analysis.

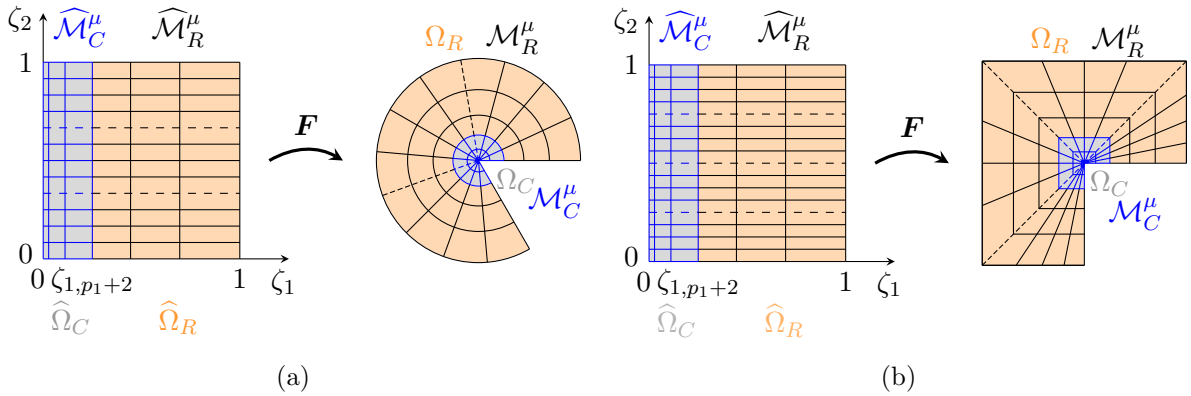

Figure 3.8: Splitting of the parametric and physical domain and the corresponding meshes. (a): Circular sector. (b): L-shaped domain.

Lemma 3.26. *Let the integers $0 \le r_1 \le s_1 \le p_1 + 1$ and $0 \le r_2 \le s_2 \le p_2 + 1$. Then, there exists a constant C depending only on $\boldsymbol{p}, \boldsymbol{\theta}$ such that for all elements $Q_{\boldsymbol{j}} \in \widehat{\mathcal{M}}^\mu$, we have*

$$\left\| \widehat{D}^{(r_1,r_2)}(\widehat{v} - \Pi^{\widehat{\Gamma}}_{\boldsymbol{p},\boldsymbol{\Xi}}\widehat{v}) \right\|_{\widehat{L}^2(Q_{\boldsymbol{j}})} \le C \left(\widetilde{h}_{1,j_1}^{s_1-r_1} \left\| \widehat{D}^{(s_1,r_2)}\widehat{v} \right\|_{\mathcal{L}^2(\widetilde{Q}_{\boldsymbol{j}})} + \widetilde{h}_{2,j_2}^{s_2-r_2} \left\| \widehat{D}^{(r_1,s_2)}\widehat{v} \right\|_{\mathcal{L}^2(\widetilde{Q}_{\boldsymbol{j}})} \right)$$

for all functions $\widehat{v} : \widehat{\Omega} \to \mathbb{R}$ with $\widehat{D}^{(s_1,r_2)}\widehat{v}$, $\widehat{D}^{(r_1,s_2)}\widehat{v} \in \mathcal{L}^2(\widetilde{\Omega}_R)$, where $\widetilde{\Omega}_R$ is defined as in (3.54).

Proof. The result is proven in [BCS12, Proposition 4.1] together with [BCS12, Remark 4.2]. □

Based on this result, we can develop an estimate on the full ring-type domain part Ω_R, with $p = \min\{p_1, p_2\}$.

Theorem 3.27. *Let $q \in \{0, 1\}$ and $s \in \mathbb{N}$ with $2 \le s \le p+1$. Further, let $v \in V_\beta^s(\widetilde{\Omega}_R)$ for all $\beta \in \mathbb{R}$ with $s - 1 - \nu < \beta < s - 1$, recall (2.4). If the mesh grading parameter satisfies condition (3.47), then there exists a constant C and a parameter β depending only on $p, \boldsymbol{\theta}, \boldsymbol{F}, W$ such that*

$$\left| v - \Pi_{V_h^\odot} v \right|_{H^q(\Omega_R)} \le C h^{s-q} \|v\|_{V_\beta^s(\widetilde{\Omega}_R)},$$

with $\widetilde{\Omega}_R$ as defined in (3.54).

Proof. Let $K_{\boldsymbol{j}} \in \mathcal{M}_R^\mu$ and $Q_{\boldsymbol{j}} = \boldsymbol{F}^{-1}(K_{\boldsymbol{j}}) \in \widehat{\mathcal{M}}_R^\mu$. By construction of the splitting from Section 3.4.2, the element $K_{\boldsymbol{j}}$ is not adjacent to the polar point, $\boldsymbol{P} \notin \overline{K_{\boldsymbol{j}}}$, and thus the Jacobian of $\boldsymbol{F}$ is bounded on $\overline{Q_{\boldsymbol{j}}}$. However, the bounds depend on the distance of $K_{\boldsymbol{j}}$ to the polar point, which is equivalent to the distance of $Q_{\boldsymbol{j}}$ to the singular edge $\widehat{\Gamma_1}$. In more detail, let $Q_{\boldsymbol{j}} = (\zeta_{1,j_1}, \zeta_{1,j_1+1}) \times (\zeta_{2,j_2}, \zeta_{2,j_2+1}) \in \mathcal{M}_R^\mu$. Then, due to equations (3.5), (3.7) and the local quasi-uniformity of the mesh, see Lemma 3.12, we have

$$|\det(J_{\boldsymbol{F}})| \sim \zeta_{1,j_1} \quad \text{and} \quad |\det(J_{\boldsymbol{F}^{-1}})| \sim \zeta_{1,j_1}^{-1} \quad \text{in } \widetilde{Q}_{\boldsymbol{j}}. \tag{3.55}$$

With (3.44), we thus obtain

$$\left\| v - \Pi^\odot_{V_h} v \right\|_{L^2(K_{\boldsymbol{j}})} \le C \left\| W\widehat{v} - \Pi^{\widehat{\Gamma}}_{\boldsymbol{p},\boldsymbol{\Xi}}(W\widehat{v}) \right\|_{\widehat{L}^2_{1/2}(Q_{\boldsymbol{j}})} \le C\zeta_{1,j_1}^{1/2} \left\| W\widehat{v} - \Pi^{\widehat{\Gamma}}_{\boldsymbol{p},\boldsymbol{\Xi}}(W\widehat{v}) \right\|_{\widehat{L}^2(Q_{\boldsymbol{j}})}$$

and with (3.45), it follows

$$|v-\Pi_{V_h}v|^2_{H^1(K_{\boldsymbol{j}})} \leq C\Bigg(\zeta_{1,j_1}\left\|\widehat{\partial}_1\left(W\widehat{v}-\Pi^{\widehat{\Gamma}}_{\boldsymbol{p},\boldsymbol{\Xi}}(W\widehat{v})\right)\right\|^2_{\widehat{L}^2(Q_{\boldsymbol{j}})}+\zeta_{1,j_1}\left\|W\widehat{v}-\Pi^{\widehat{\Gamma}}_{\boldsymbol{p},\boldsymbol{\Xi}}(W\widehat{v})\right\|^2_{\widehat{L}^2(Q_{\boldsymbol{j}})} \tag{3.56}$$

$$+\zeta^{-1}_{1,j_1}\left\|\widehat{\partial}_2\left(W\widehat{v}-\Pi^{\widehat{\Gamma}}_{\boldsymbol{p},\boldsymbol{\Xi}}(W\widehat{v})\right)\right\|^2_{\widehat{L}^2(Q_{\boldsymbol{j}})}+\zeta^{-1}_{1,j_1}\left\|W\widehat{v}-\Pi^{\widehat{\Gamma}}_{\boldsymbol{p},\boldsymbol{\Xi}}(W\widehat{v})\right\|^2_{\widehat{L}^2(Q_{\boldsymbol{j}})}\Bigg). \tag{3.57}$$

First, we estimate the terms in line (3.56). Therefore, we use Lemma 3.26 with $s_1=s$, $s_2=s-q$, $r_1=q$ and $r_2=0$ and apply the Leibniz formula (3.46), where we note that the weight function W and its inverse W^{-1} as well as their derivatives are bounded [BBSV14]. In more detail, we recall that the weight function has the form (3.9) and consequently, all derivatives $\widehat{D}^{\boldsymbol{\alpha}}W$ for $\boldsymbol{\alpha}\geq(1,0)$ vanish. It follows for $q\in\{0,1\}$ that

$$\begin{aligned}\left\|\widehat{\partial}^q_1\left(W\widehat{v}-\Pi^{\widehat{\Gamma}}_{\boldsymbol{p},\boldsymbol{\Xi}}(W\widehat{v})\right)\right\|_{\widehat{L}^2(Q_{\boldsymbol{j}})} &\leq C\left(\widetilde{h}^{s-q}_{1,j_1}\left\|\widehat{D}^{(s,0)}(W\widehat{v})\right\|_{\mathcal{L}^2(\widetilde{Q}_{\boldsymbol{j}})}+\widetilde{h}^{s-q}_{2,j_2}\left\|\widehat{D}^{(q,s-q)}(W\widehat{v})\right\|_{\mathcal{L}^2(\widetilde{Q}_{\boldsymbol{j}})}\right)\\ &\leq C\left(\widetilde{h}^{s-q}_{1,j_1}\sum_{\substack{\boldsymbol{\alpha}\leq(s,0)\\ \boldsymbol{\alpha}\geq(s,0)}}\left\|\widehat{D}^{\boldsymbol{\alpha}}\widehat{v}\right\|_{\mathcal{L}^2(\widetilde{Q}_{\boldsymbol{j}})}+\widetilde{h}^{s-q}_{2,j_2}\sum_{\substack{\boldsymbol{\alpha}\leq(q,s-q)\\ \boldsymbol{\alpha}\geq(q,0)}}\left\|\widehat{D}^{\boldsymbol{\alpha}}\widehat{v}\right\|_{\mathcal{L}^2(\widetilde{Q}_{\boldsymbol{j}})}\right)\\ &=\left(\widetilde{h}^{s-q}_{1,j_1}\left\|\widehat{D}^{(s,0)}\widehat{v}\right\|_{\mathcal{L}^2(\widetilde{Q}_{\boldsymbol{j}})}+\widetilde{h}^{s-q}_{2,j_2}\sum_{\alpha_2=0}^{s-q}\left\|\widehat{D}^{(q,\alpha_2)}\widehat{v}\right\|_{\mathcal{L}^2(\widetilde{Q}_{\boldsymbol{j}})}\right).\end{aligned}$$

Now, we transfer these norms to the physical domain based on the ideas from Section 3.3.2. More precisely, we first perform an integral transformation and employ (3.28) as well as the bound (3.55) for the determinant of the inverse parameterization. Then, we bound the norms of the derivatives with respect to the $\boldsymbol{F}$-coordinates by the norms of the classical physical derivatives as shown in Lemma 3.18. Such an argument will be used multiple times in the following and will be referred to as a change of variables. It follows

$$\begin{aligned}&\zeta^{1/2}_{1,j_1}\left\|\widehat{\partial}^q_1\left(W\widehat{v}-\Pi^{\widehat{\Gamma}}_{\boldsymbol{p},\boldsymbol{\Xi}}(W\widehat{v})\right)\right\|_{\widehat{L}^2(Q_{\boldsymbol{j}})}\\ &\leq C\left(\frac{\zeta_{1,j_1}}{\zeta_{1,j_1}}\right)^{1/2}\left(\widetilde{h}^{s-q}_{1,j_1}\left\|D^{(s,0)}_{\boldsymbol{F}}v\right\|_{\mathcal{L}^2(\widetilde{K}_{\boldsymbol{j}})}+\widetilde{h}^{s-q}_{2,j_2}\sum_{\alpha_2=0}^{s-q}\left\|D^{(q,\alpha_2)}_{\boldsymbol{F}}v\right\|_{\mathcal{L}^2(\widetilde{K}_{\boldsymbol{j}})}\right)\\ &\leq C\left(\widetilde{h}^{s-q}_{1,j_1}\sum_{|\boldsymbol{\gamma}|\leq s}\|D^{\boldsymbol{\gamma}}v\|_{\mathcal{L}^2(\widetilde{K}_{\boldsymbol{j}})}+\widetilde{h}^{s-q}_{2,j_2}\sum_{\alpha_2=0}^{s-q}\sum_{|\boldsymbol{\gamma}|\leq q+\alpha_2}\|r^{\alpha_2}D^{\boldsymbol{\gamma}}v\|_{\mathcal{L}^2(\widetilde{K}_{\boldsymbol{j}})}\right)\\ &\leq C\,h^{s-q}\left((\zeta_{1,j_1})^{(1-\mu)(s-q)}\sum_{|\boldsymbol{\gamma}|\leq s}\|D^{\boldsymbol{\gamma}}v\|_{\mathcal{L}^2(\widetilde{K}_{\boldsymbol{j}})}+\sum_{\alpha_2=0}^{s-q}\sum_{|\boldsymbol{\gamma}|\leq q+\alpha_2}\|r^{\alpha_2}D^{\boldsymbol{\gamma}}v\|_{\mathcal{L}^2(\widetilde{K}_{\boldsymbol{j}})}\right),\end{aligned} \tag{3.58}$$

where, in the last step, we inserted the mesh properties (3.14) with $h=\max\{h_1,h_2\}$. Due to the local quasi-uniformity of the mesh, recall Lemma 3.12, and relation (3.8), we further have

$$\zeta_{1,j_1}\sim\zeta_1(\boldsymbol{x})\sim r(\boldsymbol{x})\quad\text{ for all }\boldsymbol{x}\in\widetilde{K}_{\boldsymbol{j}}, \tag{3.59}$$

with $\boldsymbol{\zeta}(\boldsymbol{x})=(\zeta_1(\boldsymbol{x}),\zeta_2(\boldsymbol{x}))=\boldsymbol{F}^{-1}(\boldsymbol{x})\in\widetilde{Q}_{\boldsymbol{j}}$. Moreover, we set $\beta=(1-\mu)(s-q)$. Then, as $\mu\in(0,1]$ satisfies condition (3.47), it holds

$$\beta\leq s-q\quad\text{ and }\quad\beta>\left(1-\frac{\nu-q+1}{s-q}\right)(s-q)=s-q-(\nu-q+1)=s-1-\nu. \tag{3.60}$$

By combining (3.58), (3.59) and (3.60), we obtain

$$\begin{aligned}
&\zeta_{1,j_1}^{1/2}\left\|\widehat{\partial}_1^q\left(W\widehat{v}-\Pi_{\boldsymbol{p},\boldsymbol{\Xi}}^{\widehat{\Gamma}}(W\widehat{v})\right)\right\|_{\widehat{L}^2(Q_{\boldsymbol{j}})}\\
&\le C\,h^{s-q}\left(\sum_{|\boldsymbol{\gamma}|\le s}\left\|r^{\beta}D^{\boldsymbol{\gamma}}v\right\|_{L^2(\widetilde{K}_{\boldsymbol{j}})}+\sum_{\alpha_2=0}^{s-q}\sum_{|\boldsymbol{\gamma}|\le q+\alpha_2}\left\|r^{\beta-(s-q)+\alpha_2}D^{\boldsymbol{\gamma}}v\right\|_{L^2(\widetilde{K}_{\boldsymbol{j}})}\right)\\
&\le C\,h^{s-q}\left(\sum_{|\boldsymbol{\gamma}|\le s}\left\|r^{\beta}D^{\boldsymbol{\gamma}}v\right\|_{L^2(\widetilde{K}_{\boldsymbol{j}})}+\sum_{\alpha_2=0}^{s-q}\sum_{|\boldsymbol{\gamma}|\le q+\alpha_2}\left\|r^{\beta-s+|\boldsymbol{\gamma}|}D^{\boldsymbol{\gamma}}v\right\|_{L^2(\widetilde{K}_{\boldsymbol{j}})}\right)\\
&\le C\,h^{s-q}\left(\sum_{|\boldsymbol{\gamma}|\le s}\left\|r^{\beta}D^{\boldsymbol{\gamma}}v\right\|_{L^2(\widetilde{K}_{\boldsymbol{j}})}+\sum_{|\boldsymbol{\gamma}|\le s}\left\|r^{\beta-s+|\boldsymbol{\gamma}|}D^{\boldsymbol{\gamma}}v\right\|_{L^2(\widetilde{K}_{\boldsymbol{j}})}\right)\\
&\le C\,h^{s-q}\left(\|v\|_{H^s_\beta(\widetilde{K}_{\boldsymbol{j}})}+\|v\|_{V^s_\beta(\widetilde{K}_{\boldsymbol{j}})}\right)\le C\,h^{s-q}\|v\|_{V^s_\beta(\widetilde{K}_{\boldsymbol{j}})}.
\end{aligned}$$

Next, we estimate the first term in line (3.57) by applying Lemma 3.26 for $s_1=s-1$, $s_2=s$, $r_1=0$ and $r_2=1$ as well as the Leibniz formula,

$$\begin{aligned}
\left\|\widehat{\partial}_2\left(W\widehat{v}-\Pi_{\boldsymbol{p},\boldsymbol{\Xi}}^{\widehat{\Gamma}}(W\widehat{v})\right)\right\|_{\widehat{L}^2(Q)}&\le C\left(\widetilde{h}_{1,j_1}^{s-1}\left\|\widehat{D}^{(s-1,1)}(W\widehat{v})\right\|_{\mathcal{L}^2(\widetilde{Q}_{\boldsymbol{j}})}+\widetilde{h}_{2,j_2}^{s-1}\left\|\widehat{D}^{(0,s)}(W\widehat{v})\right\|_{\mathcal{L}^2(\widetilde{Q}_{\boldsymbol{j}})}\right)\\
&\le C\left(\widetilde{h}_{1,j_1}^{s-1}\sum_{\alpha_2=0}^{1}\left\|\widehat{D}^{(s-1,\alpha_2)}\widehat{v}\right\|_{\mathcal{L}^2(\widetilde{Q}_{\boldsymbol{j}})}+\widetilde{h}_{2,j_2}^{s-1}\sum_{\alpha_2=0}^{s}\left\|\widehat{D}^{(0,\alpha_2)}\widehat{v}\right\|_{\mathcal{L}^2(\widetilde{Q}_{\boldsymbol{j}})}\right).
\end{aligned}$$

Then, we apply a change of variables and exploit the mesh properties (3.14) and (3.59),

$$\begin{aligned}
&\zeta_{1,j_1}^{-1/2}\left\|\widehat{\partial}_2\left(W\widehat{v}-\Pi_{\boldsymbol{p},\boldsymbol{\Xi}}^{\widehat{\Gamma}}(W\widehat{v})\right)\right\|_{\widehat{L}^2(Q)}\\
&\le C\,(\zeta_{1,j_1}\zeta_{1,j_1})^{-1/2}\left(\widetilde{h}_{1,j_1}^{s-1}\sum_{\alpha_2=0}^{1}\left\|D_{\boldsymbol{F}}^{(s-1,\alpha_2)}v\right\|_{\mathcal{L}^2(\widetilde{K}_{\boldsymbol{j}})}+\widetilde{h}_{2,j_2}^{s-1}\sum_{\alpha_2=0}^{s}\left\|D_{\boldsymbol{F}}^{(0,\alpha_2)}v\right\|_{\mathcal{L}^2(\widetilde{K}_{\boldsymbol{j}})}\right)\\
&\le C\,\zeta_{1,j_1}^{-1}\left(\widetilde{h}_{1,j_1}^{s-1}\sum_{\alpha_2=0}^{1}\sum_{|\boldsymbol{\gamma}|\le s-1+\alpha_2}\|r^{\alpha_2}D^{\boldsymbol{\gamma}}v\|_{\mathcal{L}^2(\widetilde{K}_{\boldsymbol{j}})}+\widetilde{h}_{2,j_2}^{s-1}\sum_{\alpha_2=0}^{s}\sum_{|\boldsymbol{\gamma}|\le\alpha_2}\|r^{\alpha_2}D^{\boldsymbol{\gamma}}v\|_{\mathcal{L}^2(\widetilde{K}_{\boldsymbol{j}})}\right)\\
&\le C\,h^{s-1}\left((\zeta_{1,j_1})^{(1-\mu)(s-1)}\sum_{\alpha_2=0}^{1}\sum_{|\boldsymbol{\gamma}|\le s+\alpha_2-1}\|r^{\alpha_2-1}D^{\boldsymbol{\gamma}}v\|_{L^2(\widetilde{K}_{\boldsymbol{j}})}+\sum_{\alpha_2=0}^{s}\sum_{|\boldsymbol{\gamma}|\le\alpha_2}\|r^{\alpha_2-1}D^{\boldsymbol{\gamma}}v\|_{L^2(\widetilde{K}_{\boldsymbol{j}})}\right).
\end{aligned}$$

We set again $\beta=(1-\mu)(s-q)$ for $q=1$ and recall that (3.60) is satisfied. It follows

$$\begin{aligned}
&\zeta_{1,j_1}^{-1/2}\left\|\widehat{\partial}_2\left(W\widehat{v}-\Pi_{\boldsymbol{p},\boldsymbol{\Xi}}^{\widehat{\Gamma}}(W\widehat{v})\right)\right\|_{\widehat{L}^2(Q)}\\
&\le C\,h^{s-1}\left(\sum_{\alpha_2=0}^{1}\sum_{|\boldsymbol{\gamma}|\le s+\alpha_2-1}\left\|r^{\beta+\alpha_2-1}D^{\boldsymbol{\gamma}}v\right\|_{L^2(\widetilde{K}_{\boldsymbol{j}})}+\sum_{\alpha_2=0}^{s}\sum_{|\boldsymbol{\gamma}|\le\alpha_2}\left\|r^{\beta-(s-1)+\alpha_2-1}D^{\boldsymbol{\gamma}}v\right\|_{L^2(\widetilde{K}_{\boldsymbol{j}})}\right)\\
&\le C\,h^{s-1}\left(\sum_{\alpha_2=0}^{1}\sum_{|\boldsymbol{\gamma}|\le s+\alpha_2-1}\left\|r^{\beta-s+|\boldsymbol{\gamma}|}D^{\boldsymbol{\gamma}}v\right\|_{L^2(\widetilde{K}_{\boldsymbol{j}})}+\sum_{\alpha_2=0}^{s}\sum_{|\boldsymbol{\gamma}|\le\alpha_2}\left\|r^{\beta-s+|\boldsymbol{\gamma}|}D^{\boldsymbol{\gamma}}v\right\|_{L^2(\widetilde{K}_{\boldsymbol{j}})}\right)\\
&\le C\,h^{s-1}\sum_{|\boldsymbol{\gamma}|\le s}\left\|r^{\beta-s+|\boldsymbol{\gamma}|}D^{\boldsymbol{\gamma}}v\right\|_{L^2(\widetilde{K}_{\boldsymbol{j}})}=C\,h^{s-1}\|v\|_{V^s_\beta(\widetilde{K}_{\boldsymbol{j}})}.
\end{aligned}$$

The second term in line (3.57) can be computed similarly,

$$\begin{aligned}
&\zeta_{1,j_1}^{-1/2}\left\|\left(W\widehat{v}-\Pi^{\widehat{\Gamma}}_{\boldsymbol{p},\boldsymbol{\Xi}}(W\widehat{v})\right)\right\|_{\widehat{L}^2(Q)} \leq C\left(\widetilde{h}^s_{1,j_1}\left\|\widehat{D}^{(s,0)}\widehat{v}\right\|_{\mathcal{L}^2(\widetilde{Q}_{\boldsymbol{j}})}+\widetilde{h}^s_{2,j_2}\sum_{\alpha_2=0}^{s}\left\|\widehat{D}^{(0,\alpha_2)}\widehat{v}\right\|_{\mathcal{L}^2(\widetilde{Q}_{\boldsymbol{j}})}\right)\\
&\leq C\,\zeta_{1,j_1}^{-1}\left(\widetilde{h}^s_{1,j_1}\sum_{|\boldsymbol{\gamma}|\leq s}\|D^{\boldsymbol{\gamma}}v\|_{\mathcal{L}^2(\widetilde{K}_{\boldsymbol{j}})}+\widetilde{h}^s_{2,j_2}\sum_{\alpha_2=0}^{s}\sum_{|\boldsymbol{\gamma}|\leq\alpha_2}\|r^{\alpha_2}D^{\boldsymbol{\gamma}}v\|_{\mathcal{L}^2(\widetilde{K}_{\boldsymbol{j}})}\right)\\
&\leq C\,h^{s-1}\left(\sum_{|\boldsymbol{\gamma}|\leq s}\left\|r^{\beta}D^{\boldsymbol{\gamma}}v\right\|_{L^2(\widetilde{K}_{\boldsymbol{j}})}+\sum_{\alpha_2=0}^{s}\sum_{|\boldsymbol{\gamma}|\leq\alpha_2}\left\|r^{\beta-s+\alpha_2}D^{\boldsymbol{\gamma}}v\right\|_{L^2(\widetilde{K}_{\boldsymbol{j}})}\right)\\
&\leq C\,h^{s-1}\left(\|v\|_{H^s_\beta(\widetilde{K}_{\boldsymbol{j}})}+\sum_{\alpha_2=0}^{s}\sum_{|\boldsymbol{\gamma}|\leq\alpha_2}\left\|r^{\beta-s+|\boldsymbol{\gamma}|}D^{\boldsymbol{\gamma}}v\right\|_{L^2(\widetilde{K}_{\boldsymbol{j}})}\right)\\
&\leq C\,h^{s-1}\|v\|_{V^s_\beta(\widetilde{K}_{\boldsymbol{j}})}.
\end{aligned}$$

Finally, we sum over all elements and remark that the overlap of support extensions depends only on the polynomial degree p and is thus bounded with respect to h. We obtain

$$\left|v-\Pi_{V_h^\odot}v\right|^2_{H^q(\Omega_R)}=\sum_{K\in\mathcal{M}^\mu_R}\left|v-\Pi^\odot_{V_h}v\right|^2_{H^q(K)}\leq C\,h^{2(s-q)}\sum_{K\in\mathcal{M}^\mu_R}\|v\|^2_{V^s_\beta(\widetilde{K}_{\boldsymbol{j}})}\leq Ch^{2(s-q)}\|v\|^2_{V^s_\beta(\widetilde{\Omega}_R)}$$

for $q\in\{0,1\}$ and the assertion follows. □

Estimates on Ω_C

Next, we analyze the projection error on the small polar domain Ω_C that is surrounding the polar point. Therefore, we adopt the proof strategy from [ASS02], where a similar error estimate has been shown for interpolation with linear finite elements. The radial size of the corresponding parametric strip $\widehat{\Omega}_C$ will be denoted by $h_{1,\widehat{\Omega}_C}=\zeta_{1,p_1+2}$ such that $\widehat{\Omega}_C=\left(0,h_{1,\widehat{\Omega}_C}\right]\times(0,1)$, recall (3.53).

Theorem 3.28. *Let $q\in\{0,1\}$, $s\in\mathbb{N}$ with $2\leq s\leq p+1$ and $v\in V^s(\widetilde{\Omega}_C)$. Then, there exists a positive constant C depending only on $p,\boldsymbol{\theta},\boldsymbol{F},W$ such that*

$$\left|v-\Pi_{V_h^\odot}v\right|_{H^q(\Omega_C)}\leq Ch^{s-q}_{1,\widehat{\Omega}_C}\|v\|_{V^s(\widetilde{\Omega}_C)},$$

with $\widetilde{\Omega}_C$ as defined in (3.54).

Proof. Similar to the proof of Theorem 3.27, we transform the projection error to the polar coordinate system as illustrated in Section 3.3.4. For $q=0$, we thus have

$$\left\|v-\Pi_{V_h^\odot}v\right\|^2_{L^2(\Omega_C)}\leq C\left\|W\widehat{v}-\Pi^{\widehat{\Gamma}}_{\boldsymbol{p},\boldsymbol{\Xi}}(W\widehat{v})\right\|^2_{\mathcal{L}^2_{1/2}(\widehat{\Omega}_C)},$$

and for $q=1$, it follows

$$\begin{aligned}
\left|v-\Pi_{V_h^\odot}v\right|^2_{H^1(\Omega_C)}\leq C\Big(&\left\|\widehat{\partial}_1\left(W\widehat{v}-\Pi^{\widehat{\Gamma}}_{\boldsymbol{p},\boldsymbol{\Xi}}(W\widehat{v})\right)\right\|^2_{\mathcal{L}^2_{1/2}(\widehat{\Omega}_C)}+\left\|W\widehat{v}-\Pi^{\widehat{\Gamma}}_{\boldsymbol{p},\boldsymbol{\Xi}}(W\widehat{v})\right\|^2_{\mathcal{L}^2_{1/2}(\widehat{\Omega}_C)} &(3.61)\\
+\left\|\widehat{\partial}_2\left(W\widehat{v}-\Pi^{\widehat{\Gamma}}_{\boldsymbol{p},\boldsymbol{\Xi}}(W\widehat{v})\right)\right\|^2_{\mathcal{L}^2_{-1/2}(\widehat{\Omega}_C)}&+\left\|W\widehat{v}-\Pi^{\widehat{\Gamma}}_{\boldsymbol{p},\boldsymbol{\Xi}}(W\widehat{v})\right\|^2_{\mathcal{L}^2_{-1/2}(\widehat{\Omega}_C)}\Big). &(3.62)
\end{aligned}$$

However, in contrast to Theorem 3.27, where the projection error on Ω_R is considered, the Jacobian of the inverse of the polar parameterization $\boldsymbol{F}$ is not bounded on Ω_C, see (3.7). In the following Lemmata 3.30, 3.31 and 3.32, we will thus show that each of the weighted error terms is bounded by the bent polar Sobolev norm of v introduced in Section 3.3.3. With equation (3.42) and the transformation (3.41) back to the physical domain, we obtain the assertion,

$$\left|v - \Pi_{V_h^{\odot}} v\right|_{H^q(\Omega_C)} \leq C h_{1,\widehat{\Omega}_C}^{s-q} \|\widehat{v}\|_{\mathcal{H}^s_{\odot}\left(\widetilde{\widehat{\Omega}}_C\right)} \leq C h_{1,\widehat{\Omega}_C}^{s-q} \|\widehat{v}\|_{\mathcal{V}^s_{\odot}\left(\widetilde{\widehat{\Omega}}_C\right)} \leq C h_{1,\widehat{\Omega}_C}^{s-q} \|v\|_{V^s(\widetilde{\Omega}_C)},$$

where $\widetilde{\widehat{\Omega}}_C$ and $\widetilde{\Omega}_C$ are defined as in (3.54). □

An essential ingredient for the following estimates is the bijective scaling transformation between the parametric domain $\widehat{\Omega}$ and the reference domain $\mathring{\Omega} := (0, 1/h_{1,\widehat{\Omega}_C}) \times (0,1)$, given by

$$\mathring{\boldsymbol{\Phi}} : \mathring{\Omega} \to \widehat{\Omega}, \quad \mathring{\boldsymbol{\Phi}}(\mathring{\zeta}_1, \mathring{\zeta}_2) = \begin{pmatrix} h_{1,\widehat{\Omega}_C} \mathring{\zeta}_1 \\ \mathring{\zeta}_2 \end{pmatrix} = \begin{pmatrix} \zeta_1 \\ \zeta_2 \end{pmatrix}. \tag{3.63}$$

In this way, the size of the reference domain corresponding to the parametric strip $\widehat{\Omega}_C$, namely

$$\mathring{\Omega}_C := \mathring{\boldsymbol{\Phi}}^{-1}\left(\widehat{\Omega}_C\right) = (0,1)^2,$$

is independent of the global mesh size h, and a typical scaling argument can be applied. The transformation and reference domains are illustrated visually in Figure 3.9. Any quantity that is transformed to the reference domain will be marked accordingly with a circle on top, e.g. $\mathring{v} = \widehat{v} \circ \mathring{\boldsymbol{\Phi}}$, and will be called the corresponding reference quantity or scaled quantity. Similarly, we denote the derivatives of a scaled function $\mathring{v} : \mathring{\Omega} \to \mathbb{R}$ by

$$\mathring{D}^{\boldsymbol{\alpha}} \mathring{v} := \frac{\partial^{\alpha_1}}{\partial \mathring{\zeta}_1^{\alpha_1}} \frac{\partial^{\alpha_2} \mathring{v}}{\partial \mathring{\zeta}_2^{\alpha_2}} \quad \text{and} \quad \mathring{\partial}_1 \mathring{v} = \frac{\partial \mathring{v}}{\partial \mathring{\zeta}_1}, \, \mathring{\partial}_2 \mathring{v} = \frac{\partial \widehat{v}}{\partial \mathring{\zeta}_2}, \, \mathring{\partial}_{11} \mathring{v} = \frac{\partial^2 \mathring{v}}{\partial \mathring{\zeta}_1^2}, \, \ldots.$$

Moreover, we define the reference domain of the extended parametric strip $\widetilde{\widehat{\Omega}}_C$, recall (3.54), by

$$\widetilde{\mathring{\Omega}}_C := \mathring{\boldsymbol{\Phi}}^{-1}\left(\widetilde{\widehat{\Omega}}_C\right) = \left(0, h_{1,\widetilde{\widehat{\Omega}}_C} \big/ h_{1,\widehat{\Omega}_C}\right) \times (0,1),$$

which is displayed in the top row of Figure 3.10. Its size is also independent of the mesh size, since the relation $h_{1,\widetilde{\widehat{\Omega}}_C} / h_{1,\widehat{\Omega}_C} \sim 1$ holds due to the local quasi-uniformity of the mesh, recall Lemma 3.12. Finally, we introduce the corresponding physical reference domains, which are obtained using the transformation

$$\breve{\boldsymbol{\Phi}} : \breve{\Omega} \to \Omega, \quad \breve{\boldsymbol{\Phi}}(\breve{x}, \breve{y}) = \begin{pmatrix} h_{1,\widehat{\Omega}_C} \breve{x} \\ h_{1,\widehat{\Omega}_C} \breve{y} \end{pmatrix} = \begin{pmatrix} x \\ y \end{pmatrix}, \tag{3.64}$$

with $\breve{\Omega} := \breve{\boldsymbol{\Phi}}^{-1}(\Omega)$, as illustrated in the bottom row of Figure 3.10. Similarly to the parametric reference configuration, the sizes of $\breve{\Omega}_C := \breve{\boldsymbol{\Phi}}^{-1}(\Omega_C)$ and $\widetilde{\breve{\Omega}}_C := \breve{\boldsymbol{\Phi}}^{-1}\left(\widetilde{\Omega}_C\right)$ are independent of h. Any scaled quantity will be marked accordingly with a breve on top.

We start with a stability result for the scaled version of the quasi-interpolant defined in (2.37), which will be used more often in the remainder of this section.

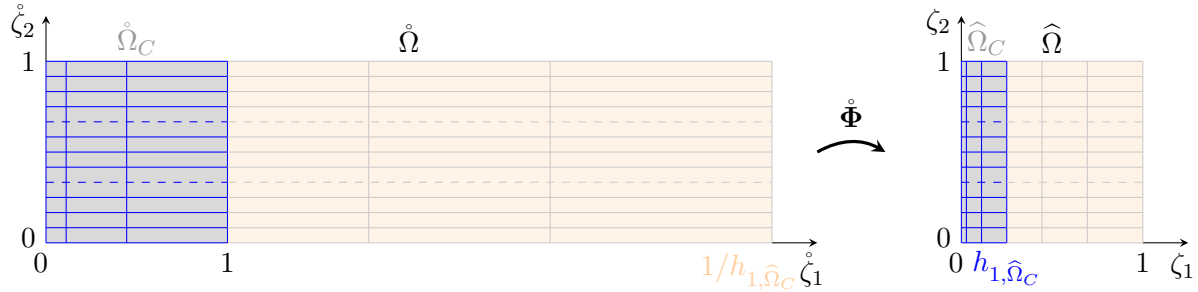

Figure 3.9: Illustration of the scaling transformation $\mathring{\mathbf{\Phi}}$ with the reference domains $\mathring{\Omega}$ and $\mathring{\Omega}_C$ and the corresponding parametric domains $\widehat{\Omega}$ and $\widehat{\Omega}_C$, respectively.

Lemma 3.29. *Let either* $\mathring{v} \in \widehat{H}^s_{1/2}\left(\widetilde{\mathring{\Omega}}_C\right)$ *or* $\mathring{v} \in \mathcal{H}^s_{1/2}\left(\widetilde{\mathring{\Omega}}_C\right)$ *for* $s \geq 2$*. Then, it holds*

$$\left\|\mathring{\partial}_1^q\left(\mathring{\Pi}^{\widehat{\Gamma}}_{\boldsymbol{p},\boldsymbol{\Xi}}\,\mathring{v}\right)\right\|^2_{\widehat{L}^2_{1/2}(\mathring{\Omega}_C)} \leq C\|\mathring{v}\|^2_{\widehat{H}^s_{1/2}\left(\widetilde{\mathring{\Omega}}_C\right)} \quad \text{or} \quad \left\|\mathring{\partial}_1^q\left(\mathring{\Pi}^{\widehat{\Gamma}}_{\boldsymbol{p},\boldsymbol{\Xi}}\,\mathring{v}\right)\right\|^2_{\mathcal{L}^2_{1/2}(\mathring{\Omega}_C)} \leq C\|\mathring{v}\|^2_{\mathcal{H}^s_{1/2}\left(\widetilde{\mathring{\Omega}}_C\right)},$$

respectively, for $q \in \{0,1\}$*.*

Proof. Let $q \in \{0,1\}$ and $\mathring{v} \in \widehat{H}^s_{1/2}\left(\widetilde{\mathring{\Omega}}_C\right)$. By using the representation (2.38) of $\mathring{\Pi}^{\widehat{\Gamma}}_{\boldsymbol{p},\boldsymbol{\Xi}}$ and the stability property of the dual functionals [Sch07, Theorem 4.41], we compute

$$\begin{aligned}
\left\|\mathring{\partial}_1^q\left(\mathring{\Pi}^{\widehat{\Gamma}}_{\boldsymbol{p},\boldsymbol{\Xi}}\,\mathring{v}\right)\right\|^2_{\widehat{L}^2_{1/2}(\mathring{\Omega}_C)} &= \int_{\mathring{\Omega}_C}\left|\mathring{\partial}_1^q\left(\sum_{\boldsymbol{i}\in\boldsymbol{I}}\mathring{\lambda}^{\widehat{\Gamma}}_{\boldsymbol{i},\boldsymbol{p}}(\mathring{v})\mathring{B}_{\boldsymbol{i},\boldsymbol{p}}\right)\right|^2 \mathring{\zeta}_1\,\mathrm{d}\mathring{\zeta}_1\,\mathrm{d}\mathring{\zeta}_2 \\
&\leq \int_{\mathring{\Omega}_C}\left(\sum_{\boldsymbol{i}\in\boldsymbol{I}}\left|\mathring{\lambda}^{\widehat{\Gamma}}_{\boldsymbol{i},\boldsymbol{p}}(\mathring{v})\,\mathring{\partial}_1^q\mathring{B}_{\boldsymbol{i},\boldsymbol{p}}\right|\right)^2 \mathring{\zeta}_1\,\mathrm{d}\mathring{\zeta}_1\,\mathrm{d}\mathring{\zeta}_2 \\
&\leq \int_{\mathring{\Omega}_C}\left(\sum_{\boldsymbol{i}\in\boldsymbol{I}} C\|\mathring{v}\|_{L^\infty\left(\widetilde{\mathring{\Omega}}_C\right)}\left|\mathring{\partial}_1^q\mathring{B}_{\boldsymbol{i},\boldsymbol{p}}\right|\right)^2 \mathring{\zeta}_1\,\mathrm{d}\mathring{\zeta}_1\,\mathrm{d}\mathring{\zeta}_2 \\
&\leq C\|\mathring{v}\|^2_{C^0\left(\widetilde{\mathring{\Omega}}_C\right)}\int_{\mathring{\Omega}_C}\left(\sum_{\boldsymbol{i}\in\boldsymbol{I}}\left|\mathring{\partial}_1^q\mathring{B}_{\boldsymbol{i},\boldsymbol{p}}\right|\right)^2 \mathring{\zeta}_1\,\mathrm{d}\mathring{\zeta}_1\,\mathrm{d}\mathring{\zeta}_2.
\end{aligned}$$

The diameter of the reference domain $\mathring{\Omega}_C$ does not depend on the mesh size, and we have the embedding $\widehat{H}^s_{1/2}\left(\widetilde{\mathring{\Omega}}_C\right) \hookrightarrow C^0\left(\widetilde{\mathring{\Omega}}_C\right)$, see [MR82, Theorem 4.7]. Hence, we obtain

$$\left\|\mathring{\partial}_1^q\left(\mathring{\Pi}^{\widehat{\Gamma}}_{\boldsymbol{p},\boldsymbol{\Xi}}\,\mathring{v}\right)\right\|^2_{\widehat{L}^2_{1/2}(\mathring{\Omega}_C)} \leq C\|\mathring{v}\|^2_{C^0\left(\widetilde{\mathring{\Omega}}_C\right)}\int_{\mathring{\Omega}_C} 1\,\mathrm{d}\mathring{\zeta}_1\,\mathrm{d}\mathring{\zeta}_2 \leq C\|\mathring{v}\|^2_{C^0\left(\widetilde{\mathring{\Omega}}_C\right)} \leq C\|\mathring{v}\|^2_{\widehat{H}^s_{1/2}\left(\widetilde{\mathring{\Omega}}_C\right)}.$$

To prove the assertion for bent Sobolev norms, we simply apply the estimate above on every mesh element and sum over all elements. □

Now, we estimate the two terms in line (3.61), that is, the projection error and its first parametric derivative in the $\mathcal{L}^2_{1/2}(\widehat{\Omega}_C)$-norm.

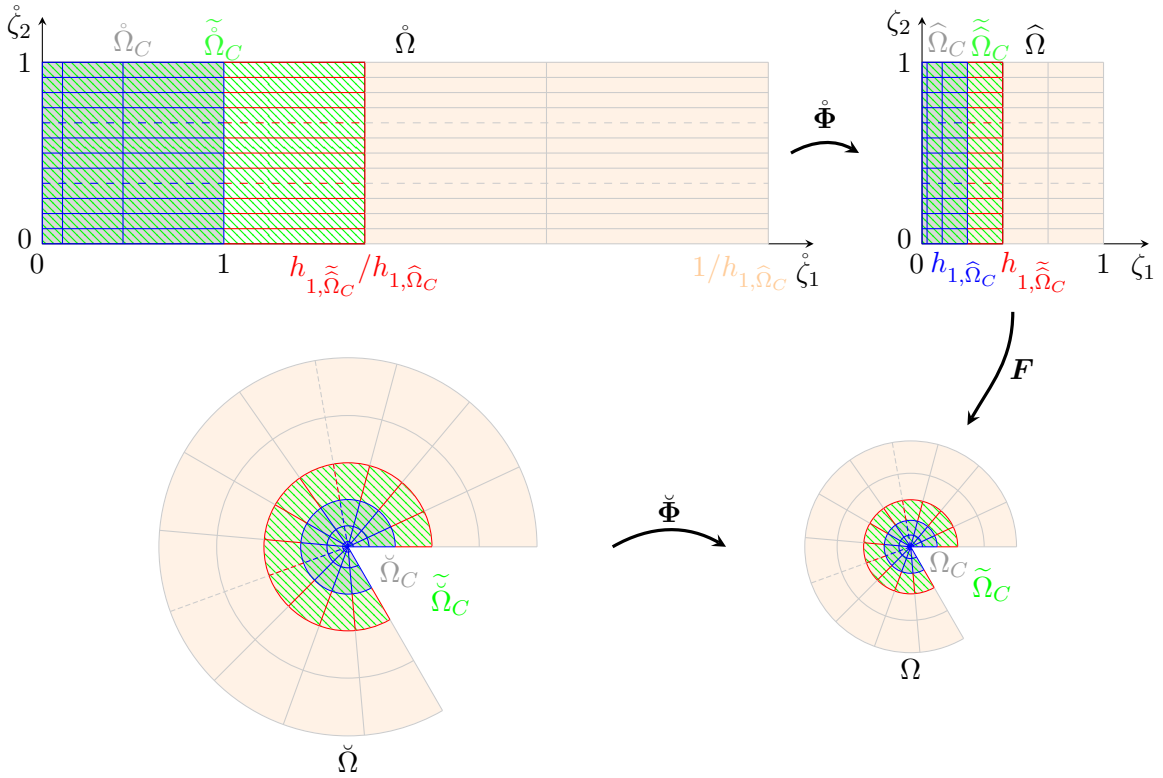

Figure 3.10: First row: Illustration of the parametric scaling transformation (3.63), with the extended parametric strip $\widetilde{\widehat{\Omega}}_C$ and the corresponding reference domain $\widetilde{\mathring{\Omega}}_C$ being hatched in green. Second row: Illustration of the physical scaling transformation (3.64), with the extended small polar domain $\widetilde{\Omega}_C$ and the corresponding reference domain $\widetilde{\breve{\Omega}}_C$ being hatched in green.

Lemma 3.30. *Let the assumptions of Theorem 3.28 hold. Then, for $q \in \{0,1\}$, it follows*

$$\left\| \widehat{\partial}_1^q \left(W\widehat{v} - \Pi^{\widehat{\Gamma}}_{\boldsymbol{p},\boldsymbol{\Xi}}(W\widehat{v}) \right) \right\|_{\mathcal{L}^2_{1/2}(\widehat{\Omega}_C)} \leq C h^{s-q}_{1,\widehat{\Omega}_C} \|\widehat{v}\|_{\mathcal{H}^s_{\odot}\left(\widetilde{\widehat{\Omega}}_C\right)}.$$

Proof. First, we apply a typical scaling argument using the reference configuration introduced above and, to simplify notation, we set $\mathring{v} = \mathring{W}\mathring{v}$. We obtain

$$\begin{aligned}
\left\| \widehat{\partial}_1^q \left(W\widehat{v} - \Pi^{\widehat{\Gamma}}_{\boldsymbol{p},\boldsymbol{\Xi}}(W\widehat{v}) \right) \right\|_{\mathcal{L}^2_{1/2}(\widehat{\Omega}_C)} &= \left(\int_{\widehat{\Omega}_C} \left(\widehat{\partial}_1^q \left(W\widehat{v} - \Pi^{\widehat{\Gamma}}_{\boldsymbol{p},\boldsymbol{\Xi}}(W\widehat{v}) \right) \right)^2 \zeta_1 \, \mathrm{d}\boldsymbol{\zeta} \right)^{1/2} \\
&= \left(\int_{\mathring{\Omega}_C} \left(\frac{\mathring{\partial}_1^q \left(\mathring{W}\mathring{v} - \mathring{\Pi}^{\widehat{\Gamma}}_{\boldsymbol{p},\boldsymbol{\Xi}}(\mathring{W}\mathring{v}) \right)}{h^q_{1,\widehat{\Omega}_C}} \right)^2 h_{1,\widehat{\Omega}_C} \mathring{\zeta}_1 \, h_{1,\widehat{\Omega}_C} \, \mathrm{d}\mathring{\zeta}_1 \, \mathrm{d}\mathring{\zeta}_2 \right)^{1/2} \\
&= h^{1-q}_{1,\widehat{\Omega}_C} \left\| \mathring{\partial}_1^q \left(\mathring{v} - \mathring{\Pi}^{\widehat{\Gamma}}_{\boldsymbol{p},\boldsymbol{\Xi}} \mathring{v} \right) \right\|_{\mathcal{L}^2_{1/2}(\mathring{\Omega}_C)}. \qquad (3.65)
\end{aligned}$$

In the rest of the chapter, such estimates will be used more often. The underlying steps will not be carried out in detail anymore, but we will refer to it as scaling argument.

Next, let $\mathcal{P}_{s-1}$ be the space of piecewise polynomials up to degree $s-1$ on $\mathring{\Omega}_C$ and $\mathring{\Pi}$ be the scaled projector from the bent Sobolev space to the spline space of degree $s-1$ that satisfies property (3.43). Due to Lemma 3.29, we have

$$\begin{aligned}
&\left\|\mathring{\partial}_1^q\left(\mathring{v}-\mathring{\Pi}^{\widehat{\Gamma}}_{\boldsymbol{p},\boldsymbol{\Xi}}\mathring{v}\right)\right\|_{\mathcal{L}^2_{1/2}(\mathring{\Omega}_C)} = \inf_{\mathring{w}\in\mathcal{P}_{s-1}}\left\|\mathring{\partial}_1^q\left(\mathring{v}-\mathring{\Pi}(\mathring{v})-\mathring{w}-\mathring{\Pi}^{\widehat{\Gamma}}_{\boldsymbol{p},\boldsymbol{\Xi}}(\mathring{v}-\mathring{\Pi}(\mathring{v})-\mathring{w})\right)\right\|_{\mathcal{L}^2_{1/2}(\mathring{\Omega}_C)}\\
&\leq \inf_{\mathring{w}\in\mathcal{P}_{s-1}}\left(\left\|\mathring{\partial}_1^q\left(\mathring{v}-\mathring{\Pi}(\mathring{v})-\mathring{w}\right)\right\|_{\mathcal{L}^2_{1/2}(\mathring{\Omega}_C)}+\left\|\mathring{\partial}_1^q\left(\mathring{\Pi}^{\widehat{\Gamma}}_{\boldsymbol{p},\boldsymbol{\Xi}}(\mathring{v}-\mathring{\Pi}(\mathring{v})-\mathring{w})\right)\right\|_{\mathcal{L}^2_{1/2}(\mathring{\Omega}_C)}\right)\\
&\leq C\inf_{\mathring{w}\in\mathcal{P}_{s-1}}\left\|\mathring{v}-\mathring{\Pi}(\mathring{v})-\mathring{w}\right\|_{\mathcal{H}^s_{1/2}\left(\widetilde{\mathring{\Omega}}_C\right)} = \inf_{\mathring{w}\in\mathcal{P}_{s-1}}\left\|\mathring{v}-\mathring{\Pi}(\mathring{v})-\mathring{w}\right\|_{\widehat{H}^s_{1/2}\left(\widetilde{\mathring{\Omega}}_C\right)}.
\end{aligned}$$

Then, we apply the weighted Deny-Lions-type argument [MR82, Theorem 4.6],

$$\inf_{\mathring{w}\in\mathcal{P}_{s-1}}\|\mathring{z}-\mathring{w}\|_{\widehat{H}^s_{1/2}\left(\widetilde{\mathring{\Omega}}_C\right)} \leq C|\mathring{z}|_{\widehat{H}^s_{1/2}\left(\widetilde{\mathring{\Omega}}_C\right)} \tag{3.66}$$

for $\mathring{z}=\mathring{v}-\mathring{\Pi}(\mathring{v})\in\widehat{H}^s_{1/2}\left(\widetilde{\mathring{\Omega}}_C\right)$. Finally, we combine all the steps and use again the definition of $\mathring{\Pi}$, a scaling argument, the embedding (3.42) and the Leibniz formula (3.46) to compute

$$\begin{aligned}
&\left\|\widehat{\partial}_1^q\left(W\widehat{v}-\Pi^{\widehat{\Gamma}}_{\boldsymbol{p},\boldsymbol{\Xi}}(W\widehat{v})\right)\right\|_{\widehat{L}^2_{1/2}(\widehat{\Omega}_C)} \leq Ch^{1-q}_{1,\widehat{\Omega}_C}\inf_{\mathring{w}\in\mathcal{P}_{s-1}}\left\|\mathring{v}-\mathring{\Pi}(\mathring{v})-\mathring{w}\right\|_{\widehat{H}^s_{1/2}\left(\widetilde{\mathring{\Omega}}_C\right)}\\
&\leq Ch^{1-q}_{1,\widehat{\Omega}_C}\left|\mathring{v}-\mathring{\Pi}(\mathring{v})\right|_{\widehat{H}^s_{1/2}\left(\widetilde{\mathring{\Omega}}_C\right)}\\
&= Ch^{1-q}_{1,\widehat{\Omega}_C}|\mathring{v}|_{\mathcal{H}^s_{1/2}\left(\widetilde{\mathring{\Omega}}_C\right)}\\
&\leq Ch^{s-q}_{1,\widehat{\Omega}_C}|W\widehat{v}|_{\mathcal{H}^s_{1/2}\left(\widetilde{\mathring{\Omega}}_C\right)} \leq Ch^{s-q}_{1,\widehat{\Omega}_C}\|\widehat{v}\|_{\mathcal{H}^s_{\odot}\left(\widetilde{\mathring{\Omega}}_C\right)},
\end{aligned}$$

and the demonstration is complete. □

In the proof of Lemma 3.30, the projector $\mathring{\Pi}$ that satisfies property (3.43) was only inserted for the interplay between bent Sobolev norms and their non-bent counterparts, recall Section 3.3.3. This adds a further technicality to the proof, which is not in the scope of this thesis, and has already been investigated in detail in standard approximation literature [BBSV14]. For the sake of simplicity, we will not elaborate this argument anymore in the rest of our analysis and, without loss of generality, we will assume that pull-backs of functions are sufficiently smooth across mesh lines. The generalization can always be done by inserting the projector $\mathring{\Pi}$ at the correct places, as shown in the demonstration of Lemma 3.30.

To continue the proof of Theorem 3.28, we estimate the first term in line (3.62) in the next lemma.

Lemma 3.31. *Let the assumptions of Theorem 3.28 hold. Then, it follows*

$$\left\|\widehat{\partial}_2\left(W\widehat{v}-\Pi^{\widehat{\Gamma}}_{\boldsymbol{p},\boldsymbol{\Xi}}(W\widehat{v})\right)\right\|_{\widehat{L}^2_{-1/2}(\widehat{\Omega}_C)} \leq Ch^{s-1}_{1,\widehat{\Omega}_C}\|\widehat{v}\|_{\mathcal{H}^s_{\odot}\left(\widetilde{\mathring{\Omega}}_C\right)}.$$

Proof. Let $c \in \mathbb{R}$ such that $\widehat{v}(0,\cdot) = v \circ \boldsymbol{F}(0,\cdot) = v(\boldsymbol{P}) = c$. We define the auxiliary function $\widehat{v}_0 = \widehat{v} - c\widehat{B}_{1,p_1}$, which satisfies $(W\widehat{v}_0)(0,\cdot) = (W\widehat{v})(0,\cdot) - cW\widehat{B}_{1,p_1}(0) = 0$. Moreover, we have

$$\Pi^{\widehat{\Gamma}}_{\boldsymbol{p},\boldsymbol{\Xi}}(W\widehat{v}_0) = \Pi^{\widehat{\Gamma}}_{\boldsymbol{p},\boldsymbol{\Xi}}(W\widehat{v}) - \Pi^{\widehat{\Gamma}}_{\boldsymbol{p},\boldsymbol{\Xi}}(cWB_{1,p_1}) = \Pi^{\widehat{\Gamma}}_{\boldsymbol{p},\boldsymbol{\Xi}}(W\widehat{v}) - cWB_{1,p_1}$$

and it follows $W\widehat{v}_0 - \Pi^{\widehat{\Gamma}}_{\boldsymbol{p},\boldsymbol{\Xi}}(W\widehat{v}_0) = W\widehat{v} - \Pi^{\widehat{\Gamma}}_{\boldsymbol{p},\boldsymbol{\Xi}}(W\widehat{v})$ and $\Pi^{\widehat{\Gamma}}_{\boldsymbol{p},\boldsymbol{\Xi}}(W\widehat{v}_0)(0,\cdot) = 0$. Using a scaling argument and the notation $\mathring{v}_0 = \mathring{W}\mathring{v}_0$, we compute

$$\begin{aligned}
\left\|\widehat{\partial}_2\left(W\widehat{v} - \Pi^{\widehat{\Gamma}}_{\boldsymbol{p},\boldsymbol{\Xi}}(W\widehat{v})\right)\right\|_{\widehat{L}^2_{-1/2}(\widehat{\Omega}_C)} &= \left\|\widehat{\partial}_2\left(W\widehat{v}_0 - \Pi^{\widehat{\Gamma}}_{\boldsymbol{p},\boldsymbol{\Xi}}(W\widehat{v}_0)\right)\right\|_{\widehat{L}^2_{-1/2}(\widehat{\Omega}_C)} \\
&\leq \left\|\widehat{\partial}_2(W\widehat{v}_0)\right\|_{\widehat{L}^2_{-1/2}(\widehat{\Omega}_C)} + \left\|\widehat{\partial}_2\left(\Pi^{\widehat{\Gamma}}_{\boldsymbol{p},\boldsymbol{\Xi}}(W\widehat{v}_0)\right)\right\|_{\widehat{L}^2_{-1/2}(\widehat{\Omega}_C)} \\
&\leq \left\|\mathring{\partial}_2\mathring{v}_0\right\|_{\widehat{L}^2_{-1/2}(\mathring{\Omega}_C)} + \left\|\mathring{\partial}_2\left(\mathring{\Pi}^{\widehat{\Gamma}}_{\boldsymbol{p},\boldsymbol{\Xi}}\mathring{v}_0\right)\right\|_{\widehat{L}^2_{-1/2}(\mathring{\Omega}_C)},
\end{aligned}$$

where all terms are well-defined despite the negative weight of the norms as the corresponding functions vanish for $\zeta_1 = 0$. In Lemma 3.36, we show that the second derivative of our projector can be written as another projector, and in Lemma 3.37, we estimate the corresponding norm. Hence, we obtain

$$\left\|\widehat{\partial}_2\left(W\widehat{v} - \Pi^{\widehat{\Gamma}}_{\boldsymbol{p},\boldsymbol{\Xi}}(W\widehat{v})\right)\right\|_{\widehat{L}^2_{-1/2}(\widehat{\Omega}_C)} \leq C\left\|\mathring{\partial}_2\mathring{v}_0\right\|_{\widehat{L}^2_{-1/2}\left(\mathring{\widetilde{\Omega}}_C\right)} \leq C\left\|\mathring{\partial}_2\mathring{v}_0\right\|_{\widehat{L}^2_{-1}\left(\mathring{\widetilde{\Omega}}_C\right)}.$$

It is shown in [MR82, Corollary 4.1] that, under the condition $\mathring{\partial}_2\mathring{v}_0(0,\cdot) = 0$, the inequality

$$\left\|\mathring{\partial}_2\mathring{v}_0\right\|_{\widehat{L}^2_{-1}\left(\mathring{\widetilde{\Omega}}_C\right)} \leq C\left|\mathring{\partial}_2\mathring{v}_0\right|_{\widehat{H}^1\left(\mathring{\widetilde{\Omega}}_C\right)}$$

holds. By a scaling argument, it follows

$$\begin{aligned}
\left|\mathring{\partial}_2\mathring{v}_0\right|_{\widehat{H}^1\left(\mathring{\widetilde{\Omega}}_C\right)} &\leq C\left(\left\|\mathring{\partial}_{12}\mathring{v}_0\right\|_{\widehat{L}^2\left(\mathring{\widetilde{\Omega}}_C\right)} + \left\|\mathring{\partial}_{22}\mathring{v}_0\right\|_{\widehat{L}^2\left(\mathring{\widetilde{\Omega}}_C\right)}\right) \\
&\leq C\left(\left\|\mathring{\partial}_{12}\mathring{v}_0\right\|_{\widehat{L}^2_{-1/2}\left(\mathring{\widetilde{\Omega}}_C\right)} + \left\|\mathring{\partial}_{22}\mathring{v}_0\right\|_{\widehat{L}^2_{-3/2}\left(\mathring{\widetilde{\Omega}}_C\right)}\right) \\
&\leq Ch_{1,\widehat{\Omega}_C}\left(\left\|\widehat{\partial}_{12}(W\widehat{v}_0)\right\|_{\widehat{L}^2_{-1/2}\left(\widetilde{\widehat{\Omega}}_C\right)} + \left\|\widehat{\partial}_{22}(W\widehat{v}_0)\right\|_{\widehat{L}^2_{-3/2}\left(\widetilde{\widehat{\Omega}}_C\right)}\right) \\
&\leq Ch_{1,\widehat{\Omega}_C}\|\widehat{v}\|_{\mathcal{H}^2_{\odot}\left(\widetilde{\widehat{\Omega}}_C\right)},
\end{aligned}$$

which yields the assertion for $s = 2$. For higher regularity $s \geq 3$, the proof needs to be adapted. We

rewrite the error in terms of the projector $\mathring{\Pi}^{\widehat{\Gamma},\mathring{\partial}_2}_{\boldsymbol{p},\boldsymbol{\Xi}}$ derived in Lemma 3.36, and compute

$$\begin{aligned}
&\left\|\widehat{\partial}_2\left(W\widehat{v}-\Pi^{\widehat{\Gamma}}_{\boldsymbol{p},\boldsymbol{\Xi}}(W\widehat{v})\right)\right\|_{\widehat{L}^2_{-1/2}(\widehat{\Omega}_C)} = \left\|\mathring{\partial}_2\left(\mathring{v}_0-\mathring{\Pi}^{\widehat{\Gamma}}_{\boldsymbol{p},\boldsymbol{\Xi}}\mathring{v}_0\right)\right\|_{\widehat{L}^2_{-1/2}(\mathring{\Omega}_C)}\\
&= \left\|\mathring{\partial}_2\mathring{v}_0-\mathring{\Pi}^{\widehat{\Gamma},\mathring{\partial}_2}_{(p_1,p_2-1),\boldsymbol{\Xi}}\left(\widehat{\partial}_2\mathring{v}_0\right)\right\|_{\widehat{L}^2_{-1/2}(\mathring{\Omega}_C)} \leq C\left\|\mathring{\partial}_2\mathring{v}_0-\mathring{\Pi}^{\widehat{\Gamma},\mathring{\partial}_2}_{(p_1,p_2-1),\boldsymbol{\Xi}}\left(\widehat{\partial}_2\mathring{v}_0\right)\right\|_{\widehat{L}^2_{-1}(\mathring{\Omega}_C)}\\
&\leq C\left|\mathring{\partial}_2\mathring{v}_0-\mathring{\Pi}^{\widehat{\Gamma},\mathring{\partial}_2}_{(p_1,p_2-1),\boldsymbol{\Xi}}\left(\widehat{\partial}_2\mathring{v}_0\right)\right|_{\widehat{H}^1(\mathring{\Omega}_C)} = C\inf_{\mathring{w}\in\mathcal{P}_{s-2}}\left|\mathring{\partial}_2\mathring{v}_0-\mathring{w}+\mathring{\Pi}^{\widehat{\Gamma},\mathring{\partial}_2}_{(p_1,p_2-1),\boldsymbol{\Xi}}\left(\widehat{\partial}_2\mathring{v}_0-\mathring{w}\right)\right|_{\widehat{H}^1(\mathring{\Omega}_C)}\\
&\leq C\inf_{\mathring{w}\in\mathcal{P}_{s-2}}\left(\left|\mathring{\partial}_2\mathring{v}_0-\mathring{w}\right|_{\widehat{H}^1(\mathring{\Omega}_C)}+\left|\mathring{\Pi}^{\widehat{\Gamma},\mathring{\partial}_2}_{(p_1,p_2-1),\boldsymbol{\Xi}}\left(\widehat{\partial}_2\mathring{v}_0-\mathring{w}\right)\right|_{\widehat{H}^1(\mathring{\Omega}_C)}\right)\\
&\leq C\inf_{\mathring{w}\in\mathcal{P}_{s-2}}\left\|\mathring{\partial}_2\mathring{v}_0-\mathring{w}\right\|_{\widehat{H}^1\left(\mathring{\widetilde{\Omega}}_C\right)}. \qquad (3.67)
\end{aligned}$$

In the last step, we used the H^1-stability of the new projector $\mathring{\Pi}^{\widehat{\Gamma},\mathring{\partial}_2}_{\boldsymbol{p},\boldsymbol{\Xi}}$ which can be shown as in [BBSV14]. Finally, by applying the embedding $\widehat{H}^{s-1}_{1/2}(\mathring{\Omega}_C)\hookrightarrow\widehat{H}^1(\mathring{\Omega}_C)$ from [MR82, Remark 4.1], the Deny-Lions type estimate (3.66), a scaling argument and the relation (3.42), we obtain

$$\begin{aligned}
\left\|\widehat{\partial}_2\left(W\widehat{v}-\Pi^{\widehat{\Gamma}}_{\boldsymbol{p},\boldsymbol{\Xi}}(W\widehat{v})\right)\right\|_{\widehat{L}^2_{-1/2}(\widehat{\Omega}_C)} &\leq C\inf_{\mathring{w}\in\mathcal{P}_{s-2}}\left\|\mathring{\partial}_2\mathring{v}_0-\mathring{w}\right\|_{\widehat{H}^{s-1}_{1/2}\left(\mathring{\widetilde{\Omega}}_C\right)} \leq C\left|\mathring{\partial}_2\mathring{v}_0\right|_{\widehat{H}^{s-1}_{1/2}\left(\mathring{\widetilde{\Omega}}_C\right)}\\
&\leq C|\mathring{v}_0|_{\widehat{H}^s_{1/2}\left(\mathring{\widetilde{\Omega}}_C\right)} \leq Ch^{s-1}_{1,\widehat{\Omega}_C}|W\widehat{v}_0|_{\widehat{H}^s_{1/2}\left(\widetilde{\widehat{\Omega}}_C\right)}\\
&\leq Ch^{s-1}_{1,\widehat{\Omega}_C}\|\widehat{v}\|_{\mathcal{H}^s_{1/2}\left(\widetilde{\widehat{\Omega}}_C\right)} \leq Ch^{s-1}_{1,\widehat{\Omega}_C}\|\widehat{v}\|_{\mathcal{H}^s_{\odot}\left(\widetilde{\widehat{\Omega}}_C\right)},
\end{aligned}$$

and the assertion is established. □

Finally, we estimate the last term in line (3.62).

Lemma 3.32. *Let the assumptions of Theorem 3.28 hold. Then, it follows*

$$\left\|W\widehat{v}-\Pi^{\widehat{\Gamma}}_{\boldsymbol{p},\boldsymbol{\Xi}}(W\widehat{v})\right\|_{\widehat{L}^2_{-1/2}(\widehat{\Omega}_C)} \leq Ch^{s-1}_{1,\widehat{\Omega}_C}\|\widehat{v}\|_{\mathcal{H}^s_{\odot}\left(\widetilde{\widehat{\Omega}}_C\right)}.$$

Proof. As in the proof of Lemma 3.31, we use again the auxiliary functions $\widehat{v}_0=\widehat{v}-c\widehat{B}_{1,p_1}$ and set $\mathring{v}_0=\mathring{W}\mathring{v}_0$. A scaling argument yields

$$\left\|W\widehat{v}-\Pi^{\widehat{\Gamma}}_{\boldsymbol{p},\boldsymbol{\Xi}}(W\widehat{v})\right\|_{\widehat{L}^2_{-1/2}(\widehat{\Omega}_C)} = \left\|W\widehat{v}_0-\Pi^{\widehat{\Gamma}}_{\boldsymbol{p},\boldsymbol{\Xi}}(W\widehat{v}_0)\right\|_{\widehat{L}^2_{-1/2}(\widehat{\Omega}_C)} = \left\|\mathring{v}_0-\mathring{\Pi}^{\widehat{\Gamma}}_{\boldsymbol{p},\boldsymbol{\Xi}}\mathring{v}_0\right\|_{\widehat{L}^2_{-1/2}(\mathring{\Omega}_C)}.$$

Then, due to the H^1-stability of $\mathring{\Pi}^{\widehat{\Gamma}}_{\boldsymbol{p},\boldsymbol{\Xi}}$, we can show similar to (3.67) that

$$\left\|\mathring{v}_0-\mathring{\Pi}^{\widehat{\Gamma}}_{\boldsymbol{p},\boldsymbol{\Xi}}\mathring{v}_0\right\|_{\widehat{L}^2_{-1/2}(\mathring{\Omega}_C)} \leq C\inf_{\mathring{w}\in\mathcal{P}_{s-1}}\|\mathring{v}_0-\mathring{w}\|_{\widehat{H}^1\left(\mathring{\widetilde{\Omega}}_C\right)}.$$

With the embedding $\widehat{H}^s_{1/2}(\mathring{\Omega}_C)\hookrightarrow\widehat{H}^1(\mathring{\Omega}_C)$ for $s\geq 2$, see [MR82, Remark 4.1], the Deny-Lions type estimate (3.66), another scaling argument and the relation (3.42), it follows

$$\begin{aligned}
\left\|\mathring{v}_0-\mathring{\Pi}^{\widehat{\Gamma}}_{\boldsymbol{p},\boldsymbol{\Xi}}\mathring{v}_0\right\|_{\widehat{L}^2_{-1/2}(\mathring{\Omega}_C)} &\leq C\inf_{\mathring{w}\in\mathcal{P}_{s-1}}\|\mathring{v}_0-\mathring{w}\|_{\widehat{H}^s_{1/2}\left(\mathring{\widetilde{\Omega}}_C\right)} \leq C|\mathring{v}_0|_{\widehat{H}^s_{1/2}\left(\mathring{\widetilde{\Omega}}_C\right)}\\
&\leq Ch^{s-1}_{1,\widehat{\Omega}_C}|W\widehat{v}_0|_{\widehat{H}^s_{1/2}\left(\widetilde{\widehat{\Omega}}_C\right)} \leq Ch^{s-1}_{1,\widehat{\Omega}_C}\|\widehat{v}\|_{\mathcal{H}^s_{\odot}\left(\widetilde{\widehat{\Omega}}_C\right)}
\end{aligned}$$

and the proof is complete. □

Recall that by proving Lemmata 3.30, 3.31 and 3.32, the proof of Theorem 3.28 is complete. For now, we have assumed that $v \in V^s(\widetilde{\Omega}_C)$. However, as seen in Section 2.1.2, this is generally not the case for solutions of PDEs on polar domains with corners. Therefore, we show a corresponding result to Theorem 3.28 for functions with reduced regularity by moving to a weighted function space setting.

Theorem 3.33. *Let $q \in \{0,1\}$ and $s \in \mathbb{N}$ with $2 \le s \le p+1$. Further, let $v \in V^s_\beta(\widetilde{\Omega}_C)$ for all $\beta \in \mathbb{R}$ with $s-1-\nu < \beta < s-1$. Then, there is a positive constant C and a parameter β depending only on $p, \boldsymbol{\theta}, \boldsymbol{F}, W$ such that*

$$\left| v - \Pi_{V_h^\odot} v \right|_{H^q(\Omega_C)} \le C h_{1,\widehat{\Omega}_C}^{s-q-\beta} \|v\|_{V^s_\beta(\widetilde{\Omega}_C)},$$

with $\widetilde{\Omega}_C$ as defined in (3.54).

Proof. Just as in the proof of Theorem 3.28, we estimate the four error terms of the sum in (3.61) and (3.61). First, we adapt the stability result stated in Lemma 3.29, which is needed to estimate the first two terms. To that end, we use the embedding $H^s_\beta\left(\breve{\widetilde{\Omega}}_C\right) \hookrightarrow H^{s-\beta}\left(\breve{\widetilde{\Omega}}_C\right)$ from [Ros92] on the physical scaled reference domain defined in (3.64), and combine it with the usual Sobolev embedding $H^{s-\beta}\left(\breve{\widetilde{\Omega}}_C\right) \hookrightarrow C^0\left(\overline{\breve{\widetilde{\Omega}}_C}\right)$ for $\beta < s-1$, see for instance [AF03]. Then, with the proof of Lemma 3.29, embedding (2.2) and transformation (3.40), we obtain

$$\begin{aligned}\left\| \mathring{\partial}_1^q \left(\mathring{\Pi}^{\widehat{\Gamma}}_{\boldsymbol{p},\boldsymbol{\Xi}} \mathring{v} \right) \right\|_{\widehat{L}^2_{1/2}(\mathring{\Omega}_C)} &\le C \|\mathring{v}\|_{C^0\left(\overline{\breve{\widetilde{\Omega}}_C}\right)} = C \|\breve{v}\|_{C^0\left(\overline{\breve{\widetilde{\Omega}}_C}\right)} \le C \|\breve{v}\|_{H^{s-\beta}\left(\breve{\widetilde{\Omega}}_C\right)} \\ &\le C \|\breve{v}\|_{H^s_\beta\left(\breve{\widetilde{\Omega}}_C\right)} \le C \|\breve{v}\|_{V^s_\beta\left(\breve{\widetilde{\Omega}}_C\right)} \le C \|\mathring{v}\|_{\widehat{V}^s_{\odot,\beta}\left(\mathring{\widetilde{\Omega}}_C\right)}. \end{aligned} \tag{3.68}$$

Moreover, we use transformation (3.40) and the embeddings $V^{s-\beta}\left(\breve{\widetilde{\Omega}}_C\right) \hookrightarrow V^1\left(\breve{\widetilde{\Omega}}_C\right)$ from [Pfe14, Lemma 2.29] and $V^s_\beta\left(\breve{\widetilde{\Omega}}_C\right) \hookrightarrow V^{s-\beta}\left(\breve{\widetilde{\Omega}}_C\right)$ from [Ros92], where $s-\beta > 1$ is required, to show

$$\|\mathring{v}\|_{\widehat{V}^1_\odot\left(\mathring{\widetilde{\Omega}}_C\right)} \le C \|\breve{v}\|_{V^1\left(\breve{\widetilde{\Omega}}_C\right)} \le C \|\breve{v}\|_{V^{s-\beta}\left(\breve{\widetilde{\Omega}}_C\right)} \le C \|\breve{v}\|_{V^s_\beta\left(\breve{\widetilde{\Omega}}_C\right)} \le C \|\mathring{v}\|_{\widehat{V}^s_{\odot,\beta}\left(\mathring{\widetilde{\Omega}}_C\right)}. \tag{3.69}$$

By the scaling argument (3.65) and the estimates (3.68), (3.39) and (3.69), it follows

$$\begin{aligned}\left\| \widehat{\partial}_1^q \left(W\widehat{v} - \Pi^{\widehat{\Gamma}}_{\boldsymbol{p},\boldsymbol{\Xi}}(W\widehat{v}) \right) \right\|_{\widehat{L}^2_{1/2}(\widehat{\Omega}_C)} &\le C h_{1,\widehat{\Omega}_C}^{1-q} \left\| \mathring{\partial}_1^q \left(\mathring{v} - \mathring{\Pi}^{\widehat{\Gamma}}_{\boldsymbol{p},\boldsymbol{\Xi}} \mathring{v} \right) \right\|_{\widehat{L}^2_{1/2}(\mathring{\Omega}_C)} \\ &\le C h_{1,\widehat{\Omega}_C}^{1-q} \left(\|\mathring{v}\|_{\widehat{H}^1_{1/2}(\mathring{\Omega}_C)} + \left\| \mathring{\partial}_1^q \left(\mathring{\Pi}^{\widehat{\Gamma}}_{\boldsymbol{p},\boldsymbol{\Xi}} \mathring{v} \right) \right\|_{\widehat{L}^2_{1/2}(\mathring{\Omega}_C)} \right) \\ &\le C h_{1,\widehat{\Omega}_C}^{1-q} \left(\|\mathring{v}\|_{\widehat{V}^1_\odot\left(\mathring{\widetilde{\Omega}}_C\right)} + \|\mathring{v}\|_{\widehat{V}^s_{\odot,\beta}\left(\mathring{\widetilde{\Omega}}_C\right)} \right) \\ &\le C h_{1,\widehat{\Omega}_C}^{1-q} \|\mathring{v}\|_{\widehat{V}^s_{\odot,\beta}\left(\mathring{\widetilde{\Omega}}_C\right)} \le C h_{1,\widehat{\Omega}_C}^{s-q-\beta} \|\widehat{v}\|_{\mathcal{V}^s_{\odot,\beta}\left(\widehat{\widetilde{\Omega}}_C\right)}. \end{aligned}$$

Note that the V-spaces scale perfectly, which was exploited in the last line above in combination with the Leibniz formula. Next, we adapt the proof of Lemma 3.31. Let $\widehat{v}_0$ be the auxiliary function defined there such that $\widehat{v}_0(0,\cdot) = 0$ and let $\mathring{v}_0 = \mathring{W}\mathring{v}_0$ be the corresponding scaling, recall (3.63).

By combining Lemmata 3.36 and 3.37, the definition of polar weighted Sobolev norms and (3.69), we obtain

$$\begin{aligned}\left\|\widehat{\partial}_2\left(W\widehat{v}-\Pi^{\widehat{\Gamma}}_{\boldsymbol{p},\boldsymbol{\Xi}}(W\widehat{v})\right)\right\|_{\widehat{L}^2_{-1/2}(\widehat{\Omega}_C)} &= \left\|\mathring{\partial}_2\left(\mathring{v}_0-\mathring{\Pi}^{\widehat{\Gamma}}_{\boldsymbol{p},\boldsymbol{\Xi}}\mathring{v}_0\right)\right\|_{\widehat{L}^2_{-1/2}(\mathring{\Omega}_C)}\\ &= \left\|\mathring{\partial}_2\mathring{v}_0-\mathring{\Pi}^{\widehat{\Gamma},\mathring{\partial}_2}_{(p_1,p_2-1),\boldsymbol{\Xi}}(\widehat{\partial}_2\mathring{v}_0)\right\|_{\widehat{L}^2_{-1/2}(\mathring{\Omega}_C)}\\ &\le C\left\|\mathring{\partial}_2\mathring{v}_0\right\|_{\widehat{L}^2_{-1/2}\left(\widetilde{\mathring{\Omega}}_C\right)} \le C\|\mathring{v}_0\|_{\widehat{V}^1_{\odot}\left(\widetilde{\mathring{\Omega}}_C\right)} \le C\|\mathring{v}_0\|_{\widehat{V}^s_{\odot,\beta}\left(\widetilde{\mathring{\Omega}}_C\right)}\\ &\le Ch^{s-1-\beta}_{1,\widehat{\Omega}_C}\|\widehat{v}\|_{\mathcal{V}^s_{\odot,\beta}\left(\widetilde{\widehat{\Omega}}_C\right)},\end{aligned}$$

where, in the last step, we used again the perfect scaling of V-spaces.

Finally, the proof of Lemma 3.32 is modified analogously. Similar to Lemma 3.37, stability of the projector $\mathring{\Pi}^{\widehat{\Gamma}}_{\boldsymbol{p},\boldsymbol{\Xi}}$ in the $L^2_{-1/2}(\mathring{\Omega}_C)$-norm can be shown, and it follows

$$\begin{aligned}\left\|\mathring{v}_0-\mathring{\Pi}^{\widehat{\Gamma}}_{\boldsymbol{p},\boldsymbol{\Xi}}\mathring{v}_0\right\|_{\widehat{L}^2_{-1/2}(\mathring{\Omega}_C)} &\le C\|\mathring{v}_0\|_{\widehat{L}^2_{-1/2}\left(\widetilde{\mathring{\Omega}}_C\right)} \le C\|\mathring{v}_0\|_{\widehat{V}^1_{\odot}\left(\widetilde{\mathring{\Omega}}_C\right)}\\ &\le C\|\mathring{v}_0\|_{\widehat{V}^s_{\odot,\beta}\left(\widetilde{\mathring{\Omega}}_C\right)} \le Ch^{s-1-\beta}_{1,\widehat{\Omega}_C}\|\widehat{v}\|_{\mathcal{V}^s_{\odot,\beta}\left(\widetilde{\widehat{\Omega}}_C\right)}.\end{aligned}$$

Hence, we have estimated all four terms in (3.61) and (3.61). By the transformation (3.41) of the weighted polar Sobolev norms back to the physical domain, we obtain

$$\left|v-\Pi_{V^{\odot}_h}v\right|_{H^q(\Omega_C)} \le Ch^{s-q-\beta}_{1,\widehat{\Omega}_C}\|\widehat{v}\|_{\mathcal{V}^s_{\odot,\beta}\left(\widetilde{\widehat{\Omega}}_C\right)} \le Ch^{s-q-\beta}_{1,\widehat{\Omega}_C}\|v\|_{V^s_\beta(\widetilde{\Omega}_C)},$$

and the demonstration is complete. □

Estimates on the full domain Ω

Now, we are in the position to show an overall projection error estimate on polar domains with corners and prove optimal convergence for suitable grading parameters.

Theorem 3.34. *Let $q\in\{0,1\}$ and $s\in\mathbb{N}$ with $2\le s\le p+1$. Further, let $v\in V^s_\beta(\Omega)$ for all $\beta\in\mathbb{R}$ with $s-1-\nu<\beta<s-1$. If the mesh grading parameter satisfies condition (3.47), we obtain optimal convergence of the projection with respect to the mesh size h, i.e., there exists a constant C and a parameter β depending only on $p,\boldsymbol{\theta},\boldsymbol{F},W$ such that*

$$\left\|v-\Pi_{V^{\odot}_h}v\right\|_{H^q(\Omega)} \le Ch^{s-q}\|v\|_{V^s_\beta(\Omega)}.$$

Proof. By the splitting of the model domain defined in Section 3.4.2, we obtain

$$\left\|v-\Pi_{V^{\odot}_h}v\right\|^2_{H^q(\Omega)} = \left\|v-\Pi_{V^{\odot}_h}v\right\|^2_{H^q(\Omega_C)} + \left\|v-\Pi_{V^{\odot}_h}v\right\|^2_{H^q(\Omega_R)}.$$

The second term has been estimated in Theorem 3.27. For the first term, we use Theorem 3.33 and the mesh properties (3.14), where $h_{1,\Omega_C}\sim\widetilde{h}_{1,j_1}$ holds by definition of Ω_C and Lemma 3.12. Besides, we set $\beta=(1-\mu)(s-q)$ such that (3.60) is satisfied. It follows

$$\begin{aligned}\left\|v-\Pi_{V^{\odot}_h}v\right\|^2_{H^q(\Omega_C)} &\le Ch^{2(s-q-\beta)}_{1,\Omega_C}\|v\|^2_{V^s_\beta(\widetilde{\Omega}_C)} = Ch^{2(s-q)(1-1+\mu)}_{1,\Omega_C}\|v\|^2_{V^s_\beta(\widetilde{\Omega}_C)}\\ &\le Ch^{2(s-q)\mu/\mu}_1\|v\|^2_{V^s_\beta(\widetilde{\Omega}_C)} = Ch^{2(s-q)}_1\|v\|^2_{V^s_\beta(\widetilde{\Omega}_C)}.\end{aligned}$$

In total, for comparable refinement in both directions, that is, $h_1 \sim h_2$ and $h = \max\{h_1, h_2\}$, we have

$$\left\| v - \Pi_{V_h}^{\widehat{\Gamma}} v \right\|_{H^q(\Omega)}^2 \leq C h^{2(s-q)} \left(\|v\|_{V_\beta^s(\widetilde{\Omega}_C)}^2 + \|v\|_{V_\beta^s(\widetilde{\Omega}_R)}^2 \right) \leq C h^{2(s-q)} \|v\|_{V_\beta^s(\Omega)}^2,$$

where we use that $\widetilde{\Omega}_C$ and $\widetilde{\Omega}_R$ have bounded intersection with respect to h, and the assertion is proven. □

The main results of our analysis, in particular Theorem 3.21 and Corollary 3.24, follow immediately from Theorem 3.34. In addition, Corollaries 3.22 and 3.25 establish optimal convergence rates for the approximation of a specific class of smooth functions on uniform meshes. Finally, for the sake of completeness, we highlight the suboptimal convergence behavior that arises when singular functions are approximated on insufficiently graded meshes, including uniform meshes.

Remark 3.35 (Approximation of singular solutions on insufficiently graded meshes). The proof of Theorem 3.34 shows that convergence becomes suboptimal when the mesh grading parameter is not chosen small enough, that is, when condition (3.47) is violated. In particular, by adapting the proof at the relevant points, one can show that, for a grading parameter $\mu \in (0, 1]$ satisfying

$$\mu > \frac{\nu + 1 - q}{s - q},$$

the convergence rate for the H^q-error of the projection is bounded by $\frac{\nu+1-q}{\mu}$. This follows mainly from the relation $h^{s-q} < h^{\frac{\nu+1-q}{\mu}}$; see also [AH94; ASW96]. The approximation error in the H^1-norm decreases with the same order as the projection error, namely $\frac{\nu}{\mu} - \varepsilon$ for some $\varepsilon > 0$. In contrast, this is not the case in the L^2-norm: using a duality argument, one can show that the convergence order on insufficiently graded meshes is $2\frac{\nu}{\mu}$ rather than $\frac{\nu+1}{\mu} - \varepsilon$.

3.4.3 Properties of the modified quasi-interpolant

In this section, we establish key properties of the modified quasi-interpolant (2.37), which are applied in the proofs of Lemma 3.31 and Theorem 3.33 and require technical computations.

Lemma 3.36. *Let the assumptions of Theorem 3.28 hold. Then, there is a projector*

$$\mathring{\Pi}_{(p_1,p_2-1),\boldsymbol{\Xi}}^{\widehat{\Gamma},\mathring{\partial}_2} : C(\mathring{\Omega}) \to S_{(p_1,p_2-1)}(\boldsymbol{\Xi}),$$

with $\mathring{\Omega}$ as in (3.63), such that

$$\mathring{\partial}_2 \left(\mathring{\Pi}_{\boldsymbol{p},\boldsymbol{\Xi}}^{\widehat{\Gamma}} \mathring{v}_0 \right) = \mathring{\Pi}_{(p_1,p_2-1),\boldsymbol{\Xi}}^{\widehat{\Gamma},\mathring{\partial}_2} (\mathring{\partial}_2 \mathring{v}_0)$$

holds for all $\mathring{v}_0 \in C(\mathring{\Omega})$ with $\mathring{v}_0(0, \cdot) = 0$.

Proof. First, we recall representation (2.38) of the quasi-interpolant $\mathring{\Pi}_{\boldsymbol{p},\boldsymbol{\Xi}}^{\widehat{\Gamma}}$. The modified dual functionals $\lambda_{\boldsymbol{i}_\odot,\boldsymbol{p}}^{\widehat{\Gamma}}$, $\boldsymbol{i}_\odot \in I_\odot$, evaluated for a function $\mathring{v}_0 \in C(\mathring{\Omega})$ with $\mathring{v}_0(0, \cdot) = 0$, vanish, which is a

consequence of equation (3.26) with $W \equiv 1$ and $c = 0$. Then, with the formula for differentiation of B-splines [LMS18, Section 1.2.4], it follows

$$\begin{aligned}
\mathring{\partial}_2 \left(\mathring{\Pi}^{\widehat{\Gamma}}_{\boldsymbol{p},\boldsymbol{\Xi}} \mathring{v}_0\right)(\mathring{\zeta}_1, \mathring{\zeta}_2) &= \mathring{\partial}_2 \left(\sum_{\boldsymbol{i} \in \boldsymbol{I} \setminus \boldsymbol{I}_\odot} \mathring{\lambda}_{\boldsymbol{i},\boldsymbol{p}}(\mathring{v}_0) \mathring{B}_{\boldsymbol{i},\boldsymbol{p}}(\mathring{\zeta}_1, \mathring{\zeta}_2) \right) = \sum_{\boldsymbol{i} \in \boldsymbol{I} \setminus \boldsymbol{I}_\odot} \mathring{\lambda}_{\boldsymbol{i},\boldsymbol{p}}(\mathring{v}_0)\, \mathring{\partial}_2 \mathring{B}_{\boldsymbol{i},\boldsymbol{p}}(\mathring{\zeta}_1, \mathring{\zeta}_2) \\
&= \sum_{i_1=2}^{n_1} \sum_{i_2=1}^{n_2} (\mathring{\lambda}_{i_1,p_1} \otimes \mathring{\lambda}_{i_2,p_2})(\mathring{v}_0)\, \mathring{B}_{i_1,p_1}(\mathring{\zeta}_1)\, p_2 \left(\frac{\mathring{B}_{i_2,p_2-1}(\mathring{\zeta}_2)}{\mathring{\xi}_{i_2+p_2,2} - \mathring{\xi}_{i_2,2}} - \frac{\mathring{B}_{i_2+1,p_2-1}(\mathring{\zeta}_2)}{\mathring{\xi}_{i_2+p_2+1,2} - \mathring{\xi}_{i_2+1,2}} \right) \\
&= p_2 \sum_{i_1=2}^{n_1} \sum_{i_2=1}^{n_2} \mathring{\lambda}_{i_1,p_1} \left(\int_{\mathring{\xi}_{i_2,2}}^{\mathring{\xi}_{i_2+p_2+1,2}} \mathring{v}_0(\cdot,t)\, \mathring{D}^{p_2+1} \mathring{\psi}_{i_2}(t)\, \mathrm{d}t \right) \\
&\qquad \left(\frac{\mathring{B}_{i_2,p_2-1}(\mathring{\zeta}_2)}{\mathring{\xi}_{i_2+p_2,2} - \mathring{\xi}_{i_2,2}} - \frac{\mathring{B}_{i_2+1,p_2-1}(\mathring{\zeta}_2)}{\mathring{\xi}_{i_2+p_2+1,2} - \mathring{\xi}_{i_2+1,2}} \right) \mathring{B}_{i_1,p_1}(\mathring{\zeta}_1) \\
&= p_2 \sum_{i_1=2}^{n_1} \mathring{\lambda}_{i_1,p_1} \left(\sum_{i_2=1}^{n_2} \int_{\mathring{\xi}_{i_2,2}}^{\mathring{\xi}_{i_2+p_2+1,2}} \mathring{v}_0(\cdot,t)\, \mathring{D}^{p_2+1} \mathring{\psi}_{i_2}(t)\, \mathrm{d}t \right. \\
&\qquad \left. \left(\frac{\mathring{B}_{i_2,p_2-1}(\mathring{\zeta}_2)}{\mathring{\xi}_{i_2+p_2,2} - \mathring{\xi}_{i_2,2}} - \frac{\mathring{B}_{i_2+1,p_2-1}(\mathring{\zeta}_2)}{\mathring{\xi}_{i_2+p_2+1,2} - \mathring{\xi}_{i_2+1,2}} \right) \right) \mathring{B}_{i_1,p_1}(\mathring{\zeta}_1).
\end{aligned}$$

By reordering the sum that appears as an argument of the dual functional $\mathring{\lambda}_{i_1,p_1}$, we obtain

$$\begin{aligned}
&\sum_{i_2=1}^{n_2} \int_{\mathring{\xi}_{i_2,2}}^{\mathring{\xi}_{i_2+p_2+1,2}} \mathring{v}_0(\cdot,t)\, \mathring{D}^{p_2+1} \mathring{\psi}_{i_2}(t)\, \mathrm{d}t \left(\frac{\mathring{B}_{i_2,p_2-1}(\mathring{\zeta}_2)}{\mathring{\xi}_{i_2+p_2,2} - \mathring{\xi}_{i_2,2}} - \frac{\mathring{B}_{i_2+1,p_2-1}(\mathring{\zeta}_2)}{\mathring{\xi}_{i_2+p_2+1,2} - \mathring{\xi}_{i_2+1,2}} \right) \\
&= \int_{\mathring{\xi}_{1,2}}^{\mathring{\xi}_{1+p_2+1,2}} \mathring{v}_0(s,t)\, \mathring{D}^{p_2+1} \mathring{\psi}_1(t)\, \mathrm{d}t\, \frac{\mathring{B}_{1,p_2-1}(\mathring{\zeta}_2)}{\mathring{\xi}_{1+p_2,2} - \mathring{\xi}_{1,2}} \\
&\quad + \sum_{i_2=2}^{n_2} \left(\int_{\mathring{\xi}_{i_2,2}}^{\mathring{\xi}_{i_2+p_2+1,2}} \mathring{v}_0(s,t)\, \mathring{D}^{p_2+1} \mathring{\psi}_{i_2}(t)\, \mathrm{d}t - \int_{\mathring{\xi}_{i_2-1,2}}^{\mathring{\xi}_{i_2+p_2,2}} \mathring{v}_0(s,t)\, \mathring{D}^{p_2+1} \mathring{\psi}_{i_2-1}(t)\, \mathrm{d}t \right) \frac{\mathring{B}_{i_2,p_2-1}(\mathring{\zeta}_2)}{\mathring{\xi}_{i_2+p_2,2} - \mathring{\xi}_{i_2,2}} \\
&\quad - \int_{\mathring{\xi}_{n_2,2}}^{\mathring{\xi}_{n_2+p_2+1,2}} \mathring{v}_0(s,t)\, \mathring{D}^{p_2+1} \mathring{\psi}_{n_2}(t)\, \mathrm{d}t\, \frac{\mathring{B}_{n_2+1,p_2-1}(\mathring{\zeta}_2)}{\mathring{\xi}_{n_2+p_2+1,2} - \mathring{\xi}_{n_2+1,2}} \\
&= \sum_{i_2=2}^{n_2} \left(\int_{\mathring{\xi}_{i_2,2}}^{\mathring{\xi}_{i_2+p_2+1,2}} \mathring{v}_0(s,t)\, \mathring{D}^{p_2+1} \mathring{\psi}_{i_2}(t)\, \mathrm{d}t - \int_{\mathring{\xi}_{i_2-1,2}}^{\mathring{\xi}_{i_2+p_2,2}} \mathring{v}_0(s,t)\, \mathring{D}^{p_2+1} \mathring{\psi}_{i_2-1}(t)\, \mathrm{d}t \right) \frac{\mathring{B}_{i_2,p_2-1}(\mathring{\zeta}_2)}{\mathring{\xi}_{i_2+p_2,2} - \mathring{\xi}_{i_2,2}}.
\end{aligned}$$

The first and last term of the reordered sum vanish since Ξ_2 is an open knot vector and fractions with zero denominator are defined to have value zero. Next, we rewrite the term in brackets,

$$\begin{aligned}
&\int_{\mathring{\xi}_{i_2,2}}^{\mathring{\xi}_{i_2+p_2+1,2}} \mathring{v}_0(s,t)\, \mathring{D}^{p_2+1} \mathring{\psi}_{i_2}(t)\, \mathrm{d}t - \int_{\mathring{\xi}_{i_2-1,2}}^{\mathring{\xi}_{i_2+p_2,2}} \mathring{v}_0(s,t)\, \mathring{D}^{p_2+1} \mathring{\psi}_{i_2-1}(t)\, \mathrm{d}t \\
&= \int_{\mathring{\xi}_{i_2,2}}^{\mathring{\xi}_{i_2+p_2+1,2}} \mathring{v}_0(s,t)\, \mathring{D}^{p_2+1} \mathring{\psi}_{i_2}(t)\, \mathrm{d}t - \int_{\mathring{\xi}_{i_2,2}}^{\mathring{\xi}_{i_2+p_2+1,2}} \mathring{v}_0(s,\alpha(t))\, \mathring{D}^{p_2+1} (\mathring{\psi}_{i_2-1} \circ \alpha(t)) \big|\alpha'(t)\big|\, \mathrm{d}t, \quad (3.70)
\end{aligned}$$

where we use the transformation $\alpha(t) := t - h_2$ based on the mesh size h_2 in angular direction.

With definitions (2.25) and (2.26), we further compute

$$
\begin{aligned}
&\psi_{i_2-1}(t-h_2) = G_{i_2-1}(t-h_2)\Phi_{i_2-1}(t-h_2)\\
&= g\left(\frac{2(t-h_2)-\xi_{i_2-1,2}-\xi_{i_2+p_2,2}}{\xi_{i_2+p_2,2}-\xi_{i_2-1,2}}\right)\left(\frac{(t-h_2-\xi_{i_2,2})\cdots(t-h_2-\xi_{i_2+p_2-1,2})}{p_2!}\right)\\
&= g\left(\frac{2t-(\xi_{i_2-1,2}+h_2)-(\xi_{i_2+p_2,2}+h_2)}{\xi_{i_2+p_2+1,2}-h_2-(\xi_{i_2,2}-h_2)}\right)\left(\frac{(t-(\xi_{i_2,2}+h_2))\cdots(t-(\xi_{i_2+p_2-1,2}+h_2))}{p_2!}\right)\\
&= g\left(\frac{2t-\xi_{i_2,2}-\xi_{i_2+p_2+1,2}}{\xi_{i_2+p_2+1,2}-\xi_{i_2,2}}\right)\left(\frac{(t-\xi_{i_2+1,2})\cdots(t-\xi_{i_2+p_2,2}))}{p_2!}\right)\\
&= G_{i_2}(t)\Phi_{i_2}(t)\\
&= \psi_{i_2}(t).
\end{aligned}
$$

It follows that the expression (3.70) can be written in terms of a new dual functional,

$$
\mu_{i_2,p_2-1}(\mathring{w}) := \int_{\mathring{\xi}_{i_2,2}}^{\mathring{\xi}_{i_2+p_2+1,2}} \int_{\alpha(t)}^{t} \mathring{w}(z)\,\mathrm{d}z\,\mathring{D}^{p_2+1}\mathring{\psi}_{i_2}(t)\,\mathrm{d}t,
$$

with $\mathring{w}(\cdot) = \mathring{\partial}_2\mathring{v}_0(s,\cdot)$. By combining all results, we obtain

$$
\begin{aligned}
\mathring{\partial}_2\left(\mathring{\Pi}^{\widehat{\Gamma}}_{\boldsymbol{p},\boldsymbol{\Xi}}\mathring{v}_0\right) &= p_2\sum_{i_1=2}^{n_1}\lambda_{i_1,p_1}\left(\sum_{i_2=2}^{n_2}\mu_{i_2,p_2-1}(\mathring{\partial}_2\mathring{v}_0(s,\cdot))\frac{\mathring{B}_{i_2,p_2-1}(\mathring{\zeta}_2)}{\mathring{\xi}_{i_2+p_2,2}-\mathring{\xi}_{i_2,2}}\right)\mathring{B}_{i_1,p_1}(\mathring{\zeta}_1)\\
&= p_2\sum_{i_1=2}^{n_1}\sum_{i_2=2}^{n_2}\left(\lambda_{i_1,p_1}\otimes\mu_{i_2,p_2-1}\right)(\mathring{\partial}_2\mathring{v}_0)\mathring{B}_{i_1,p_1}(\mathring{\zeta}_1)\frac{\mathring{B}_{i_2,p_2-1}(\mathring{\zeta}_2)}{\mathring{\xi}_{i_2+p_2,2}-\mathring{\xi}_{i_2,2}}\\
&= \mathring{\Pi}^{\widehat{\Gamma},\mathring{\partial}_2}_{(p_1,p_2-1),\boldsymbol{\Xi}}(\mathring{\partial}_2\mathring{v}_0),
\end{aligned}
$$

where

$$
\mathring{\Pi}^{\widehat{\Gamma},\mathring{\partial}_2}_{(p_1,p_2-1),\boldsymbol{\Xi}}(\mathring{w}) := p_2\sum_{i_1=2}^{n_1}\sum_{i_2=2}^{n_2}\left(\lambda_{i_1,p_1}\otimes\mu_{i_2,p_2-1}\right)(\mathring{w})\mathring{B}_{i_1,p_1}(\mathring{\zeta}_1)\frac{\mathring{B}_{i_2,p_2-1}(\mathring{\zeta}_2)}{\mathring{\xi}_{i_2+p_2,2}-\mathring{\xi}_{i_2,2}} \tag{3.71}
$$

is the resulting new projector. □

Lemma 3.37. *Let the notation of Lemmata 3.31 and 3.36 hold. Then, there is a constant $C>0$ such that*

$$
\left\|\mathring{\Pi}^{\widehat{\Gamma},\mathring{\partial}_2}_{(p_1,p_2-1),\boldsymbol{\Xi}}(\mathring{\partial}_2\mathring{v}_0)\right\|_{\widehat{L}^2_{-1/2}(\mathring{\Omega}_C)} \leq C\left\|\mathring{\partial}_2\mathring{v}_0\right\|_{\widehat{L}^2_{-1/2}\left(\widetilde{\mathring{\Omega}}_C\right)}
$$

for all $\mathring{v}_0\in C(\mathring{\Omega})$ with $\mathring{v}_0(0,\cdot)=0$.

Proof. We recall the definitions of the projector (3.71) and the scaling transformation (3.63) and

apply the continuous Cauchy-Schwarz inequality to compute

$$
\begin{aligned}
&\left\|\mathring{\Pi}^{\widehat{\Gamma},\mathring{\partial}_2}_{(p_1,p_2-1),\boldsymbol{\Xi}}(\mathring{\partial}_2\mathring{v}_0)\right\|^2_{\widehat{L}^2_{-1/2}(\mathring{\Omega}_C)}\\
&\leq p_2^2\sum_{i_1=2}^{n_1}\sum_{i_2=2}^{n_2}\left|(\lambda_{i_1,p_1}\otimes\mu_{i_2,p_2-1})(\mathring{\partial}_2\mathring{v}_0)\right|^2\int_{\mathring{\Omega}_C}\left|\mathring{\zeta}_1^{-1/2}\,\mathring{B}_{i_1,p_1}(\mathring{\zeta}_1)\frac{\mathring{B}_{i_2,p_2-1}(\mathring{\zeta}_2)}{\mathring{\xi}_{i_2+p_2+1,2}-\mathring{\xi}_{i_2,2}}\right|^2\mathrm{d}\mathring{\zeta}_1\,\mathrm{d}\mathring{\zeta}_2\\
&= p_2^2\sum_{i_1=2}^{n_1}\sum_{i_2=2}^{n_2}\left|\int_{\mathring{\xi}_{i_1,1}}^{\mathring{\xi}_{i_1+p_1+1,1}}\int_{\mathring{\xi}_{i_2,2}}^{\mathring{\xi}_{i_2+p_2+1,2}}\int_{\alpha(t)}^{t}\mathring{\partial}_2\mathring{v}_0(s,z)\,\mathrm{d}z\,\mathring{D}^{p_2+1}\mathring{\psi}_{i_2}(t)\;\mathrm{d}t\,\mathring{D}^{p_1+1}\mathring{\psi}_{i_1}(s)\,\mathrm{d}s\right|^2 Ch_2^{-2}\\
&\leq Ch_2^{-2}\sum_{i_1=2}^{n_1}\sum_{i_2=2}^{n_2}\left|\int_{\mathring{\xi}_{i_1,1}}^{\mathring{\xi}_{i_1+p_1+1,1}}\int_{\mathring{\xi}_{i_2,2}}^{\mathring{\xi}_{i_2+p_2+1,2}}\int_{\mathring{\xi}_{i_2-1,2}}^{\mathring{\xi}_{i_2+p_2+1,2}}\left|\mathring{\partial}_2\mathring{v}_0(s,z)\right|\mathrm{d}z\,\mathring{D}^{p_2+1}\mathring{\psi}_{i_2}(t)\;\mathrm{d}t\,\mathring{D}^{p_1+1}\mathring{\psi}_{i_1}(s)\,\mathrm{d}s\right|^2\\
&= Ch_2^{-2}\left(\int_{\mathring{\xi}_{i_2-1,2}}^{\mathring{\xi}_{i_2+p_2+1,2}}\mathring{D}^{p_2+1}\mathring{\psi}_{i_2}\,\mathrm{d}t\right)^2\sum_{i_1=2}^{n_1}\sum_{i_2=2}^{n_2}\left|\int_{\mathring{\xi}_{i_1,1}}^{\mathring{\xi}_{i_1+p_1+1,1}}\int_{\mathring{\xi}_{i_2-1,2}}^{\mathring{\xi}_{i_2+p_2+1,2}}\left|\mathring{\partial}_2\mathring{v}_0(s,z)\right|\mathrm{d}z\mathring{D}^{p_1+1}\mathring{\psi}_{i_1}(s)\,\mathrm{d}s\right|^2\\
&\leq C\sum_{i_1=2}^{n_1}\sum_{i_2=2}^{n_2}\left|\int_{\mathring{\xi}_{i_1,1}}^{\mathring{\xi}_{i_1+p_1+1,1}}\int_{\mathring{\xi}_{i_2-1,2}}^{\mathring{\xi}_{i_2+p_2+1,2}}\left|\mathring{\partial}_2\mathring{v}_0(s,z)\mathring{D}^{p_1+1}\mathring{\psi}_{i_1}(s)\right|\mathrm{d}z\,\mathrm{d}s\right|^2.
\end{aligned}
$$

Then, we set $E_{(i_1,i_2)}:=(\mathring{\xi}_{i_1,1},\mathring{\xi}_{i_1+p_1+1,1})\times(\mathring{\xi}_{i_2-1,2},\mathring{\xi}_{i_2+p_2+1,2})\subset\widetilde{\mathring{\Omega}}$ and simplify the term above by using the continuous and discrete Cauchy-Schwarz inequality combined with the equivalence of finite-dimensional norms,

$$
\begin{aligned}
&C\sum_{i_1=2}^{n_1}\sum_{i_2=2}^{n_2}\left|\int_{\mathring{\xi}_{i_1,1}}^{\mathring{\xi}_{i_1+p_1+1,1}}\int_{\mathring{\xi}_{i_2-1,2}}^{\mathring{\xi}_{i_2+p_2+1,2}}\left|\mathring{\partial}_2\mathring{v}_0(s,z)\mathring{D}^{p_1+1}\mathring{\psi}_{i_1}(s)\right|\mathrm{d}z\,\mathrm{d}s\right|^2\\
&\leq C\sum_{i_1=2}^{n_1}\sum_{i_2=2}^{n_2}\left(\int_{E_{(i_1,i_2)}}\left|\mathring{\partial}_2\mathring{v}_0(s,z)\right|^2\mathrm{d}z\,\mathrm{d}s\right)\left(\int_{E_{(i_1,i_2)}}\left|\mathring{D}^{p_1+1}\mathring{\psi}_{i_1}(s)\right|^2\mathrm{d}z\,\mathrm{d}s\right)\\
&\leq C\left(\sum_{i_1=2}^{n_1}\sum_{i_2=2}^{n_2}\left(\int_{E_{(i_1,i_2)}}\left|\mathring{\partial}_2\mathring{v}_0(s,z)\right|^2\mathrm{d}z\,\mathrm{d}s\right)^2\right)^{1/2}\left(\sum_{i_1=2}^{n_1}\sum_{i_2=2}^{n_2}\left(\int_{E_{(i_1,i_2)}}\left|\mathring{D}^{p_1+1}\mathring{\psi}_{i_1}(s)\right|\mathrm{d}z\,\mathrm{d}s\right)^2\right)^{1/2}\\
&\leq C\left(\sum_{i_1=2}^{n_1}\sum_{i_2=2}^{n_2}\int_{E_{(i_1,i_2)}}\left|\mathring{\partial}_2\mathring{v}_0(s,z)\right|^2\mathrm{d}z\,\mathrm{d}s\right)\left(\sum_{i_1=2}^{n_1}\sum_{i_2=2}^{n_2}\int_{E_{(i_1,i_2)}}\left|\mathring{D}^{p_1+1}\mathring{\psi}_{i_1}(s)\right|\mathrm{d}z\,\mathrm{d}s\right)\\
&\leq C\sum_{i_1=2}^{n_1}\sum_{i_2=2}^{n_2}\left\|\mathring{\partial}_2\mathring{v}_0\right\|^2_{L^2(E_{(i_1,i_2)})}\sum_{i_1=2}^{n_1}\sum_{i_2=2}^{n_2}h_2h_1\leq C\left\|\mathring{\partial}_2\mathring{v}_0\right\|^2_{\widehat{L}^2\left(\widetilde{\mathring{\Omega}}_C\right)}\cdot 1\leq C\left\|\mathring{\partial}_2\mathring{v}_0\right\|^2_{\widehat{L}^2_{-1/2}\left(\widetilde{\mathring{\Omega}}_C\right)},
\end{aligned}
$$

and the demonstration is complete. □

3.5 Numerical Examples for graded Galerkin IGA

In this section, we report numerical tests previously presented in Section 6 of [AZ26] that confirm our theoretical results for Galerkin IGA with graded meshes in the vicinity of polar corners. All experiments are carried out using the computing package GeoPDEs 3.2.2 [FRV11; Váz16]. The graded h-refinement method introduced in Section 3.2.2 can be implemented easily in GeoPDEs by adapting one line of the standard knot refining routine *kntrefine* provided in the package. The

polar spline basis (3.23) is constructed by applying the extraction operator described in [TSHH17, Section 3.3.2] to the standard set of basis functions. If homogeneous Dirichlet boundary conditions are considered on one of the edges adjacent to the polar corner, this step can even be omitted, and the collapsing edge can be treated as a Dirichlet edge. Moreover, numerical studies have even shown that, from a computational point of view, it is possible to work with the standard singular basis functions (3.18), which is due to the use of quadrature rules, see for instance [AZ24b].

Throughout the examples, the maximum NURBS degree used is $p = 5$. Therefore, all integrals are computed using a Gauss–Legendre quadrature rule with 36 Gauss points per mesh element, where 6 quadrature nodes are employed in both univariate directions. Unless stated otherwise, for each degree p, we consider NURBS of maximal regularity $k = p - 1$ within the coarse mesh elements, recall Remark 3.9.

Example 3.38 (**Smooth solution**)**.** In the first example, we solve the Poisson equation on a quarter of the unit disk. We impose homogeneous Dirichlet BCs on the re-entrant edges and non-homogeneous Dirichlet conditions on the circular arc, derived from the exact solution

$$u : \Omega \to \mathbb{R}, \quad u(x, y) = \hat{u}(r, \varphi) = r^\nu \sin(\nu\varphi),$$

with $\nu = 2$. Here and in the following, the inverted breve accent is used to denote the considered function in polar coordinates, e.g., $\hat{u}(r, \varphi) = u(r\cos\varphi, r\sin\varphi) = u(x, y)$. Figure 3.11a shows a numerical approximation of the solution computed on a uniform mesh with 16 subdivisions in each parametric direction. The double angle formula yields that the exact solution represents a polynomial in the physical domain,

$$u(x, y) = \hat{u}(r, \varphi) = r^2 \sin(2\varphi) = 2r^2 \sin\varphi\cos\varphi = 2xy.$$

Thus, the solution is smooth in the classical sense, with $u \in H^s(\Omega)$ for all $s \in \mathbb{N}$. In contrast, with respect to the V-spaces, we only have $u \in V^s_\beta(\Omega)$ for all $s \in \mathbb{N}$ and $\beta \in \mathbb{R}$ with $s - 1 - \nu < \beta < s - 1$, where $\nu = 2$. Consequently, in the sense of Corollary 3.25, where $\nu > s - 1$ is required, the integrability condition is limited to order $s \leq 2$, see also Remark 3.23.

Figures 3.11b and 3.11c show the approximation errors in the $H^1(\Omega)$- and $L^2(\Omega)$-norms plotted against the mesh size h, for NURBS of degree p on uniformly refined meshes corresponding to the grading parameter $\mu = 1$. As predicted by Corollary 3.25, we observe optimal convergence rates of order 1 in the $H^1(\Omega)$-norm and 2 in the $L^2(\Omega)$-norm for lowest-order NURBS. Higher order approximations also display optimal rates of order p in the $H^1(\Omega)$-norm and $p + 1$ in the $L^2(\Omega)$-norm, but his behavior is not covered by the present theory and indicates that Corollary 3.25 is not sharp. In particular, higher order optimal approximation of polynomials in the physical domain remains to be shown. Despite the widespread use of this standard parameterization of a quarter disk – known to contain a polar singularity – corresponding error estimates have not been established up to now, as also noted in the recent work [Tak25]. The discretization scheme examined here coincides exactly with the configuration analyzed in Section 5.1 (center-right column of Figure 8) of that paper. Although not yet complete, our results provide, at least in part, a mathematical explanation for the observed numerical convergence behavior.

Example 3.39 (**Singular solution, mild corner angle**)**.** Next, we consider a circular sector with angle $\omega = \frac{2}{3}\pi$, see Example 3.6. As test problem, we consider the Poisson equation with mixed homogeneous BCs. With the right-hand side $f : \Omega \to \mathbb{R}$, $f(x, y) = \hat{f}(r, \varphi) = -r^{\nu-1}\sin(\nu\varphi)(-2\nu-1)$, with $\nu = \frac{\pi}{2\omega} = \frac{3}{4}$, we obtain the solution

$$u : \Omega \to \mathbb{R}, \quad u(x, y) = \hat{u}(r, \varphi) = r^\nu \sin(\nu\varphi)(1 - r).$$

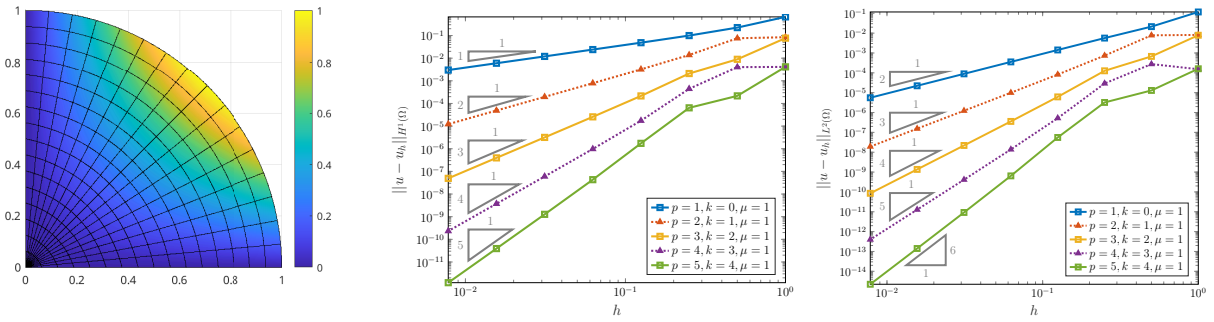

(a) (b) (c)

Figure 3.11: Solving the Poisson equation on a quarter of the unit disk: (a): Plot of a numerical solution on a uniform mesh with 16 subdivisions for bicubic NURBS ($p = 3$). (b): $H^1(\Omega)$-error of the approximation. (c): $L^2(\Omega)$-error of the approximation.

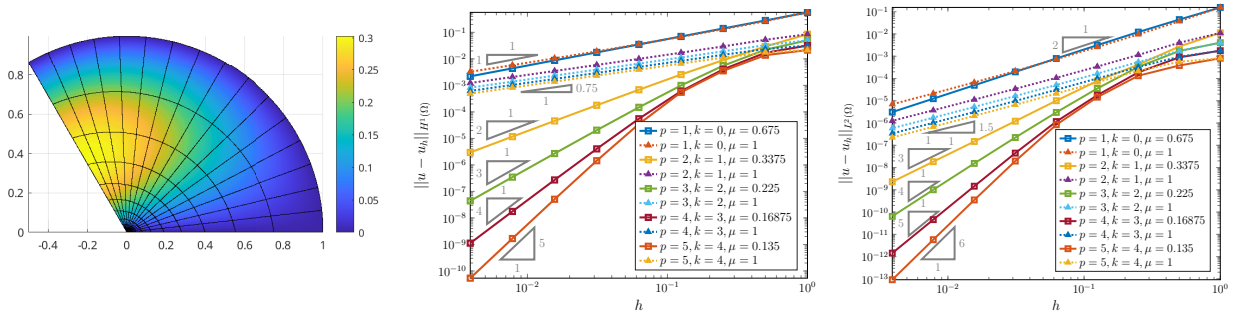

(a) (b) (c)

Figure 3.12: Solving the Poisson equation on a circular sector with inner angle $\omega = \frac{2}{3}\pi$: (a): Plot of a numerical solution on a graded mesh with 16 subdivisions using bicubic NURBS. (b): $H^1(\Omega)$-error of the approximation. (c): $L^2(\Omega)$-error of the approximation.

Figure 3.12a shows a numerical solution computed with bicubic NURBS on a graded mesh with 16 subdivisions in each parametric direction. As discussed in Section 2.1.2, the solution exhibits a singularity of type r^ν and satisfies the regularity property (2.4).

We plot the $H^1(\Omega)$- and $L^2(\Omega)$-errors of the approximations versus decreasing mesh size h in Figures 3.12b and 3.12c. For each NURBS degree p, we consider maximally smooth NURBS on both uniform and graded meshes, corresponding to grading parameters $\mu = 1$ and $\mu = 0.9\frac{\nu}{p}$, respectively, recall (3.51). As expected from Remark 3.35, the experimental convergence rates on uniform meshes are governed by the singularity and approach orders of ν and 2ν independent of the polynomial degree. In contrast, the use of graded meshes recovers optimal convergence rates of p and $p+1$ in the $H^1(\Omega)$- and $L^2(\Omega)$-norms, respectively, in full agreement with Corollary 3.24.

For additional insight, we test our method for fixed $p = 3$ and different choices of grading parameters $\mu \in \{0.7\frac{\nu}{p}, 0.9\frac{\nu}{p}, 1.1\frac{\nu}{p}, 1.3\frac{\nu}{p}\}$. The $H^1(\Omega)$-errors of the resulting approximations, together with the corresponding experimental orders of convergence (EOC), are listed in Table 3.3. Several observations confirm our theoretical findings. First, the condition (3.48) on the grading parameter, established theoretically for the approximation error estimate in Corollary 3.24, is indeed necessary to obtain optimal convergence in the $H^1(\Omega)$-norm. If the grading parameter is chosen too large, we obtain a convergence rate of $\frac{\nu}{\mu}$, as predicted in Remark 3.35; the corresponding values are reported in the last row of the table. Moreover, among the sufficiently small grading parameters, the milder

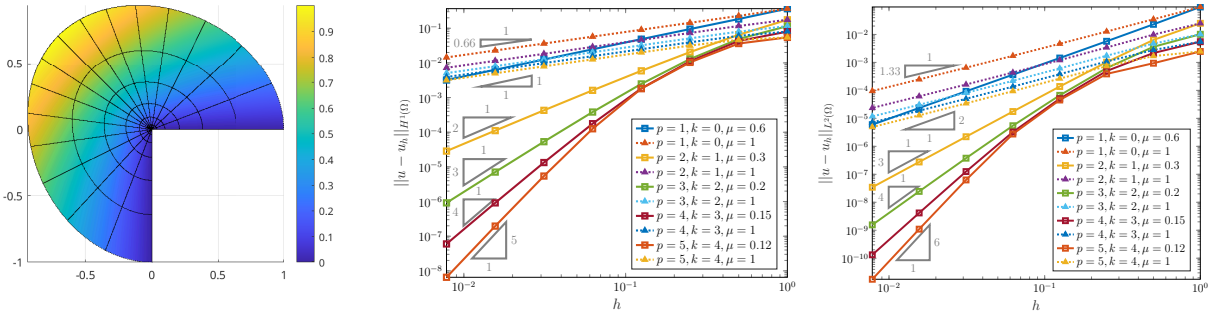

(a) (b) (c)

Figure 3.13: Solving the Poisson equation on the Quasi-Pacman domain: (a): Plot of a numerical solution on a graded mesh for biquadratic NURBS. (b): $H^1(\Omega)$-error of the approximation. (c): $L^2(\Omega)$-error of the approximation.

choice yields a better approximation constant, thereby justifying our recommendation in (3.51).

With respect to the $L^2(\Omega)$-error, the analysis of the optimal grading is more delicate. All grading parameters considered above yield optimal convergence; see Table 3.4. In fact, the threshold beyond which the approximation in the $L^2(\Omega)$-norm becomes suboptimal is higher. In the present example, it turns out that it is governed by the grading condition in (3.47) for $q = 0$, that is, the condition required for the projection error estimate. Accordingly, we report the $L^2(\Omega)$-errors obtained for milder grading parameters $\mu \in \{0.7\frac{\nu+1}{p+1}, 0.9\frac{\nu+1}{p+1}, 1.1\frac{\nu+1}{p+1}, 1.3\frac{\nu+1}{p+1}\}$ in Table 3.5. We observe that $\mu < \frac{\nu+1}{p+1}$ yields the optimal convergence rate of $p+1$, whereas larger values lead only to the suboptimal rate $2\frac{\nu}{\mu}$, as discussed in Remark 3.35; the explicit values are again computed in the last row of the table. However, deriving a corresponding approximation error estimate requires additional effort, since a standard duality argument as in the proof of Corollary 3.24 cannot be applied. This lies beyond the scope of this thesis and remains the subject of ongoing research.

Example 3.40 (**Singular solution, Quasi-Pacman domain**)**.** Now, we turn to a domain with a re-entrant corner of interior angle $\omega = \frac{3}{2}\pi$, parameterized by NURBS with knot vectors $\Xi_1 = \{0, 0, 1, 1\}$ and $\Xi_2 = \{0, 0, 0, 0, 0, \frac{1}{2}, \frac{1}{2}, 1, 1, 1, 1, 1, 1\}$. The control points and weights, listed in Tables 3.6 and 3.7, are chosen to resemble those of a circular sector composed of three $\frac{\pi}{2}$-sectors. The resulting geometry – referred to as the *Quasi-Pacman* domain – is a smoothly parameterized deformed circular sector.

We solve the Poisson equation with homogeneous Dirichlet BCs on the re-entrant edges and inhomogeneous Dirichlet conditions on the arc. The data is derived from the exact solution

$$u : \Omega \to \mathbb{R}, \quad u(x, y) = \hat{u}(r, \varphi) = r^\nu \sin(\nu\varphi),$$

with $\nu = \frac{2}{3}$, for which (2.4) holds, consistent with our theory. In Figure 3.13, we illustrate an exemplary numerical solution as well as the approximation errors for both uniform and graded meshes. As in the preceding experiment, we observe that graded meshes recover optimal convergence rates, which are not achieved by uniform meshes, as predicted by Corollary 3.24 and Remark 3.35.

Example 3.41 (**Pacman domain**)**.** We proceed by solving our model problem (2.3) on the Pacman domain, which is defined as a circular sector with angle $\omega = \frac{5}{3}\pi$, see Example 3.6. In contrast to the previous tests, the resulting parameterization only satisfies the global continuity $\boldsymbol{F} \in (C^0(\widehat{\Omega}))^2$. We consider homogeneous Dirichlet boundary conditions on the circular edge and

ndof	$\mu = 0.7\frac{\nu}{p} = 0.175$	$\mu = 0.9\frac{\nu}{p} = 0.225$	$\mu = 1.1\frac{\nu}{p} = 0.275$	$\mu = 1.3\frac{\nu}{p} = 0.325$
21	$3.1152e-02$ (0.84)	$2.4403e-02$ (1.19)	$1.9509e-02$ (1.52)	$1.7148e-02$ (1.70)
43	$8.9730e-03$ (1.80)	$5.8972e-03$ (2.05)	$4.6015e-03$ (2.08)	$4.2415e-03$ (2.02)
111	$1.6208e-03$ (2.47)	$1.0502e-03$ (2.49)	$8.6473e-04$ (2.41)	$9.0046e-04$ (2.24)
343	$2.3872e-04$ (2.76)	$1.5621e-04$ (2.75)	$1.4400e-04$ (2.59)	$1.8271e-04$ (2.30)
1191	$3.1819e-05$ (2.91)	$2.1318e-05$ (2.87)	$2.2867e-05$ (2.65)	$3.6845e-05$ (2.31)
4423	$4.0785e-06$ (2.96)	$2.7949e-06$ (2.93)	$3.5561e-06$ (2.68)	$7.4327e-06$ (2.31)
17031	$5.1514e-07$ (2.99)	$3.5904e-07$ (2.96)	$5.4703e-07$ (2.70)	$1.5004e-06$ (2.31)
66823	$6.4688e-08$ (2.99)	$4.5610e-08$ (2.98)	$8.3610e-08$ (2.71)	$3.0298e-07$ (2.31)
			$\frac{\nu}{\mu} \approx 2.727$	$\frac{\nu}{\mu} \approx 2.308$

Table 3.3: Approximation errors $\|u - u_h\|_{H^1(\Omega)}$ (and corresponding EOC) for Example 3.39 using graded refinement for NURBS of degree $p = 3$ and different grading parameters μ.

ndof	$\mu = 0.7\frac{\nu}{p} = 0.175$	$\mu = 0.9\frac{\nu}{p} = 0.225$	$\mu = 1.1\frac{\nu}{p} = 0.275$	$\mu = 1.3\frac{\nu}{p} = 0.325$
21	$2.4493e-03$ (0.97)	$1.9620e-03$ (1.29)	$1.5030e-03$ (1.68)	$1.1171e-03$ (2.10)
43	$6.6336e-04$ (1.88)	$3.4249e-04$ (2.52)	$1.9903e-04$ (2.92)	$1.3291e-04$ (3.07)
111	$7.2785e-05$ (3.19)	$3.4341e-05$ (3.32)	$1.9388e-05$ (3.36)	$1.2380e-05$ (3.42)
343	$6.3356e-06$ (3.52)	$2.7859e-06$ (3.62)	$1.4709e-06$ (3.72)	$8.9655e-07$ (3.79)
1191	$4.6612e-07$ (3.76)	$1.9391e-07$ (3.84)	$9.8908e-08$ (3.89)	$5.9093e-08$ (3.92)
4423	$3.1232e-08$ (3.90)	$1.2670e-08$ (3.94)	$6.3674e-09$ (3.96)	$3.7708e-09$ (3.97)
17031	$2.0124e-09$ (3.96)	$8.0748e-10$ (3.97)	$4.0316e-10$ (3.98)	$2.3776e-10$ (3.99)
66823	$1.2754e-10$ (3.98)	$5.0927e-11$ (3.99)	$2.5350e-11$ (3.99)	$1.4920e-11$ (3.99)

Table 3.4: Approximation errors $\|u - u_h\|_{L^2(\Omega)}$ (and corresponding EOC) for Example 3.39 using graded refinement for NURBS of degree $p = 3$ and different grading parameters μ.

ndof	$\mu = 0.7\frac{\nu+1}{p+1} = 0.30625$	$\mu = 0.9\frac{\nu+1}{p+1} = 0.39375$	$\mu = 1.1\frac{\nu+1}{p+1} = 0.48125$	$\mu = 1.3\frac{\nu+1}{p+1} = 0.56875$
21	$1.2519e-03$ (1.94)	$7.5249e-04$ (2.67)	$6.8751e-04$ (2.80)	$9.3552e-04$ (2.36)
43	$1.5235e-04$ (3.04)	$9.1751e-05$ (3.04)	$8.1623e-05$ (3.07)	$1.2520e-04$ (2.90)
111	$1.4460e-05$ (3.40)	$8.0499e-06$ (3.51)	$7.8000e-06$ (3.39)	$1.6438e-05$ (2.93)
343	$1.0625e-06$ (3.77)	$5.7681e-07$ (3.80)	$7.2531e-07$ (3.43)	$2.2601e-06$ (2.86)
1191	$7.0447e-08$ (3.91)	$3.8372e-08$ (3.91)	$7.0128e-08$ (3.37)	$3.2612e-07$ (2.79)
4423	$4.5073e-09$ (3.97)	$2.4766e-09$ (3.95)	$7.1729e-09$ (3.29)	$4.8921e-08$ (2.74)
17031	$2.8458e-10$ (3.99)	$1.5773e-10$ (3.97)	$7.6996e-10$ (3.22)	$7.5423e-09$ (2.70)
66823	$1.7869e-11$ (3.99)	$9.9888e-12$ (3.98)	$8.5371e-11$ (3.17)	$1.1833e-09$ (2.67)
			$\frac{2\nu}{\mu} \approx 3.117$	$\frac{2\nu}{\mu} \approx 2.637$

Table 3.5: Approximation errors $\|u - u_h\|_{L^2(\Omega)}$ (and corresponding EOC) for Example 3.39 using graded refinement for NURBS of degree $p = 3$ and different grading parameters μ.

$\boldsymbol{c}_{(i_1,i_2)}$	$i_2=1$	$i_2=2$	$i_2=3$	$i_2=4$	$i_2=5$	$i_2=6$	$i_2=7$
$i_1=1$	$(0,0)^T$	$(0,0)^T$	$(0,0)^T$	$(0,0)^T$	$(0,0)^T$	$(0,0)^T$	$(0,0)^T$
$i_1=2$	$(1,0)^T$	$(1,1)^T$	$(0,1)^T$	$(-1,1)^T$	$(-1,0)^T$	$(-1,-1)^T$	$(0,-1)^T$

Table 3.6: Definition of control points $\boldsymbol{c_i}$, $\boldsymbol{i} \in \boldsymbol{I}$, for a polar parameterization of the Quasi-Pacman domain.

$w_{(i_1,i_2)}$	$i_2=1$	$i_2=2$	$i_2=3$	$i_2=4$	$i_2=5$	$i_2=6$	$i_2=7$
$i_1=1$	1	$\frac{1}{\sqrt{2}}$	1	$\frac{1}{\sqrt{2}}$	1	$\frac{1}{\sqrt{2}}$	1
$i_1=2$	1	$\frac{1}{\sqrt{2}}$	1	$\frac{1}{\sqrt{2}}$	1	$\frac{1}{\sqrt{2}}$	1

Table 3.7: Definition of weights $w_{\boldsymbol{i}}$, $\boldsymbol{i} \in \boldsymbol{I}$, for a polar parameterization of the Quasi-Pacman domain.

homogeneous Neumann BCs on the re-entrant edges. With the right-hand side $f : \Omega \to \mathbb{R}$, $f(x,y) = \hat{f}(r,\varphi) = -r^{\nu-1}\cos(\nu\varphi)(-2\nu-1)$, with $\nu = \frac{\pi}{\omega} = \frac{3}{5}$, we obtain the solution

$$u : \Omega \to \mathbb{R}, \quad u(x,y) = \hat{u}(r,\varphi) = r^{\nu}\cos(\nu\varphi)(1-r),$$

which has the required regularity (2.4). Note that this is not always the case when Neumann BCs are considered at the corner, however, in the present setting, the solution has the required properties by construction. In Figure 3.14a, we illustrate a numerical approximation with cubic NURBS on a graded mesh, obtained after subdividing each of the coarse mesh elements shown in Figure 3.1b four times in radial direction and one time in angular direction. Note that the function and the corresponding mesh lines are visualized in the style of a surface plot. The $H^1(\Omega)$- and $L^2(\Omega)$-errors are plotted for decreasing mesh size h in Figures 3.14b and 3.14c, using both uniform and graded meshes. Again, graded meshes recover optimal rates, as expected from the approximation error estimate in Corollary 3.24.

Finally, we investigate the impact of the C^0-lines at the interfaces of the coarse mesh elements. Compared with the Quasi-Pacman domain from the previous example, which is based on a global C^2-parameterization and deals with a similar singularity, we observe no loss in convergence. Moreover, in Figure 3.15, we display the errors for C^0- and C^{p-1}-smooth NURBS, where higher continuity is only present within the coarse elements. The results clearly show that increased smoothness – although not global – leads to significantly smaller error constants per degree of freedom, both in the energy and L^2-norm. Since the space of C^0-splines on the parametric domain coincides with the classical finite element space, this demonstrates an advantage of our method over classical FEM, in addition to the benefit of exact representation of circular geometries.

Example 3.42 (**L-shaped domain, comparison with adaptive hierarchical refinement**). Finally, we solve the Poisson equation on the L-shaped domain, parameterized as explained in Example 3.8. We compare the results of our mesh grading approach with the adaptive hierarchical refinement available in GeoPDEs [GV18], where the domain is represented by two trapezoidal patches connected with C^0-coupling.

Case 1: mild singularity We first consider an example from the literature, see [BGKV20, Section 5, Example 1], namely the approximation of the function

$$u : \Omega \to \mathbb{R}, \quad u(x,y) = \hat{u}(r,\varphi) = r^{\nu}\sin(\nu\varphi)$$

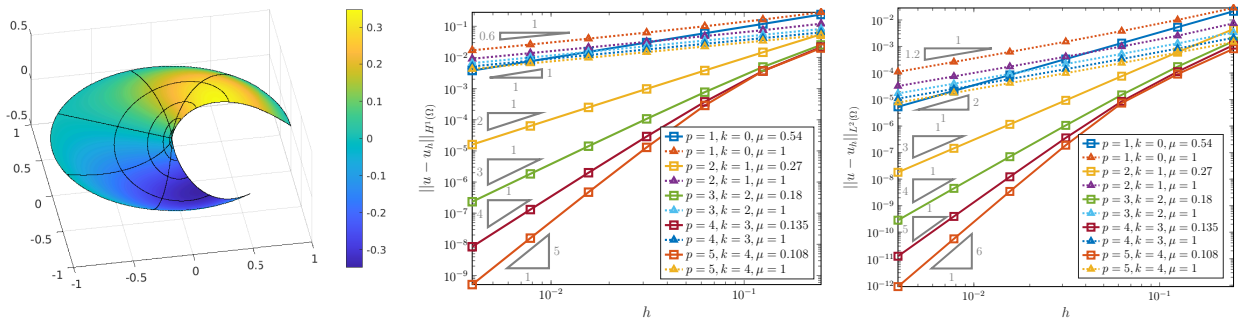

(a) (b) (c)

Figure 3.14: Solving the Poisson equation on the Pacman domain: (a): Surface plot of an approximation on a graded mesh for bicubic NURBS. (b): $H^1(\Omega)$-error of the approximation. (c): $L^2(\Omega)$-error of the approximation.

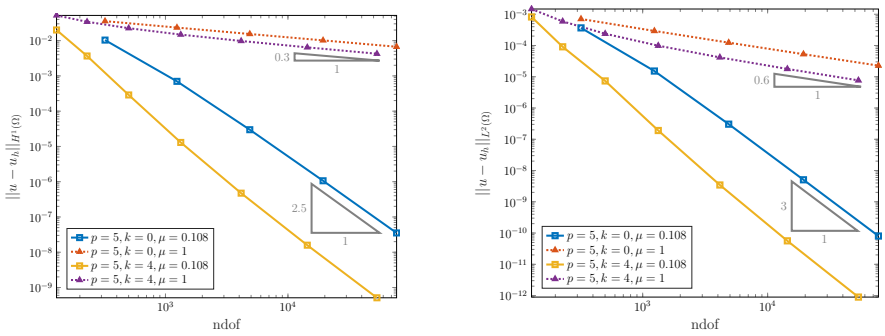

(a) (b)

Figure 3.15: Solving the Poisson equation on the Pacman domain with smoothness $k = 0$ and $k = p-1$: (a): $H^1(\Omega)$-error of the approximation. (b): $L^2(\Omega)$-error of the approximation.

with the mild singular exponent $\nu = \frac{4}{3}$. Similar to the mentioned paper, the adaptive simulation starts from a coarse 4×4 mesh on each patch with Dörfler's parameter equal to 0.9 for the marking of the elements. A numerical solution on a graded mesh and the $H^1(\Omega)$- and $L^2(\Omega)$-errors for both methods versus the number of degrees of freedom are shown in Figure 3.16, where we note that $h^{-2} \sim \text{ndof}$ holds. Both approaches achieve the expected convergence rates of $\frac{p}{2}$ in $H^1(\Omega)$ and $\frac{p+1}{2}$ in $L^2(\Omega)$, with the adaptive method slightly more accurate per degree of freedom. However, memory limitations in the hierarchical GeoPDEs implementation prevent computations with very large numbers of degrees of freedom, whereas fine graded meshes are easily generated in our approach. Although this is not a strict performance comparison – GeoPDEs may not be optimized for hierarchical splines – it illustrates the simplicity and efficiency of our mesh grading scheme.

Case 2: strong singularity and mixed boundary conditions As a second test case, we consider mixed BC at the re-entrant corner and homogeneous Dirichlet BC elsewhere, i.e., we have the strong singular exponent $\nu = \frac{1}{3}$. The right-hand side is chosen as

$$f : \Omega \to \mathbb{R}, \quad f(x, y) = \hat{f}(r, \varphi) = r^\nu \left((4 + 4\nu - 2r^2 - \nu r^2) \sin(\nu\varphi) + \nu r^2 \sin(\varphi(\nu - 4)) \right),$$

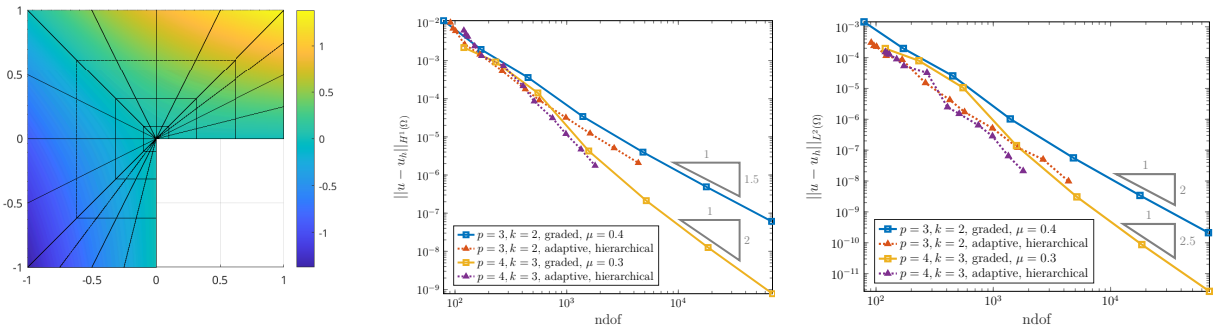

(a) (b) (c)

Figure 3.16: Solving the Poisson equation with a weak singular exponent on the L-shaped domain with graded and adaptive hierarchical refinement: (a): Plot of the numerical solution on a graded mesh for biquadratic NURBS. (b): $H^1(\Omega)$-error of the approximation. (c): $L^2(\Omega)$-error of the approximation.

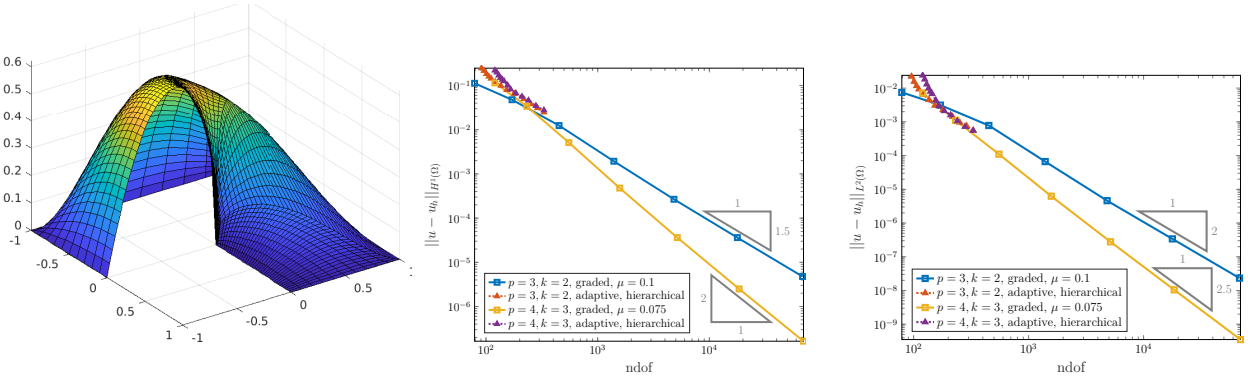

(a) (b) (c)

Figure 3.17: Solving the Poisson equation with a strong singular exponent on the L-shaped domain with graded and adaptive hierarchical refinement: (a): Plot of the exact solution, where some mesh lines are inserted for visualization purposes. (b): $H^1(\Omega)$-error of the approximation. (c): $L^2(\Omega)$-error of the approximation.

which yields the manufactured solution

$$u : \Omega \to \mathbb{R}, \quad u(x, y) = \hat{u}(r, \varphi) = r^\nu \sin(\nu\varphi)(1 - r^2 + r^4 \cos^2(\varphi) \sin^2(\varphi)).$$

The identity $(1 - x)(1 + x)(1 - y)(1 + y) = 1 - r^2 + r^4 \cos^2 \varphi \sin^2 \varphi$ ensures that $u = 0$ on Γ_2. As discussed in Section 2.1.2, the solution satisfies $u \in V^s_\beta(\Omega)$ for all $(s, \beta) \in \mathbb{N} \times \mathbb{R}$ with $s - 1 - \nu < \beta < s - 1 + \nu$. A surface plot of the exact solution is shown in Figure 3.17a, where some mesh lines are inserted for visualization purposes.

Figures 3.17b and 3.17c report the $H^1(\Omega)$- and $L^2(\Omega)$-errors versus the number of degrees of freedom for both methods. In this case, adaptive hierarchical refinement struggles to reproduce the optimal convergence rates achieved by graded meshes. In addition, our method allows straightforward computations on very fine meshes, yielding very small absolute errors, which were not attainable with the adaptive refinement.

We end our series of numerical results with a variation of the Poisson equation in which a jumping material coefficient is considered. This also leads to a typical corner singularity of the solution, but

with a different singular exponent than in the previous cases. More precisely, we investigate the configuration described in [Nic93, Example 2.29].

Example 3.43. The overall domain is a circular sector with opening angle $\omega = \frac{3}{2}\pi$, which is now decomposed into two subdomains,

$$\Omega_1 = \{r(\cos\varphi, \sin\varphi) : r \in (0,1),\ \varphi \in (\sigma_0, \sigma_1)\}, \quad \Omega_2 = \{r(\cos\varphi, \sin\varphi) : r \in (0,1),\ \varphi \in (\sigma_1, \sigma_2)\},$$

where we choose $\sigma_0 = 0$, $\sigma_1 = \frac{1}{2}\pi$ and $\sigma_2 = \frac{3}{2}\pi$. On these subdomains we consider two separate Laplace equations with the coefficients $\kappa_1 = 10^4$ and $\kappa_2 = 1$, together with suitable interface and boundary conditions,

$$\begin{aligned} \kappa_i \Delta u_i &= 0 && \text{in } \Omega_i,\ i = 1,2, \\ u_1 &= u_2 && \text{on } \Sigma, \\ \kappa_1 \frac{\partial \hat{u}_1}{\partial \varphi} &= \kappa_2 \frac{\partial \hat{u}_2}{\partial \varphi} && \text{on } \Sigma, \\ u_i &= 0 && \text{on } \Gamma_{D_0,i},\ i = 1,2, \\ u_i &= g && \text{on } \Gamma_{D_g,i},\ i = 1,2. \end{aligned}$$

The interface between both subdomains is given by

$$\Sigma = \{r(\cos\varphi, \sin\varphi) : r \in (0,1),\ \varphi = \sigma_1\}$$

and the homogeneous Dirichlet boundaries are defined as the re-entrant edges,

$$\Gamma_{D_0,1} = \{r(\cos\varphi, \sin\varphi) : r \in (0,1),\ \varphi = \sigma_0\}, \quad \Gamma_{D_0,2} = \{r(\cos\varphi, \sin\varphi) : r \in (0,1),\ \varphi = \sigma_2\}.$$

The circular non-homogeneous Dirichlet boundary is denoted by

$$\Gamma_{D_g,1} = \{r(\cos\varphi, \sin\varphi) : r = 1,\ \varphi \in (\sigma_0, \sigma_1)\}, \quad \Gamma_{D_g,2} = \{r(\cos\varphi, \sin\varphi) : r = 1,\ \varphi \in (\sigma_1, \sigma_2)\},$$

and the data g is derived from the exact solution

$$\hat{u}(r,\varphi) = \begin{cases} \hat{u}_1(r,\varphi) = r^\nu D_1 \sin(\nu(\varphi - \sigma_0)) & \text{if } \varphi \in (\sigma_0, \sigma_1), \\ \hat{u}_2(r,\varphi) = r^\nu (C_2 \cos(\nu(\varphi - \sigma_1)) + D_2 \sin(\nu(\varphi - \sigma_1))) & \text{if } \varphi \in (\sigma_1, \sigma_2). \end{cases} \tag{3.72}$$

Here, the constants C_2, D_1, D_2 are chosen such that the boundary and interface conditions are satisfied, leading to the linear system

$$\begin{aligned} C_2 \cos(\nu\,\omega_2) + D_2 \sin(\nu\,\omega_2) &= 0, \\ C_2 - D_1 \sin(\nu\,\omega_1) &= 0, \\ D_2 - \frac{\kappa_1}{\kappa_2} D_1 \cos(\nu\,\omega_1) &= 0, \end{aligned}$$

where $\omega_1 = \sigma_1 - \sigma_0 = \frac{\pi}{2}$ and $\omega_2 = \sigma_2 - \sigma_1 = \pi$. This homogeneous system admits a nontrivial solution if and only if the associated coefficient matrix is singular. We denote the corresponding determinant by $D_2^D(\nu)$, and obtain the characteristic equation

$$D_2^D(\nu) = \kappa_2 \cos(\nu\omega_2)\sin(\nu\omega_1) + \kappa_1 \sin(\nu\omega_2)\,\cos(\nu\omega_1) = 0, \tag{3.73}$$

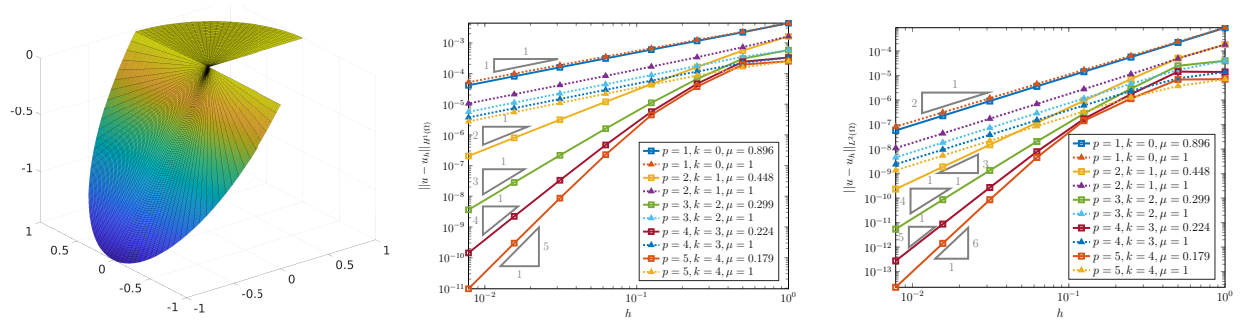

(a) (b) (c)

Figure 3.18: Solving the Poisson equation on a circular sector with a jumping material coefficient: (a): Exact solution, with selected mesh lines added for visualization. (b): $H^1(\Omega)$-error of the approximation. (c): $L^2(\Omega)$-error of the approximation.

which determines the singular exponent ν. We are particularly interested in the smallest positive solution of (3.73). To this end, we substitute $a = \nu\frac{\pi}{2}$, that is, $\nu = \frac{2}{\pi}a$, in equation (3.73), and it follows

$$D_2^D(\nu) = \cos(2a)\sin(a) + 10000\sin(2a)\cos(a) = 0.$$

By applying the trigonometric identities $\cos(2a) = \cos^2(a) - \sin^2(a)$ and $\sin(2a) = 2\sin(a)\cos(a)$, we obtain

$$D_2^D(\nu) = \sin(a)(\cos^2(a) - \sin^2(a)) + 20000\sin(a)\cos^2(a) = \sin(a)((20002)\cos^2(a) - 1).$$

Hence, it is either $a = n\pi$ or $a = \arccos\left(\frac{1}{\sqrt{20002}}\right)$, and therefore the smallest singular exponent is

$$\nu = \frac{2}{\pi}\arccos\left(\frac{1}{\sqrt{20002}}\right) \approx 0.9955.$$

Consequently, we have $\nu \notin \mathbb{N}$, even though the difference to 1 is quite small. Nevertheless, this implies that the exact solution (3.72) exhibits a corner singularity. It is plotted in Figure 3.18a and, by construction, satisfies the weighted regularity property (2.4).

For the discretization of the domain, we use the knot vectors described in Example 3.6. In this case, it is specifically advantageous that the discretization inherently enforces C^0-continuity across the interface Σ. In Figures 3.12b and 3.12c, we report the $H^1(\Omega)$- and $L^2(\Omega)$-errors for decreasing mesh size h, using both uniform and graded meshes with grading parameters $\mu = 1$ and $\mu = 0.9\frac{\nu}{p}$, respectively. We observe that graded meshes recover the optimal convergence rates also for this variation of our standard model problem.

3.6 Graded collocation toward polar corners

Finally, we transfer the idea of graded mesh refinement toward polar corners to the framework of isogeometric collocation.

3.6.1 Construction of graded collocation points

Let Ω be a polar domain with corner, as described in Section 3.2.1, constructed from the coarse knot vectors Ξ_l^0, $l = 1, 2$. The most common approach to define isogeometric collocation points required

for the formulation (2.14) is to use the Greville abscissae (GA) of both knot vectors, as introduced in Section 2.2, combine them by a tensor product approach and map them to the physical domain via the parameterization $\boldsymbol{F}$. To obtain more accurate approximations, the knot vectors are refined with standard refinement algorithms, resulting in uniform p_l-open knot vectors Ξ_l^{u}, $l = 1, 2$, and the GA of the refined knot vectors are computed, which we denote by $\gamma_{l,j_l,p_l}^{\mathrm{u}}$, $j_l = 1, \dots, n_l$, $l = 1, 2$. As we always consider open knot vectors, we have $\gamma_{l,1,p_l}^{\mathrm{u}} = 0$ and $\gamma_{l,n_l,p_l}^{\mathrm{u}} = 1$, whereas all other points lie in $(0, 1)$. The final collocation points are then given by

$$\boldsymbol{\tau}_{(j_1,j_2)}^{\mathrm{u}} = \boldsymbol{F}(\widehat{\tau}_{(j_1,j_2)}^{\mathrm{u}}), \quad \widehat{\tau}_{(j_1,j_2)}^{\mathrm{u}} = (\gamma_{1,j_1,p_1}^{\mathrm{u}}, \gamma_{2,j_2,p_2}^{\mathrm{u}}), \quad j_l = 1, \dots, n_l, \ l = 1, 2. \tag{3.74}$$

Here, $\boldsymbol{\tau}_{(j_1,j_2)}^{\mathrm{u}} \in \Omega$, $j_l = 2, 3, \dots, n_l - 1$, are collocation points in the interior of the physical domain, while the remaining points lie on its boundary Γ. In Figure 3.19a, we illustrate this construction for a circular sector with angle $\omega = \frac{2}{3}\pi$, which is parameterized by the polar mapping described in Example 3.6. The visualization is inspired by [Aur+10].

Now, as in the Galerkin framework, the standard collocation method does not yield optimal convergence rates when approximating PDE solutions with corner singularities. In analogy to local mesh refinement, where mesh elements are accumulated near the corner, it is therefore natural to strengthen the concentration of collocation points in the vicinity of the singularity.

To this end, we can also employ the graded mesh refinement approach proposed in Section 3.2.2. As explained therein, a locally refined Bézier mesh can be constructed by replacing the knot vector Ξ_1^{u} with the graded one Ξ_1. Therefore, in the first step, we replace the uniform NURBS basis used for the collocation ansatz (2.13) by a graded basis constructed from the graded knot vector Ξ_1. In the second step, we employ the GA of the graded knot vector, denoted by γ_{1,j_1,p_1}, $j_l = 1, \dots, n_l$, for the construction of the collocation points. More precisely, by definition of the Greville abscissae (2.21) and the graded knot vector (3.10), we have

$$\gamma_{1,j_1,p_1} = \frac{1}{p_1}\left((\xi_{1,j_1+1}^{\mathrm{u}})^{\frac{1}{\mu}} + \cdots + (\xi_{1,j_1+p_1}^{\mathrm{u}})^{\frac{1}{\mu}}\right), \quad j_1 = 1, \dots, n_1.$$

Note that reversing this procedure, i.e., first constructing the uniform Greville abscissae and subsequently applying the grading, leads to poor numerical performance. In the second parametric direction, the mesh is not graded, and we employ the usual uniform Greville abscissae $\gamma_{2,j_2,p_2} = \gamma_{2,j_2,p_2}^{\mathrm{u}}$, $j_2 = 1, \dots, n_2$. The resulting graded collocation points are then given by

$$\boldsymbol{\tau}_{(j_1,j_2)} = \boldsymbol{F}(\widehat{\tau}_{(j_1,j_2)}), \quad \widehat{\tau}_{(j_1,j_2)} = (\gamma_{1,j_1,p_1}, \gamma_{2,j_2,p_2}), \quad j_l = 1, \dots, n_l, \ l = 1, 2. \tag{3.75}$$

Since the polar parameterization $\boldsymbol{F}$ collapses the left edge of the parametric domain onto the polar corner $\boldsymbol{P}$, the resulting set of collocation points is strongly concentrated in the vicinity of the corner. This effect is illustrated in Figure 3.19b for the circular sector with angle $\omega = \frac{2}{3}\pi$. In the following, the collocation points defined in (3.75) are referred to as graded GA, whereas the classical points in (3.74) are called uniform GA. In analogy with the Galerkin framework, uniform GA correspond to graded GA with $\mu = 1$, so that the latter can be viewed as a generalization of the standard construction.

In general, the approximation of smooth PDE solutions based on isogeometric collocation with GA exhibits lower convergence orders than corresponding Galerkin methods [Aur+10]. This observation has motivated the investigation of alternative choices of collocation points in the literature. Particularly notable are clustered superconvergent points (CSP), as they achieve convergence orders comparable to Galerkin methods for odd NURBS degrees [MST17].

The construction of CSP is rather technical and is therefore omitted here. Details can be found in [MST17] and the references cited therein. For our purposes, it suffices to note that the construction

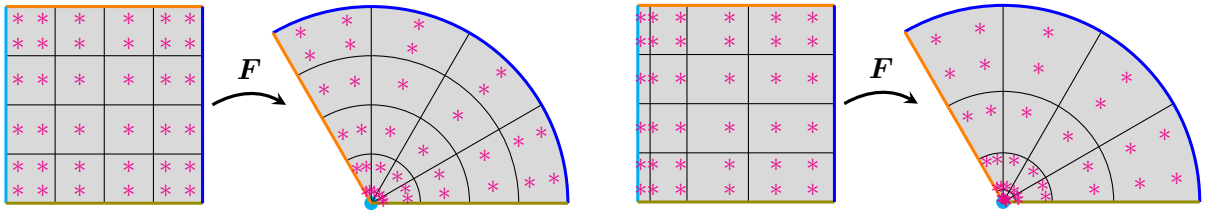

(a) (b)

Figure 3.19: Bézier meshes and associated interior GA collocation points (3.75), shown as asterisks, for quartic NURBS defined by the knot vectors Ξ_1 and $\Xi_2 = \{0,0,0,0,0,\frac{1}{4},\frac{1}{2},\frac{3}{4},1,1,1,1,1\}$. (a): Uniform GA ($\mu = 1$): $\Xi_1 = \{0,0,0,0,0,\frac{1}{4},\frac{1}{2},\frac{3}{4},1,1,1,1,1\}$. (b): Graded GA ($\mu < 1$): $\Xi_1 = \{0,0,0,0,0,\frac{1}{16},\frac{1}{4},\frac{9}{16},1,1,1,1,1\}$. The 28 collocation points on the boundary are not shown.

	Galerkin	Collocation - GA		Collocation - CSP	
		odd p	even p	odd p	even p
L^2-norm	$p+1$	$p-1$	p	$p+1$	p
H^1-norm	p	$p-1$	p	p	p

Table 3.8: Convergence rates for the approximation of smooth PDE solutions with isogeometric collocation methods [MST17].

is likewise based on the underlying knot vectors. Hence, in the spirit of the graded GA approach described above, we introduce graded clustered superconvergent points by replacing the knot vector in the first direction with its graded counterpart and computing the CSP with respect to the graded knot vector. Similar to the graded GA, the resulting graded CSP are locally concentrated near the polar corner.

3.6.2 Numerical tests

To the best of our knowledge, a general approximation theory for two-dimensional isogeometric collocation methods is currently not available [Aur+10]. Hence, it is far beyond the limits of this dissertation to establish a theoretical basis for graded collocation toward polar corners. Instead, we present two numerical examples illustrating the performance of graded collocation and assessing the choice of the grading parameter. Since the basis functions used in (2.13) are required to be at least C^2-continuous, and the maximum smoothness of splines of degree p is C^{p-1}, one typically considers splines of degree $p \geq 3$.

As mentioned above, the achievable convergence rates in the collocation setting differ from those in the Galerkin framework. In particular, they depend on the parity of the NURBS degree and on the choice of collocation points. Table 3.8 summarizes the convergence rates reported in the literature for the approximation of smooth solutions using standard isogeometric collocation with GA and CSP [Aur+10; MST17]. For collocation with NURBS of degree p and GA, the approximation order is $p-1$ for odd p and p for even p, both in the $H^1(\Omega)$- and $L^2(\Omega)$-norms. In contrast, for CSP and odd p, the convergence rates are p in the $H^1(\Omega)$-norm and $p+1$ in the $L^2(\Omega)$-norm, corresponding to the optimal Galerkin order, while for even p the convergence rate is p in both norms.

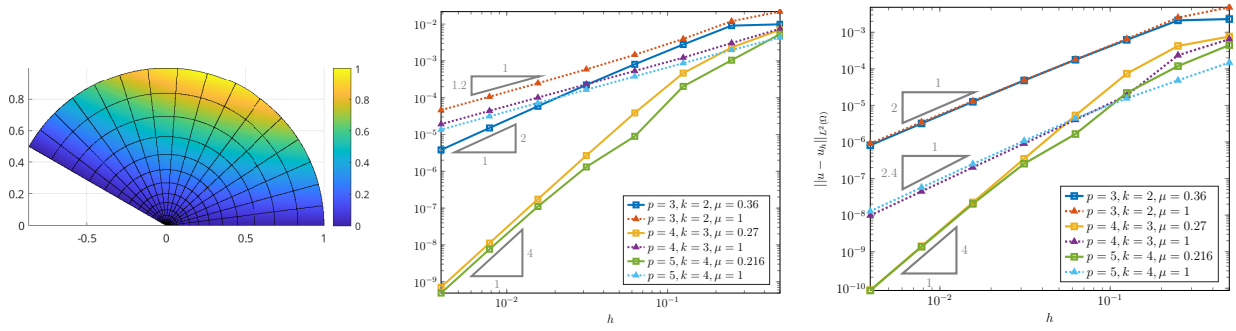

(a) (b) (c)

Figure 3.20: Solving Example 3.44 using uniform and graded collocation with GA: (a): Plot of a numerical solution on a graded mesh with 16 subdivisions for bicubic NURBS. (b): $H^1(\Omega)$-error of the approximation. (c): $L^2(\Omega)$-error of the approximation.

Note that the approximation errors in this section are plotted with respect to the mesh size, although collocation is not strictly a mesh-based method. Nevertheless, the collocation points are constructed with respect to the underlying mesh, and the mesh size is denoted by h, as in the Galerkin framework, see Section 3.4.1. Moreover, the numerical examples include inhomogeneous boundary conditions, which are not considered in the model problem (2.3) and therefore do not appear in the collocation formulation (2.14). However, they can be incorporated following standard procedures, see, for instance, [Aur+10].

Example 3.44. First, we consider a circular sector with angle $\omega = \frac{5}{6}\pi$. As test problem, we consider the Poisson equation with homogeneous Dirichlet BC at the straight edges and inhomogeneous BC on the circular arc, induced by the exact solution

$$u : \Omega \to \mathbb{R}, \quad u(x, y) = \hat{u}(r, \varphi) = r^\nu \sin(\nu\varphi)$$

with $\nu = \frac{6}{5}$. Figure 3.20a shows a collocation solution computed with bicubic NURBS and GA corresponding to the displayed graded mesh with 16 subdivisions in each parametric direction. As discussed in Section 2.1.2, the solution exhibits a singularity of type r^ν and satisfies the regularity property (2.4).

We plot the $H^1(\Omega)$- and $L^2(\Omega)$-errors of the collocation approximations using GA in Figures 3.20b and 3.20c. For each NURBS degree p, we consider maximally smooth splines with both uniform and graded GA, corresponding to grading parameters $\mu = 1$ and $\mu = 0.9\frac{\nu}{p}$, respectively. For uniform collocation, the accuracy is governed by the singularity and approaches convergence orders of ν and 2ν, independently of the polynomial degree, in the $H^1(\Omega)$- and $L^2(\Omega)$-norms, respectively. Only for the odd degree $p = 3$ is the full L^2-rate of $p - 1$ attained, since $p - 1 = 2 < 2\nu = \frac{12}{5}$. In contrast, graded meshes recover the expected convergence rates for GA provided in Table 3.8. In Figures 3.21a and 3.21b, we repeat the experiment using uniform and graded CSP. Again, uniform meshes yield suboptimal approximation rates, whereas graded meshes recover the convergence orders listed in Table 3.8.

Since no theoretical analysis is currently available for graded collocation, we additionally investigate the influence of the grading parameter numerically. For GA, we report the $H^1(\Omega)$-errors using NURBS of degree $p \in \{4, 5\}$ and grading parameters $\mu \in \{0.7\frac{\nu}{p}, 0.9\frac{\nu}{p}, 1.1\frac{\nu}{p}, 1.3\frac{\nu}{p}\}$ in Tables 3.9 and 3.10, together with the corresponding experimental orders of convergence (EOC). The results indicate that the condition (3.48) on the grading parameter in the Galerkin framework is also

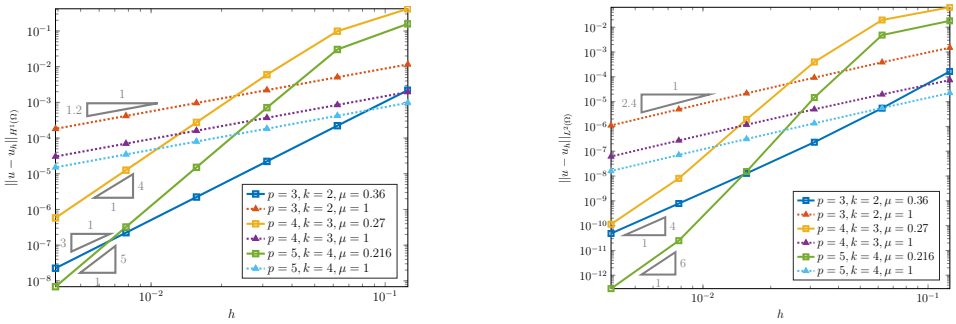

(a) (b)

Figure 3.21: Solving Example 3.44 using uniform and graded collocation with CSP: (a): $H^1(\Omega)$-error of the approximation. (b): $L^2(\Omega)$-error of the approximation.

appropriate for collocation. An excessively small choice of μ reduces the approximation constant, while values of μ that violate condition (3.48) lead to a loss of convergence, thereby supporting our standard choice (3.51). In the latter case, at least for the even degree $p = 4$, we conjecture that the reduced convergence rate is given by $\frac{\nu}{\mu}$, in analogy with the behavior observed for graded Galerkin methods; see Remark 3.35. Accordingly, the expected reduced rates are listed in the last row of the table. For CSP, the corresponding study is presented in Table 3.11 for $p = 3$. Again, optimal convergence rates are observed for $\mu < \frac{\nu}{p}$, whereas larger values result in suboptimal approximation behavior, which we likewise conjecture to follow a rate of $\frac{\nu}{\mu}$. Moreover, for our preferred choice $\mu = 0.9\frac{\nu}{p}$, we observe a slightly higher convergence rate than expected from the polynomial degree. At present, we cannot provide a theoretical explanation for this effect. It may be attributed to pre-asymptotic behavior or to superconvergence phenomena specific to this example. With respect to the $L^2(\Omega)$-norm, less restrictive grading parameters may also yield optimal convergence. However, we do not pursue this aspect further here, as our primary focus lies on optimal approximation in the $H^1(\Omega)$-norm. A systematic study of optimized grading strategies for convergence in the $L^2(\Omega)$-norm remains an interesting topic for future research, both in the Galerkin and collocation frameworks; see also the discussion in Example 3.39.

Example 3.45. We continue by studying the Poisson equation on a singularly parametrized triangle with vertices $\left(-0.5, \frac{\sqrt{3}}{2}\right), (1, 0)$, and the polar corner at $(0, 0)$, forming an interior polar angle of $\omega = \frac{2}{3}\pi$. As test problem, we consider the Poisson equation with mixed homogeneous BC at the polar corner and non-homogeneous Dirichlet BC at the remaining edge, derived from the exact solution

$$u : \Omega \to \mathbb{R}, \quad u(x, y) = \hat{u}(r, \varphi) = r^\nu \sin(\nu\varphi).$$

with $\nu = \frac{3}{4}$. Figure 3.22a shows a numerical solution computed with bicubic NURBS. The graded mesh with 16 subdivisions in each parametric direction, with respect to which the Greville abscissae are constructed, is also displayed. As discussed in Section 2.1.2, the solution exhibits a singularity of type r^ν and satisfies the regularity property (2.4). Due to the stronger singularity compared to Example 3.44 and the resulting small grading parameters, particularly for larger p, many graded collocation points are located very close to the polar corner $\boldsymbol{P}$, see Figure 3.19a. As a consequence, the collocation matrix (2.16) is reported by the GeoPDEs implementation to be nearly singular. Hence, solving the linear collocation system (2.15) with a direct solver becomes more delicate, as rounding errors may significantly affect the numerical results. However, this issue can be effectively

ndof	$\mu = 0.7\frac{\nu}{p} = 0.21$	$\mu = 0.9\frac{\nu}{p} = 0.27$	$\mu = 1.1\frac{\nu}{p} = 0.33$	$\mu = 1.3\frac{\nu}{p} = 0.39$
36	$9.4443e-03$	$7.0182e-03$	$5.4118e-03$	$4.7894e-03$
64	$1.9444e-03$ (2.28)	$2.3109e-03$ (1.60)	$2.3640e-03$ (1.19)	$2.2391e-03$ (1.10)
144	$7.9842e-04$ (1.28)	$4.6580e-04$ (2.31)	$3.2316e-04$ (2.87)	$2.6716e-04$ (3.07)
400	$6.9746e-05$ (3.52)	$3.8722e-05$ (3.59)	$3.0675e-05$ (3.40)	$3.1915e-05$ (3.07)
1296	$4.6403e-06$ (3.91)	$2.6828e-06$ (3.85)	$2.6505e-06$ (3.53)	$3.7837e-06$ (3.08)
4624	$2.9572e-07$ (3.97)	$1.7557e-07$ (3.93)	$2.2121e-07$ (3.58)	$4.4835e-07$ (3.08)
17424	$1.8637e-08$ (3.99)	$1.1224e-08$ (3.97)	$1.8162e-08$ (3.61)	$5.3132e-08$ (3.08)
67600	$1.1695e-09$ (3.99)	$7.0965e-10$ (3.98)	$1.4782e-09$ (3.62)	$6.2965e-09$ (3.08)
			$\frac{\nu}{\mu} \approx 3.636$	$\frac{\nu}{\mu} \approx 3.077$

Table 3.9: Approximation errors $\|u - u_h\|_{H^1(\Omega)}$ (and corresponding EOC) for Example 3.44 using graded collocation with GA, NURBS degree $p = 4$ and different grading parameters μ.

ndof	$\mu = 0.7\frac{\nu}{p} = 0.168$	$\mu = 0.9\frac{\nu}{p} = 0.216$	$\mu = 1.1\frac{\nu}{p} = 0.264$	$\mu = 1.3\frac{\nu}{p} = 0.312$
49	$7.0594e-03$	$5.3325e-03$	$3.6476e-03$	$2.3017e-03$
81	$9.4774e-04$ (2.90)	$1.0453e-03$ (2.35)	$1.1518e-03$ (1.66)	$1.0380e-03$ (1.15)
169	$4.4795e-04$ (1.08)	$2.0297e-04$ (2.36)	$1.1509e-04$ (3.32)	$8.8559e-05$ (3.55)
441	$1.1543e-05$ (5.28)	$8.9380e-06$ (4.51)	$8.2603e-06$ (3.80)	$8.4056e-06$ (3.40)
1369	$2.2094e-06$ (2.39)	$1.3139e-06$ (2.77)	$9.3778e-07$ (3.14)	$8.7012e-07$ (3.27)
4761	$2.1042e-07$ (3.39)	$1.1083e-07$ (3.57)	$7.7680e-08$ (3.59)	$7.6714e-08$ (3.50)
17689	$1.4869e-08$ (3.82)	$7.6399e-09$ (3.86)	$5.5236e-09$ (3.81)	$6.1649e-09$ (3.64)
68121	$9.6248e-10$ (3.95)	$4.9222e-10$ (3.96)	$3.6673e-10$ (3.91)	$4.7129e-10$ (3.71)

Table 3.10: Approximation errors $\|u - u_h\|_{H^1(\Omega)}$ (and corresponding EOC) for Example 3.44 using graded collocation with GA, NURBS degree $p = 5$ and different grading parameters μ.

ndof	$\mu = 0.7\frac{\nu}{p} = 0.28$	$\mu = 0.9\frac{\nu}{p} = 0.36$	$\mu = 1.1\frac{\nu}{p} = 0.44$	$\mu = 1.3\frac{\nu}{p} = 0.52$
121	$1.7388e-03$	$2.1964e-03$	$3.2777e-03$	$4.6822e-03$
361	$1.0114e-04$ (4.10)	$2.2245e-04$ (3.30)	$4.9844e-04$ (2.72)	$9.4969e-04$ (2.30)
1225	$6.6712e-06$ (3.92)	$2.2254e-05$ (3.32)	$7.5327e-05$ (2.73)	$1.9188e-04$ (2.31)
4489	$5.9459e-07$ (3.49)	$2.2267e-06$ (3.32)	$1.1376e-05$ (2.73)	$3.8756e-05$ (2.31)
17161	$6.6994e-08$ (3.15)	$2.2358e-07$ (3.32)	$1.7179e-06$ (2.73)	$7.8280e-06$ (2.31)
67081	$8.1778e-09$ (3.03)	$2.2584e-08$ (3.31)	$2.5942e-07$ (2.73)	$1.5811e-06$ (2.31)
			$\frac{\nu}{\mu} \approx 2.727$	$\frac{\nu}{\mu} \approx 2.308$

Table 3.11: Approximation errors $\|u - u_h\|_{H^1(\Omega)}$ (and corresponding EOC) for Example 3.44 using graded collocation with CSP, NURBS degree $p = 3$ and different grading parameters μ.

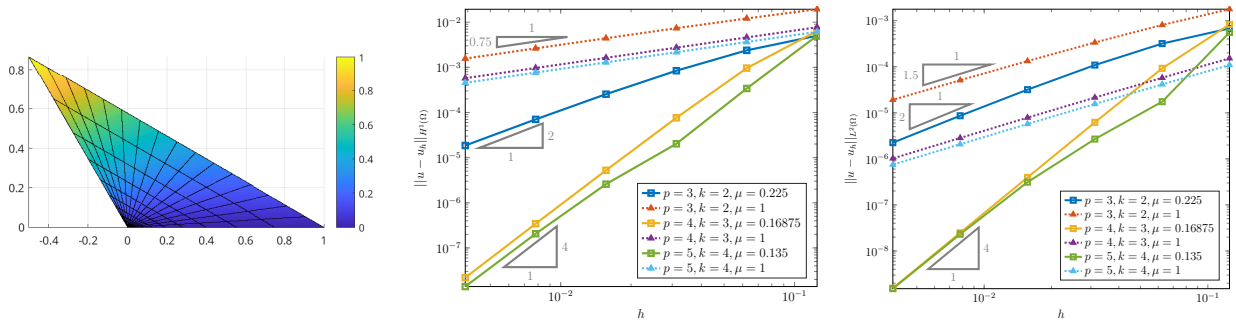

(a) (b) (c)

Figure 3.22: Solving Example 3.45 using graded collocation with GA: (a): Plot of a numerical solution on a graded mesh with 16 subdivisions for bicubic NURBS. (b): $H^1(\Omega)$-error of the approximation. (c): $L^2(\Omega)$-error of the approximation.

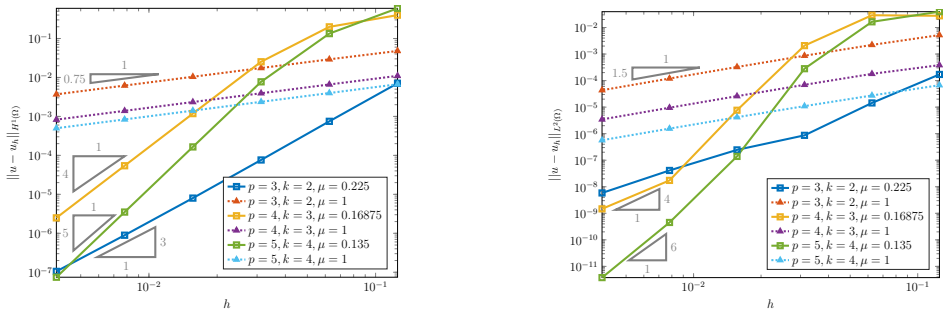

(a) (b)

Figure 3.23: Solving Example 3.45 using graded collocation with CSP: (a): $H^1(\Omega)$-error of the approximation. (b): $L^2(\Omega)$-error of the approximation.

mitigated by applying iterative refinement [Wil63], which we employed for all computations in this example.

We plot the $H^1(\Omega)$- and $L^2(\Omega)$-errors of the approximations versus decreasing mesh size h in Figures 3.22b and 3.22c. For each NURBS degree p, we consider maximally smooth NURBS for both uniform and graded GA, corresponding to grading parameters $\mu = 1$ and $\mu = 0.9\frac{\nu}{p}$, respectively. As in the previous example, the experimental convergence rates for uniform collocation are limited by ν and 2ν in the $H^1(\Omega)$- and $L^2(\Omega)$-norms. In contrast, the use of grading recovers the achievable convergence rates with GA, namely $p-1$ for the odd degrees $p \in \{3, 5\}$ and p for the even degree $p = 4$, both in the $H^1(\Omega)$- and $L^2(\Omega)$-norms.

Using CSP, we obtain the results shown in Figure 3.23. Again, graded collocation points yield a clear improvement in convergence. Figure 3.23a shows that grading recovers the H^1-convergence rates of p for odd p and $p-1$ for even p. However, for the higher polynomial degrees $p \in \{4, 5\}$, the absolute error on coarse meshes is considerably larger, so that substantial refinement is required before surpassing the accuracy obtained with $p = 3$. This behavior may be related to the condition number of the collocation matrix and requires further investigation, which is beyond the scope of this dissertation. Finally, Figure 3.23b shows that graded CSP also achieve the optimal L^2-convergence rates of $p+1$ and p for odd and even p, respectively.

3.6.3 Scope, limitations and outlook

We conclude this section by briefly discussing the scope, current limitations, and outlook for the proposed graded collocation approach.

Collocation methods employ high-degree smooth NURBS functions by default, since the PDE is required to be satisfied in the classical sense. Consequently, reduced solution regularity leads to a significant loss in the achievable convergence rate of standard collocation methods, making the treatment of corner singularities essential – even when the singularity is relatively mild, as in the numerical examples presented here. This effect becomes even more pronounced for higher-order problems. For instance, solving the biharmonic equation requires collocation spaces that are at least C^4-smooth, i.e., of degree $p \geq 5$.

In this context, a grading scheme can be incorporated into classical isogeometric collocation methods to increase the concentration of collocation points near corner singularities. The present approach should primarily be viewed as a proof of concept, demonstrating that ideas from graded mesh refinement in the Galerkin framework can be transferred naturally to isogeometric collocation. Although a corresponding approximation theory is not yet available, the method is straightforward to implement and numerically effective.

The graded collocation strategy introduced here is, however, subject to several restrictions. One limitation is that grading toward the polar corner restricts the admissible parameterizations: no C^0-lines are allowed, as these would produce basis functions not contained in $C^2(\overline{\Omega})$, which is incompatible with the collocation principle. In particular, circular sectors with opening angle $\omega > \pi$ cannot be treated; see Remark 3.9. This limitation could potentially be overcome by employing Tchebycheffian splines in the construction of the parameterization [RMS23; Spe22; Spe25].

Another restriction is that sufficient continuity of the basis functions at the polar corner is not guaranteed a priori and must be enforced depending on the boundary condition prescribed there. For simplicity, we therefore restrict our attention to the case of homogeneous Dirichlet BCs at the polar corner, so that no collocation points are placed there. The treatment of other BCs would require extending our approach to C^k-smooth polar splines with $k \geq 2$ [ST21; TSHH17].

CHAPTER 4

IGA of the Laplace eigenvalue problem on circular sectors

In this chapter, we apply the method developed in Section 3.2 to the Laplace eigenvalue problem (EVP) on circular sectors. The presentation builds on [AZ24a] and is complemented here by corresponding error estimates. Section 4.1 motivates the choice of this model problem and highlights the novel contributions of our work. In Section 4.2, we derive analytical solutions of the Laplace EVP on circular sectors and analyze the relevant regularity properties of the associated eigenfunctions. Section 4.3 establishes error estimates for the approximation of eigenvalues and eigenfunctions using graded mesh refinement toward the polar corner. Finally, in Section 4.4, we report numerical experiments that demonstrate optimal convergence rates, thereby confirming our theoretical results for this model eigenvalue problem. In addition, we show that smooth spline spaces are particularly advantageous on graded meshes when approximating a fixed number of eigenvalues. The combination with a hierarchical mesh structure is also investigated, which yields different computational results.

4.1 Motivation and novelties

The motivation for this chapter is partly based on Section 1 of [AZ24a]. The Laplace eigenvalue problem

$$-\Delta u = \lambda u \quad \text{in } \Omega$$

on arbitrary domains $\Omega \subset \mathbb{R}^d$, together with suitable boundary conditions, is of fundamental importance in numerous areas of applied mathematics. The resulting spectrum is crucial for many applications, e.g., because of the geometric information it encodes about the underlying domain [Kac66; RWP06]. An overview of state-of-the-art results in this direction, together with a new contribution, is presented in Chapter 5. Moreover, the Laplace EVP naturally arises in the analysis of other partial differential equations that model everyday physical phenomena. A classical example is the wave equation in two spatial dimensions, which models the vibration of a membrane. After applying separation of variables, the problem reduces to the associated Laplace EVP [BO91]. For some one-, two- or three-dimensional model domains such as lines, rectangles, circular sectors or balls, the exact Laplace eigenvalues and eigenfunctions are known explicitly [Cle62; Ray45; Str08]. Yet, for more general domains, analytical solutions are typically unavailable, and numerical methods are therefore required to compute the spectrum.

Isogeometric analysis provides powerful tools for the accurate simulation of the Laplace eigenvalues. More precisely, it has been demonstrated in the literature – both numerically and analytically – that spline and NURBS spaces offer superior approximation properties for spectral problems, especially in one dimension and on two-dimensional domains of rectangular type [CHR07; CRBH06; CHB09; Gar+19; HHRS21; HRS08; HER14; MSS22; SMS19; SMS20]. In particular, when high-order smooth spline spaces are employed, the full discrete spectrum approximates the corresponding exact eigenvalues with remarkable accuracy. The increased inter-element continuity of the basis functions leads to significantly improved spectral approximation constants and ensures a uniform error distribution across the spectrum. In contrast, higher-order finite element discretizations typically exhibit so-called spectral branches, where the error increases abruptly beyond certain eigenvalue indices. Consequently, spline-based methods provide a more stable and reliable approximation of the entire spectrum.

In the settings discussed in the literature, the underlying eigenfunctions are smooth. This naturally raises the question of whether IGA can achieve similarly accurate spectral approximations on more complex domains, particularly in the presence of singularities and reduced eigenfunction regularity. Circular sectors constitute an ideal test case for this investigation. Their Laplace eigenfunctions exhibit a characteristic corner singularity at the origin, and the eigenpairs are available in explicit form, enabling a precise numerical validation of the spectral approximation properties. In addition, circular sectors highlight one of the fundamental motivations of IGA, namely the exact representation of curved computational geometries by means of NURBS basis functions [HCB05]. In contrast to standard finite element methods, circular sectors can be represented exactly within the isogeometric framework [Lu09].

To obtain an accurate approximation of the Laplace spectrum, the corner singularity of the eigenfunctions on circular sectors must be addressed in the numerical solution process. The existing results on powerful spectral approximation properties have been achieved using standard single-patch IGA or closely related methods. Therefore, we aim for an approach that is as close as possible to the standard method to maintain comparability between our results and the existing ones, which motivates the use of a boundary-fitted instead of a trimmed approach. Since we consider a model problem where the location of the singularity is known, the local refinement can be set up a priori and there is no need for adaptive strategies that require more computational effort. This again leads to the graded mesh refinement approach introduced in Section 3.2. For further motivation of the chosen method within the IGA setting, we refer the reader to Section 3.1.

The main novelties of this chapter are:

- a detailed analysis of the regularity properties of Laplace eigenfunctions on circular sectors, including a characterization of the distribution of smooth and singular eigenmodes,
- the application of graded polar mesh refinement, as introduced in Section 3.2, to the Laplace eigenvalue problem on circular sectors, accompanied by a comprehensive numerical study,
- an extension of the error estimates presented in Section 3.4 for boundary value problems to the eigenvalue setting,
- a validation of the spectral accuracy of isogeometric analysis on circular sectors, at least for the lower part of the spectrum, which extends existing results for rectangular domains,
- a theoretical and numerical demonstration that mesh grading leads to a well-balanced distribution of the approximation error across the computed eigenvalues,
- the development of a hierarchical refinement strategy that can be combined with graded meshes to avoid anisotropic elements in the physical domain, as visualized in Figure 1.1c, together with an investigation of the resulting distinct approximation properties for smooth eigenfunctions.

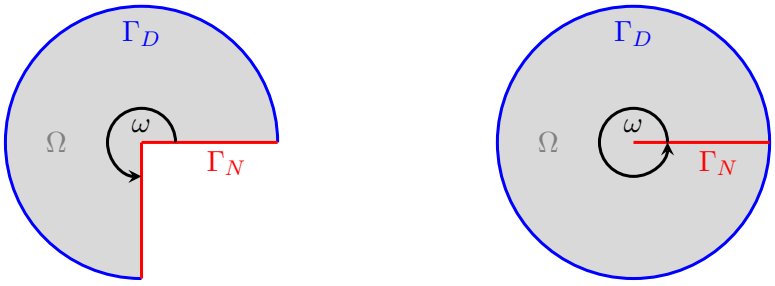

(a) (b)

Figure 4.1: Circular sectors Ω with angle ω and the corresponding Dirichlet and Neumann boundaries. (a): $\omega = \frac{3}{2}\pi$. (b): $\omega = 2\pi$.

4.2 The Laplace eigenvalue problem on circular sectors

In this section, we analyze the Laplace EVP on circular sectors in detail. We describe its analytical solutions and discuss their regularity properties. As a representative example, we then focus on the unit disk with a crack, i.e., a circular sector with opening angle 2π. The presentation largely follows Section 2 of [AZ24a], with a more elaborate derivation of the analytical solution.

4.2.1 Analytical solutions

Consider the Laplace EVP

$$\begin{aligned} -\Delta u &= \lambda u && \text{in } \Omega, \\ u &= 0 && \text{on } \Gamma_D, \\ \frac{\partial u}{\partial n} &= 0 && \text{on } \Gamma_N, \end{aligned} \tag{4.1}$$

where the model domain $\Omega = \{(r\cos\varphi, r\sin\varphi) \in \mathbb{R}^2 : 0 < r < 1,\ 0 < \varphi < \omega\}$ is a circular sector with opening angle $\omega \in (0, 2\pi]$. The Dirichlet boundary $\Gamma_D = \{(\cos\varphi, \sin\varphi) \in \mathbb{R}^2 : 0 \le \varphi \le \omega\}$ corresponds to the circular arc, while the Neumann boundary consists of the two angle legs, $\Gamma_N = \{(r\cos\varphi, r\sin\varphi) \in \mathbb{R}^2 : 0 \le r < 1,\ \varphi \in \{0, \omega\}\}$. Although circular sectors have already appeared several times in this thesis, we illustrate the model domain and its boundary once more for completeness here. Figure 4.1 shows the cases $\omega = \frac{3}{2}\pi$ and $\omega = 2\pi$.

The analytical solution of the Laplace EVP on circular sectors is well known and has been extensively studied in the literature. According to Rayleigh, the theory of vibrations of a circular membrane was first introduced by Clebsch [Cle62; Ray45]. Later on, Rayleigh himself derived the eigenmodes of circular sectors. Further contributions to the problem can be found, among others, in [GN13; KS84]. In this section, we briefly recapitulate the main ideas and results. Our presentation follows the notation of [Str08, Chapter 10.2], where the vibrations of a circular membrane are developed comprehensively.

First, we rewrite problem (4.1) in polar coordinates, where we use the inverted breve accent to denote the considered function in polar coordinates, that is,

$$\breve{u}(r, \varphi) = u(r\cos\varphi, r\sin\varphi) = u(x, y).$$

It follows

$$\begin{aligned} -\frac{1}{r}\frac{\partial \hat{u}}{\partial r} - \frac{\partial^2 \hat{u}}{\partial r^2} - \frac{1}{r^2}\frac{\partial^2 \hat{u}}{\partial \varphi^2} &= \lambda \hat{u} && \text{for } (r,\varphi) \in (0,1)\times(0,\omega), \\ \hat{u} &= 0 && \text{for } r = 1,\ \varphi \in [0,\omega], \\ \frac{\partial \hat{u}}{\partial \varphi} &= 0 && \text{for } r \in [0,1),\ \varphi \in \{0,\omega\}. \end{aligned}$$

By introducing the separation ansatz $\hat{u}(r,\varphi) = R(r)\Phi(\varphi)$, we obtain

$$\frac{r^2 R''(r) + rR'(r)}{R(r)} + r^2\lambda = -\frac{\Phi''(\varphi)}{\Phi(\varphi)}.$$

Hence, both sides must be equal to a constant $\sigma \in \mathbb{R}$. Taking the boundary conditions into account, we find that

$$r^2 R''(r) + rR'(r) + (\lambda r^2 - \sigma)R(r) = 0, \qquad R(1) = 0 \tag{4.2}$$

and

$$\Phi''(\varphi) + \sigma\,\Phi(\varphi) = 0, \qquad \Phi'(0) = \Phi'(\omega) = 0. \tag{4.3}$$

The eigenvalue problem (4.3) has the solutions

$$\sigma_\ell = \nu_\ell^2 \quad \text{and} \quad \Phi_\ell(\varphi) = a_\ell \cos(\nu_\ell\,\varphi) \quad \text{with } \nu_\ell = \ell\,\frac{\pi}{\omega},\ a_\ell \in \mathbb{R},\ \ell \in \mathbb{N}_0.$$

Solving the boundary value problem (4.2) for R is slightly more technical. The model problem (4.1) possesses only positive eigenvalues, see, e.g., [Str08, Chapter 10.1]. We therefore introduce the substitution $\rho(r) := r\sqrt{\lambda}$ and define $\tilde{R}(\rho(r)) := R\left(\frac{\rho(r)}{\sqrt{\lambda}}\right) = R(r)$. Applying the chain rule yields

$$\begin{aligned} \frac{\partial R}{\partial r}(r) &= \frac{\partial \tilde{R}}{\partial \rho}(\rho(r)) \cdot \sqrt{\lambda}, \\ \frac{\partial^2 R}{\partial r^2}(r) &= \frac{\partial^2 \tilde{R}}{\partial \rho^2}(\rho(r)) \cdot \lambda. \end{aligned}$$

Inserting both expressions into equation (4.2) yields Bessel's differential equation

$$\rho^2 \frac{d^2\tilde{R}}{d\rho^2} + \rho\frac{d\tilde{R}}{d\rho} + (\rho^2 - \nu_\ell^2)\tilde{R} = 0. \tag{4.4}$$

In general, the Bessel equation has solutions of the form $\tilde{R}(\rho) = \alpha J_{\nu_\ell}(\rho) + \beta Y_{\nu_\ell}(\rho)$, where J_{ν_ℓ} and Y_{ν_ℓ} are Bessel functions to the order ν_ℓ of the first and second kind, respectively, and $\alpha, \beta \in \mathbb{R}$. However, the Bessel functions of the second kind have a pole at $\rho = 0$ and thus result in unphysical solutions, i.e., it is $\beta = 0$. Without loss of generality, we set $\alpha = 1$ and obtain the relevant solution of equation (4.4) by

$$\tilde{R}(\rho(r)) = J_{\nu_\ell}(\rho(r)) = \sum_{j=0}^{\infty} \frac{(-1)^j}{j!\,\Gamma(\nu_\ell + j + 1)} \left(\frac{\rho(r)}{2}\right)^{2j+\nu_\ell},$$

where Γ denotes the Gamma function. Hence, the function

$$R(r) = \tilde{R}(\rho(r)) = J_{\nu_\ell}(\rho(r)) = J_{\nu_\ell}(\eta\, r) \quad \text{with } \eta = \sqrt{\lambda} \text{ and } \nu_\ell = \ell\frac{\pi}{\omega} \text{ for } \ell \in \mathbb{N}_0$$

solves the equation initially considered in problem (4.2) for $\sigma = \nu_\ell^2$. Since we also require homogeneous Dirichlet boundary conditions on the circular boundary, that is, $R(1) = 0$, we obtain the condition $J_{\nu_\ell}(\eta) = 0$. As a consequence, η has to be a root of the Bessel function J_{ν_ℓ}.

Let J_{ν_ℓ} be the Bessel function of the first kind to the order ν_ℓ, and let $\eta_{\nu_\ell,m}$ be its m-th positive root for $m \in \mathbb{N}$. Then, the exact eigenfunctions can be expressed in polar coordinates as

$$u_{\nu_\ell,m}(r,\varphi) = a_{\nu_\ell,m}\, J_{\nu_\ell}(\eta_{\nu_\ell,m}\, r)\cos(\nu_\ell\,\varphi), \tag{4.5}$$

with $a_{\nu_\ell,m} \in \mathbb{R}$ and $\nu_\ell = \ell\frac{\pi}{\omega}$ for $\ell \in \mathbb{N}_0$. Throughout this chapter, we set $a_{\nu_\ell,m} = 1$ for all $\ell \in \mathbb{N}_0$ and $m \in \mathbb{N}$ for simplicity. We refer to the functions in (4.5) as the Laplace eigenfunctions or eigenmodes of circular sectors. Note that we do not denote these functions with an inverted breve accent even though they are expressed in polar coordinates. We omit this notation here and in what follows, as the underlying coordinate system is always clear from the context. The corresponding Laplace eigenvalues and eigenfrequencies of circular sectors are given by

$$\lambda_{\nu_\ell,m} = \eta_{\nu_\ell,m}^2 \qquad \text{and} \qquad \bar{\omega}_{\nu_\ell,m} = \sqrt{\lambda_{\nu_\ell,m}} = \eta_{\nu_\ell,m}, \tag{4.6}$$

respectively. Ordering the eigenvalues and eigenfrequencies in ascending order, we denote them by λ_n and $\bar{\omega}_n = \sqrt{\lambda_n}$, $n = 1, 2, \ldots$, respectively. The zeros of Bessel functions and their asymptotic behavior are well established in the literature [ASR88; Elb01; GN13; Olv51; Olv52; Wat95]. For example, from [ASR88, Chapter 9.5], we know that

$$\eta_{\nu_\ell,1} < \eta_{\nu_\ell+1,1} < \eta_{\nu_\ell,2} < \eta_{\nu_\ell+1,2} < \eta_{\nu_\ell,3} < \ldots \qquad \text{for any } \ell \in \mathbb{N}_0,$$

In [GN13], the authors provide a compact summary of two important asymptotic formulas. For fixed ν_ℓ and large m, McMahon's expansion, $\eta_{\nu_\ell,m} \sim \pi(m + \nu_\ell/2 - 1/4)) + \mathcal{O}(m^{-1})$, holds [Wat95]. For fixed m and large ν_ℓ, Olver's expansion, $\eta_{\nu_\ell,m} \sim \nu_\ell + \delta_m \nu_\ell^{1/3} + \mathcal{O}(\nu_\ell^{-1/3})$, holds with known coefficients δ_m [Elb01; Olv51; Olv52]. Hence, it is

$$\eta_{\nu_\ell,m} \to \infty \quad \text{for } \ell \to \infty \qquad \text{and} \qquad \eta_{\nu_\ell,m} \to \infty \quad \text{for } m \to \infty.$$

In particular, the sequences of eigenvalues $(\lambda_k)_{k\in\mathbb{N}}$ and eigenfrequencies $(\bar{\omega}_k)_{k\in\mathbb{N}}$ satisfy

$$0 < \lambda_1 \leq \lambda_2 \leq \ldots \to \infty \qquad \text{and} \qquad 0 < \bar{\omega}_1 \leq \bar{\omega}_2 \leq \ldots \to \infty. \tag{4.7}$$

Beyond this, we conjecture that the eigenvalues (4.6) are pairwise distinct and that the sequence (4.7) is strictly monotonically increasing. Bourget's hypothesis states that Bessel functions J_{n_1} and J_{n_2} to different integer orders $n_1, n_2 \in \mathbb{N}$ have no common positive zeros. A proof of this result, as well as several extensions of Bourget's hypothesis, have since been established [Wat95]. Together with the findings above, this motivates our conjecture that the Bessel functions J_{ν_ℓ}, with $\nu_\ell = \ell\frac{\pi}{\omega}$ and $\ell \in \mathbb{N}_0$, likewise do not share common zeros. However, we are not aware of a reference that proves this precise statement. An illustration of the pairwise distinct zeros in the interval $[0, 10]$ for the case $\omega = 2\pi$ is provided in Figure 4.3.

4.2.2 Regularity of the eigenfunctions

Next, we investigate the regularity of the Laplace eigenfunctions on circular sectors, which admit the following useful product representation.

Remark 4.1. The eigenfunctions (4.5) can be written in separated variables as

$$u_{\nu_\ell,m}(r,\varphi) = R(r)\,\Phi(\varphi), \tag{4.8}$$

where $\Phi(\varphi) = \cos(\nu_\ell\,\varphi)$ is a smooth function satisfying $\left\|\Phi^{(l)}\right\|_{L^\infty(\Omega)} \leq \nu_\ell^l$, $l \in \mathbb{N}_0$, and $R(r) = J_{\nu_\ell}(\eta_{\nu_\ell,m}\,r)$ is a Bessel function. The radial factor R contains all information about the regularity of the eigenfunctions. Typically, solutions of boundary value problems on circular sectors are expressed as sums of such products. Hence, the pure product structure (4.8) is a particular feature of the eigenvalue problem (4.1).

Motivated by Remark 4.1, we introduce some general properties of Bessel functions to assess the regularity of the Laplace eigenfunctions (4.5). For small arguments, an asymptotic representation of Bessel functions of the first kind to any order $\nu \notin \{-1,-2,-3,\dots\}$ is given by Abramowitz and Stegun [ASR88, Formula 9.1.7, p. 360],

$$J_\nu(z) \sim \frac{1}{\Gamma(\nu+1)}\left(\frac{z}{2}\right)^\nu \qquad \text{for } z \to 0, \tag{4.9}$$

Since $\nu_\ell = \ell\,\frac{\pi}{\omega}$, relation (4.9) implies that every eigenfunction $u_{\nu_\ell,m}$, $\ell \in \mathbb{N}_0$, $m \in \mathbb{N}$, satisfies

$$u_{\nu_\ell,m}(r,\varphi) = J_{\nu_\ell}(\eta_{\nu_\ell,m}\,r)\cos(\nu_\ell\,\varphi) \sim \frac{1}{\Gamma(\nu_\ell+1)}\left(\frac{\eta_{\nu_\ell,m}\,r}{2}\right)^{\nu_\ell}\cos(\nu_\ell\,\varphi) = C r^{\nu_\ell} \qquad \text{for } r \to 0, \tag{4.10}$$

Hence, near the conical point, where $r = 0$, the Laplace eigenfunctions of circular sectors behave like the functions $r \mapsto r^{\nu_\ell}$, a property that is crucial for the regularity analysis.

Furthermore, we have an integral representation of Bessel functions of the first kind to any order ν with $\mathrm{Re}(\nu) > -\frac{1}{2}$ [ASR88, Chapter 9.1],

$$J_\nu(z) = \frac{\left(\frac{z}{2}\right)^\nu}{\pi^{1/2}\,\Gamma(\nu+\frac{1}{2})}\int_0^\pi \cos(z\cos\theta)\sin^{2\nu}\theta\,\mathrm{d}\theta,$$

Thus, for $z \in \mathbb{R}$ with $z > 0$, it is

$$|J_\nu(z)| \leq \frac{\left(\frac{z}{2}\right)^\nu}{\pi^{1/2}\,\Gamma(\nu+\frac{1}{2})}\int_0^\pi \left|\sin^{2\nu}\theta\right|\mathrm{d}\theta = C(\nu)\,z^\nu, \tag{4.11}$$

with $C(\nu) := \dfrac{\left(\frac{1}{2}\right)^\nu}{\pi^{1/2}\Gamma(\nu+\frac{1}{2})}\displaystyle\int_0^\pi \left|\sin^{2\nu}\theta\right|\mathrm{d}\theta$. Combined with the asymptotic behavior (4.10), we obtain

$$|u_{\nu_\ell,m}(r,\varphi)| = |J_{\nu_\ell}(\eta_{\nu_\ell,m}\,r)\cos(\nu_\ell\,\varphi)| \leq C(\nu_\ell)\,(\eta_{\nu_\ell,m}\,r)^{\nu_\ell}|\cos(\nu_\ell\,\varphi)| \leq C\,r^{\nu_\ell} \tag{4.12}$$

for all $\ell \in \mathbb{N}_0$, $m \in \mathbb{N}$ and $(r,\varphi) \in (0,1)\times(0,\omega)$.

Next, we consider the gradient $\nabla u = \left(\frac{\partial u}{\partial x_1}, \frac{\partial u}{\partial x_2}\right)^T$ of an eigenfunction $u = u_{\nu_\ell,m}$, $\ell \in \mathbb{N}_0$, $m \in \mathbb{N}$, with x_1 and x_2 being the Cartesian coordinates in $\mathbb{R}^2$. The eigenmodes can be differentiated using the recursion relation for Bessel functions [Str08, Chapter 10.5],

$$J_\nu'(z) = \frac{\nu}{z}J_\nu(z) - J_{\nu+1}(z), \tag{4.13}$$

By changing to polar coordinates and setting $\eta = \eta_{\nu_\ell,m}$, it follows

$$\begin{aligned}
|\nabla u| &\leq C \left(\left| \frac{\partial u}{\partial r} \right| + \frac{1}{r} \left| \frac{\partial u}{\partial \varphi} \right| \right) \\
&= C \left(\left| \frac{\partial \left(J_{\nu_\ell}(\eta\, r) \right)}{\partial r} \cos(\nu_\ell\, \varphi) \right| + \frac{1}{r} |J_{\nu_\ell}(\eta\, r)\, \nu_\ell\, \sin(\nu_\ell\, \varphi)| \right) \\
&= C \left(\left| \left(\frac{\nu_\ell}{r}\, J_{\nu_\ell}(\eta\, r) - \eta\, J_{\nu_\ell+1}(\eta\, r) \right) \cos(\nu_\ell\, \varphi) \right| + \frac{1}{r} |J_{\nu_\ell}(\eta\, r)\, \nu_\ell\, \sin(\nu_\ell\, \varphi)| \right) \qquad (4.14) \\
&\leq C \left(\frac{2\nu_\ell}{r} |\, J_{\nu_\ell}(\eta\, r)| + \eta |J_{\nu_\ell+1}(\eta\, r)| \right) \\
&\leq C \left(\frac{2\nu_\ell}{r} (\eta r)^{\nu_\ell} + \eta (\eta r)^{\nu_\ell+1} \right) \\
&\leq C\, r^{\nu_\ell - 1}, \qquad (4.15)
\end{aligned}$$

where we used the bound (4.11) of the considered Bessel functions and $r \leq 1$. Moreover, the constant C depends on ν_ℓ and m. We repeat the same argumentation for the higher derivatives and obtain

$$|D^{\boldsymbol{\alpha}} u_{\nu_\ell,m}| \leq C r^{\nu_\ell - |\boldsymbol{\alpha}|} \qquad (4.16)$$

for all $\ell \in \mathbb{N}_0, m \in \mathbb{N}$ and $\boldsymbol{\alpha} \in \mathbb{N}_0^2$, where we recall the multi-index notation (2.1).

Based on this observation, we determine the Sobolev regularity of the eigenmodes in the following lemmata. From their explicit formula (4.5), it follows that the eigenfunctions are smooth away from the corner $\boldsymbol{P} = \boldsymbol{0}$. Therefore, in the proofs below, it suffices to analyze their regularity near the conical point.

Lemma 4.2. *The Laplace eigenfunctions (4.5) of a circular sector with angle $\omega \in (0, 2\pi]$ satisfy*

$$u_{\nu_\ell,m} \in H^s(\Omega) \quad \text{for all } s \geq 0 \text{ with } s < \nu_\ell + 1,$$

where $\nu_\ell = \ell \frac{\pi}{\omega}$, $\ell \in \mathbb{N}_0$ and $m \in \mathbb{N}$.

Proof. Estimate (4.16) implies that the eigenfunction $u_{\nu_\ell,m}$ and its derivatives can be controlled by the function $r \mapsto r^{\nu_\ell}$ and its derivatives. It is well known that this function belongs to $H^s(\Omega)$ for all $s \geq 0$ satisfying $\nu_\ell - s > -1$, that is, for $s < \nu_\ell + 1$. □

In general, the classical Sobolev regularity result stated in Lemma 4.2 is not sharp. For instance, consider the case $\ell = 0$. Then, it is $\nu_0 = 0$, and Lemma 4.2 only yields that $u_{\nu_0,m} \in H^s(\Omega)$ for all $s < 1$. Indeed, the eigenfunctions $u_{\nu_0,m}$ are of a different nature in the sense that

$$u_{\nu_\ell,m}(0,0) = \begin{cases} 0 & \text{if } \ell > 0, \\ 1 & \text{if } \ell = 0, \end{cases} \qquad (4.17)$$

Nevertheless, it is clear that the functions $u_{\nu_0,m}$ belong at least to $H^1(\Omega)$, since they are solutions of the weak form of our model problem (4.1), which will be discussed more detailed in Section 4.3.1. In fact, the following result shows that Lemma 4.2 is not sharp for all eigenmodes $u_{\nu_\ell,m}$ with $\nu_\ell \in \mathbb{N}_0$.

Lemma 4.3. *Let $\ell \in \mathbb{N}_0$ and $m \in \mathbb{N}$. The Laplace eigenfunctions of circular sectors (4.5) satisfy*

$$u_{\nu_\ell,m} \in H^s(\Omega) \quad \text{for all } s \geq 0$$

if and only if $\nu_\ell = \ell \frac{\pi}{\omega} \in \mathbb{N}_0$. For $\nu_\ell \notin \mathbb{N}_0$, the regularity result shown in Lemma 4.2 is sharp.

Proof. First, let $\nu_\ell = \ell\frac{\pi}{\omega} \notin \mathbb{N}_0$. Exploiting the asymptotic representation (4.10), we observe that $u_{\nu_\ell,m}$ behaves like $r \mapsto r^{\nu_\ell}$ for $r \to 0$. Consequently, it is $u_{\nu_\ell,m} \notin H^s(\Omega)$ for all $s \geq \nu_\ell + 1$ and Lemma 4.2 is sharp.

Now, let $n := \nu_\ell = \ell\frac{\pi}{\omega} \in \mathbb{N}_0$. Estimate (4.12) yields that

$$|u_{n,m}(r,\varphi)| = |J_n(\eta_{n,m}\, r)\cos(n\,\varphi)| \leq Cr^n|\cos(n\,\varphi)|.$$

With the relations between Cartesian and polar coordinates, $(x,y) = (r\cos\varphi, r\sin\varphi)$ and $r^2 = x^2+y^2$, it holds

$$\begin{aligned}
|u_{n,m}(r,\varphi)| &\leq Cr^n|\cos(n\,\varphi)| \\
&= Cr^n\left|\sum_{j=0}^{\lfloor\frac{n}{2}\rfloor}(-1)^j\binom{n}{2j}(\sin\varphi)^{2j}(\cos\varphi)^{n-2j}\right| \\
&= C\left|\sum_{j=0}^{\lfloor\frac{n}{2}\rfloor}(-1)^j\binom{n}{2j}r^{2j}(\sin\varphi)^{2j}\,r^{n-2j}(\cos\varphi)^{n-2j}\right| \\
&= C\left|\sum_{j=0}^{\lfloor\frac{n}{2}\rfloor}(-1)^j\binom{n}{2j}y^{2j}\,x^{n-2j}\right| \\
&= C|P_0(x,y)|
\end{aligned}$$

with the polynomial $P_0(x,y) := \sum_{j=0}^{\lfloor\frac{n}{2}\rfloor}(-1)^j\binom{n}{2j}y^{2j}\,x^{n-2j}$, where we used a multiple-angle formula for the cosinus [BSMM01, Chapter 2.6.2]. Hence, it is clear that $u \in L^2(\Omega)$. Next, we recall estimate (4.14) and apply a multiple-angle formula for the sinus [BSMM01, Chapter 2.6.2] to obtain

$$\begin{aligned}
|\nabla u_{n,m}| &\leq C\left(\left|\left(\frac{n}{r}\,J_n(\eta_{n,m}\,r) - \eta_{n,m}\,J_{n+1}(\eta_{n,m}\,r)\right)\cos(n\,\varphi)\right| + \frac{1}{r}|J_n(\eta_{n,m}\,r)\,n\,\sin(n\,\varphi)|\right) \\
&\leq C\left(\left(r^{n-1}-r^{n+1}\right)|\cos(n\,\varphi)| + r^{n-1}|\sin(n\,\varphi)|\right) \\
&\leq Cr^{n-1}\left(|\cos(n\,\varphi)| + |\sin(n\,\varphi)|\right) \\
&\leq Cr^{n-1}\left(\sum_{j=0}^{\lfloor\frac{n}{2}\rfloor}\binom{n}{2j}|\sin\varphi|^{2j}|\cos\varphi|^{n-2j} + \sum_{j=0}^{\lfloor\frac{n-1}{2}\rfloor}\binom{n}{2j+1}|\sin\varphi|^{2j+1}|\cos\varphi|^{n-2j-1}\right) \\
&\leq Cr^{n-1}\left(\sum_{j=0}^{\lfloor\frac{n}{2}\rfloor}\binom{n}{2j}|\sin\varphi|^{2j-1}|\cos\varphi|^{n-2j} + \sum_{j=0}^{\lfloor\frac{n-1}{2}\rfloor}\binom{n}{2j+1}|\sin\varphi|^{2j}|\cos\varphi|^{n-2j-1}\right) \\
&= C\left(\sum_{j=0}^{\lfloor\frac{n}{2}\rfloor}\binom{n}{2j}|r\sin\varphi|^{2j-1}|r\cos\varphi|^{n-2j} + \sum_{j=0}^{\lfloor\frac{n-1}{2}\rfloor}\binom{n}{2j+1}|r\sin\varphi|^{2j}|r\cos\varphi|^{n-2j-1}\right) \\
&= C\left(\sum_{j=0}^{\lfloor\frac{n}{2}\rfloor}\binom{n}{2j}|x|^{2j-1}|y|^{n-2j} + \sum_{j=0}^{\lfloor\frac{n-1}{2}\rfloor}\binom{n}{2j+1}|x|^{2j}|y|^{n-2j-1}\right) \\
&\leq CP_1(|x|,|y|)
\end{aligned}$$

with the polynomial $P_1(x,y) = \sum_{j=0}^{\lfloor \frac{n}{2} \rfloor} \binom{n}{2j} x^{2j-1} y^{n-2j} + \sum_{j=0}^{\lfloor \frac{n-1}{2} \rfloor} \binom{n}{2j+1} x^{2j} y^{n-2j-1}$. Note that for some of the inequalities above it is essential that $r \in [0,1]$ and $|\sin\varphi| \in [0,1]$. Thus, it follows that $\nabla u_{n,m} \in L^2(\Omega)$ and $u_{n,m} \in H^1(\Omega)$. Similarly, for higher derivatives $D^{\boldsymbol{\alpha}} u_{n,m}$ for any multi-index $\boldsymbol{\alpha} \in \mathbb{N}_0^2$, there exists a polynomial $P_{|\boldsymbol{\alpha}|}$ such that

$$|D^{\boldsymbol{\alpha}} u_{n,m}| \leq C P_{|\boldsymbol{\alpha}|}(|x|,|y|).$$

Therefore, it is $D^{\boldsymbol{\alpha}} u_{n,m} \in L^2(\Omega)$ for all $\boldsymbol{\alpha} \in \mathbb{R}^2$ and we obtain

$$u_{n,m} \in H^s(\Omega) \quad \text{for all } s \in \mathbb{N}_0,$$

Using an interpolation argument for the fractional Sobolev spaces, it immediately follows that $u_{n,m} \in H^s(\Omega)$ for all $s \geq 0$ and the assertion is proven. □

Throughout this chapter, we will call the eigenfunctions $u_{\nu_\ell,m}$ with $\nu_\ell \in \mathbb{N}_0$ and $m \in \mathbb{N}$ smooth in the sense of Lemma 4.3. To conclude the classical Sobolev regularity analysis, we derive some simple but illustrative conclusions from the two lemmata above.

Remark 4.4.

1. For all $\ell \in \mathbb{N}_0$ and $m \in \mathbb{N}$ it is $u_{\nu_\ell,m} \in H^1(\Omega)$.
2. The eigenfunctions $u_{\nu_0,m}$ of circular sectors with arbitrary angles $\omega \in (0, 2\pi]$ are smooth for all $m \in \mathbb{N}$.
3. Consider a circular sector whose angle ω satisfies $\frac{\pi}{\omega} \in \mathbb{N}$, that is, $\omega = \frac{\pi}{N}$ for some $N \in \mathbb{N}$. Then all its Laplace eigenfunctions $u_{\nu_\ell,m}$ are smooth as $\nu_\ell = \ell\frac{\pi}{\omega} \in \mathbb{N}_0$ for all $\ell \in \mathbb{N}_0$.
4. If the angle of a circular sector can not be expressed as a product of a rational number and π, i.e., $\omega \neq q\pi$ for all $q \in \mathbb{Q}$, it is $\nu_\ell = \ell\frac{\pi}{\omega} \notin \mathbb{N}$ for all $\ell \in \mathbb{N}$, that is, none of the eigenfunctions $u_{\nu_\ell,m}$ for $\ell > 0$ is smooth.
5. The eigenfunctions $u_{\nu_1,m}$ of circular sectors with angles $\omega \in (\pi, 2\pi]$ do not belong to $H^2(\Omega)$ for all $m \in \mathbb{N}$. They contain the strongest singularity among all eigenfunctions, which is of type r^{ν_1} near the conical point of the circular sector, where $\nu_1 = \frac{\pi}{\omega} \in [\frac{1}{2}, 1)$.

Finally, we assess the regularity of the eigenfunctions in terms of the weighted Sobolev spaces introduced in Definition 2.1.

Lemma 4.5. *Let $\ell \in \mathbb{N}_0$ with $\ell \geq 1$ and $m \in \mathbb{N}$. The eigenfunctions (4.5) satisfy*

$$u_{\nu_\ell,m} \in V^s_\beta(\Omega) \quad \text{for all } (s,\beta) \in \mathbb{N} \times \mathbb{R} \text{ with } s \geq 2 \text{ and } s - 1 - \nu_\ell < \beta < s - 1 + \nu_\ell, \tag{4.18}$$

and for $\ell = 0$, i.e., $\nu_\ell = 0$, we have

$$u_{0,m} - u_{0,m}(\mathbf{0}) \in V^s_\beta(\Omega) \quad \text{for all } (s,\beta) \in \mathbb{R} \text{ with } s \geq 2 \text{ and } s - 1 - \nu_1 < \beta < s - 1. \tag{4.19}$$

Proof. Estimate (4.16) implies that every eigenfunction $u_{\nu_\ell,m}$ behaves like r^{ν_ℓ} near the conical point. For $\nu_\ell > 0$, that is, for $\ell \geq 1$, it is well known that the function $r \mapsto r^{\nu_\ell}$ belongs to the weighted V-spaces stated in (4.18). For $\nu_\ell = 0$, the eigenfunctions have a constant contribution at the corner, recall (4.17). After subtracting this constant term, the regularity (4.19) follows as in the proof of [ANZ25, Lemma A.1]. □

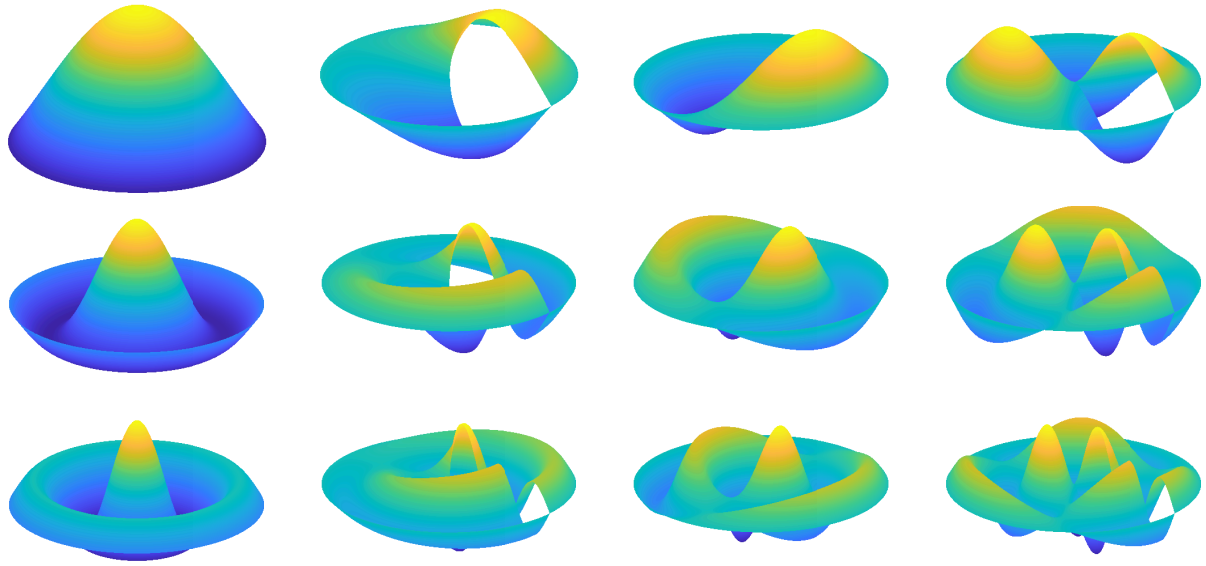

Figure 4.2: Illustration of 12 Laplace eigenfunctions $u_{\nu_\ell,m}$ of the unit disk with crack. Columns from left to right: $\nu_\ell = 0, \frac{1}{2}, 1, \frac{3}{2}$. Rows from top to bottom: $m = 1, 2, 3$.

4.2.3 Eigenfunctions of the unit disk with crack

To gain a deeper understanding of the model problem (4.1) and its exact solutions, we will now discuss a specific example: the circular sector with angle $\omega = 2\pi$, which represents the unit disk with a crack located along the positive x-axis, as presented in Figure 4.1b. All other circular sectors with smaller angles $\omega < 2\pi$ can be interpreted as analogs or even simplifications of the case $\omega = 2\pi$.

The Laplace eigenfunctions of the unit disk with crack are given by the formula (4.5) with $\nu_\ell = \frac{\ell}{2}$ for $\ell \in \mathbb{N}_0$. Utilizing the regularity results outlined in Section 4.2.2, we categorize the eigenmodes into two types:

(A) $\nu_\ell \in \mathbb{N}_0$, i.e., $\ell = 2n$ for $n \in \mathbb{N}_0$. As indicated in Lemma 4.3, the corresponding eigenfunctions $u_{n,m}$ are smooth for all $m \in \mathbb{N}$. Exemplary eigenfunctions, namely $u_{\nu_0,m}$ and $u_{\nu_2,m}$ for $m \in \{1, 2, 3\}$, are showcased in the first and third columns of Figure 4.2. It is noteworthy that the crack is not visible in graphical representations of these eigenfunctions. This absence is due to the product form (4.8) of the eigenmodes and the 2π-periodicity of the angular functions $\varphi \mapsto \cos(\nu_\ell \varphi) = \cos(n\varphi)$.

(B) $\nu_\ell \notin \mathbb{N}_0$, i.e., $\ell = 2n + 1$ for $n \in \mathbb{N}_0$. The corresponding eigenfunctions $u_{n+\frac{1}{2},m}$ have a singularity of type $r^{n+\frac{1}{2}}$ and are only contained in $H^s(\Omega)$ for all $s < n + \frac{3}{2}$, recall Lemma 4.2. As an example, the eigenmodes $u_{\nu_1,m}$ and $u_{\nu_3,m}$ for $m \in \{1, 2, 3\}$ have singularities of type $r^{1/2}$ and $r^{3/2}$, respectively, and are presented in the second and fourth columns of Figure 4.2. Here, the crack is clearly visible since the functions $\varphi \mapsto \cos(\nu_\ell\varphi) = \cos\big((n + \frac{1}{2})\varphi\big)$ are not 2π-periodic.

As indicated in Remark 4.1, the regularity properties of the Laplace eigenmodes of circular sectors are based on the corresponding Bessel functions. In Figure 4.3, we visualize the Bessel functions J_{ν_ℓ} to the orders $\nu_\ell \in \{0, \frac{1}{2}, 1, \frac{3}{2}, \ldots, \frac{11}{2}, 6\}$, which are all the half-integer and integer Bessel functions with zeros in the interval $[0, 10]$. The asymptotic behavior (4.9) can be clearly observed, i.e., $J_{\nu_\ell}(z) \sim z^{\nu_\ell}$ for $z \to 0$, and J_0 differs from the other Bessel functions in the sense

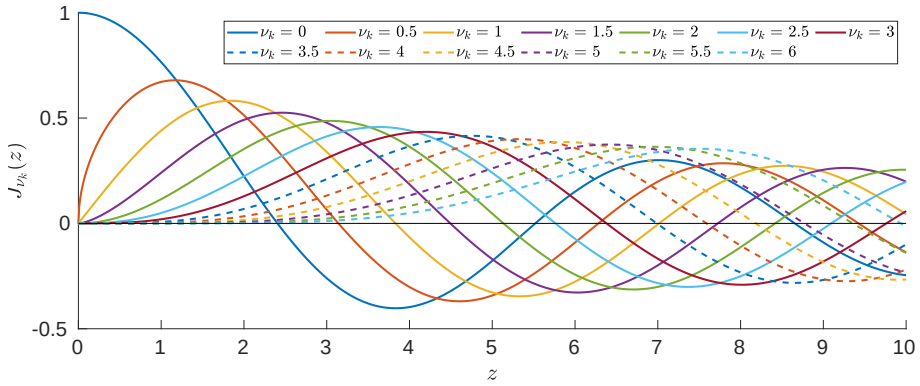

Figure 4.3: Visualization of the Bessel functions J_{ν_ℓ} to the orders $\nu_\ell \in \{0, 0.5, 1, \dots, 5.5, 6\}$ in the interval $[0, 10]$.

that $J_0(0) = 1$ and $J_{\nu_\ell}(0) = 0$ for $\nu_\ell \neq 0$. Bessel functions of half-integer order can be expressed explicitly [Str08, Chapter 10.5]. For instance, it holds

$$J_{\frac{1}{2}}(z) = \sqrt{\frac{2}{\pi z}} \sin z,$$

which once again highlights the presence of a singularity of type $z^{1/2}$ in the Bessel function $J_{\frac{1}{2}}$.

Table 4.1 provides the eigenfrequencies of the unit disk with crack within the interval $[0, 10]$, listed in ascending order. They are given by the zeros of the functions depicted in Figure 4.3. Each eigenfrequency is associated with a specific root of a Bessel function, indicating the corresponding eigenfunction and its regularity. The eigenfrequencies $\bar{\omega}_2$, $\bar{\omega}_8$ and $\bar{\omega}_{20}$, highlighted in dark orange, correspond to eigenfunctions with the strongest singularity, $u_{1/2,1}$, $u_{1/2,2}$ and $u_{1/2,3}$, respectively. Likewise, the frequencies $\bar{\omega}_4$ and $\bar{\omega}_{13}$, marked in light orange, belong to eigenfunctions with the second strongest singularity, $u_{3/2,1}$ and $u_{3/2,2}$, respectively, and so forth. Note that the occurrence of eigenfunctions characterized by identical singularities becomes rare as the frequencies increase. Loosely speaking, as $N \to \infty$, we observe that out of N^2 eigenfunctions, approximately N contain a singularity of type $r^{1/2}$, $r^{3/2}$, and so on.

4.3 Isogeometric discretization and numerical analysis

Having analyzed the explicit solution of the Laplace eigenvalue problem on circular sectors, we now turn to its numerical approximation using isogeometric analysis. In this section, we describe how the graded mesh refinement strategy studied in Chapter 3 for boundary value problems can be applied to the Laplace eigenvalue problem on circular sectors. We further derive corresponding error estimates that ensure optimal convergence of the proposed approach. The arguments presented here are based in part on [AZ24a, Section 4] and [ANZ25, Section 4.1].

4.3.1 Variational formulation

We begin by discretizing the model problem and briefly recall how the Galerkin method, described in Section 2.1.3, is formulated for eigenvalue problems. The variational formulation of (4.1) reads as follows: Find $(\lambda, u) \in \mathbb{R} \times V_0 \setminus \{0\}$ such that

$$a(u, v) = \lambda\, b_{\mathrm{eig}}(u, v) \quad \forall v \in V_0\,, \tag{4.20}$$

Eigenfrequency	Value	$\nu_\ell = \ell/2$	m	Eigenfunction	Regularity
$\bar{\omega}_1$	2.40	0	1	$u_{0,1}$	smooth
$\bar{\omega}_2$	3.14	1/2	1	$u_{1/2,1}$	$H^{3/2-\varepsilon}(\Omega)$
$\bar{\omega}_3$	3.83	1	1	$u_{1,1}$	smooth
$\bar{\omega}_4$	4.49	3/2	1	$u_{3/2,1}$	$H^{5/2-\varepsilon}(\Omega)$
$\bar{\omega}_5$	5.14	2	1	$u_{2,1}$	smooth
$\bar{\omega}_6$	5.52	0	2	$u_{0,2}$	smooth
$\bar{\omega}_7$	5.76	5/2	1	$u_{5/2,1}$	$H^{7/2-\varepsilon}(\Omega)$
$\bar{\omega}_8$	6.28	1/2	2	$u_{1/2,2}$	$H^{3/2-\varepsilon}(\Omega)$
$\bar{\omega}_9$	6.38	3	1	$u_{3,1}$	smooth
$\bar{\omega}_{10}$	6.99	7/2	1	$u_{7/2,1}$	$H^{9/2-\varepsilon}(\Omega)$
$\bar{\omega}_{11}$	7.02	1	2	$u_{1,2}$	smooth
$\bar{\omega}_{12}$	7.59	4	1	$u_{4,1}$	smooth
$\bar{\omega}_{13}$	7.73	3/2	2	$u_{3/2,2}$	$H^{5/2-\varepsilon}(\Omega)$
$\bar{\omega}_{14}$	8.18	9/2	1	$u_{9/2,1}$	$H^{11/2-\varepsilon}(\Omega)$
$\bar{\omega}_{15}$	8.42	2	2	$u_{2,2}$	smooth
$\bar{\omega}_{16}$	8.65	0	3	$u_{0,3}$	smooth
$\bar{\omega}_{17}$	8.77	5	1	$u_{5,1}$	smooth
$\bar{\omega}_{18}$	9.10	5/2	2	$u_{5/2,2}$	$H^{7/2-\varepsilon}(\Omega)$
$\bar{\omega}_{19}$	9.36	11/2	1	$u_{11/2,1}$	$H^{13/2-\varepsilon}(\Omega)$
$\bar{\omega}_{20}$	9.42	1/2	3	$u_{1/2,3}$	$H^{3/2-\varepsilon}(\Omega)$
$\bar{\omega}_{21}$	9.76	3	2	$u_{3,2}$	smooth
$\bar{\omega}_{22}$	9.94	6	1	$u_{6,1}$	smooth

Table 4.1: The eigenfrequencies (4.7) of the unit disk with crack are listed in ascending order within the interval $[0, 10]$. As per equation (4.6), each eigenfrequency corresponds to the m-th root of a Bessel function J_{ν_ℓ}, denoted by $\bar{\omega}_n = \eta_{\nu_\ell,m}$ for some $\nu_\ell \in \{0, \frac{1}{2}, 1, \frac{3}{2}, \dots\}$ and $m \in \mathbb{N}$. Additionally, the corresponding eigenfunctions and their regularity are provided, where $\varepsilon > 0$ is an arbitrarily small constant. Rows containing eigenfunctions with the strongest and second strongest singularity are highlighted in dark orange and light orange, respectively.

where we again employ the bilinear form a defined in (2.8) and introduce

$$b_{\text{eig}} : V \times V \to \mathbb{R}, \quad b_{\text{eig}}(u, v) := \int_\Omega u\, v \,\mathrm{d}\boldsymbol{x},$$

with the spaces V and V_0 chosen as in (2.6). Both bilinear forms are bounded and a is coercive on V_0 since $\Gamma_D \neq \emptyset$, which implies that the spectrum is positive [BO91, Section 4]. More precisely, the weak eigenvalue problem (4.20) admits an unbounded sequence of eigenvalues

$$0 < \lambda_1 \leq \lambda_2 \leq \cdots \nearrow +\infty \tag{4.21}$$

with corresponding linear independent eigenfunctions $u_1, u_2, \dots \in V_0 \setminus \{0\}$ that may be chosen to satisfy the orthogonality condition

$$a(u_i, u_j) = \lambda_i\, b_{\text{eig}}(u_i, u_j) = \lambda_i\, \delta_{ij}, \quad i, j = 1, 2, \dots. \tag{4.22}$$

In the sequence (4.21), eigenvalues are generally repeated according to their geometric multiplicity. However, for the specific domain of a circular sector, we conjecture that the multiplicity is always one; see Section 4.2.1.

In the next step, let $V_{0h} \subset V_0$ be a finite-dimensional subspace. The corresponding discrete variational problem reads: Find $(\lambda_h, u_h) \in \mathbb{R} \times V_{0h} \setminus \{0\}$ such that

$$a(u_h, v_h) = \lambda_h \, b_{\text{eig}}(u_h, v_h) \quad \forall v_h \in V_{0h} \,, \tag{4.23}$$

which yields a finite sequence of eigenvalues [BO91, Section 5]

$$0 < \lambda_{1,h} \leq \lambda_{2,h} \leq \cdots \leq \lambda_{l,h}$$

and corresponding linear independent eigenfunctions $u_{1,h}, u_{2,h}, \ldots, u_{l,h} \in V_{0h} \setminus \{0\}$, where l is the dimension of V_{0h}. In particular, the eigenmodes can be selected from the discrete eigenspaces such that the orthogonality condition

$$a(u_{i,h}, u_{j,h}) = \lambda_{i,h} \, b_{\text{eig}}(u_{i,h}, u_{j,h}) = \lambda_{i,h} \, \delta_{ij}, \quad i, j = 1, 2, \ldots, l. \tag{4.24}$$

is satisfied. Finally, let $\{\phi_1, \phi_2 \ldots, \phi_l\}$ be a basis of V_{0h}, and represent u_h as a linear combination of these basis functions, see (2.10). Substituting this ansatz into the discrete weak formulation (4.23) yields the generalized matrix eigenvalue problem

$$A \, \vec{u}_h = \lambda_h \, M \, \vec{u}_h, \tag{4.25}$$

where

$$A = (a(\phi_j, \phi_i))_{i,j \in \{1,2,\ldots,l\}} \,, \quad \vec{u}_h = \left(u_h^j\right)_{j \in \{1,2,\ldots,l\}} \quad \text{and } M = (b_{\text{eig}}(\phi_j, \phi_i))_{i,j \in \{1,2,\ldots,l\}}$$

Similar to the discussion in Section 2.1.3, under appropriate assumptions on the approximation spaces V_{0h}, the discrete eigenfunctions converge to the exact ones as $h \to 0$.

4.3.2 Mesh grading and error estimates

In the following, we introduce a framework to quantify and analyze the approximation properties of such spaces for eigenvalue problems. Inspired by the classical Babuška-Osborn theory [BO91, Section 8], we define the set of unit eigenfunctions and the corresponding best approximation for an eigenvalue λ by

$$\begin{aligned} M(\lambda) &:= \left\{ u \in V_0 : u \text{ is an eigenfunction of (4.20) to the eigenvalue } \lambda, \ \|u\|_{H^1(\Omega)} = 1 \right\}, \\ \varepsilon_h(\lambda) &:= \sup_{u \in M(\lambda)} \inf_{w_h \in V_{0h}} \|u - w_h\|_{H^1(\Omega)}. \end{aligned} \tag{4.26}$$

In this context, we say that an eigenfunction u of (4.20) is a unit eigenfunction if $\|u\|_{H^1(\Omega)} = 1$; the same convention is used for the discrete eigenfunctions of (4.23). Moreover, we emphasize that the Laplace eigenvalue problem is self-adjoint, which simplifies the analysis. Since the geometric and algebraic multiplicities always coincide, defective eigenvalues cannot occur. Thus, the adjoint eigenvalue problem need not be considered, and the following approximation theorem is a direct consequence of existing results in the literature.

Theorem 4.6. *Let λ_k be an eigenvalue of the variational problem (4.20) of multiplicity $q \in \mathbb{N}$, i.e., $\lambda_k = \lambda_{k+1} = \cdots = \lambda_{k+q-1}$. Then, the estimate*

$$\lambda_k \leq \lambda_{j,h} \leq \lambda_k + C\varepsilon_h^2(\lambda_k), \quad j = k, k+1, \ldots, k+q-1$$

holds. Moreover, let $w_h \in \{u_{k,h}, u_{k+1,h}, \ldots, u_{k+q-1,h}\}$ be a unit eigenfunction of the discrete problem (4.23) corresponding to $\lambda_{k,h}$. Then, there is a unit eigenfunction $u \in M(\lambda_k)$ such that

$$\|u - w_h\|_{H^1(\Omega)} \leq C\varepsilon_h(\lambda_k). \tag{4.27}$$

Vice versa, for every unit eigenfunction $u \in M(\lambda_k)$, there exists a unit discrete function $w_h \in \operatorname{span}\{u_{k,h}, u_{k+1,h}, \ldots, u_{k+q-1,h}\}$ such that (4.27) is satisfied.

Proof. This is a classical result which has been proven in [BO91, Section 8]. □

Since we conjecture that the Laplace eigenvalues of circular sectors are all simple, see Section 4.2.1, we deduce the following corollary as a specialization of Theorem 4.6.

Corollary 4.7. *Let λ_k be a simple eigenvalue of the variational problem (4.20), i.e., $\lambda_k < \lambda_{k+1}$. Then, the estimate*

$$\lambda_k \leq \lambda_{k,h} \leq \lambda_k + C\varepsilon_h^2(\lambda_k)$$

holds. Moreover, for every unit eigenfunction $u_k \in M(\lambda_k)$, there exists a unit discrete eigenfunction $u_{k,h}$ corresponding to the eigenvalue $\lambda_{k,h}$ such that

$$\|u_k - u_{k,h}\|_{H^1(\Omega)} \leq C\varepsilon_h(\lambda_k). \tag{4.28}$$

Conversely, for every unit discrete eigenfunction $u_{k,h}$ corresponding to $\lambda_{k,h}$, there exists a unit eigenfunction $u_k \in M(\lambda_k)$ satisfying (4.28).

Proof. This follows directly from Theorem 4.6 for $q = 1$. □

Essentially, Theorem 4.6 implies that the discrete eigenvalues converge optimally to the continuous ones if the corresponding eigenfunctions are approximated with optimal order. In particular, the eigenvalues converge at twice the rate of the eigenfunction approximation. To ensure the best possible accuracy of the simulation, it is therefore necessary to construct a discrete space V_h in which the eigenfunction error (4.26) decays with optimal order. This requires a discretization that delivers high approximation power and accounts for the specific regularity of the eigenfunctions.

As discussed in Section 4.1, IGA provides superior approximation properties for spectral problems. To treat the corner singularities of the eigenfunctions while preserving spectral accuracy, an appropriate local refinement strategy is required. Since circular sectors can be parameterized exactly by a polar mapping, as described in Example 3.6, this naturally leads us back to the graded mesh refinement approach introduced in Section 3.2. In the following remark, we further justify the choice of such a parameterization.

Remark 4.8. There exist several other ways to parameterize circular sectors than using the polar-like mapping $\boldsymbol{F}$. In particular, a multi-patch approach based on biquadratic NURBS can be employed, which has been proposed in the numerical examples of [LMMT15]. The multi-patch parameterization contains another type of singularities which are located on the circular boundary [TJ11]. Hence, the singularity of the Laplace eigenfunctions does not coincide with the singularities of the isogeometric mapping, which may simplify the problem. However, we prefer the presented single-patch approach for the following reasons:

- As indicated in Section 4.1, previous results about spectral approximation properties of IGA in the literature have been shown for single-patch domains.
- A polar-like discretization seems to be more natural and intuitive when considering circular sectors in an isogeometric context.
- The multi-patch approach leads to redundant control points at the patch junctions which are absent when using only one singularly mapped patch.
- Introducing a numerical framework becomes more complicated when multiple patches are used instead of a single one. Moreover, even though the singularities in the multi-patch parameterization of circular sectors are weaker than the singularity in our single-patch mapping $\boldsymbol{F}$, the necessary regularity assumptions, as discussed in [Baz+06; BBSV14], are not fulfilled. Up to our knowledge, the multi-patch discretization of circular sectors has only been considered numerically so far, but not in the error analysis [LMMT15].

In [AZ24a, Section 4], the concept of graded mesh refinement toward the polar corner $\boldsymbol{P} = \boldsymbol{0}$ is presented explicitly for the circular sector with angle $\omega = 2\pi$, including the resulting refined knot vectors and Bézier meshes. Here, we build on the comprehensive analysis of the method developed in Chapter 3. We employ the approximation space $V_h^{\odot}$ defined in (3.19) and recall that Assumptions 3.4 and 3.5 remain in force. Note that the grading parameter $\mu \in (0, 1]$ and the polynomial degrees $\boldsymbol{p} = (p_1, p_2)$, where $p = \min\{p_1, p_2\}$, are implicitly contained in the definition of $V_h^{\odot}$, although not reflected in the notation. Moreover, $h \sim h_1 \sim h_2$ denotes a suitable mesh parameter for both the uniform and graded meshes, (3.15) and (3.16). In the following lemma, we derive a corresponding error estimate for the Laplace EVP (4.1) on circular sectors.

Lemma 4.9. *Let $(\lambda, u) = (\lambda_{\nu_\ell,m}, u_{\nu_\ell,m})$ be a Laplace eigenpair of a circular sector with angle ω; see (4.6) and (4.5), where $\nu_\ell = \ell\frac{\pi}{\omega}$, $\ell \in \mathbb{N}$, $m \in \mathbb{N}$. Assume that $\lambda = \lambda_n$ is the n-th eigenvalue in the sequence (4.7) and has multiplicity one. On the discrete level, let $V_{0h}^{\odot}$ be the approximation space defined in (3.19), consisting of graded NURBS of order p with associated grading parameter $\mu \in (0, 1]$, and let*

$$\mu < \frac{\nu_\ell}{p}, \qquad n_{\mathrm{dof}} := \dim(V_{0h}^{\odot}) \geq n. \tag{4.29}$$

Then, the discrete eigenvalue $\lambda_h = \lambda_{n,h}$ of (4.23) satisfies

$$\lambda \leq \lambda_h \leq \lambda + Ch^{2p} \sim \lambda + Cn_{\mathrm{dof}}^{-p},$$

Furthermore, for the associated unit eigenfunction $u = u_n \in M(\lambda)$, there exists a unit discrete eigenfunction $u_h = u_{n,h} \in V_{0h}^{\odot} \setminus \{0\}$ of (4.23) corresponding to the eigenvalue λ_h such that

$$\|u - u_h\|_{H^1(\Omega)} \leq Ch^p \sim Cn_{\mathrm{dof}}^{-\frac{p}{2}}.$$

Proof. First, we recall the weighted regularity (4.18) of the eigenfunctions. In particular, with $s = p - 1$, we obtain

$$u = u_{\nu_\ell,m} \in V_\beta^{p+1}(\Omega) \quad \text{for all } \beta \in \mathbb{R} \text{ with } p - \nu_\ell < \beta < p + \nu_\ell,$$

Next, we estimate the error in (4.26). Using the fact that the eigenvalue has multiplicity one and applying Theorem 3.21, we obtain

$$\varepsilon_h(\lambda) = \sup_{u \in M(\lambda)} \inf_{w_h \in V_{0h}^{\odot}} \|u - w_h\|_{H^1(\Omega)} = \inf_{w_h \in V_{0h}^{\odot}} \|u_{\nu_\ell,m} - w_h\|_{H^1(\Omega)} \leq Ch^p \|u_{\nu_\ell,m}\|_{V_\beta^{p+1}(\Omega)},$$

The extension of Theorem 3.21 to the space incorporating Dirichlet boundary conditions $V_{0h}^{\odot}$ is straightforward, since $u_{\nu_\ell,m} \in V_0$. The assertion therefore follows from Corollary 4.7, and the estimates with respect to the number of degrees of freedom follow directly from the relation $n_{\mathrm{dof}} \sim h^{-2}$, which holds due to the quadrilateral structure of the isogeometric meshes. □

From condition (4.29), there is still some freedom in choosing the grading parameter μ for practical computations. Several guidelines have been proposed in the literature; see, for instance, [AM17]. Our numerical experience, illustrated in Example 4.11, suggests the choice

$$\mu = \min\left\{0.9 \cdot \frac{\nu_\ell}{p}, 1\right\}, \tag{4.30}$$

which is consistent with our previous recommendation (3.51). However, in contrast to the boundary value problems considered in Chapter 3, eigenvalue problems admit infinitely many solutions with potentially different regularity; see the analysis in Section 4.2.2. Consequently, several aspects should be taken into account, which we summarize in the following remark.

Remark 4.10. In certain situations, the grading parameter given in (4.30) may not be optimal. Below, we discuss some useful modifications and alternative choices.

1. In Section 4.2.1, we conjecture that the sequence of eigenvalues (4.7) is strictly increasing. Therefore, for simplicity, Lemma 4.9 only considers eigenvalues of multiplicity one. If this conjecture were violated, there could exist eigenvalues $\lambda_{\nu_{\ell_1},m_1} = \lambda_{\nu_{\ell_2},m_2}$ with $\ell_1 < \ell_2$, $m_1, m_2 \in \mathbb{N}$. In such a case, the grading must be chosen with respect to the eignfunctions with the stronger singularity, i.e., $\mu < \frac{\nu_{\ell_1}}{p}$, to ensure optimal convergence.
2. The case $\ell = 0$ is not covered by Lemma 4.9 because the corresponding eigenfunctions $u_{0,m}$, $m \in \mathbb{N}$ do not have the same weighted regularity as the other modes; see Lemma 4.5. However, as noted in Remark 4.4, these eigenfunctions are always smooth. Hence, no local refinement is required, see also Example 3.38, although this case is not covered by our error estimates. Nevertheless, by using the modified weighted regularity (4.18), one can still prove an error estimate that guarantees optimal approximation of the eigenpairs $(\lambda_{0,m}, u_{0,m})$, $m \in \mathbb{N}$, with a grading parameter $\mu < \frac{\nu_1}{p}$. A similar argument has been carried out in [ANZ25, Lemma 4.5].
3. The Laplace eigenmodes of circular sectors exhibit varying regularity. Eigenfunctions with low regularity benefit from graded meshes, which recover the optimal convergence rate that uniform meshes fail to achieve. In contrast, smooth eigenfunctions are typically approximated more efficiently on uniform meshes. Unnecessary grading may deteriorate the approximation constant, yet the convergence rate remains optimal. These effects will be illustrated in our numerical experiments. If the goal is to approximate a specific eigenfunction $u = u_{\nu_\ell,m}$, it is advantageous to choose

$$\mu = \begin{cases} 1, & \text{if } \nu_\ell \in \mathbb{N}_0 \text{ or } \nu_\ell \geq p, \\ 0.9 \cdot \dfrac{\nu_\ell}{p}, & \text{else,} \end{cases} \tag{4.31}$$

   where we recall the regularity results of Lemmata 4.2 and 4.3.
4. According to Section 4.2.2, the strongest singularity that Laplace eigenfunctions of circular sectors can exhibit is of type r^{ν_1} with $\nu_1 = \frac{\pi}{\omega}$. Hence, if the goal is to approximate an arbitrary eigenfunction u that cannot be associated with a specific regularity parameter ν_ℓ, the strongest

grading must be applied,

$$\mu = \min\left\{0.9 \cdot \frac{\nu_1}{p}, 1\right\}. \tag{4.32}$$

The same strategy is appropriate when several eigenfunctions need to be approximated simultaneously with guaranteed accuracy, for instance when computing a portion of the spectrum. Conversely, if lower accuracy for a few highly singular eigenfunctions is acceptable, uniform meshes may be preferable.

4.4 Numerical experiments

Finally, we present a series of numerical experiments that demonstrate the efficiency of graded meshes for approximating the Laplace eigenvalue problem (4.1) on circular sectors, largely following Section 5 of [AZ24a]. First, we illustrate optimal convergence rates under graded h-refinement and verify the suggested grading parameters. In a second experiment, we demonstrate the advantages of the method for computing multiple eigenvalues and further examine the spectral approximation properties of maximally smooth spline spaces on circular sectors. Finally, we combine graded meshes with a hierarchical refinement strategy to avoid anisotropic elements in the physical Bézier mesh and eliminate unnecessary degrees of freedom.

Throughout this section, we focus on the circular sector Ω with angle $\omega = 2\pi$, illustrated in Figure 4.1b, which represents a unit disk with a crack on the positive x-axis. As in Section 4.2.3, it serves as a prototype for all other circular sectors with smaller angles $\omega < 2\pi$, where the same procedure can be carried out in an analogous or even simplified manner.

All numerical experiments are carried out using the Matlab computing package GeoPDEs 3.2.2 [FRV11; Váz16]. The graded h-refinement algorithm is implemented as described in Section 3.5. Since we use a maximal spline degree of 5, all integrals are evaluated using the Gauss–Legendre quadrature rule with 36 Gauss points per mesh element, where 6 quadrature points are employed in each univariate direction. All convergence rates are expressed with respect to the number of degrees of freedom n_{dof}, but without the negative sign; see Lemma 4.9. Note that this differs from the presentation used in the numerical results of Chapter 3.

4.4.1 Optimal convergence and grading parameter

In the first examples, we show that our method produces optimal convergence rates for the model problem and confirm our recommendations for the grading parameter. As discussed in Section 4.2.3, the sequence of eigenmodes consists of both singular and smooth functions which are referred to as eigenfunctions of type (A) and type (B), respectively. We exemplarily pick one eigenfunction out of each group and evaluate the resulting approximation errors.

Example 4.11 (Eigenfunction of type (A)). We approximate the eigenvalue $\lambda_{\nu_1,1}$ of the unit disk with crack and its corresponding eigenfunction $u_{\nu_1,1}$, which has the strongest possible singularity of type r^{ν_1}, where $\nu_1 = \frac{1}{2}$. In Figure 4.4, we illustrate the discrete eigenfunction throughout the gradual refinement process using NURBS of the lowest possible degree $\boldsymbol{p} = (1, 2)$ and regularity $\boldsymbol{k} = (0, 1)$. The solution is showcased for various refinements, ranging from relatively coarse to further refined ones. Figure 4.5 presents the $H^1(\Omega)$- and $L^2(\Omega)$-error of the eigenfunction and the absolute eigenvalue error using NURBS of polynomial degree $\boldsymbol{p} = (p, p)$, $p \in \{2, 3, 4\}$, and regularity $\boldsymbol{k} = (p-1, p-1)$ with varying grading parameters μ. Precisely, we set $\mu = 1$ for uniform and $\mu = 0.9\frac{\nu_1}{p}$ for graded refinement, as proposed in formula (4.30). On uniform meshes, the

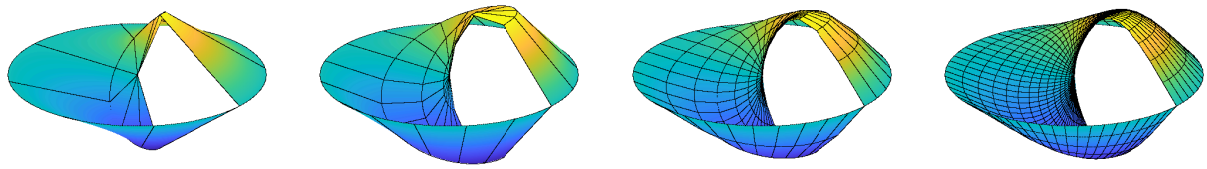

Figure 4.4: Approximation of the eigenfunction $u_{\nu_1,1}$ using NURBS of lowest possible degree $\boldsymbol{p} = (p_1, p_2) = (1, 2)$ and regularity $\boldsymbol{k} = (0, 1)$ while gradually refining the coarse mesh $2, 4, 8, 16$ times with the grading parameter $\mu = 0.9 \cdot \frac{\nu_1}{p_1} = 0.45$, recall (4.32).

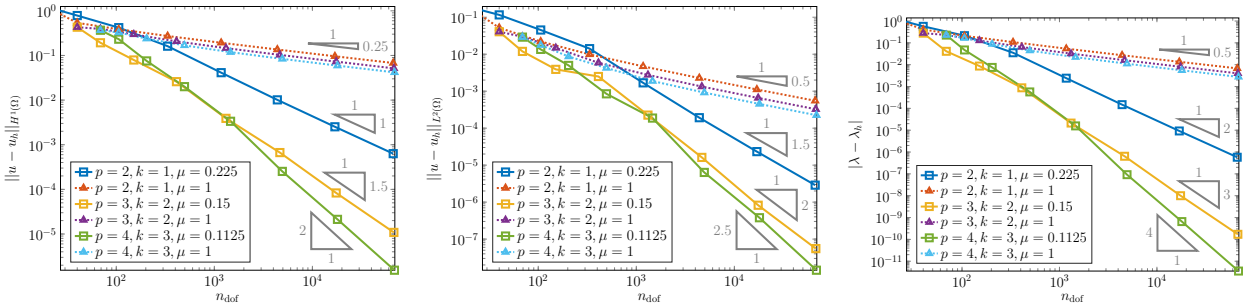

Figure 4.5: Approximation errors for the eigenfunction $u = u_{\nu_1,1}$ and its corresponding eigenvalue $\lambda = \lambda_{\nu_1,1}$ using gradually and uniformly refined NURBS of degree $\boldsymbol{p} = (p, p)$, $p \in \{2, 3, 4\}$, and regularity $\boldsymbol{k} = (p - 1, p - 1)$. We set $\mu = 0.9\frac{\nu_1}{p} = \frac{0.9}{2p}$ for graded meshes and $\mu = 1$ corresponds to uniform refinement.

eigenfunction approximation converges in the $H^1(\Omega)$- and $L^2(\Omega)$-norms with rates $\frac{\nu_1}{2} = \frac{1}{4}$ and $\frac{2\nu_1}{2} = \frac{1}{2}$, respectively, for all p, in agreement with Remark 3.35 when translated into convergence rates with respect to $n_{\mathrm{dof}} \sim h^{-2}$. In contrast, graded meshes yield the optimal convergence orders $\frac{p}{2}$ and $\frac{p+1}{2}$ with respect to the number of degrees of freedom, as predicted by the error estimate in Lemma 4.9. Consequently, under uniform refinement, the discrete eigenvalue converges to the exact one with order $\frac{1}{2}$ for any p, whereas mesh grading recovers the optimal convergence rate p.

In a second test, we compute the same eigenpair using gradually refined NURBS of degree $\boldsymbol{p} = (2, 2)$ and regularity $\boldsymbol{k} = (1, 1)$, but this time for a range of different grading parameters $\mu \in \{0.7\frac{\nu_1}{p}, 0.9\frac{\nu_1}{p}, 1.1\frac{\nu_1}{p}, 1.3\frac{\nu_1}{p}\}$. Tables 4.2 and 4.3 list the $H^1(\Omega)$-errors of the eigenfunction and the absolute eigenvalue errors, respectively, together with the corresponding experimental orders of convergence (EOC) with respect to the number of degrees of freedom n_{dof}. We observe suboptimal convergence orders for grading parameters $\mu > \frac{\nu_1}{p}$. These have not yet reached the rates $\frac{\nu_1}{2\mu}$ and $\frac{\nu_1}{\mu}$ listed in the last row of the tables, which are obtained by translating the predictions in Remark 3.35 into rates with respect to n_{dof}, indicating a pre-asymptotic effect. Among the two sufficiently graded meshes, the moderate grading with $\mu = 0.9\frac{\nu_1}{p}$ is preferable over the option $\mu = 0.7\frac{\nu_1}{p}$ due to an improved approximation constant, thereby validating our explicit recommendation (4.30). For C^0-continuous splines, we observe a similar behavior. In Tables 4.4 and 4.5, we show the $H^1(\Omega)$-errors of the eigenfunction and the absolute eigenvalue errors, respectively, together with the corresponding experimental convergence rates for NURBS of degree $\boldsymbol{p} = (2, 2)$ and regularity $\boldsymbol{k} = (0, 0)$. Again, we see that the choice $\mu = 0.9\frac{\nu_1}{p}$ leads to the best approximation constant while guaranteeing optimal convergence rates.

Moreover, a comparison of the last lines of Tables 4.2 and 4.4 indicates that the approximation constant for the $H^1(\Omega)$-error of the eigenfunction is about four times larger for C^0-continuous

n_{dof}	$\mu = 0.7\frac{\nu_1}{p} = 0.175$	$\mu = 0.9\frac{\nu_1}{p} = 0.225$	$\mu = 1.1\frac{\nu_1}{p} = 0.275$	$\mu = 1.3\frac{\nu_1}{p} = 0.325$
19	$1.2500e+00$	$1.2500e+00$	$1.2500e+00$	$1.2500e+00$
40	$8.4778e-01$ (0.59)	$7.8366e-01$ (0.71)	$7.3268e-01$ (0.82)	$6.9185e-01$ (0.90)
106	$5.3217e-01$ (0.53)	$4.1982e-01$ (0.71)	$3.4478e-01$ (0.85)	$2.9860e-01$ (0.95)
334	$2.3431e-01$ (0.76)	$1.6133e-01$ (0.89)	$1.1590e-01$ (1.01)	$9.1099e-02$ (1.10)
1174	$6.6457e-02$ (1.04)	$4.1166e-02$ (1.13)	$2.9150e-02$ (1.14)	$2.4590e-02$ (1.08)
4390	$1.6234e-02$ (1.09)	$1.0125e-02$ (1.09)	$7.4213e-03$ (1.06)	$7.0980e-03$ (0.96)
16966	$4.0166e-03$ (1.04)	$2.5243e-03$ (1.04)	$1.9224e-03$ (1.01)	$2.1679e-03$ (0.89)
66694	$1.0014e-03$ (1.02)	$6.3171e-04$ (1.02)	$5.0293e-04$ (0.98)	$6.9175e-04$ (0.84)
264454	$2.5016e-04$ (1.01)	$1.5817e-04$ (1.01)	$1.3267e-04$ (0.97)	$2.2764e-04$ (0.81)
			$\frac{\nu_1}{2\mu} \approx 0.909$	$\frac{\nu_1}{2\mu} \approx 0.769$

Table 4.2: Approximation errors $\|u - u_h\|_{H^1(\Omega)}$ (and corresponding EOC with respect to n_{dof}) for the eigenfunction $u = u_{\nu_1,1}$ using gradually refined NURBS of degree $\boldsymbol{p} = (2,2)$ and regularity $\boldsymbol{k} = (1,1)$ with different grading parameters μ.

n_{dof}	$\mu = 0.7\frac{\nu_1}{p} = 0.175$	$\mu = 0.9\frac{\nu_1}{p} = 0.225$	$\mu = 1.1\frac{\nu_1}{p} = 0.275$	$\mu = 1.3\frac{\nu_1}{p} = 0.325$
19	$1.3869e+00$	$1.3869e+00$	$1.3869e+00$	$1.3869e+00$
40	$6.4991e-01$ (1.16)	$5.7113e-01$ (1.35)	$5.1477e-01$ (1.51)	$4.7780e-01$ (1.63)
106	$2.9613e-01$ (0.89)	$2.1387e-01$ (1.11)	$1.5767e-01$ (1.34)	$1.2036e-01$ (1.56)
334	$7.2689e-02$ (1.30)	$3.5189e-02$ (1.68)	$1.8634e-02$ (1.98)	$1.1722e-02$ (2.16)
1174	$6.2156e-03$ (2.03)	$2.4139e-03$ (2.21)	$1.2198e-03$ (2.25)	$8.7535e-04$ (2.14)
4390	$3.7938e-04$ (2.16)	$1.4801e-04$ (2.16)	$7.9694e-05$ (2.11)	$7.3365e-05$ (1.92)
16966	$2.3343e-05$ (2.08)	$9.2259e-06$ (2.08)	$5.3569e-06$ (2.02)	$6.8598e-06$ (1.77)
66694	$1.4526e-06$ (2.04)	$5.7818e-07$ (2.03)	$3.6684e-07$ (1.97)	$6.9934e-07$ (1.68)
264454	$9.0687e-08$ (2.02)	$3.6253e-08$ (2.02)	$2.5533e-08$ (1.94)	$7.5794e-08$ (1.62)
			$\frac{\nu_1}{\mu} \approx 1.818$	$\frac{\nu_1}{\mu} \approx 1.538$

Table 4.3: Approximation errors $|\lambda - \lambda_h|$ (and corresponding EOC with respect to n_{dof}) for the eigenvalue $\lambda = \lambda_{\nu_1,1}$ using gradually refined NURBS of degree $\boldsymbol{p} = (2,2)$ and regularity $\boldsymbol{k} = (1,1)$ with different grading parameters μ.

n_{dof}	$\mu = 0.7\frac{\nu_1}{p} = 0.175$	$\mu = 0.9\frac{\nu_1}{p} = 0.225$	$\mu = 1.1\frac{\nu_1}{p} = 0.275$	$\mu = 1.3\frac{\nu_1}{p} = 0.325$
19	$1.2500e+00$	$1.2500e+00$	$1.2500e+00$	$1.2500e+00$
69	$8.4272e-01$ (0.34)	$7.7901e-01$ (0.41)	$7.2859e-01$ (0.47)	$6.8807e-01$ (0.52)
265	$5.0853e-01$ (0.40)	$3.8736e-01$ (0.56)	$3.1956e-01$ (0.66)	$2.7379e-01$ (0.74)
1041	$2.0838e-01$ (0.68)	$1.4368e-01$ (0.75)	$1.0577e-01$ (0.84)	$8.5486e-02$ (0.89)
4129	$6.1687e-02$ (0.90)	$3.9273e-02$ (0.96)	$2.8324e-02$ (0.98)	$2.4196e-02$ (0.94)
16449	$1.5879e-02$ (0.99)	$9.9994e-03$ (1.00)	$7.3687e-03$ (0.98)	$7.0632e-03$ (0.90)
65665	$3.9938e-03$ (1.00)	$2.5163e-03$ (1.00)	$1.9187e-03$ (0.98)	$2.1609e-03$ (0.86)
262401	$9.9992e-04$ (1.00)	$6.3120e-04$ (1.00)	$5.0257e-04$ (0.97)	$6.8945e-04$ (0.83)

Table 4.4: Approximation errors $\|u - u_h\|_{H^1(\Omega)}$ (and corresponding EOC with respect to n_{dof}) for the eigenfunction $u = u_{\nu_1,1}$ using gradually refined NURBS of degree $\boldsymbol{p} = (2,2)$ and regularity $\boldsymbol{k} = (0,0)$ with different grading parameters μ.

n_{dof}	$\mu = 0.7\frac{\nu_1}{p} = 0.175$	$\mu = 0.9\frac{\nu_1}{p} = 0.225$	$\mu = 1.1\frac{\nu_1}{p} = 0.275$	$\mu = 1.3\frac{\nu_1}{p} = 0.325$
19	$1.3869e+00$	$1.3869e+00$	$1.3869e+00$	$1.3869e+00$
69	$6.4264e-01$ (0.67)	$5.6592e-01$ (0.78)	$5.1135e-01$ (0.87)	$4.7551e-01$ (0.93)
265	$2.8072e-01$ (0.66)	$1.9449e-01$ (0.85)	$1.3751e-01$ (1.05)	$1.0247e-01$ (1.23)
1041	$5.8947e-02$ (1.19)	$2.8602e-02$ (1.46)	$1.5714e-02$ (1.65)	$1.0398e-02$ (1.74)
4129	$5.3909e-03$ (1.77)	$2.2029e-03$ (1.90)	$1.1530e-03$ (1.94)	$8.4806e-04$ (1.86)
16449	$3.6315e-04$ (1.97)	$1.4437e-04$ (1.99)	$7.8573e-05$ (1.96)	$7.2659e-05$ (1.80)
65665	$2.3079e-05$ (2.00)	$9.1678e-06$ (2.00)	$5.3367e-06$ (1.95)	$6.8164e-06$ (1.72)
262401	$1.4484e-06$ (2.00)	$5.7725e-07$ (2.00)	$3.6631e-07$ (1.94)	$6.9483e-07$ (1.65)

Table 4.5: Approximation errors $|\lambda - \lambda_h|$ (and corresponding EOC with respect to n_{dof}) for the eigenvalue $\lambda = \lambda_{\nu_1,1}$ using gradually refined NURBS of degree $\boldsymbol{p} = (2,2)$ and regularity $\boldsymbol{k} = (0,0)$ with different grading parameters μ.

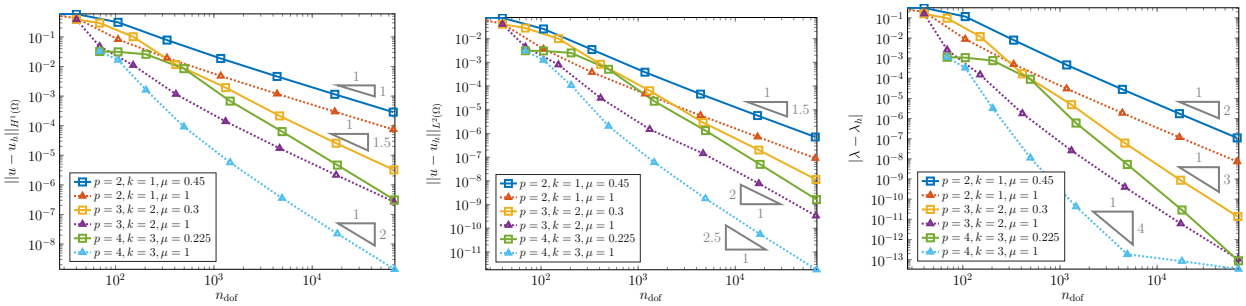

Figure 4.6: Approximation errors for the eigenfunction $u = u_{\nu_2,1}$ and its corresponding eigenvalue $\lambda = \lambda_{\nu_2,1}$ using gradually and uniformly refined NURBS of degree $\boldsymbol{p} = (p,p)$, $p \in \{2,3,4\}$, and regularity $\boldsymbol{k} = (p-1, p-1)$. We set $\mu = 0.9\frac{\nu_2}{p} = \frac{0.9}{p}$ for graded meshes and $\mu = 1$ corresponds to uniform refinement.

splines than for their smooth counterparts, while approximately the same number of degrees of freedom is used. Analogously, a comparison of Tables 4.3 and 4.5 reveals a similar trend for the eigenvalue error. We therefore conclude that smooth splines exhibit better convergence per degree of freedom than their C^0-continuous counterparts.

Example 4.12 (Eigenfunction of type (B)). Next, we approximate the eigenvalue $\lambda_{\nu_2,1}$ of the unit disk with crack and its corresponding eigenfunction $u = u_{\nu_2,1}$, where $\nu_2 = 1$. As shown in Lemma 4.3, this is a smooth function. Figure 4.6 depicts the $H^1(\Omega)$- and $L^2(\Omega)$-error of the eigenfunction and the absolute eigenvalue error using NURBS of polynomial degree $\boldsymbol{p} = (p,p)$, $p \in \{2,3,4\}$, and regularity $\boldsymbol{k} = (p-1, p-1)$ with different grading parameters μ. Here, the convergence orders under uniform and graded refinement are identical, but the approximation constant of the uniform meshes is superior. This result justifies the recommended grading parameter (4.31) when approximating a specific eigenfunction with known regularity. Similar to Example 3.38, we observe better convergence on uniform meshes than predicted by Corollary 3.22. The V-regularity stated in Lemma 4.5 is not sufficient to prove optimal higher-order convergence for this eigenfunction with the tools available in this thesis, which indicates that the error estimate may not be sharp.

4.4.2 Spectral approximation properties of smooth splines on circular sectors

As discussed before, the solution of an eigenvalue problem is not just given by single eigenvalues and eigenfunctions but by an infinite sequence of such. Therefore, we use our approach to compute multiple solutions of the model problem (4.1) in the next numerical experiment. The different regularity properties of the exact Laplace eigenfunctions, outlined in Section 4.2.2, will be crucial to understand the numerical results.

In this context, it is of interest whether some of the spectral approximation properties of smooth splines, which have been shown for rectangular domains in the literature [CHB09; HHRS21; MSS22; SMS19] can be extended to circular sectors. In most of the related works, the full discrete spectrum is approximated, that is, one discrete eigenvalue is computed per computational degree of freedom. The power of smooth splines in this setting is twofold. First, finite elements produce so-called spectral branches, i.e., the eigenvalue error jumps for higher frequencies, a phenomenon which does not occur with maximally smooth splines. Second, the overall approximation constant of smooth splines is better over the whole discrete spectrum. In the following, we conduct numerical studies to investigate comparable properties of the discrete spectrum of circular sectors.

At this point, smooth splines on circular sectors should be treated with some caution. As outlined in Example 3.6, a circular sector with angle $\omega > \pi$ is constructed from several smaller sectors using repeated knot values. Consequently, the parameterization $\boldsymbol{F}$ is only C^0-continuous along the corresponding mesh lines, see Remark 3.9. For instance, in the case of a unit disk with crack, the NURBS in the approximation space $V_{0h}^{\odot}$ are C^0-continuous along the lines $\{(r\cos\varphi, r\sin\varphi) : r \in (0,1), \varphi \in \{\frac{\pi}{2}, \pi, \frac{3\pi}{2}\}\}$, that is, along the coarse mesh lines illustrated in Figure 4.1b. However, this limitation has only a minor impact on the overall smoothness of the NURBS basis functions, since, in all regions between these C^0-interfaces, the regularity can be increased arbitrarily by applying the k-refinement algorithm introduced in Section 2.2.1.

Example 4.13. We compute the full discrete spectrum of the unit disk with crack using different parameters, all of which result in systems with a total of 916 degrees of freedom. More precisely, bicubic C^2-continuous NURBS and biquintic C^4-continuous NURBS on uniform and graded meshes are compared with their C^0-continuous counterparts. As explained in Remark 4.10, we choose the strong grading parameter $\mu = 0.9\frac{\nu_1}{p}$ for the graded meshes, since we aim to compute the entire discrete spectrum at once and some eigenfunctions exhibit the strongest singularity of type r^{ν_1}. Figure 4.7 presents the relative eigenvalue errors, ordered by the discrete eigenvalue size. For both types of mesh, it becomes evident that the approximation accuracy of the displayed spectrum increases with higher NURBS regularity, except for the very upper part of the spectrum. Hence, the positive findings concerning the approximation constant of smooth splines, which have been illustrated in the literature for rectangular domains, can be extended to the case of circular sectors, at least in the lower part of the spectrum. However, we cannot identify the appearance of spectral branches. Our results on uniform meshes optically resemble those in [BDQ15], where the Laplace-Beltrami eigenvalue problem has been considered on the unit sphere. In general, higher eigenvalues are approximated better on uniform meshes, which can be attributed to their superior approximation constants on coarse refinement levels, as also observed in Examples 4.11 and 4.12. This is also related to the fact that mesh grading, at the cost of local refinement in the vicinity of the polar corner, produces larger elements away from it; see the sketch in Figure 3.3.

Remark 4.14. In Example 4.13 and Figure 4.7, each discrete eigenvalue is associated to an exact eigenvalue by ordering both sequences in ascending order. However, this matching is not always correct, that is, a discrete eigenvalue $\lambda_{n,h}$ might be an approximation of the exact eigenvalue λ_m with $n \neq m$. Techniques for a proper association of discrete and exact eigenvalues have been

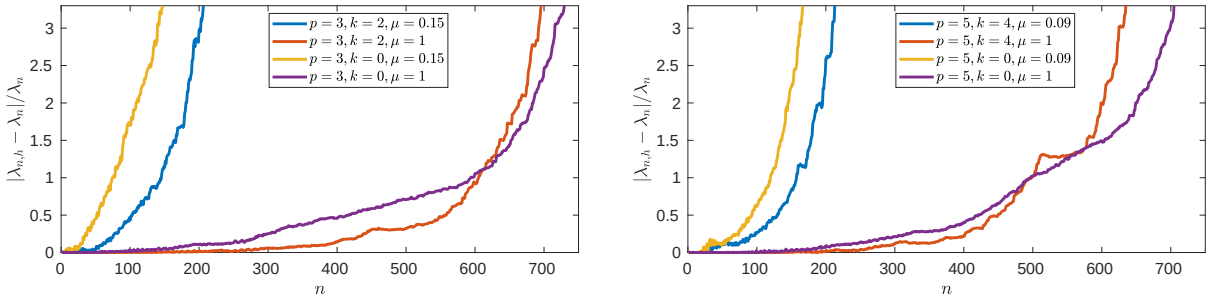

Figure 4.7: Relative eigenvalue errors, ordered by discrete eigenvalue size, using gradually and uniformly refined NURBS of degree $\boldsymbol{p} = (p, p)$ and regularity $\boldsymbol{k} = (k, k)$. A total of 916 degrees of freedom are used in all computations. For graded meshes, we set $\mu = 0.9\frac{\nu_1}{p} = \frac{0.9}{2p}$, while $\mu = 1$ corresponds to uniform refinement.

proposed in the literature, but it has also been observed that the impact of mismatching is marginal [GGHO21; HHRS21; HRS08; MSS22].

To demonstrate the strength of our proposed graded refinement approach, we need to adopt a slightly different point of view. The primary benefit of gradually refined NURBS is the optimal approximation of eigenfunctions with low regularity and their corresponding eigenvalues. This property is asymptotic which only comes into effect for an increasing number of computational degrees of freedom. Therefore, we decide to compute a fixed number of discrete eigenvalues and increase the number of degrees of freedom. Since our objective is to approximate the eigenvalues of circular sectors in the best possible way and the accuracy of Galerkin methods generally decreases for higher frequencies [SF08, Chapter 6.3], it is natural to consider only the lower discrete eigenvalues and refine the mesh. The analysis of spectral branches up to the highest discrete frequencies is of particular interest for related time-dependent problems in explicit numerical schemes since the critical time-step size calculation is inversely proportional to the maximum discrete eigenfrequency [Hug12]. However, this is beyond the scope of this dissertation.

Example 4.15. We compare the relative errors for the 100 smallest Laplace eigenvalues of the unit disk with crack using suitably graded and uniform meshes. Again, we choose the strong grading parameter $\mu = 0.9\frac{\nu_1}{p}$ since we want to approximate multiple eigenvalues at once with a guaranteed optimal convergence rate.

First, we employ biquadratic, C^1-continuous NURBS in a system with 67731 degrees of freedom, which arises for 128 subdivisions of the coarse mesh in each parametric direction as discussed in Section 3.2.2. The results are presented in the left hand plot of Figure 4.8. The uniform mesh produces some very poor approximations alongside many accurate ones. More precisely, the approximations of the eigenvalues $\lambda_2, \lambda_8, \lambda_{20}, \ldots$ are significantly less accurate than the others. Table 4.1 shows that these eigenvalues correspond to eigenfunctions with the lowest possible regularity, for which uniform refinement does not yield optimal convergence, as outlined in Example 4.11. Consequently, these eigenvalues appear as outliers in the spectral approximation, whereas the remaining eigenvalues correspond to eigenfunctions of higher regularity that are accurately approximated even on uniform meshes. In contrast, the eigenvalue errors achieved by the graded mesh are evenly distributed. All the eigenvalues are approximated with a comparable accuracy, which is naturally decreasing for higher eigenvalues. In particular, the outliers of the uniform version, $\lambda_2, \lambda_8, \lambda_{20}, \ldots$, are approximated much better on the graded mesh. However, the graded approximation of the remaining eigenvalues with corresponding eigenfunctions of higher regularity is worse than the uniform variant. For this

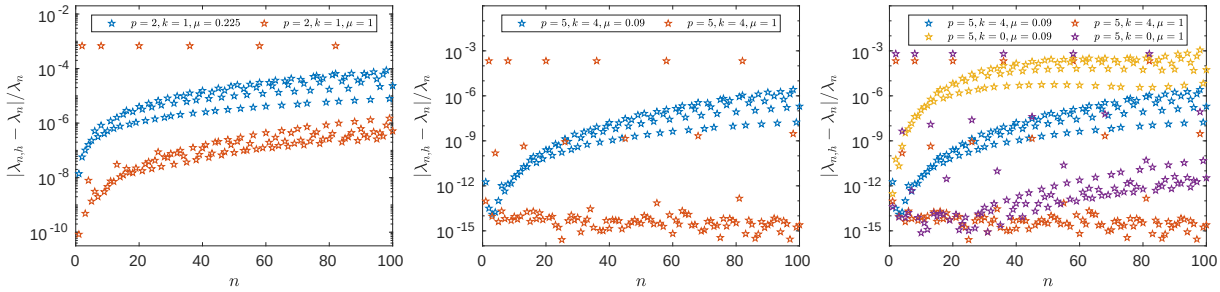

Figure 4.8: Relative errors of the first 100 eigenvalues, ordered by the size of the discrete eigenvalues, computed using graded and uniform NURBS discretizations of degree $\boldsymbol{p} = (p, p)$ and regularity $\boldsymbol{k} = (k, k)$. A total of 67731 degrees of freedom are used in all computations. For graded meshes, we set $\mu = 0.9\frac{\nu_1}{p} = \frac{0.9}{2p}$, while $\mu = 1$ corresponds to uniform refinement.

type of eigenvalues, the grading is unnecessary and has a negative effect on the approximation constant, as noted in Remark 4.10 and Example 4.12.

In a second test, we employ biquintic, C^4-continuous NURBS in a system with 67731 degrees of freedom on a uniform and graded mesh. The relative eigenvalue errors are depicted in the middle plot of Figure 4.8. Here, in addition to the poor approximations of $\lambda_2, \lambda_8, \lambda_{20}, \dots$, the uniform mesh produces a second group of outliers, given by the eigenvalues $\lambda_4, \lambda_{13}, \lambda_{26}, \dots$. In Table 4.1, we observe that these eigenvalues belong to eigenfunctions with the second strongest singularity. Due to the high degree of the NURBS, the difference between optimal and reduced convergence rates also becomes noticeable for this group of eigenvalues. Contrarily, the graded mesh produces an evenly distributed error point cloud, but less accurate results for eigenvalues that correspond to smoother eigenfunctions.

Lastly, we compare biquintic C^4-continuous NURBS with their C^0-continuous counterparts on uniform and graded meshes. The results are presented in the right hand plot of Figure 4.8. For both types of mesh, the approximation is more accurate with smooth splines, although the same number of degrees of freedom is used. The superiority of smooth splines is even clearer on graded meshes as they do not produce outliers. Hence, we can again confirm the excellent spectral approximation constant of smooth splines on circular sectors. Since we consider only the very lower part of the spectrum here, which can not be analyzed in the study conducted in Figure 4.7, this series of results complements the previous findings of Example 4.13.

In summary, the two numerical examples of this section show that the combination of mesh grading toward the polar corner with maximally smooth splines is a very powerful approach to approximate the Laplace eigenvalues of circular sectors. It is computationally cheap, accurate and produces an evenly distributed error throughout the considered eigenvalues.

4.4.3 Hierarchical meshes in combination with graded refinement

Both the graded parametric and physical Bézier meshes contain anisotropic elements. The aspect ratio of the rectangular parametric elements $Q_{\boldsymbol{j}} \in \widehat{\mathcal{M}}^{\mu}$ close to the singular edge of $\widehat{\Omega}$ is given by

$$\frac{h_2}{h_1^{1/\mu}} = C h^{1-\frac{1}{\mu}} \to \infty \quad \text{for } h_1 = h_2 = h \to 0 \text{ and } \mu < 1. \tag{4.33}$$

Thus, the elements are highly stretched in ζ_2-direction. This effect is fully induced by the mesh grading and depends on the grading parameter μ. For $\mu = 1$ and $\frac{1}{C}h_2 \leq h_1 \leq C h_2$, that is, for

evenly uniform refinement in both directions, the aspect ratio (4.33) is constant and the mesh is isotropic.

In contrast, the latter does not hold for the physical Bézier mesh. We compute the aspect ratio of the elements $K_{\boldsymbol{j}} \in \mathcal{M}^{\mu}$ close to the singular point $\boldsymbol{S}$ using the lengths of their largest edges,

$$\frac{h_1^{1/\mu}}{h_1^{1/\mu} h_2} = \frac{1}{h} \to \infty \quad \text{for } h_1 = h_2 = h \to 0. \tag{4.34}$$

The elements are highly stretched in radial direction, corresponding to the ζ_1-direction in the parametric domain. Hence, the stretching direction is reversed from the parametric to the physical mesh. Moreover, the physical mesh elements are anisotropic regardless of the mesh grading as the aspect ratio (4.34) does not depend on the grading parameter μ. Consequently, the anisotropy in the physical mesh is exclusively induced by the singular parameterization $\boldsymbol{F}$.

Therefore, we present a variation of our method that aims at improving the constructed physical Bézier mesh. To prevent the highly stretched elements near the conical point, we replace the tensor product meshes used so far by hierarchical meshes. In Figure 4.9, we illustrate the hierarchical mesh scheme exemplarily for the unit disk with crack in combination with both uniform and graded refinement. Again, this serves as a prototype for other circular sectors. Note that the refinement is fixed a priori and not chosen in an adaptive way, as it is typically the case in the context of hierarchical splines. Similar ideas have been mentioned in the context of singularly parameterized triangles [Tak12], subdivision based isogeometric analysis [Tak25], or finite element methods on spherical domains [AP05]. In GeoPDEs, the hierarchical refinement scheme can be implemented by using the extension of the package presented in [GV18]. It leads to a purely isotropic mesh in the physical domain; the corresponding aspect ratio (4.34) simplifies to

$$\frac{h_1^{1/\mu}}{h_1^{1/\mu}} = 1.$$

Besides, the hierarchical meshes offer another advantage. As outlined in Section 3.3.1, the standard isogeometric approximation space has to be modified since the basis functions associated to the control points at the center of the circular sector do not belong to the solution space of the weak problem. By employing a hierarchical approach, the number of mesh elements in the vicinity of the conical point and thus the number of such problematic basis functions is held constant over the refinement steps, which is not the case for tensor product refinement. We visualize this effect in Figure 4.10.

In the following numerical examples, we test the described hierarchical approach for approximating the Laplace eigenvalues and eigenfunctions of circular sectors.

Example 4.16 (**Eigenfunction of type (A)**)**.** We perform the same experiment as in Example 4.11, this time employing a hierarchical refinement approach. In more detail, we compute the eigenvalue $\lambda_{\nu_1,1}$ of the unit disk with crack and its corresponding eigenfunction $u_{\nu_1,1}$, which is characterized by its low regularity, on both uniform and graded hierarchical meshes. The approximation errors for NURBS of polynomial degree $\boldsymbol{p} = (p, p)$, where $p \in \{2, 3, 4\}$, and regularity $\boldsymbol{k} = (p-1, p-1)$ are presented in Figure 4.11 and closely resemble those obtained with tensor product meshes in Figure 4.5. Optimal convergence rates for the $H^1(\Omega)$- and $L^2(\Omega)$-error of the eigenfunction and the absolute eigenvalue error are recovered by using an appropriate grading parameter. An explicit comparison of the approximation errors generated by hierarchical and tensor product meshes is depicted in Figure 4.12, where NURBS of degree $\boldsymbol{p} = (4, 4)$ and regularity $\boldsymbol{k} = (3, 3)$ are gradually and uniformly refined using the grading parameters $\mu = 0.9\frac{\nu_1}{4} = 0.1125$

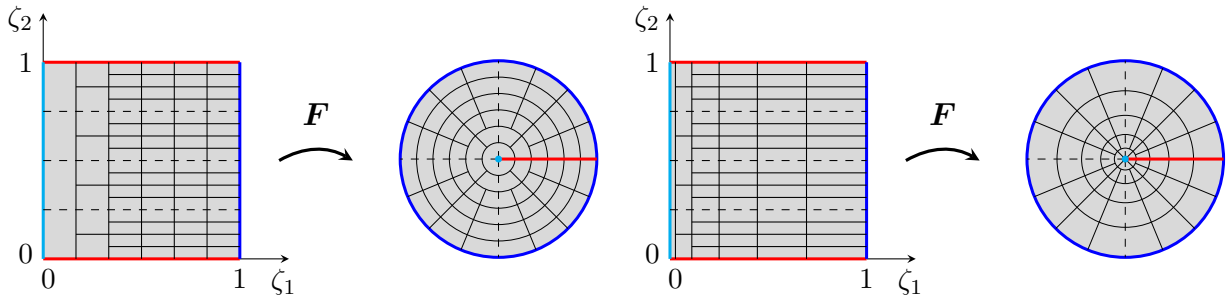

(a) (b)

Figure 4.9: Illustration of hierarchical refinement scheme. Solid black lines are used for new subdivisions and dashed black lines for the initial coarse meshes $\widehat{\mathcal{M}_0}$ and $\mathcal{M}_0$. (a) Uniform refinement ($\mu = 1$). (b) Graded refinement ($\mu < 1$).

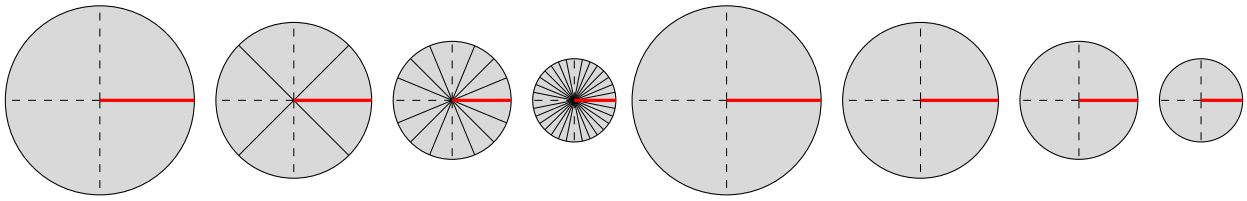

(a) (b)

Figure 4.10: Sketch of the physical mesh elements near the conical point during refinement. (a): Tensor product meshes. (b): Hierarchical meshes. The scaling between refinement steps is manipulated for better visibility.

and $\mu = 1$, respectively. We observe a slightly improved approximation constant for the hierarchical approach, which can be attributed to the reduction in degrees of freedom near the conical point, while retaining optimal convergence. In addition, the necessary grading parameter for the hierarchical approach needs to be investigated numerically in more detail by considering different choices of μ, since this type of refinement is not yet covered by our theory. However, the computational results for eigenfunctions of type (A) are omitted here, since they are very similar to those obtained with tensor product meshes in Example 4.11, reported in Tables 4.2, 4.3, 4.4, and 4.5, suggesting again a necessary condition of the form $\mu < \frac{\nu_1}{p}$.

Example 4.17 (**Eigenfunction of type (B)**)**.** Next, we repeat the experiment from Example 4.12, but now using the hierarchical refinement scheme. We approximate the smooth eigenfunction $u_{\nu_2,1}$ and its corresponding eigenvalue $\lambda_{\nu_2,1}$ of the unit disk with crack on both uniform and graded hierarchical meshes. The approximation errors for NURBS of polynomial degree $\boldsymbol{p} = (p, p)$, where $p \in \{2, 3, 4\}$, and regularity $\boldsymbol{k} = (p-1, p-1)$ are illustrated in Figure 4.13 and clearly differ from the ones obtained with tensor product refinement in Figure 4.6. Independent of the NURBS degree, the convergence rates for the $H^1(\Omega)$- and $L^2(\Omega)$-error of the eigenfunction and the absolute eigenvalue error generated by uniform hierarchical refinement are $\frac{\nu_2}{2} = \frac{1}{2}$, $\frac{2\nu_2}{2} = 1$ and $\frac{2\nu_2}{2} = 1$, respectively, and thus not optimal. In contrast, graded hierarchical meshes do produce optimal convergence rates of $\frac{p}{2}$, $\frac{p+1}{2}$ and p, respectively. The different precisions obtained with hierarchical and tensor product meshes are demonstrated explicitly in Figure 4.14, where NURBS of degree $\boldsymbol{p} = (4, 4)$ and regularity

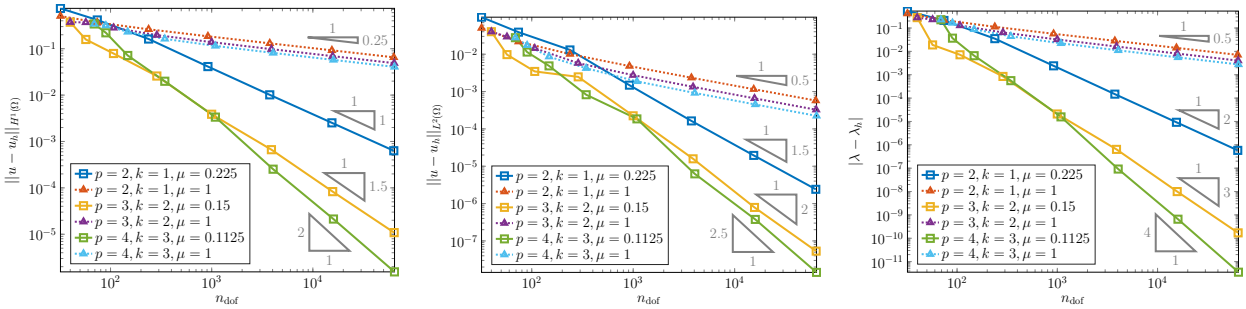

Figure 4.11: Approximation errors for the eigenfunction $u = u_{\nu_1,1}$ and its corresponding eigenvalue $\lambda = \lambda_{\nu_1,1}$ using gradually and uniformly refined hierarchical NURBS of degree $\boldsymbol{p} = (p, p)$, $p \in \{2, 3, 4\}$, and regularity $\boldsymbol{k} = (p-1, p-1)$. We set $\mu = 0.9\frac{\nu_1}{p} = \frac{0.9}{2p}$ for graded meshes and $\mu = 1$ corresponds to uniform refinement.

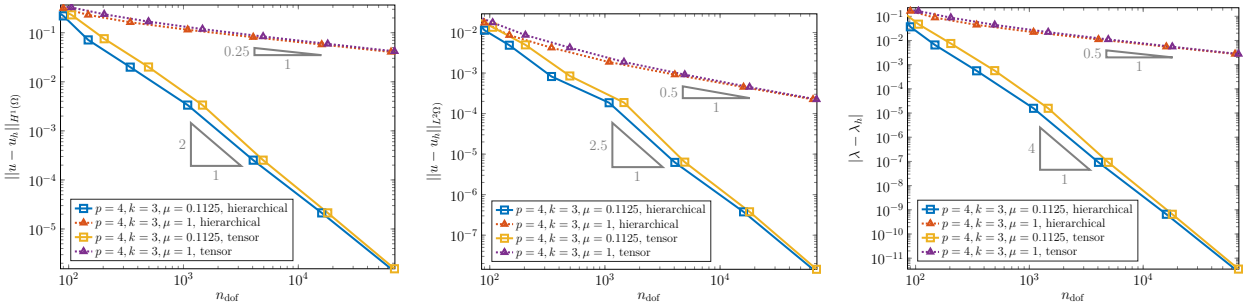

Figure 4.12: Approximation errors for the eigenfunction $u = u_{\nu_1,1}$ and its corresponding eigenvalue $\lambda = \lambda_{\nu_1,1}$ using NURBS of degree $\boldsymbol{p} = (4, 4)$ and regularity $\boldsymbol{k} = (3, 3)$ on tensor product and hierarchical meshes. We set $\mu = 0.9\frac{\nu_1}{4} = 0.1125$ for graded meshes and $\mu = 1$ corresponds to uniform refinement.

$\boldsymbol{k} = (3, 3)$ are refined both gradually and uniformly with grading parameters $\mu = 0.9\frac{\nu_1}{4} = 0.1125$ and $\mu = 1$, respectively. These results indicate that graded refinement compensates for the suboptimal approximation of smooth PDE solutions with such hierarchical splines.

To further investigate this phenomenon, we assess the optimal grading parameter for hierarchical meshes numerically. We compute the same eigenpair, now using gradually refined NURBS of degree $\boldsymbol{p} = (2, 2)$ and regularity $\boldsymbol{k} = (1, 1)$ with a range of grading parameters $\mu \in \{0.7\frac{\nu_2}{p}, 0.9\frac{\nu_2}{p}, 1.1\frac{\nu_2}{p}, 1.3\frac{\nu_2}{p}\}$. Tables 4.6 and 4.7 list the $H^1(\Omega)$-errors of the eigenfunction and the absolute eigenvalue errors, respectively, together with the corresponding experimental orders of convergence. We observe suboptimal rates for grading parameters $\mu > \frac{\nu_2}{p}$, which appear to be given by $\frac{\nu_2}{2\mu}$ for the eigenfunction error and by $\frac{\nu_2}{\mu}$ for the eigenvalue error, as stated explicitly in the last row of the tables and in systematic agreement with the rates for singular solutions discussed in Remark 3.35. For $\mu < \frac{\nu_2}{p}$, by contrast, we observe optimal convergence rates. Among the sufficiently graded meshes, the moderate grading with $\mu = 0.9\frac{\nu_2}{p}$ is preferable over the stronger grading with $\mu = 0.7\frac{\nu_2}{p}$ due to an improved approximation constant.

To close this chapter, we comment on the different approximation properties of hierarchical and tensor product meshes observed in Examples 4.16 and 4.17. For eigenfunctions of type (A), both types of mesh exhibit very similar approximation behavior, apart from a slightly different approximation constant, which suggests that an error estimate analogous to Lemma 4.9 can be

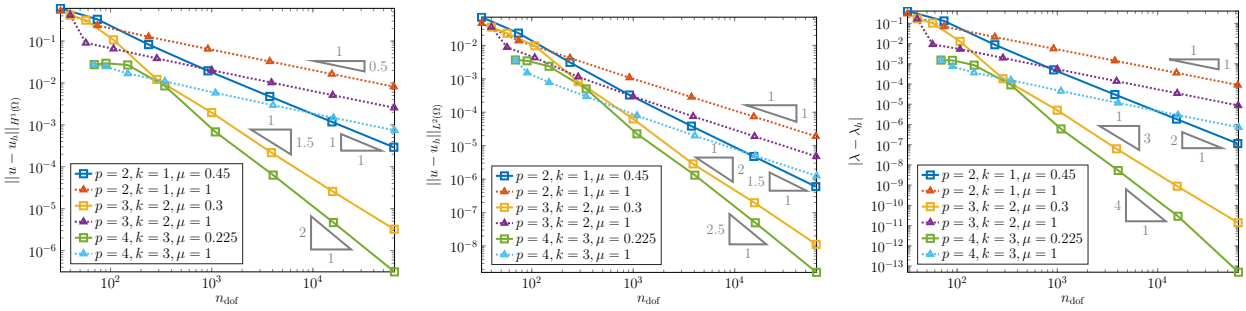

Figure 4.13: Approximation errors for the eigenfunction $u = u_{\nu_2,1}$ and its corresponding eigenvalue $\lambda = \lambda_{\nu_2,1}$ using gradually and uniformly refined hierarchical NURBS of degree $\boldsymbol{p} = (p, p)$, $p \in \{2, 3, 4\}$, and regularity $\boldsymbol{k} = (p-1, p-1)$. We set $\mu = 0.9\frac{\nu_2}{p} = \frac{0.9}{p}$ for graded meshes and $\mu = 1$ corresponds to uniform refinement.

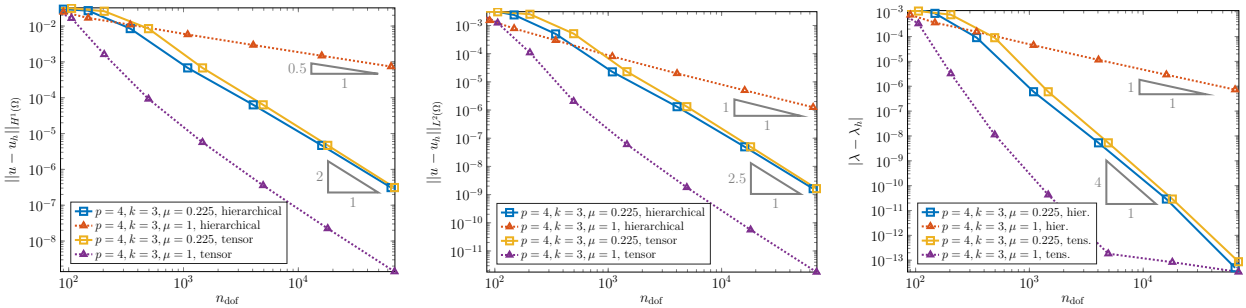

Figure 4.14: Approximation errors for the eigenfunction $u = u_{\nu_2,1}$ and its corresponding eigenvalue $\lambda = \lambda_{\nu_2,1}$ using NURBS of degree $\boldsymbol{p} = (4, 4)$ and regularity $\boldsymbol{k} = (3, 3)$ on tensor product and hierarchical meshes. We set $\mu = 0.9\frac{\nu_2}{4} = 0.225$ for graded meshes and $\mu = 1$ corresponds to uniform refinement.

established for hierarchical meshes. In contrast, the results differ clearly for eigenfunctions of type (B). In this case, uniform tensor product meshes yield optimal convergence, whereas uniformly refined hierarchical meshes lead to suboptimal rates that can be remedied by grading. Thus, the need for grading is caused not by the regularity of the approximated eigenfunction, but by the hierarchical mesh structure. Therefore, for this type of hierarchical splines, we recommend the grading parameter

$$\mu = 0.9\frac{\nu_\ell}{p}$$

for the approximation of a specific eigenfunction $u_{\nu_\ell,m}$, regardless of its type. This differs significantly from the previous guideline (4.31) for tensor product meshes, where uniform refinement is recommended for eigenfunctions of type (B).

At this point, we observe that the approximation behavior described above is closely related to the theory developed in Section 3.4. In particular, the error estimate in Corollary 3.22 yields optimal convergence on uniform meshes only for a specific class of functions with weighted regularity, but not for functions that are smooth in the classical Sobolev sense. For tensor product meshes, this estimate does not seem to be sharp; see also the discussion in Examples 3.38 and 4.12. However, for the hierarchical meshes considered here, this behavior is reflected exactly in the numerical results. By Lemma 4.3, the eigenfunctions of type (B) belong to every classical Sobolev space $H^s(\Omega)$, $s \in \mathbb{N}$,

n_{dof}	$\mu = 0.7\frac{\nu_2}{p} = 0.35$	$\mu = 0.9\frac{\nu_2}{p} = 0.45$	$\mu = 1.1\frac{\nu_2}{p} = 0.55$	$\mu = 1.3\frac{\nu_2}{p} = 0.65$
32	$5.6582e-01$	$6.0335e-01$	$6.1669e-01$	$6.1087e-01$
74	$4.3238e-01$ (0.37)	$3.3039e-01$ (0.84)	$2.6714e-01$ (1.17)	$2.3424e-01$ (1.34)
238	$1.2868e-01$ (1.10)	$8.2363e-02$ (1.26)	$6.7629e-02$ (1.25)	$7.1675e-02$ (1.08)
918	$3.0357e-02$ (1.09)	$1.9502e-02$ (1.09)	$1.7540e-02$ (1.02)	$2.2973e-02$ (0.86)
3750	$7.4289e-03$ (1.00)	$4.7691e-03$ (1.01)	$4.6465e-03$ (0.95)	$7.5817e-03$ (0.79)
15430	$1.8469e-03$ (0.99)	$1.1794e-03$ (0.99)	$1.2449e-03$ (0.93)	$2.5485e-03$ (0.77)
63110	$4.6106e-04$ (0.99)	$2.9289e-04$ (0.99)	$3.3634e-04$ (0.93)	$8.6597e-04$ (0.77)
256262	$1.1522e-04$ (0.99)	$7.2890e-05$ (0.99)	$9.1552e-05$ (0.93)	$2.9603e-04$ (0.77)
			$\frac{\nu_2}{2\mu} \approx 0.909$	$\frac{\nu_2}{2\mu} \approx 0.769$

Table 4.6: Approximation errors $\|u - u_h\|_{H^1(\Omega)}$ (and corresponding EOC with respect to n_{dof}) for the eigenfunction $u = u_{\nu_2,1}$ using gradually refined hierarchical NURBS of degree $\boldsymbol{p} = (2,2)$ and regularity $\boldsymbol{k} = (1,1)$ with different grading parameters μ.

n_{dof}	$\mu = 0.7\frac{\nu_2}{p} = 0.35$	$\mu = 0.9\frac{\nu_2}{p} = 0.45$	$\mu = 1.1\frac{\nu_2}{p} = 0.55$	$\mu = 1.3\frac{\nu_2}{p} = 0.65$
32	$4.0667e-01$	$4.0420e-01$	$3.9597e-01$	$3.8085e-01$
74	$2.0471e-01$ (0.96)	$1.3166e-01$ (1.56)	$8.8493e-02$ (2.09)	$6.9630e-02$ (2.37)
238	$2.0781e-02$ (2.08)	$8.7422e-03$ (2.47)	$5.9965e-03$ (2.45)	$6.7821e-03$ (2.12)
918	$1.2085e-03$ (2.15)	$5.0176e-04$ (2.16)	$4.0802e-04$ (2.03)	$7.0223e-04$ (1.71)
3750	$7.3097e-05$ (2.00)	$3.0168e-05$ (2.01)	$2.8704e-05$ (1.89)	$7.6576e-05$ (1.58)
15430	$4.5285e-06$ (1.97)	$1.8474e-06$ (1.98)	$2.0615e-06$ (1.86)	$8.6548e-06$ (1.54)
63110	$2.8239e-07$ (1.97)	$1.1397e-07$ (1.98)	$1.5053e-07$ (1.86)	$9.9936e-07$ (1.53)
256262	$1.7639e-08$ (1.98)	$7.0592e-09$ (1.99)	$1.1154e-08$ (1.86)	$1.1679e-07$ (1.53)
			$\frac{\nu_2}{\mu} \approx 1.818$	$\frac{\nu_2}{\mu} \approx 1.538$

Table 4.7: Approximation errors $|\lambda - \lambda_h|$ (and corresponding EOC with respect to n_{dof}) for the eigenvalue $\lambda = \lambda_{\nu_2,1}$ using gradually refined hierarchical NURBS of degree $\boldsymbol{p} = (2,2)$ and regularity $\boldsymbol{k} = (1,1)$ with different grading parameters μ.

but not to the weighted space $V_\beta^{p+1}(\Omega)$ for all $\beta \in \mathbb{R}$ with $p - \nu < \beta < p$ and $\nu > p$, for any polynomial order $p \geq 1$. Accordingly, in Example 4.17, the experimental convergence rate observed on uniformly refined hierarchical meshes is bounded by the exponent $\nu_2 = 1$, independent of the spline degree p. This suggests that the numerical analysis developed in Section 3.4 may indeed be sharp, at least for non-tensor-product meshes. These observations are consistent with the theoretical findings in [Tak25]. An intuitive explanation for the suboptimal uniform approximation behavior is that the size of hierarchical mesh elements near the conical point, as illustrated in Figure 4.10b, does not decrease sufficiently fast under uniform refinement. With appropriate grading toward the conical point, however, this issue can be compensated.

In summary, the combination of hierarchical meshes and graded refinement appears promising, although both the implementation and the analysis are more involved. A detailed study of the approximation properties is left for future work, for which the present results may serve as a starting point.

CHAPTER 5

Can one hear the shape of a crack in a drum?

In the last main chapter of this thesis, we employ the simulation framework developed in Chapter 3, and in particular its spectral approximation properties investigated in Chapter 4, for an application in the context of crack identification. The methodology and results are based on our work [ANZ25], and the central question is reflected in both the title of our paper and the title of this chapter: *Can one hear the shape of a crack in a drum?* In other words, can the geometry of a crack be determined from the Laplace spectrum of the associated domain? The problem setting is illustrated in Figure 1.2 and will be explained in detail in the next section.

The chapter is organized as follows. In Section 5.1, we motivate the topic, position our work within the existing literature, and outline the novel contributions. Section 5.2 introduces the Laplace spectrum and the heat trace of a domain together with its short-time asymptotic expansion. Based on these quantities, in Section 5.3 we analyze how cracks leave distinct spectral fingerprints in the heat trace, thereby ensuring the well-posedness of the corresponding inverse problem. Guided by the preceding insights, Section 5.4 turns to a complementary data-driven approach in which a neural network trained on simulated data is used to predict the shape of a crack in a membrane.

5.1 Motivation and novelties

This section closely follows Section 1 of [ANZ25], with a more explicit presentation of the novel contributions. Let $\Omega \subset \mathbb{R}^2$ be a bounded planar domain which contains a fracture in the form of a crack Γ_c. Assume that, for some reason, we cannot observe the fracture directly – its position, orientation, and shape are unknown. What we can assess, however, are the eigenfrequencies $(\bar{\omega}_n)_{n\in\mathbb{N}}$ of the domain, or at least a finite subset of them. In a mathematical framework, these frequencies correspond to the spectrum of the Laplace operator acting on Ω. The central question of this work is whether such a crack can be uniquely identified based solely on the spectral fingerprints of a domain. In more detail, the goal is to determine whether the Laplace spectrum encodes sufficient information about the presence, size, location, or geometry of the crack. Considering the physical interpretation of Laplace eigenvalues as the audible frequencies of a vibrating membrane, we can reformulate this problem in the spirit of Kac [Kac66] as the catchy title question *Can one hear the shape of a crack in a drum?* We will also refer to this question as the isospectral problem for cracks

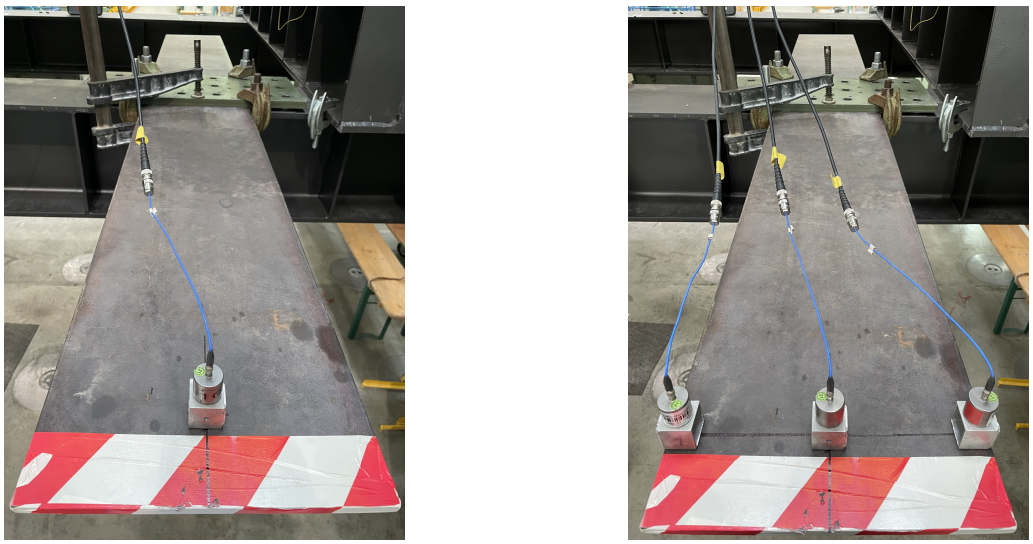

(a) (b)

Figure 5.1: Experimental setup to measure the frequencies of a plate with piezoelectric sensors. (a): One sensor. (b): Three sensors. [Photos: P. Zilk]

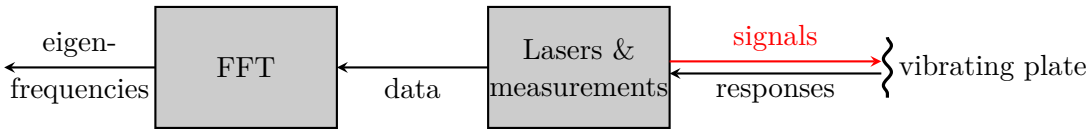

Figure 5.2: Functionality of scanning vibrometer.

in membranes. In the first part of this chapter, we decode the spectral fingerprints of a crack by a thorough analysis of the heat trace of the corresponding domain, which is defined as the sum of exponentials of the negative Laplace eigenvalues and encodes geometric information through the short-time behavior of heat diffusion. In the second part, we present a data-based perspective that allows us to localize cracks in a computational manner. A graphical abstract of our work is provided in Figure 1.2.

From an experimental point of view, the required spectral data can be assessed through a variety of modern techniques. Piezoelectric sensors, as shown in the real-world pictures in Figure 5.1, can record vibrations of macroscopic structures and are commonly used in structural health monitoring systems. For smaller, more delicate specimens, high-resolution devices such as the PSV-400 Scanning Vibrometer allow for non-contact, laser-based vibration analysis. Figure 5.2 illustrates such a setup, and photos of an actual implementation are shown in Figure 5.3.

Theoretical interest in spectral geometry is often traced back to the seminal question "Can one hear the shape of a drum?" posed by Kac in 1966 [Kac66]. While the general answer is negative – as already suggested by Milnor's earlier work [Mil64] and later proven by Gordon, Webb, and Wolpert in 1992 through their famous construction of isospectral domains [GWW92] – a significant number of positive results about what can indeed be heard have been established for specific geometries and settings. These include several fundamental spectral invariants: the area of the domain [Wey12], the perimeter length of the boundary [Ple54], curvature integrals and heat trace coefficients [MS67], as

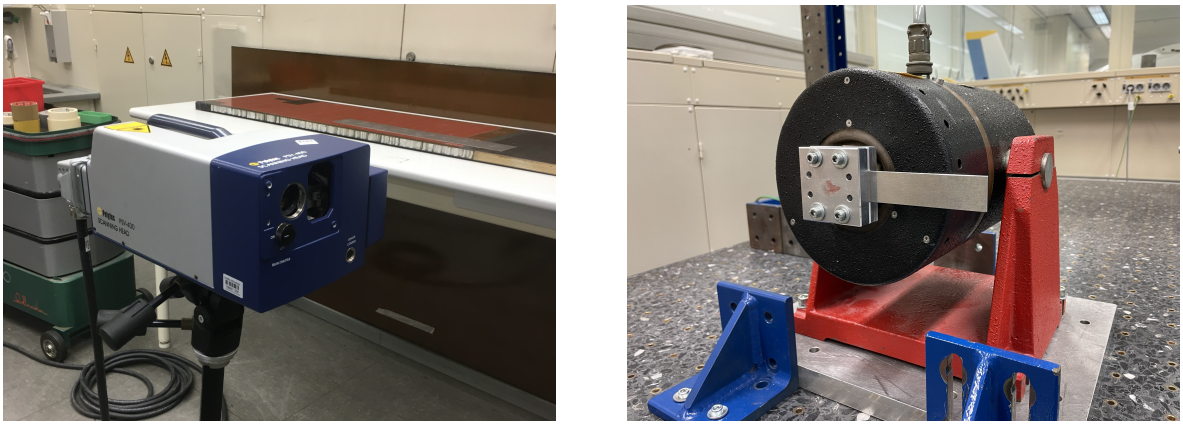

(a) (b)

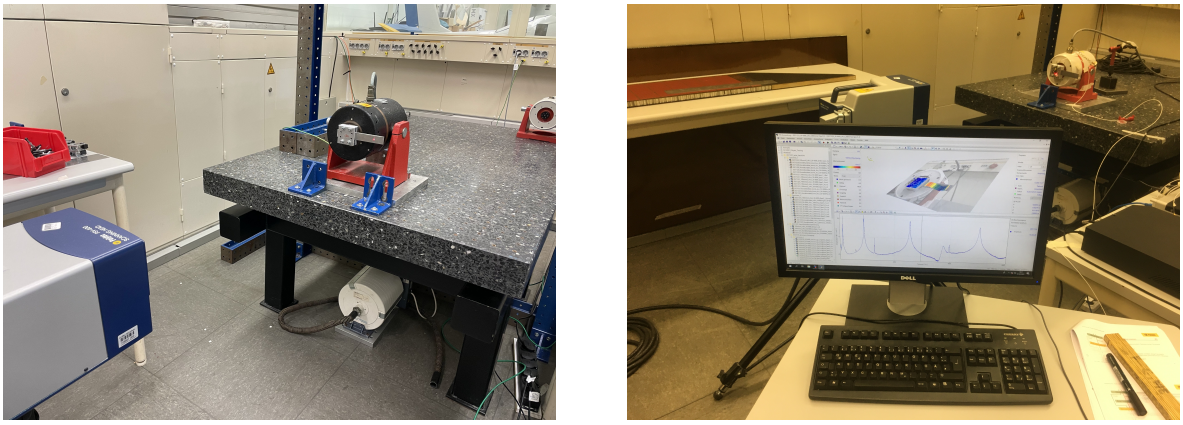

(c) (d)

Figure 5.3: Experimental setup to measure the eigenfrequencies of a small plate. (a): Laser. (b): Plate clamped on one side and connected to a vibration stimulator. (c): Complete setup. (d): Animation of the eigenmodes and eigenfrequencies. [Photos: P. Zilk]

well as topological properties such as the Euler characteristic and number of connected components or holes [Kac66; MS67]. More recently, corners and singularities in the domain have also been shown to influence the spectrum in a detectable way [LR16; NRS19; NRS24].

A deeper study of symmetry effects, including the role of group actions on isospectrality, has led to insights in both theoretical and constructive directions [LR15; Zel00]. In some cases, specific shapes are spectrally determined: the spectrum uniquely identifies rectangles and squares, and it has also been shown to determine triangles [Dur88; GM13], parallelograms [LR15], trapezoids [HLR21; HLR17], tori [NRR23], ellipses [HZ22] and even analytic domains under certain assumptions [Zel04; Zel09]. These results typically rely on a mix of analytical tools from microlocal analysis, heat kernel expansions, and wave trace formulas, which can all be defined by the Laplace spectrum.

On the application side, geometric information that is encrypted in spectral data has been exploited across diverse fields. In industry, vibration analysis is already implemented widely for non-destructive testing in order to detect the existence of material damage by a change of the associated vibrations. In computer graphics and geometric modeling, Laplace spectra have become a popular tool for shape comparison and classification. The concept of Shape DNA, introduced by Reuter et al. [RWP06], refers, by analogy to the unique identifier in human genetics, to a

compact, isometry-invariant descriptor of a shape based on its low-frequency eigenvalues. Along similar lines, Bronstein et al. developed Shape Google, a method using diffusion geometry and spectral signatures to index and retrieve 3D shapes from large databases [BBGO11]. Moreover, eigenfunctions, especially the first few, often carry geometric meaning beyond their corresponding eigenvalues. For instance, the nodal sets and critical points of eigenfunctions have been studied for tasks such as shape segmentation, skeletonization, and even modeling of biological growth patterns [GN13; Lev06; Reu+09; RWSN09]. Related spectral methods have also been applied widely in medical imaging [Nie+07; WR16]. Further advancements include the development of spectral shape descriptors like the Heat Kernel Signature and the Wave Kernel Signature, which provide insights into the local and global geometric structures of shapes. These descriptors have been instrumental in applications such as non-rigid shape retrieval and symmetry detection [ASC11; SOG09]. Moreover, the reconstruction of shapes via matching spectra is another direction of recent research [Cos+19]. This is a non-exhaustive list of spectral methods; for more references, we refer the interested reader to the literature overviews given in the works mentioned above.

In summary, the literature on shape identification via spectral geometry encompasses foundational theoretical works and practical applications, highlighting the profound connection between the geometry of a shape and its spectral characteristics. In this chapter, we bridge theory and application by studying the inverse spectral problem in domains with cracks. The main novel contributions are as follows.

- **Characterization of spectral crack fingerprints via heat trace analysis:** Using the short-time asymptotic expansion of the heat trace, we explicitly characterize certain fingerprints that cracks leave in the Laplace spectrum of the underlying domain.
- **Spectral determination of the existence, length, and angle of a crack:** Based on the derived spectral invariants, we show that the existence and length of a crack and, under additional assumptions, also the angle between the crack and the tangential direction of the boundary can be recovered from the eigenfrequencies of the domain, thereby establishing the well-posedness of the corresponding isospectral problems.
- **A data-driven framework for crack identification:** Complementing the analytical results, we propose a computational approach in which neural networks are trained on simulated eigenvalues to identify geometry parameters of cracks. Evaluation on the test set demonstrates accurate predictions.
- **Accurate solution of a parametric eigenvalue problem using IGA:** The training data is generated by computing Laplace eigenvalues of domains with cracks via isogeometric analysis, where the crack geometry depends on a set of parameters. To treat the singularities of eigenfunctions arising at crack tips, we represent the domains using polar geometry mappings and apply the graded meshes introduced in Section 3.2. The favorable spectral approximation properties of the method, as discussed in Chapter 4, enable accurate simulation of the resulting parametric eigenvalue problem.
- **Error control for spectral computations:** Based on the numerical analysis developed in Chapter 3, we derive error estimates for the numerical simulations to ensure the reliability of the computed spectra, taking into account the singular behavior near crack tips. Numerical experiments confirm our theoretical results.
- **Integration of spectral theory, numerical analysis, and machine learning:** This work combines spectral geometry, high-order numerical simulation, and data-driven methods in a unified framework for crack identification. To the best of our knowledge, such a combination has not been addressed in the literature before.

5.2 Short-time asymptotic expansion of the heat trace

We begin by fixing the notation and introducing the central spectral quantities, following Section 2 of [ANZ25]. Consider a bounded domain $\Omega \subset \mathbb{R}^2$ with boundary $\Gamma = \partial\Omega$. Moreover, let Γ_D and Γ_N be two open subsets of Γ such that $\Gamma = \overline{\Gamma_D} \cup \overline{\Gamma_N}$ and $\Gamma_D \cap \Gamma_N = \emptyset$; these are called the Dirichlet and Neumann boundaries of Ω, respectively. The Laplace EVP has already been introduced in detail in Chapter 4, where it was considered only for the specific domain of a circular sector. Here, we consider the same problem (4.1), but now on general domains. For this reason, we refer to it as the Laplace eigenvalue problem on $(\Omega, \Gamma_D, \Gamma_N)$. It is solved by non-zero eigenfunctions $u_1, u_2, \dots$, forming an orthonormal basis of $L^2(\Omega)$, see also (4.22), and by a corresponding unbounded sequence of non-negative eigenvalues $\lambda_1, \lambda_2, \dots$, which are repeated according to their multiplicity [BO91]. Another difference from Chapter 4 is that the case $\Gamma_D = \emptyset$ is also allowed, which leads to the first eigenvalue being $\lambda_1 = 0$. Hence, the resulting sequence of eigenvalues takes the slightly more general form

$$0 \leq \lambda_1 \leq \lambda_2 \leq \cdots \nearrow +\infty. \tag{5.1}$$

We call the pairs (u_i, λ_i), $i = 1, 2, \dots$, the Laplace eigenpairs of $(\Omega, \Gamma_D, \Gamma_N)$, and their components Laplace eigenfunctions and eigenvalues of $(\Omega, \Gamma_D, \Gamma_N)$, respectively. The sequence (5.1) is often labeled the Laplace spectrum, or briefly the spectrum, of $(\Omega, \Gamma_D, \Gamma_N)$. For simplicity, we sometimes refer to the corresponding quantities only of the domain Ω, without explicitly mentioning the different boundary parts. The associated eigenfrequencies $\bar{\omega}_i = \sqrt{\lambda_i}$, $i = 1, 2, \dots$, are what can be heard when a drum, consisting of a membrane spanned over Ω and clamped at Γ_D, is played [BO91]. In this context, the following remark clarifies the interpretation of the clamped boundary condition.

Remark 5.1. If u is continuous on $\overline{\Omega}$ – or at least in a neighborhood of the Dirichlet boundary, that is, on an open subset $G \subset \overline{\Omega}$ with $\overline{\Gamma_D} \subset G$ – then the Dirichlet boundary condition is satisfied on the closure $\overline{\Gamma_D}$. In physical terms, this means that the membrane is clamped along a closed portion of the boundary.

Based on the Laplace spectrum, we can define the *heat trace* of $(\Omega, \Gamma_D, \Gamma_N)$ by

$$H : (0, \infty) \to \mathbb{R}, \quad H(t) := \operatorname{Tr}\left(e^{-t\Delta}\right) := \sum_{k=1}^{\infty} e^{-\lambda_k t}. \tag{5.2}$$

The term heat trace originates from its connection to the heat equation, which models the diffusion of heat in a domain over time. Mathematically, the heat trace is the total contribution of all vibrational (or diffusive) modes at time t. Each term $e^{-\lambda_k t}$ describes how fast the n-th mode has decayed due to diffusion, and the sum gives a global measure of how much heat remains at time t. The quantity is called a trace since, formally, it represents the trace of the operator $e^{-t\Delta}$ on $L^2(\Omega)$ – that is, the sum of its diagonal entries in the orthonormal eigenbasis $\{u_i\}_{i=1}^{\infty}$.

It is crucial to note that the heat trace is fully determined by the Laplace spectrum, and is therefore called an isospectral invariant. In other words, the heat traces of two domains Ω_1 and Ω_2 differ if and only if the domains have different spectra. This property has been widely exploited in the literature to identify geometric information about a domain via its eigenfrequencies. The short-time asymptotic expansion of the heat trace establishes a direct relationship between the shape of a domain and its heat trace, since the coefficients in the expansion depend on geometric quantities. The development of this connection goes back to Weyl's seminal work in 1912 [Wey12] and has been progressively refined since; see Section 5.1. In its most general form, it has recently been established in [NRS24] for curvilinear polygonal domains as introduced in Definition 2.2. The corresponding short-time asymptotic expansion of the heat trace is stated in the following theorem.

Theorem 5.2. *Let $\Omega \subset \mathbb{R}^2$ be a bounded curvilinear polygonal domain with Dirichlet and Neumann boundaries $\Gamma = \overline{\Gamma_D} \cup \overline{\Gamma_N}$ and finitely many vertices $\boldsymbol{V}_i \in \Gamma$, $i = 0, 1, \dots, m$, with corresponding interior angles $\omega_i \in (0, 2\pi]$, $i = 0, 1, \dots, m$. Further, let*

- *$|\Omega|$ be the area of the domain,*
- *$\mathcal{E} = \{E_1, E_2, \dots, E_n\}$ denote the set of boundary edges between two vertices, and*

$$|\Gamma_D| = \sum_{E \in \mathcal{E} : E \subset \Gamma_D} |E| \quad \text{and} \quad |\Gamma_N| = \sum_{E \in \mathcal{E} : E \subset \Gamma_N} |E|$$

  be the perimeter of the Dirichlet and Neumann boundary, respectively, where $|E|$ is the perimeter of the edge E and it is assumed that either $E \subset \Gamma_D$ or $E \subset \Gamma_N$ holds for all $E \in \mathcal{E}$,
- *κ_g be the geodesic curvature of the boundary away from the vertices,*
- *$\mathcal{V} = \{\boldsymbol{V}_0, \boldsymbol{V}_1, \dots, \boldsymbol{V}_N\}$ be the set of all vertices, with $I_=$ being the set of indices $i \in \{0, 1, \dots, N\}$ such that the vertex $\boldsymbol{V}_i$ has either two adjacent Dirichlet or two adjacent Neumann edges, and $I_{\neq}$ being the complementary set of indices, that is, all i such that one Dirichlet and one Neumann edge are adjacent to $\boldsymbol{V}_i$.*

Then, the heat trace of $(\Omega, \Gamma_D, \Gamma_N)$ has the short-time asymptotic expansion

$$H(t) = H_{-1}\, t^{-1} + H_{-1/2}\, t^{-1/2} + H_0 + \mathcal{O}(t^{1/2} \log t) \tag{5.3}$$

for $t \searrow 0$, with the coefficients

$$\begin{aligned} H_{-1} &= \frac{|\Omega|}{4\pi}, \\ H_{-1/2} &= \frac{|\Gamma_N| - |\Gamma_D|}{8\sqrt{\pi}}, \\ H_0 &= \frac{1}{12\pi} \int_{\Gamma \setminus \mathcal{V}} \kappa_g \, \mathrm{d}s + \sum_{i \in I_=} \frac{\pi^2 - \omega_i^2}{24\pi\omega_i} + \sum_{i \in I_{\neq}} \frac{-\pi^2 - 2\omega_i^2}{48\pi\omega_i}. \end{aligned}$$

Proof. For interior angles $\omega_i < 2\pi$ at the vertices, the result is a simplified variant of [NRS24, Theorem 1.2]. If a vertex with angle $\omega_i = 2\pi$ occurs, the assertion follows by similar arguments, provided that homogeneous boundary conditions are prescribed on both boundary edges adjacent to that specific vertex. This requirement is guaranteed by the definition of the corresponding Laplace eigenvalue problem (4.1) considered here. □

Remark 5.3. By analyzing the asymptotic expansion in Theorem 5.2, we can immediately deduce that several geometric quantities are spectral invariants, meaning that they are uniquely determined by the Laplace spectrum.

1. The coefficient H_{-1} governs the area of the domain. In other words, one can hear the size of a drum, as first observed by Weyl [Wey12].
2. The term $H_{-1/2}$ reflects the difference between the lengths of the Neumann and Dirichlet boundaries. Hence, if one of the lengths is known a priori, the other can also be heard from the spectrum.
3. The coefficient H_0 involves a curvature integral and the contributions of the vertex angles. If all but one of these quantities are known beforehand, the remaining one can be recovered spectrally.

This strategy will be employed in Section 5.3 to analyze the spectral signatures of cracks and the associated geometric invariants under suitable assumptions.

5.3 Spectral fingerprints of a crack in the heat trace

Now, we apply the spectral results presented above to domains with cracks. In particular, based on Section 3 of [ANZ25], we identify characteristic spectral fingerprints in the corresponding heat trace using its short-time asymptotic expansion from Theorem 5.2.

5.3.1 Modeling of a crack

We begin by introducing a mathematical model for the representation of a crack. Let $\Omega \subset \mathbb{R}^2$ be a bounded domain with Dirichlet and Neumann boundaries Γ_D and Γ_N, respectively, such that $\Gamma = \overline{\Gamma_D} \cup \overline{\Gamma_N}$ and $\Gamma_D \cap \Gamma_N = \emptyset$; recall the definitions in Section 5.2.

Definition 5.4. A subset $\Gamma_c \subset \overline{\Omega}$ is called a *crack* in Ω if the following conditions hold:

1. There exists a boundary curve $\boldsymbol{\gamma}_c \colon [0,1] \to \Gamma$ with $\boldsymbol{\gamma}_c \in C^{0,1}([0,1];\mathbb{R}^2)$ such that $\Gamma_c = \boldsymbol{\gamma}_c((0,1)) \neq \emptyset$, where $\boldsymbol{\gamma}_c(0)$ and $\boldsymbol{\gamma}_c(1)$ denote the endpoints of the crack. The curve $\boldsymbol{\gamma}_c$ will sometimes be called the crack curve corresponding to the crack Γ_c.
2. For each $s \in (0,1)$, there exists $\varepsilon_s > 0$ such that the set $B_\varepsilon(\boldsymbol{\gamma}_c(s)) \cap \Omega$ is disconnected for all $\varepsilon > 0$ with $\varepsilon < \varepsilon_s$; that is, the crack locally divides the domain.
3. In order to prescribe boundary conditions on the crack, we distinguish its upper and lower side, denoted by Γ_c^+ and Γ_c^-, respectively, and set $\Gamma_c^\pm = \Gamma_c^+ \cup \Gamma_c^-$.
4. The crack is modeled as part of the Neumann boundary, i.e., $\Gamma_c^\pm \subset \Gamma_N$.
5. The crack does not disconnect the domain Ω globally.

The following characteristics of the above definition are worth highlighting:

Remark 5.5.

1. The crack is always treated as a Neumann-type boundary segment, which is physically natural, as it models a free-edge tear in a membrane.
2. The crack is only required to be Lipschitz continuous, allowing for both polygonal and curved geometries, which makes the model flexible and applicable to analytical and numerical studies.
3. The global non-disconnection condition simplifies spectral analysis. If the domain were split into disconnected components, one would need to treat each subdomain independently.

The notation in Definition 5.4 can be extended naturally to describe multiple cracks. Let $\Gamma_{c,i}$, $i = 1, \dots, n$, denote all cracks present in the domain Ω. We denote the exterior Neumann boundary – excluding the cracks – by

$$\Gamma_0^N = \Gamma^N \setminus \left(\bigcup_{i=1}^n \Gamma_{c,i}^\pm \right), \quad \text{so that } \Gamma^N = \Gamma_0^N \cup \left(\bigcup_{i=1}^n \Gamma_{c,i}^\pm \right),$$

and the total exterior boundary without the cracks by

$$\Gamma_0 = \overline{\Gamma^D} \cup \overline{\Gamma_0^N}. \tag{5.4}$$

To summarize, the boundary of a domain with cracks consists of the exterior boundary parts and the two sides of each crack, namely

$$\Gamma = \overline{\Gamma^D} \cup \overline{\Gamma^N} = \overline{\Gamma^D} \cup \overline{\Gamma_0^N} \cup \left(\bigcup_{i=1}^n \overline{\Gamma_{c,i}^\pm} \right) = \Gamma_0 \cup \left(\bigcup_{i=1}^n \overline{\Gamma_{c,i}^\pm} \right).$$

Next, we refine Definition 5.4 by introducing specific types of cracks.

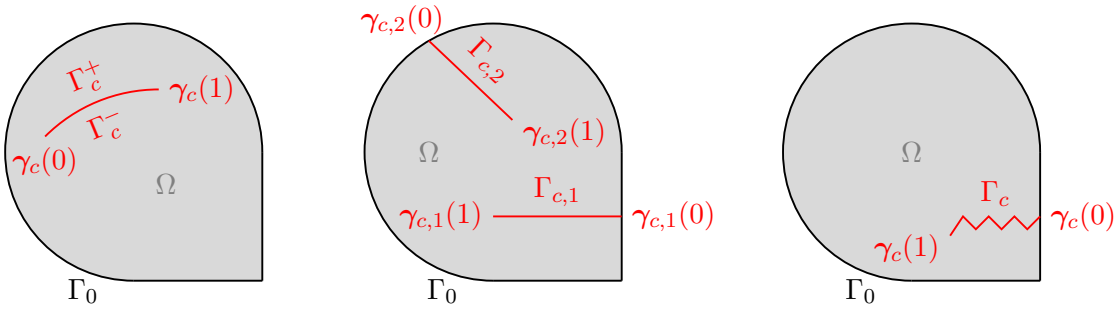

Figure 5.4: Illustration of domains with cracks of different shapes, together with the corresponding notation. (a): Curved inner crack, where the two sides of the crack are indicated. (b): Two straight outer cracks. (c): Polygonal outer crack.

Definition 5.6. Let $\Omega \subset \mathbb{R}^2$ contain a crack Γ_c. We call Γ_c

- an *inner crack* if $\overline{\Gamma_c} \cap \Gamma_0 = \emptyset$,
- an *outer crack* if $\overline{\Gamma_c} \cap \Gamma_0$ is a singleton, which we assume without loss of generality to be $\overline{\Gamma_c} \cap \Gamma_0 = \{\boldsymbol{\gamma}_c(0)\}$,
- a *straight crack* if the corresponding crack curve satisfies $\boldsymbol{\gamma}_c \in C^1([0,1])^2$ and its unit tangent vector is constant, that is, there is a vector $\boldsymbol{v} \in \mathbb{R}^2$ with $\boldsymbol{v} \neq \mathbf{0}$ such that

$$\boldsymbol{\gamma}_c'(s) = \boldsymbol{v} \quad \text{for all } s \in [0,1].$$

If multiple outer cracks are present, we assume that they do not intersect, which ensures that the domain remains connected.

Figure 5.4 illustrates representative crack configurations and the related notation introduced above.

5.3.2 Can one hear the length of a crack?

In this section, we demonstrate how the first two terms of the short-time asymptotic expansion of the heat trace allow us to determine the length of a crack from the associated Laplace spectrum. Let $\Omega \subset \mathbb{R}^2$ be a bounded curvilinear polygonal domain containing $n \in \mathbb{N}$ cracks $\Gamma_{c,i}$, $i = 1, \dots, n$, as described in Definition 5.4. According to Theorem 5.2, the heat trace of the domain admits the asymptotic expansion (5.3), which contains the spectrally invariant boundary contribution

$$H_{-1/2} = \frac{2\sum_{i=1}^{n} |\Gamma_{c,i}| + |\Gamma_N^0| - |\Gamma_D|}{8\sqrt{\pi}}. \tag{5.5}$$

The length of each crack,

$$|\Gamma_{c,i}| = \int_{\Gamma_{c,i}} 1 \, \mathrm{d}\gamma = \int_0^1 |\boldsymbol{\gamma}_{c,i}'(s)| \, \mathrm{d}s,$$

contributes twice to the coefficient (5.5) with a positive sign, since Neumann boundary conditions are imposed on both sides $\Gamma_{c,i}^{\pm}$ of the crack. As outlined in Remark 5.3, information on the total

length of all cracks $\sum_{i=1}^{n} |\Gamma_{c,i}|$ can be obtained from the coefficient $H_{-1/2}$, provided that the remaining boundary lengths $|\Gamma_0^N|$ and $|\Gamma_D|$ are given. This observation directly yields the following result.

Corollary 5.7 (**One can hear the existence of cracks in a drum**). *Let Ω be a domain with n cracks $\Gamma_{c,i}$, $i = 1, \dots, n$, as described above. Moreover, let $\widetilde{\Omega}$ be the congruent domain without cracks, i.e., $\Omega = \widetilde{\Omega} \setminus \left(\cup_{i=1}^{n} \overline{\Gamma_{c,i}}\right)$ and*

$$\overline{\widetilde{\Omega}} = \overline{\Omega}, \quad \widetilde{\Gamma} = \Gamma_0, \quad \widetilde{\Gamma}_D = \Gamma_D, \quad \widetilde{\Gamma}_N = \Gamma_0^N,$$

where $\widetilde{\Gamma}$, $\widetilde{\Gamma}_D$ and $\widetilde{\Gamma}_N$ denote the related boundary parts of $\widetilde{\Omega}$, see Figures 5.5a and 5.5b for an illustration. Then, Ω and $\widetilde{\Omega}$ are not isospectral, meaning that the Laplace spectra of $(\Omega, \Gamma_D, \Gamma_N)$ and $(\widetilde{\Omega}, \widetilde{\Gamma}_D, \widetilde{\Gamma}_N)$ differ. Consequently, the presence of a crack can be heard from the spectrum.

Proof. Let $H^{\Omega}_{-1/2}$ and $H^{\widetilde{\Omega}}_{-1/2}$ denote the coefficients in the asymptotic expansions (5.3) of the heat traces of $(\Omega, \Gamma_D, \Gamma_N)$ and $(\widetilde{\Omega}, \widetilde{\Gamma}_D, \widetilde{\Gamma}_N)$, respectively. Then, equation (5.5) yields

$$H^{\Omega}_{-1/2} > H^{\widetilde{\Omega}}_{-1/2}\,.$$

Since the coefficient is a spectral invariant, the spectra of the two domains cannot coincide. □

Following the strategy explained in Remark 5.3, we draw further conclusions for situations in which the geometry of the corresponding domain without crack is available a priori. More precisely, we assume that the exterior boundary (5.4) is known beforehand, which also determines the area of the domain in the planar setting. Then, all contributions to the first two heat trace coefficients H_{-1} and $H_{-1/2}$ are prescribed, except for the contribution involving the total crack length $\sum_{i=1}^{n} |\Gamma_{c,i}|$ in (5.5). Intuitively, this corresponds to a situation in which a specimen is accessible from the outside, while the existence and geometry of possible cracks extending into the interior remain unknown and subject to investigation. Under these assumptions, the coefficient (5.5) is monotonically increasing with respect to the total crack length, which leads to the following conclusion.

Remark 5.8. Recalling the definition of the heat trace in (5.2), where the eigenvalues enter the exponent with a negative sign, we find the general trend that as the total crack length increases, the eigenfrequencies of the domain decrease. In other words, a drum with more or longer cracks is expected to vibrate more slowly – an observation consistent with physical intuition.

Finally, an illustrative example demonstrates how the boundary contribution in the heat trace expansion enables precise crack identification under suitable assumptions.

Example 5.9 (**One can hear a straight crack with fixed starting point and tangent vector**). When additional information about the crack is available, determining its length may suffice to reconstruct its shape. For instance, let Ω contain a single straight crack Γ_c, represented by the corresponding crack curve $\boldsymbol{\gamma}_c \colon [0,1] \to \Gamma$, and assume that both the starting point $\boldsymbol{\gamma}_c(0)$ and the constant unit tangent vector $\boldsymbol{v} \in \mathbb{R}^2$ are known a priori, see Definition 5.6. An exemplary domain configuration is displayed in Figure 5.5c. Then, by recovering the length $|\Gamma_c|$ from the spectrum via the boundary coefficient

$$H_{-1/2} = \frac{2|\Gamma_c| + |\Gamma_0^N| - |\Gamma_D|}{8\sqrt{\pi}},$$

the complete parameterization of the crack can be reconstructed as

$$\boldsymbol{\gamma}_c(t) = \boldsymbol{\gamma}_c(0) + t\,|\Gamma_c|\,\boldsymbol{v}, \quad t \in [0,1].$$

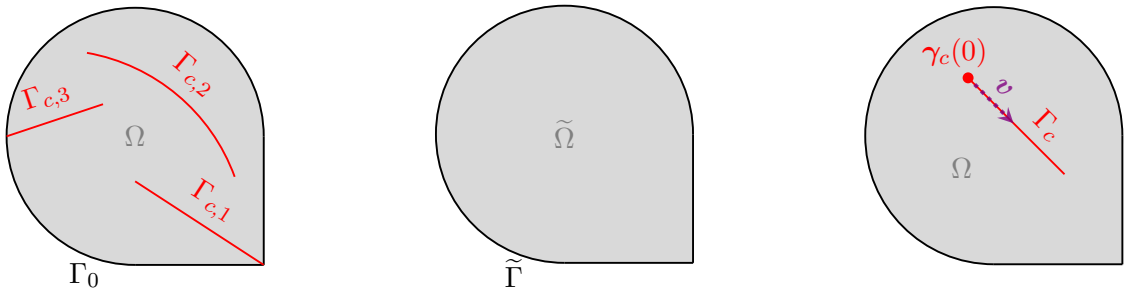

(a) (b) (c)

Figure 5.5: (a): Domain with three cracks. (b): Corresponding domain without cracks. (c): Domain with a straight crack, whose starting point and the tangential vector are known.

5.3.3 Can one hear the angle of a crack?

Next, we extend our analysis by including the third term in the short-time asymptotic expansion of the heat trace. Under certain assumptions, this term enables us to determine the angle of a crack from the associated Laplace spectrum.

Let Ω be a bounded curvilinear polygonal domain, and denote by $\mathcal{V} = \{\boldsymbol{V}_i \in \Gamma : i = 0, 1, 2, \dots, N\}$ the set of its vertices, each related with an interior angle $\omega_i \in (0, 2\pi]$. From now on, let Ω have exactly one crack Γ_c. As stated in Theorem 5.2, the third term in the short-time asymptotic expansion of the heat trace is given by

$$H_0 = \frac{1}{12\pi} \int_{\Gamma \setminus \mathcal{V}} \kappa_g \, \mathrm{d}s + \sum_{i \in I_=} \frac{\pi^2 - \omega_i^2}{24\pi\omega_i} + \sum_{i \in I_{\neq}} \frac{-\pi^2 - 2\omega_i^2}{48\pi\omega_i}, \tag{5.6}$$

where $I_=$ and $I_{\neq}$ denote the index sets corresponding to the adjacent boundary conditions.

We then specify to what extent the crack contributes to this quantity, and we start with the curvature integral. Since the two sides Γ_c^+ and Γ_c^- of the crack are traversed with opposite orientations, the geodesic curvature changes sign. Recalling the notation $\Gamma_c^{\pm} = \Gamma_c^+ \cup \Gamma_c^-$, we obtain

$$\int_{\Gamma_c^{\pm} \setminus \mathcal{V}} \kappa_g \, \mathrm{d}s = \int_{\Gamma_c^+ \setminus \mathcal{V}} \kappa_g \, \mathrm{d}s + \int_{\Gamma_c^- \setminus \mathcal{V}} \kappa_g \, \mathrm{d}s = \int_{\Gamma_c^+ \setminus \mathcal{V}} \kappa_g \, \mathrm{d}s + \int_{\Gamma_c^+ \setminus \mathcal{V}} (-\kappa_g) \, \mathrm{d}s = 0, \tag{5.7}$$

meaning that the crack does not contribute to the curvature integral.

However, the crack introduces new vertices, including at least one crack tip, which constitutes a vertex with an interior angle of 2π. In addition, a crack can alter existing corner contributions. For example, if the crack originates at a corner, it may split this corner up into two distinct new vertices. Hence, the quantity

$$H_0^{\mathcal{V}} := \sum_{i \in I_=} \frac{\pi^2 - \omega_i^2}{24\pi\omega_i} + \sum_{i \in I_{\neq}} \frac{-\pi^2 - 2\omega_i^2}{48\pi\omega_i} \tag{5.8}$$

certainly contains information about the crack. We refer to the expression (5.8) as the *corner contribution* to the heat trace, since it depends solely on the interior angles at the corners of the domain. Moreover, let I_c be the set of indices such that $\mathcal{V}_c := \{\boldsymbol{V}_i : i \in I_c\}$ represents the set of all corners associated to the crack. Then, we define

$$H_0^{\mathcal{V}_c} := \sum_{i \in I_= \cap I_c} \frac{\pi^2 - \omega_i^2}{24\pi\omega_i} + \sum_{i \in I_{\neq} \cap I_c} \frac{-\pi^2 - 2\omega_i^2}{48\pi\omega_i} \tag{5.9}$$

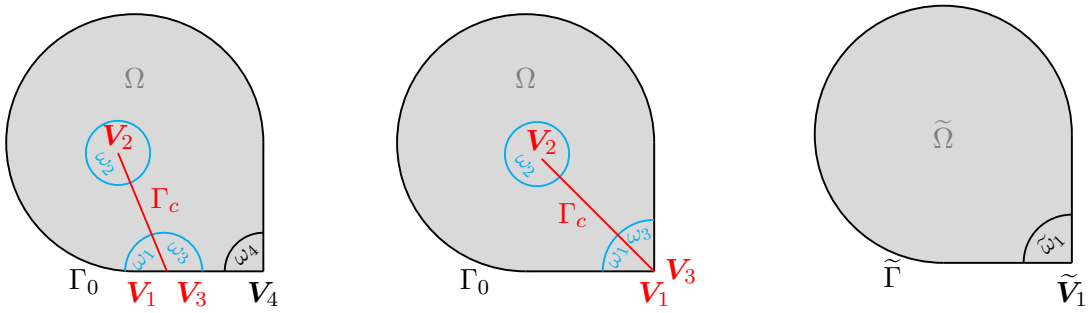

Figure 5.6: Sketch of all the corners and corresponding inner angles of different domains. (a): Domain with straight outer crack. (b): Domain with straight outer crack starting at a corner. (c): Corresponding domain without crack.

as the *crack corner contribution* to the heat trace. It can be used to extract geometric parameters of the crack from the spectral data, a strategy we will explore in more detail subsequently.

For simplicity, we begin by considering straight cracks, and further distinguish between inner and outer cracks; see Definition 5.6. If Γ_c is an inner straight crack, it introduces two vertices of the domain with interior angle 2π. Then, the crack corner contribution (5.9) is given by

$$2 \cdot \frac{\pi^2 - (2\pi)^2}{24\pi(2\pi)} = 2 \cdot \left(-\frac{1}{16}\right) = -\frac{1}{8}, \tag{5.10}$$

since we always consider Neumann boundary conditions along the crack. This contribution does not appear in the heat trace of the corresponding domain without the inner crack, which once again confirms that the existence of an inner straight crack can be heard – an observation we previously made in Corollary 5.7. However, an inner crack does not leave any trace of its position in the spectral data. The contribution (5.10) is always identical for any straight inner crack in the domain. Therefore, the only geometric information that is encoded in the heat trace in this case is the crack's length, as discussed in Section 5.3.2.

We proceed with the analysis of straight outer cracks, for which a more detailed investigation is possible. In this case, it is necessary to distinguish between several configurations, depending on the origin of the crack and the adjacent boundary conditions. First, we assume that the crack does not originate at a corner. To formalize this, let $\widetilde{\mathcal{V}} = \{\widetilde{\boldsymbol{V}}_1, \widetilde{\boldsymbol{V}}_2, \dots, \widetilde{\boldsymbol{V}}_n\}$ denote the set of vertices in the boundary of the corresponding domain $\widetilde{\Omega}$ without the crack, as constructed in Corollary 5.7. Then, we assume that $\boldsymbol{\gamma}_c(0) \notin \widetilde{\mathcal{V}}$, i.e., the crack starts at a point where the boundary is smooth. Under this assumption, a straight outer crack introduces three new corners, which we label $\boldsymbol{V}_1, \boldsymbol{V}_2$ and $\boldsymbol{V}_3$, see Figures 5.6a and 5.6c for an illustration. The crack tip represents a vertex with interior angle of $\omega_2 = 2\pi$ and is surrounded by Neumann boundary, that is, $2 \in I_=$. The other two corners occur where the crack intersects the outer boundary. These correspond to interior angles ω_1 and ω_3 and are subject to either Neumann or mixed Dirichlet-Neumann BCs, depending on the adjacent boundary segments. The total crack corner contribution (5.9) to the short-time asymptotic expansion of the heat trace is therefore given by

$$H_0^{\mathcal{V}_c} = -\frac{1}{16} + \sum_{i \in I_= \cap \{1,3\}} \frac{\pi^2 - \omega_i^2}{24\pi\omega_i} + \sum_{i \in I_{\neq} \cap \{1,3\}} \frac{-\pi^2 - 2\omega_i^2}{48\pi\omega_i}. \tag{5.11}$$

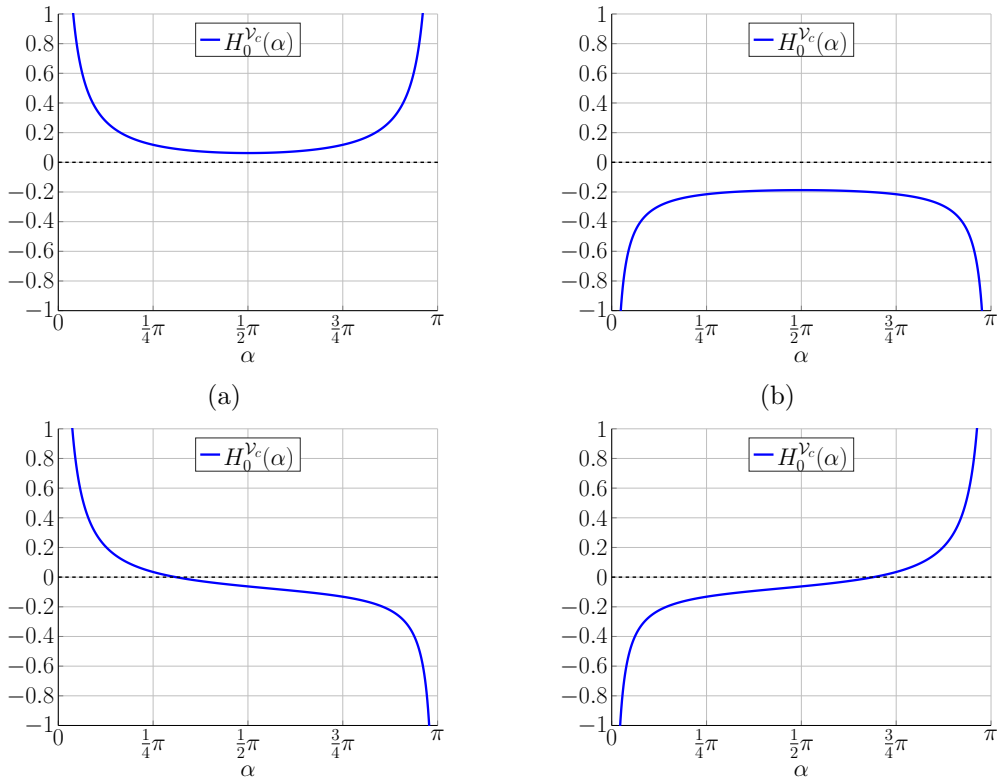

Figure 5.7: Crack corner contribution (5.12) of a straight crack for the four types of adjacent boundary conditions. (a): $1,3 \in I_=$. (b): $1,3 \in I_{\neq}$. (c): $1 \in I_=, 3 \in I_{\neq}$. (d): $1 \in I_{\neq}, 3 \in I_=$.

Depending on the adjacent BCs along the outer boundary, we can further characterize the crack corner contribution. We set $\omega_1 = \alpha$ and note that $\omega_3 = \delta - \alpha$ with $\delta = \pi$, since the crack does not originate at a corner; see also Figure 5.6a for a visualization. This yields a parameterized expression of the crack corner contribution (5.11) in terms of the free angle $\alpha \in (0, \delta)$,

$$H_0^{\mathcal{V}_c}(\alpha) = \begin{cases} -\frac{1}{16} + \frac{\pi^2-\alpha^2}{24\pi\alpha} + \frac{\pi^2-(\delta-\alpha)^2}{24\pi(\delta-\alpha)} = -\frac{1}{16} + \frac{\pi}{24}\left(\frac{1}{\alpha} + \frac{1}{\delta-\alpha}\right) - \frac{\delta}{24\pi}, & \text{if } 1,3 \in I_=, \\ -\frac{1}{16} + \frac{-\pi^2-2\alpha^2}{48\pi\alpha} + \frac{-\pi^2-2(\delta-\alpha)^2}{48\pi(\delta-\alpha)} = -\frac{1}{16} + \frac{\pi}{48}\left(-\frac{1}{\alpha} - \frac{1}{\delta-\alpha}\right) - \frac{\delta}{24\pi}, & \text{if } 1,3 \in I_{\neq}, \\ -\frac{1}{16} + \frac{\pi^2-\alpha^2}{24\pi\alpha} + \frac{-\pi^2-2(\delta-\alpha)^2}{48\pi(\delta-\alpha)} = -\frac{1}{16} + \frac{\pi}{48}\left(\frac{2}{\alpha} - \frac{1}{\delta-\alpha}\right) - \frac{\delta}{24\pi}, & \text{if } 1 \in I_=, 3 \in I_{\neq}, \\ -\frac{1}{16} + \frac{-\pi^2-2\alpha^2}{48\pi\alpha} + \frac{\pi^2-(\delta-\alpha)^2}{24\pi(\delta-\alpha)} = -\frac{1}{16} + \frac{\pi}{48}\left(-\frac{1}{\alpha} + \frac{2}{\delta-\alpha}\right) - \frac{\delta}{24\pi}, & \text{if } 1 \in I_{\neq}, 3 \in I_=. \end{cases} \tag{5.12}$$

It can be shown that $H_0^{\mathcal{V}_c}(\alpha) \neq 0$ for all $\alpha \in (0, \pi)$ if $1,3 \in I_=$ and $1,3 \in I_{\neq}$. In the mixed boundary cases, the contribution may vanish, but only for a single specific angle, which can be computed using the procedure described in the subsequent Example 5.12. This behavior is illustrated in Figure 5.7, where we plot the respective functions $H_0^{\mathcal{V}_c} : (0,\pi) \to \mathbb{R},\ \alpha \mapsto H_0^{\mathcal{V}_c}(\alpha)$ for the four types of adjacent boundary conditions.

Finally, we consider the remaining case of a straight outer crack that originates at a corner. Without loss of generality, we assume that $\boldsymbol{\gamma}_c(0) = \widetilde{\boldsymbol{V}}_1$, where $\widetilde{\boldsymbol{V}}_1$ is a vertex of the corresponding domain $\widetilde{\Omega}$ without the crack, associated with an interior angle $\widetilde{\omega}_1$. An example of such a geometry is illustrated in Figures 5.6b and 5.6c. In this configuration, the corner contribution (5.8) of the

domain without the crack includes a term related to the vertex $\widetilde{\boldsymbol{V}}_1$,

$$\widetilde{H}_0^{\widetilde{\boldsymbol{V}}_1} := \begin{cases} \frac{\pi^2-\widetilde{\omega}_1^2}{24\pi\widetilde{\omega}_1}, & \text{if } 1 \in \widetilde{I}_=, \\ \frac{-\pi^2-2\widetilde{\omega}_1^2}{48\pi\widetilde{\omega}_1}, & \text{if } 1 \in \widetilde{I}_{\neq}, \end{cases}$$

which does not appear in the heat trace of the domain with crack. Instead, this single corner contribution is replaced by two new terms resulting from the splitting of the vertex. Precisely, we obtain the crack corner contribution $H_0^{\mathcal{V}_c}(\alpha)$ from equation (5.12), where $\delta = \widetilde{\omega}_1$ and $\alpha \in (0, \widetilde{\omega}_1)$. The total corner contributions (5.8) to the heat traces H and $\widetilde{H}$ of the domain with and without crack, respectively, satisfy the relation

$$H_0^{\mathcal{V}}(\alpha) = \widetilde{H}_0^{\widetilde{\mathcal{V}}} + H_0^{\mathcal{V}_c}(\alpha) - \widetilde{H}_0^{\widetilde{\boldsymbol{V}}_1}.$$

Building on the study of straight cracks, we now consider a general Lipschitz continuous crack Γ_c, as allowed in our setting; see Remark 5.5. On each smooth crack segment, no additional contribution to the third coefficient in the heat trace expansion (5.6) arises, since the curvature contributions on both sides of the crack cancel as demonstrated in Equation (5.7). In contrast, each interior crack vertex introduces two additional terms in the corner contribution (5.8). If the interior angle at a vertex on one side of the crack is ω_i, the corresponding angle on the opposite side is $2\pi - \omega_i$. Since both adjacent edges belong to the crack, Neumann boundary conditions are imposed on each side of those vertices. Hence, each interior crack corner contributes the quantity

$$\frac{\pi^2 - \omega_i^2}{24\pi\omega_i} + \frac{\pi^2 - (2\pi - \omega_i)^2}{24\pi(2\pi - \omega_i)}$$

to the heat trace. Together with the original contributions from straight cracks given in (5.10) and (5.12), this yields a recipe to compute the crack corner contribution for cracks of arbitrary Lipschitz continuous shape.

Throughout this analysis, it becomes evident that every crack – except for a few isolated cases – leaves visible fingerprints in the corner contribution (5.8) to the heat trace. These signatures do not appear in the heat trace of the corresponding domain without a crack. Hence, the existence of cracks can also be detected through the corner contribution, thereby extending the observations made in Corollary 5.7.

Going one step further, the question arises whether the crack corner contribution to the heat trace can be used to recover angle-related geometric information about the crack. To this end, and similarly to Section 5.3.2, we assume that the geometry of the background domain without crack is available a priori, that is, the exterior boundary (5.4) is prescribed. In addition, we assume that all non-crack contributions to the coefficient H_0 in (5.6) are known, namely the curvature term and the ordinary corner contributions of vertices that are not related to the crack. In the following example, we investigate to what extent the spectrum then determines the angles associated with the starting point of a straight outer crack in such a setup.

Example 5.10 (**Hearing the angle of a straight outer crack**)**.** Let Ω contain a straight outer crack Γ_c, see again Figures 5.6a and 5.6b for illustrative examples. With the numbering of the vertices induced by the crack as defined above, the aim is to recover the angles ω_1 and ω_3 at the vertices $\boldsymbol{V}_1$ and $\boldsymbol{V}_3$ from the crack corner contribution. In this sense, we refer to ω_1 as the angle of the straight outer crack throughout the remainder of the thesis. Depending on the geometry of Γ_0 in the vicinity of the crack's starting point $\boldsymbol{\gamma}_c(0) = \boldsymbol{V}_1 = \boldsymbol{V}_3$, the angle ω_1 can be expressed in terms of ω_3, namely $\omega_1 = \delta - \omega_3$ for some $\delta \in (0, 2\pi)$. For instance, in the configuration shown in Figure 5.6a, we have $\omega_1 = \pi - \omega_3$, while in Figure 5.6b, it holds $\omega_3 = \widetilde{\omega}_1 - \omega_1$ with $\widetilde{\omega}_1$ from Figure 5.6c.

We first consider the case in which both $\boldsymbol{V}_1$ and $\boldsymbol{V}_3$ have adjacent Neumann boundary edges, i.e., $1, 3 \in I_=$. Then, the crack contribution (5.12) to the heat trace is given by

$$H_0^{\mathcal{V}_c}(\alpha) = -\frac{1}{16} + \frac{\pi}{24}\left(\frac{1}{\alpha} + \frac{1}{\delta - \alpha}\right) - \frac{\delta}{24\pi}, \tag{5.13}$$

and it contains the contributions from the vertices $\boldsymbol{V}_1$ and $\boldsymbol{V}_3$. Now, we show that the function $H_0^{\mathcal{V}_c} : [0, \delta] \to \mathbb{R}, \alpha \mapsto H_0^{\mathcal{V}_c}(\alpha)$ is strictly monotonous in $[0, \delta/2]$ and $[\delta/2, \delta]$. To this end, we compute the derivative

$$\left(H_0^{\mathcal{V}_c}\right)'(\alpha) = \frac{1}{24}\left(-\frac{\pi}{\alpha^2} + \frac{\pi}{(\delta - \alpha)^2}\right) = \frac{\pi}{24\alpha^2}\left(\left(\frac{\alpha}{\delta - \alpha}\right)^2 - 1\right).$$

The expression in parentheses is strictly negative for $\alpha < \delta/2$, and strictly positive for $\alpha > \delta/2$. The monotonicity is also evident from the graph shown in Figure 5.7a for the case $\delta = \pi$. Moreover, the crack corner contribution (5.13) is symmetric with respect to α, in the sense that $H_0^{\mathcal{V}_c}(\alpha) = H_0^{\mathcal{V}_c}(\delta - \alpha)$. Therefore, the equation

$$H_0^{\mathcal{V}_c}(\alpha) = H_0^{\mathcal{V}_c}(\omega_1) \tag{5.14}$$

has exactly two solutions: $\alpha = \omega_1$ and $\alpha = \delta - \omega_1 = \omega_3$. Hence, we can determine both angles at the vertices $\boldsymbol{V}_1$ and $\boldsymbol{V}_3$ from the spectrum, even though, for $\omega_1 \neq \delta/2$, we cannot distinguish which angle corresponds to which vertex. If, in addition, we know whether ω_1 is the larger or the smaller angle, i.e., $\omega_1 \geq \delta/2$ or $\omega_1 \leq \delta/2$, then equation (5.14) admits a unique solution, and the angles ω_1 and ω_3 can be uniquely identified from the heat trace.

The remaining cases of adjacent boundary edges can be treated analogously. For $1, 3 \in I_{\neq}$, we obtain exactly the same result, since the function displayed in Figure 5.7b exhibits the same symmetry and monotonicity properties. In contrast, in the mixed cases, the functions shown in Figures 5.7c and 5.7d are monotonous over the entire interval $(0, \delta)$, and equation (5.14) admits a unique solution without requiring an additional constraint. This behavior is consistent with our intuition, as mixed boundary conditions are inherently non-symmetric, and naturally lead to a non-symmetric crack corner contribution.

In summary, this example demonstrates that, under the assumption that the background domain without crack is known, the angles at the starting point of a straight outer crack can indeed be determined from the short-time asymptotic expansion of the heat trace, in particular from its constant term, which includes the crack corner contribution. As the heat trace depends solely on the eigenfrequencies of the domain, this implies that one can, in principle, hear the angle of a straight outer crack.

The ability to hear the angle of a crack becomes even more useful when the location of its starting point is available a priori. In this case, it is possible to recover the exact shape of the crack from spectral data, as demonstrated in the following example. This represents an improvement over Example 5.9, where the tangent vector was additionally required.

Example 5.11 (**One can hear a straight outer crack with fixed starting point**)**.** Consider again the situation from Example 5.10, and, additionally, let the starting point $\boldsymbol{\gamma}_c(0) \in \Gamma_0$ be known in advance. Since this is the more common case, we assume that identical boundary conditions are imposed on the remaining boundary. From the preceding analysis, it follows that the angle ω_1 can be determined up to symmetry from the heat trace. Furthermore, the geometry of the exterior boundary Γ_0 is known, and we denote the corresponding unit tangent vector at the starting point

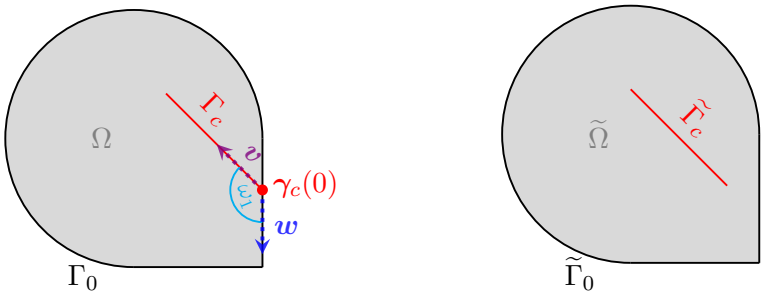

Figure 5.8: (a): Schematic representation of a domain with a straight outer crack and known starting point, including the unit tangent vectors of both the crack and the adjacent boundary. (b): Corresponding domain with inner crack of same length.

$\boldsymbol{\gamma}_c(0)$ by $\boldsymbol{w}$. Then, ω_1 represents the angle between the vectors $\boldsymbol{w}$ and $\boldsymbol{v}$, where $\boldsymbol{v}$ is the constant unit tangent vector of the straight crack. To eliminate the symmetry ambiguity, we assume that it is known a priori whether ω_1 is the larger or the smaller angle. All quantities are illustrated in Figure 5.8a, where we specifically indicate the chosen orientation of $\boldsymbol{w}$. From this, the vector $\boldsymbol{v}$ can be computed via the relation

$$\cos\omega_1 = \boldsymbol{v}\cdot\boldsymbol{w}\,.$$

Moreover, as established in Section 5.3.2, the length $|\Gamma_c|$ of the crack can also be extracted from the spectrum. Therefore, one can reconstruct the full parameterization of the crack,

$$\boldsymbol{\gamma}_c\colon [0,1]\to\Gamma,\quad \boldsymbol{\gamma}_c(t)=\boldsymbol{\gamma}_c(0)+t\,|\Gamma_c|\,\boldsymbol{v}.$$

Finally, we consider another situation in which the corner contribution of the heat trace is useful to extract geometric information about the crack.

Example 5.12 (Distinction of a straight inner crack from a straight outer crack). Let Ω contain a straight outer crack Γ_c with angle $\alpha=\omega_1$ at the starting point, as described previously. Let $\widetilde{\Omega}$ be another domain that does not possess the outer crack, but instead a straight inner crack $\widetilde{\Gamma}_c$, with

$$\overline{\widetilde{\Omega}}=\overline{\Omega},\quad \widetilde{\Gamma}_0=\Gamma_0,\quad \widetilde{\Gamma}_D=\Gamma_D,\quad \widetilde{\Gamma}_0^N=\Gamma_0^N,$$

where $\widetilde{\Gamma}_0,\widetilde{\Gamma}_D,\widetilde{\Gamma}_0^N$ denote the usual boundary parts of $\widetilde{\Omega}$. Such a configuration is presented visually in Figure 5.8. Note that in the special case illustrated there, the inner and outer crack are equally long. From Equations (5.10) and (5.12), we find that the respective corner contributions differ, i.e., $H_0^{\mathcal{V}}\neq\widetilde{H}_0^{\widetilde{\mathcal{V}}}$, provided that

$$H_0^{\mathcal{V}_c}(\alpha)\neq\widetilde{H}_0^{\widetilde{\mathcal{V}_c}}=-\frac{1}{8}. \tag{5.15}$$

To investigate when this condition is satisfied, we consider the quadratic equations arising from

$H_0^{\mathcal{V}_c}(\alpha) = -\frac{1}{8}$, where we recall Equation (5.12) and δ is defined as in Example 5.10,

$$\begin{cases} (2\delta - 3\pi)\,\alpha^2 + (-2\delta^2 + 3\pi\delta)\,\alpha + 2\pi^2\delta = 0 & \text{if } 1,3 \in I_=, \\ (2\delta - 3\pi)\,\alpha^2 + (-2\delta^2 + 3\pi\delta)\,\alpha - \delta\pi^2 = 0 & \text{if } 1,3 \in I_{\neq}, \\ (2\delta - 3\pi)\alpha^2 + (-2\delta^2 + 3\pi\delta - 3\pi^2)\alpha + 2\pi^2\delta = 0, & \text{if } 1 \in I_=, 3 \in I_{\neq}, \\ (2\delta - 3\pi)\alpha^2 + (-2\delta^2 + 3\pi\delta + 3\pi^2)\alpha - \pi^2\delta = 0, & \text{if } 1 \in I_{\neq}, 3 \in I_=. \end{cases} \tag{5.16}$$

The first two equations in (5.16) do not have a solution $\alpha \in (0, \delta)$ for any $\delta \in (0, 2\pi)$. Hence, if the adjacent boundary conditions around the crack are symmetric, i.e., $1,3 \in I_=$ or $1,3 \in I_{\neq}$, condition (5.15) is satisfied independent of the angle of the crack. The last two equations in (5.16) always have one solution $\alpha \in (0, \delta)$. For $\delta \neq \frac{3}{2}\pi$, it is given by

$$\alpha = \begin{cases} \frac{2\delta^2 - 3\pi\delta + 3\pi^2 - \sqrt{(-2\delta^2 + 3\pi\delta - 3\pi^2)^2 - 8\pi^2\delta(2\delta - 3\pi)}}{2(2\delta - 3\pi)}, & \text{if } 1 \in I_=, 3 \in I_{\neq}, \\ \frac{2\delta^2 - 3\pi\delta - 3\pi^2 + \sqrt{(-2\delta^2 + 3\pi\delta + 3\pi^2)^2 + 4\pi^2\delta(2\delta - 3\pi)}}{2(2\delta - 3\pi)}, & \text{if } 1 \in I_{\neq}, 3 \in I_=. \end{cases} \tag{5.17}$$

For $\delta = \frac{3}{2}\pi$, the considered equations are linear and yield the solutions

$$\alpha = \begin{cases} \pi, & \text{if } 1 \in I_=, 3 \in I_{\neq}, \\ \frac{\pi}{2}, & \text{if } 1 \in I_{\neq}, 3 \in I_=. \end{cases}$$

For the most common configuration where the crack originates from an edge and not from a corner, i.e., $\omega = \pi$, the observed behavior can be verified by considering Figure 5.7. For the symmetric cases, we see that (5.15) is satisfied for all angles $\alpha \in (0, \pi)$. In the non-symmetric cases, the condition is violated if and only if

$$\alpha = \begin{cases} \pi(\sqrt{3} - 1), & \text{if } 1 \in I_=, 3 \in I_{\neq}, \\ \pi(2 - \sqrt{3}), & \text{if } 1 \in I_{\neq}, 3 \in I_=. \end{cases}$$

Consequently, in all but those exceptional isolated cases, the heat trace of a domain with an inner straight crack differs from that of a similar domain with an outer straight crack, and therefore the cracks can be distinguished from their spectral fingerprints.

To conclude this section, we provide a brief overview of our analytical findings. Based on the spectral invariants arising from the short-time asymptotic expansion of the heat trace (5.3), we have shown that the spectrum of a domain uniquely determines

- the existence of at least one crack, see Corollary 5.7,
- the length of a crack, see Example 5.9,
- the angle of a straight outer crack, up to a symmetry constraint, see Example 5.10,
- whether a straight crack is an outer or an inner crack, except in the case where the angle of the outer crack satisfies (5.17).

5.4 Hearing the shape of a crack - A data-driven perspective

In contrast to the analytical investigations presented above, this section adopts a data-driven perspective on the isospectral problem for cracks in membranes. We provide a proof-of-concept demonstration of how the shape of a crack can be inferred from the eigenvalues of the underlying

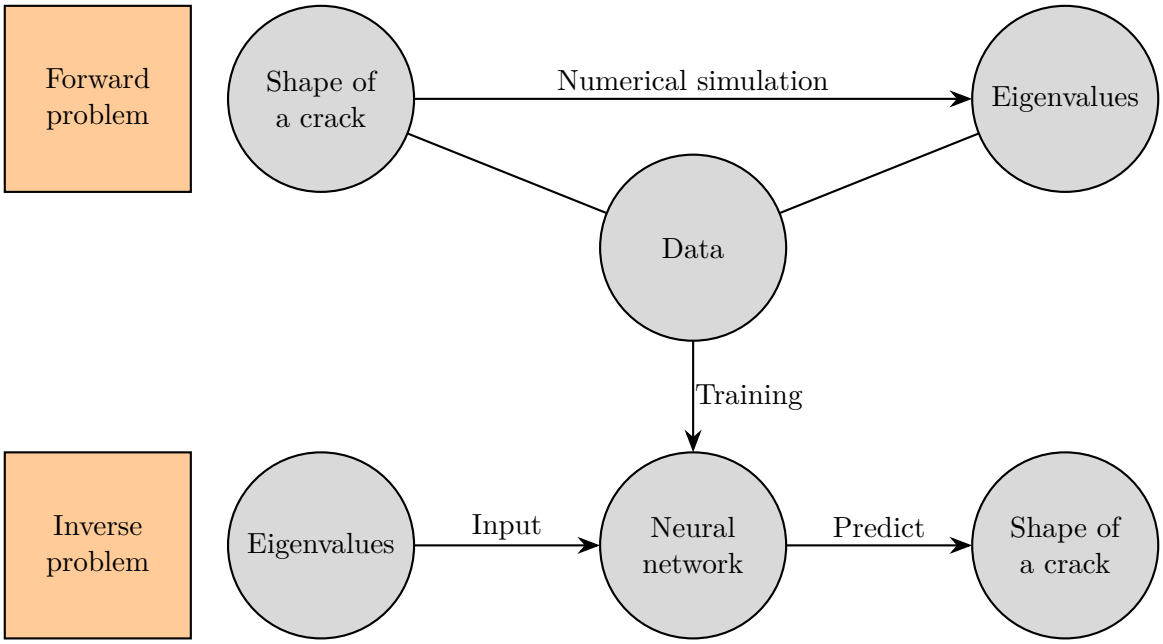

Figure 5.9: Schematic overview of our data-driven approach. The forward problem (top row) is solved via numerical simulation to generate eigenvalue data from domains with known crack geometries. This data is used to train a neural network that approximates the inverse mapping (bottom row).

domain using a computational framework that integrates numerical simulations and machine learning.

The data-based approach is outlined schematically in Figure 5.9. We formulate the central task as an inverse problem: given a finite subset of eigenvalues of a domain with a crack, the goal is to predict geometric parameters of the domain – precisely, the presence and shape of the crack. A promising strategy for addressing such inverse problems is the use of neural networks. Due to their universal approximation capabilities, neural networks are well-suited to learning complex, potentially nonlinear mappings between data spaces. However, their effectiveness relies critically on the availability of sufficiently rich and accurate training data. This is where the forward problem, illustrated in the top row in Figure 5.9, plays a crucial role: it provides a means of generating training data by simulating the Laplace spectrum of domains with cracks. By systematically varying the geometry of the crack and solving the corresponding parametric eigenvalue problem numerically, we construct a dataset that encodes the relationship between geometry and spectral response, which enables the neural network to learn the inverse mapping from eigenvalues to crack shape. These simulations serve as a computational surrogate for experimental data acquisition, and must be designed to approximate the true spectra with sufficient accuracy.

5.4.1 Solving the forward problem via IGA and graded mesh refinement

In the first step, we elaborate on the solution of the forward problem within our data-driven framework, that is, the approximation of Laplace eigenpairs of domains with cracks. The presentation is based on Section 4.1 of [ANZ25], but is given here in condensed form, since many of the required preliminaries have already been introduced earlier in this thesis. Ensuring high-fidelity simulations

is particularly challenging in regions where the eigenfunctions exhibit corner singularities, such as those occurring at crack tips, which we briefly discuss in the following.

For simplicity, let Ω be a domain with an outer crack Γ_c, which has a single crack tip; see Definition 5.6. Let $r_0(\boldsymbol{x})$ denote the distance from a point $\boldsymbol{x} \in \Omega$ to the crack tip. Then, the eigenfunctions are generally expected to exhibit singular behavior of the form r_0^ν in the vicinity of the crack tip, where $\nu < 1$ is the singular exponent [Dau88]. Since the interior angle at the associated corner is 2π and Neumann boundary conditions are imposed on both sides of the crack, see Definition 5.4, it is well known that the singular exponent is given by $\nu = \frac{1}{2}$. In certain symmetric domains, some eigenfunctions may remain smooth despite the presence of a crack, as demonstrated by the study on circular sectors in Chapter 4, but such cases are exceptional. The regularity properties of the corresponding eigenfunctions are discussed more explicitly in Section 5.4.2. Briefly, we can only expect

$$\eta u \in H^s(\Omega) \quad \text{for all } s < \frac{3}{2}, \tag{5.18}$$

where $\eta : \Omega \to \mathbb{R}$ denotes a smooth cut-off function that equals 1 in a neighborhood of the crack tip and vanishes away from it. Therefore, as outlined in Chapter 1, standard finite element or isogeometric methods – regardless of the polynomial degree p of the shape functions – cannot achieve optimal convergence rates, since they require eigenfunctions in $H^{p+1}(\Omega)$. This limitation can be overcome by local or adaptive refinement strategies.

In the present work, we therefore adopt the method introduced in Section 3.2, as it well suited to such a setting for several reasons. In view of its favorable spectral approximation properties, isogeometric analysis generally provides an appropriate framework for this purpose. In particular, as demonstrated in Chapter 4 for the model problem of the circular sector, polar splines spaces on graded meshes enable the accurate approximation of a finite portion of the Laplace spectrum on domains with corners. A further advantage of this approach is the simplicity and automation of the meshing process, which is particularly important for generating large amounts of training data. Mesh refinement in IGA is carried out on the parametric square and subsequently mapped to the computational domain, making the procedure straightforward, efficient, and robust under small perturbations of the geometry; see Remark 5.15 for more details. Finally, mesh grading can be prescribed a priori because the singular behavior at the crack tip is analytically well understood. This avoids the complexity of adaptive refinement and advanced spline technologies while preserving a simple mesh structure; see Sections 3.1 and 4.1, as well as Remark 3.11.

Having justified our choice, we now turn to the precise implementation of the proposed method in this specific situation. We begin by explaining how domains with cracks can be parameterized using polar mappings of the kind introduced in Section 3.2.1. Let Ω be a domain with polygonal outer boundary Γ_0 containing a straight outer crack Γ_c, and assume that Ω is star shaped with respect to the crack tip. More general domains with cracks are discussed later in Remark 5.17. Let the corners of the domain be denoted by $\boldsymbol{V}_0, \boldsymbol{V}_1, \boldsymbol{V}_2, \dots, \boldsymbol{V}_m$, where $\boldsymbol{V}_0 = \boldsymbol{\gamma}_c(1)$ represents the crack tip, $\boldsymbol{V}_1 = \boldsymbol{V}_m = \boldsymbol{\gamma}_c(0)$ the vertices at the crack start, and $\boldsymbol{V}_2, \dots, \boldsymbol{V}_{m-1}$ the remaining vertices of the outer boundary. Note that this ordering of the vertices may differ from the conventions previously adopted in Section 5.3.3. An illustrative example of such a domain, namely a unit square with a crack, together with the resulting polar parameterization, is shown in Figure 5.10a; it is described explicitly in Example 5.13. We employ the open, linear knot vectors

$$\Xi_1^0 = \{0, 0, 1, 1\}, \quad \Xi_2^0 = \left\{0, 0, \frac{1}{m-1}, \frac{2}{m-1}, \dots, \frac{m-2}{m-1}, 1, 1\right\}$$

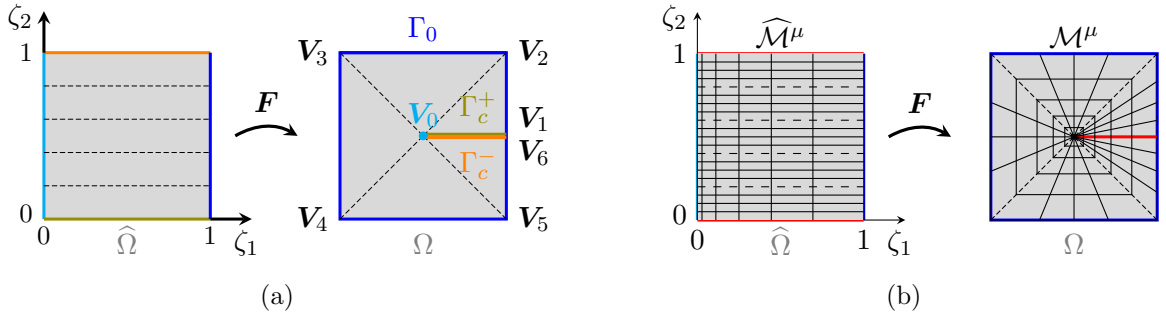

Figure 5.10: Discretization of a unit square with a symmetric crack. (a): Illustration of the polar parameterization. (b): Graded mesh refinement toward the crack tip.

and choose the corresponding control points $\boldsymbol{c_i}$, with indices $\boldsymbol{i} = (i_1, i_2)$ in the index set $\boldsymbol{I} = \{\boldsymbol{i} = (i_1, i_2) : i_1 = 1, 2,\ i_2 = 1, 2, \dots, m\}$ as follows. The control points associated with the left edge of the parametric domain are placed at the crack tip,

$$\boldsymbol{c}_{(1,i_2)} = \boldsymbol{V}_0 = \boldsymbol{\gamma}_c(1), \quad i_2 = 1, \dots, m, \tag{5.19}$$

which define the polar corner of the domain, while those on the right edge correspond to the remaining vertices, including the crack start,

$$\boldsymbol{c}_{(2,i_2)} = \boldsymbol{V}_{i_2}, \quad i_2 = 1, \dots, m. \tag{5.20}$$

Finally, all weights are set uniformly to $w_{\boldsymbol{i}} = 1$, $\boldsymbol{i} \in \boldsymbol{I}$, so that the weight function is identically equal to one, satisfies Assumption 3.5, and the NURBS basis functions reduce to standard B-splines. Based on this choice, the isogeometric parameterization defined in (2.34) takes the form

$$\boldsymbol{F} : \widehat{\Omega} \to \Omega, \quad \boldsymbol{F}(\zeta_1, \zeta_2) = (1 - \zeta_1)\boldsymbol{V}_0 + \zeta_1 \boldsymbol{G}(\zeta_2), \tag{5.21}$$

where $\widehat{\Omega} = (0, 1)^2$ is the parametric domain and $\boldsymbol{G} = (G_1, G_2)^T : [0, 1] \to \mathbb{R}^2$ maps onto the outer boundary Γ_0. This is consistent with Assumption 3.4, now generalized to polar points that do not lie at the origin. The left edge of the parametric domain collapses into the crack tip, that is, the parametrization (5.21) exhibits the classical polar singularity,

$$\boldsymbol{F}(0, \zeta_2) = \boldsymbol{V}_0 = \boldsymbol{\gamma}_c(1), \quad \zeta_2 \in (0, 1). \tag{5.22}$$

The upper and lower parametric edges are mapped onto the lower and upper sides Γ_c^- and Γ_c^+ of the crack, respectively, while the right boundary edge is mapped onto the outer boundary Γ_0 via the mapping $\boldsymbol{G}$. Below, this construction is illustrated by a representative example.

Example 5.13 (**Square with symmetric crack: Geometry setup**)**.** We consider a square-shaped membrane containing a horizontal outer crack extending from the midpoint of the right edge to the center of the square. The domain can be represented by a polar parameterization defined by the knot vectors $\Xi_1^0 = \{0, 0, 1, 1\}$ and $\Xi_2^0 = \{0, 0, \frac{1}{5}, \frac{2}{5}, \frac{3}{5}, \frac{4}{5}, 1, 1\}$, together with the control points listed in Table 5.1, chosen as indicated in (5.19) and (5.20), and the weights $w_{\boldsymbol{i}} = 1$ for all $\boldsymbol{i} \in \boldsymbol{I}$. The resulting mapping is visualized in Figure 5.10a. We refer to this configuration as the unit square with symmetric crack, and the numerical solution of the corresponding Laplace eigenvalue problem (5.23) will be explained in the continuation of the example.

$\boldsymbol{c}_{(i_1,i_2)}$	$i_2 = 1$	$i_2 = 2$	$i_2 = 3$	$i_2 = 4$	$i_2 = 5$	$i_2 = 6$
$i_1 = 1$	$(0.5, 0.5)^T$	$(0.5, 0.5)^T$	$(0.5, 0.5)^T$	$(0.5, 0.5)^T$	$(0.5, 0.5)^T$	$(0.5, 0.5)^T$
$i_1 = 2$	$(1, 0.5)^T$	$(1, 1)^T$	$(0, 1)^T$	$(0, 0)^T$	$(1, 0)^T$	$(0.5, 1)^T$

Table 5.1: Definition of control points $\boldsymbol{c_i}$, $\boldsymbol{i} \in \boldsymbol{I}$, for a polar parameterization of the unit square with symmetric crack.

After setting up the geometry description, we continue with the numerical solution of the Laplace eigenvalue problem, which can be discretized as described in Section 4.3.1. We denote by

$$0 \leq \lambda_{1,h} \leq \lambda_{2,h} \leq \cdots \leq \lambda_{l,h}$$

the discrete eigenvalues corresponding to the exact sequence (4.7), and by $u_{1,h}, u_{2,h}, \ldots, u_{l,h} \in V_{0h} \setminus \{0\}$ the associated discrete eigenfunctions, which can be chosen to satisfy (4.24). In contrast to the circular sectors considered in Chapter 4, where we conjectured that all eigenvalues are simple, general domains and boundary decompositions $(\Omega, \Gamma_D, \Gamma_N)$ commonly possess eigenvalues of higher multiplicity. We therefore seek to establish a generalization of Lemma 4.9 to arbitrary domains with outer cracks. Nevertheless, the fundamental Theorem 4.6 is formulated for eigenvalues of any multiplicity, and therefore also applies in the present setting.

As motivated above, we employ the graded refinement described in Section 3.2 to handle the corner singularity at the crack tip, which is set up to coincide with the polar point of the parameterization (5.21). Figure 5.10b shows representative meshes in the parametric and computational domains for the unit square with a crack described in Example 5.13. The approximation space $V_{0h}^{\odot}$ is chosen as in (3.19), where the following quantities are implicitly contained in the notation:

- the grading parameter $\mu \in (0, 1]$,
- the polynomial degrees of the univariate spline spaces, p_1 and p_2. For simplicity, we set $p = p_1 = p_2$ in the following,
- the mesh sizes in both parametric directions, h_1 and h_2. Here, we assume that $h_1 \sim h_2$ and define $h = \max\{h_1, h_2\}$ as the overall mesh size on the parametric domain.

By combining the approximation properties of the space (3.19) with Theorem 4.6 and assuming sufficient regularity of the eigenfunctions under consideration, we can derive suitable error estimates. In particular, the regularity of the eigenmodes in a neighborhood of the crack tip, where the eigenfunctions exhibit singular behavior, can be characterized using weighted Sobolev spaces; see also the related corner singularities arising in solutions of the Poisson equation discussed in Section 2.1.2. Let again $r_0 = r_0(\boldsymbol{x})$ denote the distance from a point $\boldsymbol{x} = (x_1, x_2) \in \Omega$ to the crack tip $\boldsymbol{V}_0$. As a generalization of Definition 2.1, where only the distance to $\boldsymbol{0}$ was used as weight, we define the weighted Sobolev spaces $V^s_{\beta,0}(\Omega)$ for $s \in \mathbb{N}_0$ and $\beta \in \mathbb{R}$ by

$$V^s_{\beta,0}(\Omega) := \{v \in \mathcal{D}'(\Omega) : \|v\|_{V^s_\beta(\Omega)} < \infty\},$$

with the norm

$$\|v\|_{V^s_{\beta,0}(\Omega)} := \left(\sum_{|\boldsymbol{\alpha}| \leq s} \left\| r_0^{\beta - s + |\boldsymbol{\alpha}|} D^{\boldsymbol{\alpha}} v \right\|^2_{L^2(\Omega)} \right)^{1/2} = \left(\sum_{|\boldsymbol{\alpha}| \leq s} \int_\Omega \left| r_0(\boldsymbol{x})^{\beta - s + |\boldsymbol{\alpha}|} D^{\boldsymbol{\alpha}} v(\boldsymbol{x}) \right|^2 \mathrm{d}\boldsymbol{x} \right)^{1/2}.$$

These spaces will be used in the following lemma, which establishes optimal convergence of the proposed approximation of the Laplace EVP on domains with cracks.

Lemma 5.14. *Let Ω be a polygonal domain with a single crack, star shaped with respect to the crack tip $\boldsymbol{V}_0$, and represented by an isogeometric polar parameterization $\Omega = \boldsymbol{F}(\widehat{\Omega})$ of the form (5.21). Consider the eigenvalue $\lambda = \lambda_k$ of the variational problem (4.20), with multiplicity $q \in \mathbb{N}$, i.e., $\lambda_k = \lambda_{k+1} = \cdots = \lambda_{k+q-1}$. Assume that there exists $s \in \mathbb{N}$ with $s \geq 2$ such that every eigenfunction $u \in M(\lambda)$ satisfies*

$$u - u(\boldsymbol{V}_0) \in V^s_{\beta,0}(\Omega) \quad \text{for all } \beta \in \mathbb{R} \text{ with } s - \frac{3}{2} < \beta < s - 1.$$

On the discrete level, let $V^{\odot}_{0h}$ be the approximation space (3.19), where we choose

$$p = s - 1, \qquad \mu < \frac{1}{2p}, \qquad \dim(V^{\odot}_{0h}) \geq k + q - 1.$$

Then, the corresponding discrete eigenvalues of (4.23) satisfy

$$\lambda \leq \lambda_{j,h} \leq \lambda + Ch^{2p}, \quad j = k, k+1, \ldots, k+q-1.$$

Furthermore, for each unit eigenfunction $u \in M(\lambda)$, there exists a unit discrete function $u_h \in \operatorname{span}\{u_{k,h}, u_{k+1,h}, \ldots, u_{k+q-1,h}\}$ such that

$$\|u - u_h\|_{H^1(\Omega)} \leq Ch^p.$$

Proof. We estimate the error in (4.26) using the modified space $V^{\odot}_{0h}$. Since constants belong to the space of mapped B-splines, we have $u(\boldsymbol{V}_0) \in V^{\odot}_h$. Moreover, approximation properties of $V^{\odot}_h$ are provided in [AZ26]. If the grading parameter satisfies $\mu < \frac{\nu}{p} = \frac{1}{2p}$, it follows

$$\begin{aligned}\varepsilon_h(\lambda) &= \sup_{u \in M(\lambda)} \inf_{w_h \in V^{\odot}_{0h}} \|u - w_h\|_{H^1(\Omega)} = \sup_{u \in M(\lambda)} \inf_{w_h \in V^{\odot}_{0h}} \|u - u(\boldsymbol{V}_0) - (w_h - u(\boldsymbol{V}_0))\|_{H^1(\Omega)} \\ &= \sup_{u \in M(\lambda)} \inf_{v_h \in V^{\odot}_{h,*}} \|u - u(\boldsymbol{V}_0) - v_h\|_{H^1(\Omega)} \leq \sup_{u \in M(\lambda)} Ch^p \|u - u(\boldsymbol{V}_0)\|_{V^{p+1}_{\beta,0}(\Omega)},\end{aligned}$$

where we define $V^{\odot}_{h,*} = \{v \in V^{\odot}_h : v = -u(\boldsymbol{V}_0) \text{ on } \Gamma_D\}$. The results in [AZ26] address homogeneous boundary conditions away from the polar point, but the extension to this inhomogeneous case is immediate, as the constant boundary datum is contained in the approximation space, $u(\boldsymbol{V}_0) \in V^{\odot}_h$. The assertion then follows directly from Theorem 4.6. □

In the following, we present numerical results that support our theoretical findings. As mentioned previously, Chapter 4 includes several tests for a unit disk with a crack along the positive x-axis, for which the analytical solution is known. Here, we consider examples for which exact solutions are not available. The error is therefore computed with respect to a reference solution obtained on a very fine mesh of the same type, that is, with the same polynomial degree and grading parameter. The experiments are again carried out using the isogeometric analysis package GeoPDEs 3.2.2 [Váz16] and the graded h-refinement scheme is implemented as demonstrated in Section 3.5. All integrals are evaluated using the Gauss–Legendre quadrature rule with 36 Gauss points per mesh element, corresponding to 6 quadrature nodes in each parametric direction.

Continuation of Example 5.13 (Square with symmetric crack: Numerical results). We compute the solution of the Laplace eigenvalue problem on the unit square with a symmetric crack, given by

$$\begin{aligned} -\Delta u &= \lambda u && \text{in } \Omega := \widetilde{\Omega} \setminus \overline{\Gamma_c}\,, \\ u &= 0 && \text{on } \Gamma_D = \Gamma_0\,, \\ \frac{\partial u}{\partial \nu} &= 0 && \text{on } \Gamma_c^{\pm}\,, \end{aligned} \tag{5.23}$$

where $\widetilde{\Omega} = (0,1)^2$ is the unit square, $\Gamma_0 = \partial\widetilde{\Omega}$ its boundary, and

$$\Gamma_c = \{\boldsymbol{x} \in \mathbb{R}^2 : \boldsymbol{x} = (1-z, 0.5)^T, z \in (0, 0.5)\}$$

is the crack. The eigenfunctions belonging to the first ten Laplace eigenvalues are visualized as surface plots in Figure 5.11. Owing to the symmetry of the domain, not all eigenfunctions exhibit the characteristic singularity of type $r_0^{1/2}$ at the crack tip; this singular behavior appears only in certain modes, such as the second and eighth eigenfunctions. The same phenomenon was observed for the unit disk with a crack studied in Section 4.2.3.

To investigate the effect of the singularity on the numerical approximation, we perform a convergence study for the second eigenpair as a representative case. Figure 5.12 presents the $H^1(\Omega)$-error of the eigenfunction and the absolute eigenvalue error for NURBS of polynomial degree $\boldsymbol{p} = (p, p)$, $p \in \{1, 2, 3, 4\}$, and regularity $\boldsymbol{k} = (p-1, p-1)$, with varying grading parameters μ. Precisely, we choose $\mu = 1$ for uniform and $\mu = \frac{0.9}{2p}$ for graded refinement. On uniform meshes, the convergence rate of the $H^1(\Omega)$-error of the approximated eigenfunction with respect to the mesh size h is bounded and strictly less than 1, regardless of the polynomial degree. In contrast, graded meshes yield the expected optimal convergence order p. Likewise, the discrete eigenvalue converges with suboptimal order strictly less than 2 under uniform refinement, whereas mesh grading restores the desired convergence rate of $2p$.

By assessing the exact regularity of the eigenfunctions of this domain, we find that the optimal approximation behavior on graded meshes confirms our theoretical predictions from Lemma 5.14. To this end, let η be a cut-off function that equals 1 near the crack tip and vanishes away from it. Lemma 5.19, which is rather technical and therefore deferred to the subsequent section, implies that $(1-\eta)u$ belongs to $H^s(\Omega)$ for all $s \in \mathbb{N}$. Moreover, since r_0^{β} remains bounded away from the crack tip and $(1-\eta)u = 0$ in its vicinity, we obtain $(1-\eta)u \in V^s_{\beta,0}(\Omega)$ for all $s \in \mathbb{N}$ and $\beta \in \mathbb{R}$. Combined with Lemma 5.18, which is also presented in the following section, and the decomposition

$$u - u(\boldsymbol{V}_0) = \eta u - u(\boldsymbol{V}_0) + (1-\eta)u,$$

this shows that the regularity assumption on the eigenfunctions required in Lemma 5.14 is satisfied.

Finally, we highlight a convenient feature of the presented approach that facilitates the modeling of varying cracks and will be exploited in the subsequent numerical example.

Remark 5.15 (Automated mesh generation for various cracks). Let Ω be a domain with a straight outer crack Γ_c, represented by a polar parameterization of the form (5.21), and let $\widetilde{\Omega}$ denote the related domain without the crack, i.e., $\Omega = \widetilde{\Omega} \setminus \overline{\Gamma_c}$. If $\widetilde{\Omega}$ is fixed and only the endpoints of the outer crack are varied, the present approach enables a straightforward modeling of the resulting geometries: it suffices to modify the control points associated with the three vertices defining the crack; see (5.19) and (5.20). In particular, the corresponding meshes are generated

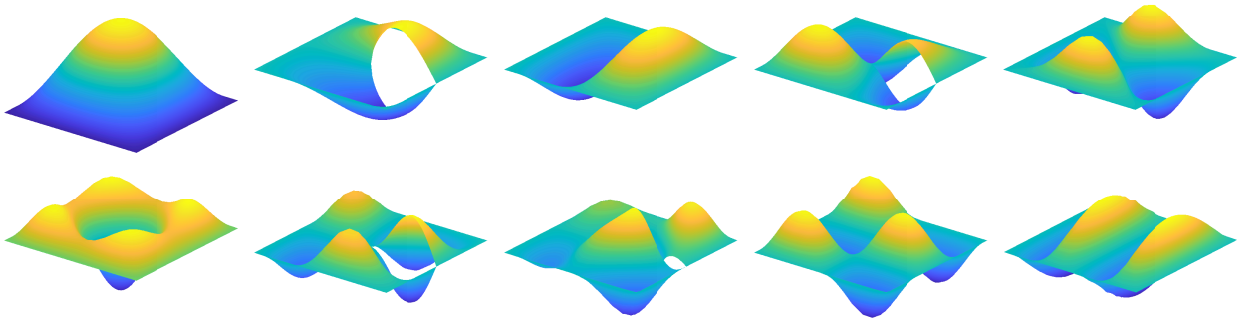

Figure 5.11: Illustration of the eigenfunctions corresponding to the first ten Laplace eigenvalues of the unit square with a horizontal crack of length $l = 0.5$.

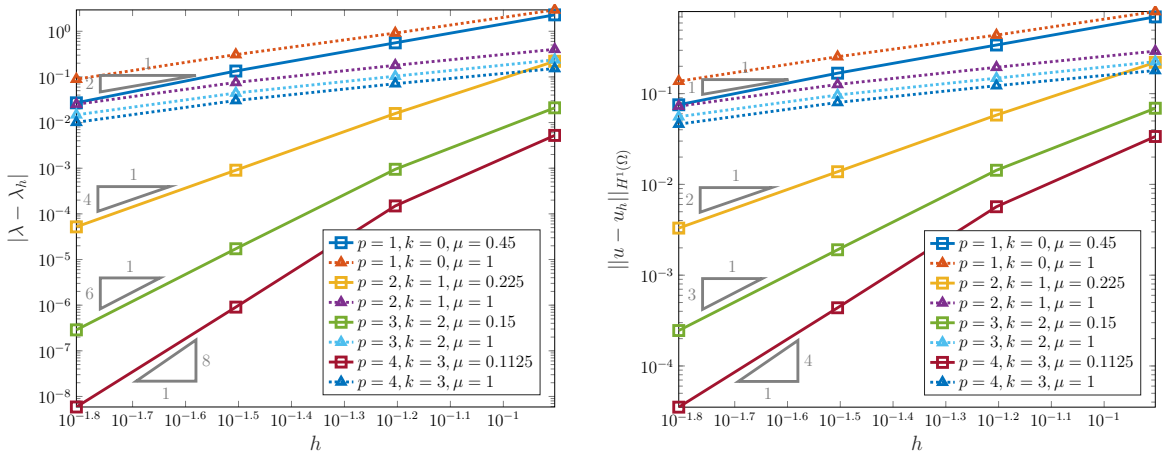

Figure 5.12: Approximation errors for the eigenfunction $u = u_2$ and its associated eigenvalue $\lambda = \lambda_2$ using gradually and uniformly refined B-splines of degree $\boldsymbol{p} = (p, p)$, $p \in \{1, 2, 3, 4\}$, and regularity $\boldsymbol{k} = (p - 1, p - 1)$. We set $\mu = \frac{0.9}{2p}$ for graded meshes and $\mu = 1$ corresponds to uniform refinement.

automatically, since the same parametric mesh is employed and mapped to the computational domain via the modified parameterization, while remaining graded toward the crack tip. This represents a significant advantage of the proposed approach, given that our objective is to perform many computations to generate data for a neural network, as outlined in Figure 1.2.

Example 5.16. We complement the study in Example 5.13 by investigating how the spectrum of the Laplace operator evolves as the crack length varies. More precisely, we consider the eigenvalue problem (5.23), where $\widetilde{\Omega} = (0, 1)^2$ is the unit square, $\Gamma_0 = \partial\widetilde{\Omega}$ its boundary, and

$$\Gamma_c = \{\boldsymbol{x} \in \mathbb{R}^2 : \boldsymbol{x} = (1 - z, 0.5)^T, z \in (0, l)\}$$

is a straight horizontal crack of variable length $l \in (0, 1)$, with the crack tip being located at $\boldsymbol{V}_0 = (1 - l, 0.5)$. Hence, we consider a parametric eigenvalue problem with respect to the parameter l. As outlined in Remark 5.15, our approach enables the computation of these results by simply adjusting the control points (5.19) at the crack tip. The eigenfunctions have the same regularity as in Example 5.13, and therefore the qualitative convergence analysis is analogous and omitted here. Instead, we focus on a quantitative evaluation of the resulting eigenvalues and eigenfunctions.

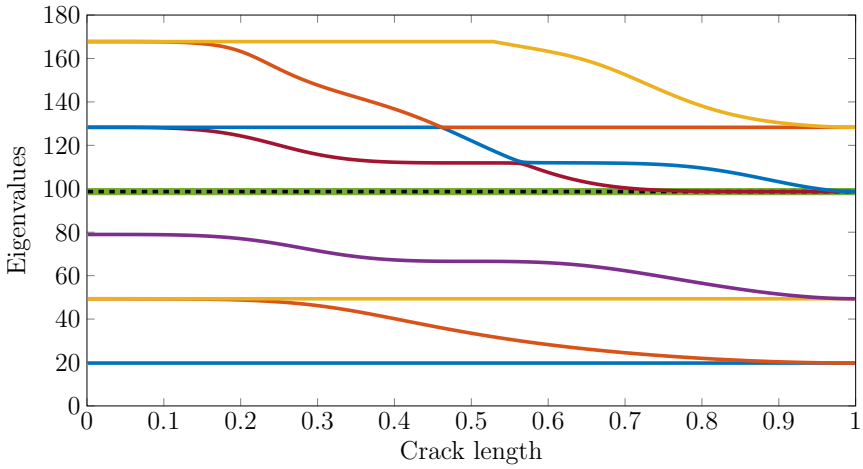

Figure 5.13: Development of the first ten eigenvalues of a unit square with horizontal crack of varying length $l \in (0, 1)$.

In Figure 5.13, the first ten eigenvalues are shown as functions of the crack length, where several characteristic behaviors can be observed. As suggested by our analysis of the coefficient of the second term in the heat trace expansion in Section 5.3.2, and in particular by Remark 5.8, the eigenvalues tend to decrease as the crack length increases. Moreover, we see that eigenvalues of higher multiplicity split and later merge in different compositions, and eigenvalue branches may cross. The fifth and sixth eigenvalues remain equal for all crack lengths; to emphasize this, the sixth eigenvalue is shown as a dashed line. Initially, the spectrum corresponds to that of the unit square and consists of six distinct eigenvalues: two simple and four double ones. As the crack length increases, the spectrum gradually transitions toward that of two disconnected rectangles, resulting in four distinct eigenvalues: three of multiplicity two and one of multiplicity four.

To support our intuition, we visualize the corresponding modes for a short crack of length $l = 0.1$ in Figure 5.14 and for a long crack of length $l = 0.9$ in Figure 5.15. We observe that some eigenfunctions are associated with identical or nearly identical eigenvalues, thereby forming, or approximately forming, higher-dimensional eigenspaces. For example, the fifth and sixth eigenfunctions belong to a double eigenvalue for all crack lengths and thus span a two-dimensional eigenspace. In general, the structure of the eigenspaces changes as the crack length varies. The second eigenfunction serves as a representative example of this behavior. In the domain with a short crack, the second and third modes have nearly equal eigenvalues, suggesting that they approximately span a two-dimensional eigenspace. As the crack grows longer and the domain approaches a disconnected configuration, the eigenvalue associated with the second mode shifts and begins to align more closely with that of the first eigenmode.

To summarize this section, we have shown that our numerical method is well suited for data generation by solving a parametric eigenvalue problem, as it offers the following advantages:

- efficient and accurate spectral approximation,
- simple local refinement toward the crack tip to resolve the singularity, and
- automated mesh generation for varying crack parameters.

Finally, we briefly comment on the limitations and possible extensions of the proposed computational approach, particularly for more complex domains and crack configurations.

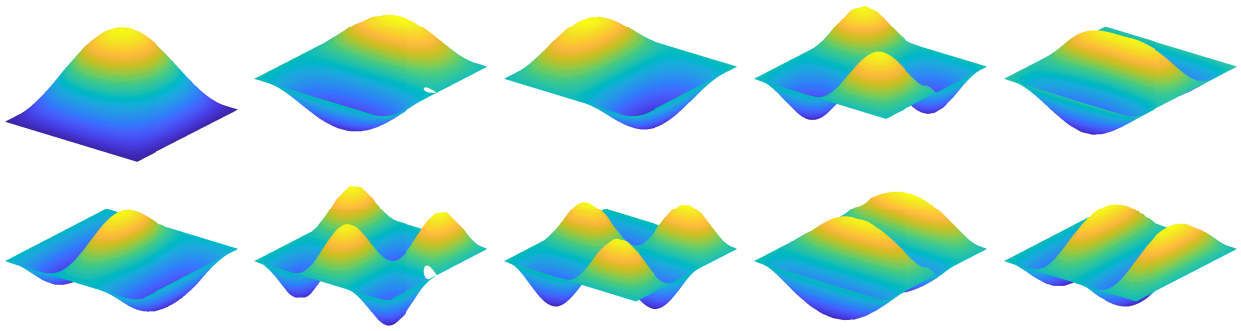

Figure 5.14: Illustration of the eigenfunctions corresponding to the first ten Laplace eigenvalues for a unit square with a horizontal crack of length $l = 0.1$.

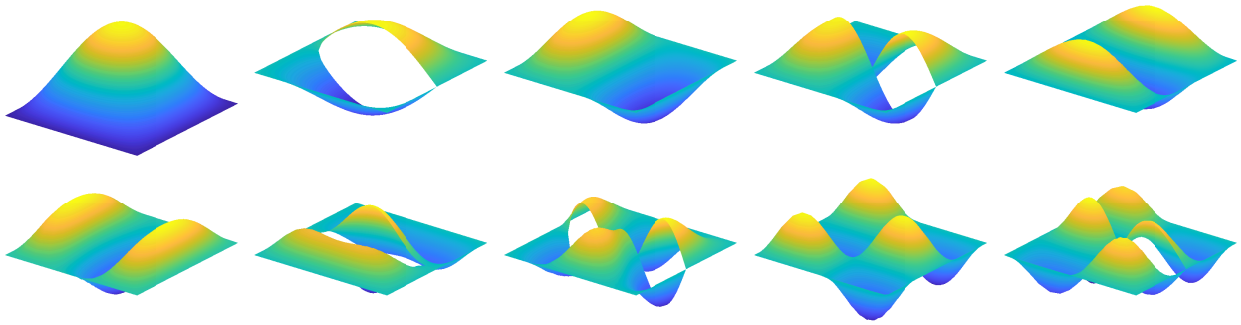

Figure 5.15: Illustration of the eigenfunctions corresponding to the first ten Laplace eigenvalues for a unit square with a horizontal crack of length $l = 0.9$.

Remark 5.17 (Extensions to more general domains). The presented mesh refinement strategy based on polar parameterizations is currently restricted to domains with straight outer cracks that are star-shaped with respect to the crack tip. For more complex domain and crack geometries, the method can be extended to a multi-patch setting. For instance, to discretize domains containing inner straight cracks, the domain can be subdivided into several polar triangles, which are then coupled along their interfaces. An illustrative parameterization of a polar triangle and the required couplings between the triangular patches are shown in Figure 5.16, recall also Example 3.7. In this way, graded meshes that are locally refined toward both crack tips can also be constructed. Moreover, the eigenfunctions may exhibit additional singularities at other corners of the domain [Dau88], where local refinement is likewise required; such cases can be handled in a similar manner. More general regularity results are discussed in the following section.

5.4.2 Regularity of the eigenfunctions

The error estimates stated in Lemma 5.14 rely crucially on the regularity assumptions made there. To justify these requirements, this section collects technical results concerning the regularity of Laplace eigenfunctions on domains with cracks, originally developed in the appendix of [ANZ25]. We begin by describing their behavior in a neighborhood of the crack tip.

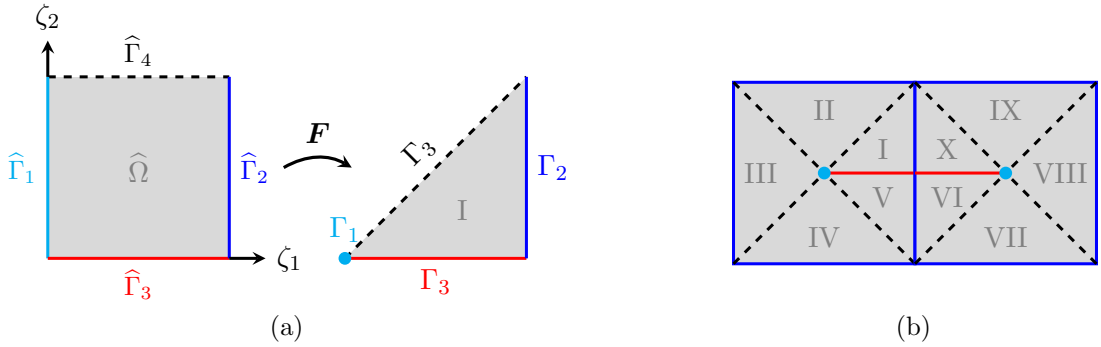

Figure 5.16: Multipatch discretization of a domain with an inner crack using ten patches of polar triangles. (a): Polar parameterization of triangle I. (b): Composition of all patches. The dashed lines indicate inner patch interfaces that must be coupled.

Lemma 5.18. *Let Ω be a domain with an outer crack, and let η be a cut-off function that equals 1 near the crack tip $\boldsymbol{V}_0$ and vanishes away from it. Then, the corresponding Laplace eigenfunctions u of Ω satisfy*

$$\eta u - u(\boldsymbol{V}_0) \in V^s_{\beta,0}(\Omega) \quad \text{for all } (s,\beta) \in \mathbb{N}\times\mathbb{R} \text{ with } s \geq 2 \text{ and } s - \frac{3}{2} < \beta < s-1. \tag{5.24}$$

Proof. This result is proven in [ANZ25, Lemma A.1]. □

We now turn to the overall regularity of Laplace eigenfunctions on domains with cracks. As noted in Remark 5.17, singularities may also occur at corners other than the crack tips. For each vertex $\boldsymbol{V}_i \in \mathcal{V}$, $i = 0,\dots,N$, let $r_i = r_i(\boldsymbol{x})$ denote the distance from a point $\boldsymbol{x} \in \Omega$ to $\boldsymbol{V}_i$. Similar to the solutions of the Poisson equation discussed in Section 2.1.2, Laplace eigenfunctions typically exhibit singularities of the form $r_i^{\nu_i}$ near such corners, where the singular exponent $\nu_i \geq 0$ depends on the interior angle ω_i and the boundary conditions along the adjacent edges, with $\nu_i = \frac{\pi}{\omega_i}$ in the pure Neumann or Dirichlet case and $\nu_i = \frac{\pi}{2\omega_i}$ in the mixed case.

The regularity can again be described in terms of weighted Sobolev spaces, where the weights are now taken with respect to the corresponding corner. For $s \in \mathbb{N}$ and $\beta \in \mathbb{R}$, we define the weighted Sobolev spaces $H^s_{\beta,i}(\Omega)$ and $V^s_{\beta,i}(\Omega)$ around the corner $\boldsymbol{V}_i$ by

$$H^s_{\beta,i}(\Omega) := \{v \in \mathcal{D}'(\Omega) : \|v\|_{H^s_{\beta,i}(\Omega)} < \infty\}, \qquad V^s_{\beta,i}(\Omega) := \{v \in \mathcal{D}'(\Omega) : \|v\|_{V^s_{\beta,i}(\Omega)} < \infty\},$$

with norms

$$\|v\|^2_{H^s_{\beta,i}(\Omega)} := \sum_{|\boldsymbol{\alpha}|\leq s} \left\| r_i^{\beta} D^{\boldsymbol{\alpha}} v \right\|^2_{L^2(\Omega)}, \qquad \|v\|_{V^s_{\beta,i}(\Omega)} := \sum_{|\boldsymbol{\alpha}|\leq s} \left\| r_i^{\beta-s+|\boldsymbol{\alpha}|} D^{\boldsymbol{\alpha}} v \right\|^2_{L^2(\Omega)}.$$

Let η_i, $i = 0,1,\dots,N$, be cut-off functions that equal 1 near the vertex $\boldsymbol{V}_i$ and vanish in the vicinity of every other corner. Then, in weighted H-spaces, we have

$$\eta_i u \in H^s_{\beta,i}(\Omega) \quad \text{for all } (s,\beta) \in \mathbb{N}\times\mathbb{R} \text{ with } s \geq 2 \text{ and } s-1-\nu_i < \beta < s-1+\nu_i,$$

see, e.g., [CDN12, Theorem 7.2]. A corresponding result in weighted V-spaces is available for Dirichlet or mixed boundary conditions at the corner, see [NP94, Chapter 2, Theorem 3.1], namely

$$\eta_i u \in V^s_{\beta,i}(\Omega) \quad \text{for all } (s,\beta) \in \mathbb{N}\times\mathbb{R} \text{ with } s \geq 2 \text{ and } s-1-\nu_i < \beta < s-1+\nu_i.$$

For Neumann BCs at the corner, we can show as in Lemma 5.18 that

$$\eta_i u - u(\boldsymbol{V}_i) \in V^s_{\beta,i}(\Omega) \quad \text{for all } (s,\beta) \in \mathbb{N} \times \mathbb{R} \text{ with } s \geq 2 \text{ and } s - 1 - \nu_i < \beta < s - 1 + \nu_i.$$

However, the results above describe only the lowest regularity one can expect in general, whereas in many situations the actual regularity is higher. For instance, for the unit disk with a crack on the positive x-axis, the analysis of the exact solutions carried out in Section 4.2.3 shows that the only singularity occurs at the crack tip and that some eigenfunctions are even completely smooth in the classical Sobolev sense. In the following, we present another positive example: the eigenfunctions of a square with a perpendicular outer crack are smooth at all vertices away from the crack tip, all of which have an interior angle of 90°. This observation applies in particular to the domains considered in Example 5.16, see also Figure 5.17.

Lemma 5.19. *Let $\Omega = (0,1)^2 \setminus \overline{\Gamma_c}$ contain a horizontal crack of the form*

$$\Gamma_c = \{\boldsymbol{x} \in \mathbb{R}^2 : \boldsymbol{x} = (1-z, h)^T,\ z \in (0,l)\}$$

of length $l \in (0,1)$ and height $h \in (0,1)$. Let η be a cut-off function that equals 1 in the vicinity of the crack tip and vanishes near the other corners of the domain. Then, we have

$$(1-\eta)u \in H^s(\Omega) \quad \text{for all } s \in \mathbb{N}.$$

Proof. The assertion is shown in [ANZ25, Lemma A.2]. □

5.4.3 Solving the inverse problem via neural networks

In the final section of this chapter, the inverse problem illustrated in Figure 5.9 is addressed using a machine learning method. The exposition largely follows Section 4.2 of [ANZ25]. We train a neural network on simulated data, generated by numerically solving the presented forward problem, to predict the shape of a crack from the eigenvalues of the corresponding domain. In recent years, neural networks have attracted significant attention and proven highly effective for the solution of inverse problems. Their success depends on the availability of large amounts of high-quality training data. The accuracy of the data has already been verified in Section 5.4.1. Additionally, arbitrary amounts of training samples can be generated by running a series of simulations, where we benefit from the automated meshing process in isogeometric analysis, as explained in Remark 5.15.

However, to ensure meaningful results, the underlying inverse problem must be well-defined, in the sense that a solution exists and is unique. For this purpose, we draw on our observations from Section 5.3, in particular on Examples 5.9 and 5.11, where we identified suitable settings in which uniqueness can be guaranteed for the considered inverse problems. Moreover, the existence of a solution is given because all eigenvalue inputs to the neural networks, in both the training and test sets, were obtained by computing the eigenvalues of actual domains. For both scenarios, the numerical results reported in the following demonstrate that the trained neural networks can successfully reconstruct the crack shapes, highlighting the potential of such an approach for non-destructive testing, damage identification, and process optimization.

In our examples, the geometry of the crack is described by at most two parameters. The prediction accuracy for a crack parameter θ is evaluated using standard statistical metrics on a test dataset of size $N_t \in \mathbb{N}$. We denote the true parameter values by $\theta^{(j)}$, $j = 1, \ldots, N_t$, with mean $\overline{\theta}$, and the corresponding predicted values by $\tilde{\theta}^{(j)}$, $j = 1, \ldots, N_t$. In Table 5.2, the accuracy metrics employed for the parameter θ are defined. The mean squared error MSE_θ penalizes larger deviations more strongly than smaller ones and serves as a reliable indicator of overall model fit. The mean absolute

$\mathrm{MSE}_\theta = \frac{1}{N_t}\sum_{j=1}^{N_t}\left(\theta^{(j)} - \tilde{\theta}^{(j)}\right)^2$	$\mathrm{MAE}_\theta = \frac{1}{N_t}\sum_{j=1}^{N_t}\left\lvert\theta^{(j)} - \tilde{\theta}^{(j)}\right\rvert$
$\mathrm{MaxE}_\theta = \max_{j=1,2,\dots N_t}\left\lvert\theta^{(j)} - \tilde{\theta}^{(j)}\right\rvert$	$R^2_\theta = 1 - \frac{\sum_{j=1}^{N_t}\left(\theta^{(j)} - \tilde{\theta}^{(j)}\right)^2}{\sum_{j=1}^{N_t}\left(\theta^{(j)} - \overline{\theta}\right)^2}$

Table 5.2: Definition of accuracy metrics for the prediction of a crack parameter θ.

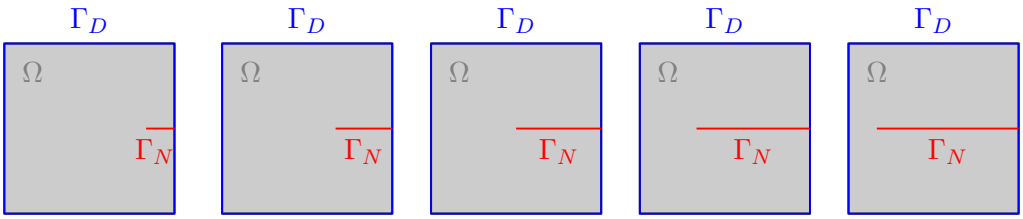

Figure 5.17: Examples of horizontal cracks in the unit square with varying length.

error MAE_θ captures the average magnitude of prediction errors, providing an intuitive measure of accuracy. The maximum error MaxE_θ identifies the worst-case deviation, reflecting the lower bound of prediction performance. Finally, the coefficient of determination R^2_θ quantifies the proportion of variance in the target values explained by the model.

Example 5.20. In the first experiment, we test our data-driven approach on a setup that corresponds to Examples 5.9 and 5.16. Using the algorithm described in Section 5.4.1, we perform a series of simulations for the Laplace eigenvalue problem (5.23), with the crack length parameter l varying across the dataset. Some representative geometries are shown in Figure 5.17. We generate a dataset of 999 samples by varying l in steps of 0.001 over the interval $(0.001, 0.999)$. The simulation parameters for all samples are as follows: B-spline degree $p = 3$, continuity $k = 2$, a graded mesh obtained by 64 uniform subdivisions of the coarse mesh and subsequent grading with parameter $\mu = \frac{0.9}{2p} = 0.15$, and Gauss quadrature with four points in each parametric direction.

Our objective is to train a neural network to predict the crack length l from the first n_{eig} eigenvalues $\lambda_1, \lambda_2, \dots, \lambda_{n_{\text{eig}}}$. The network architecture is shown in Figure 5.18, and is implemented in MATLAB using the Deep Learning Toolbox. The model consists of an input layer with n_{eig} neurons, where the data is normalized and rescaled to the interval $[-1, 1]$, followed by a fully connected hidden layer with $n_{\text{eig}}/2$ neurons and rectified linear unit (ReLU) activation functions, which set negative outputs to zero. A single neuron in the output layer produces the final prediction. The network is trained using MATLAB's `trainNetwork` function with a regression layer at the output, which computes the mean squared error as the loss. Although this configuration is no longer the default in recent MATLAB releases, it provides the most reliable performance for the present problem. We allocate 70% of the dataset for training and the remaining 30% is used for testing. The training process is based on the Adam optimizer with an initial learning rate of 0.01. The dataset is shuffled at every epoch, and the maximum number of epochs is set to 1000. The hyperparameters of the neural network and the training process were selected by manual tuning,

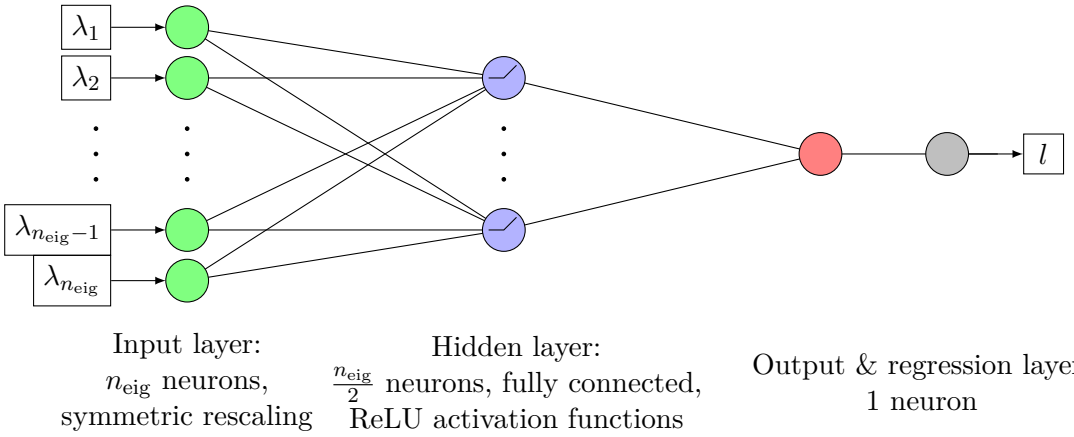

Figure 5.18: Neural network architecture used for predicting the crack length l from the first n_{eig} eigenvalues.

n_{eig}	MSE_l	MAE_l	MaxE_l	R_l^2
4	$7.4550e-04$	$2.2198e-02$	$7.6846e-02$	$9.9145e-01$
8	$2.1248e-04$	$1.1693e-02$	$3.8099e-02$	$9.9756e-01$
16	$4.3224e-05$	$4.4628e-03$	$2.5054e-02$	$9.9950e-01$
32	$3.3991e-05$	$4.5637e-03$	$1.8756e-02$	$9.9961e-01$
64	$9.2959e-06$	$2.3742e-03$	$1.1497e-02$	$9.9989e-01$
128	$8.4589e-06$	$2.1677e-03$	$9.5827e-03$	$9.9990e-01$

Table 5.3: Accuracy metrics for predicting the crack length using a neural network trained on n_{eig} input eigenvalues.

with the goal of keeping the network architecture simple while obtaining satisfactory prediction accuracy. The training loss, given by the mean squared error, is plotted in Figure 5.19. For all values of n_{eig}, the loss converges to a small value, with accuracy improving as more eigenvalues are used.

After the training phase, we assess the performance of the neural network on the test dataset. Figure 5.20 compares the predicted crack lengths with the true values, where proximity to the diagonal indicates high prediction accuracy. A good fit is observed for all values of l, with the predictions becoming consistently more accurate as n_{eig} increases. The results are particularly strong for $n_{\text{eig}} \geq 32$. Finally, we evaluate the prediction performance using the accuracy metrics defined in Table 5.2. The results, shown in Table 5.3, confirm the effectiveness of the method and show a clear improvement in all metrics as more eigenvalues are taken into account. In particular, the mean absolute error and maximum error values indicate that the crack length can be localized with an average error of approximately 2×10^{-3} and a worst-case error of about 10^{-2}. Since the samples in the dataset differ by as little as 10^{-3}, these results underscore the high precision of the prediction.

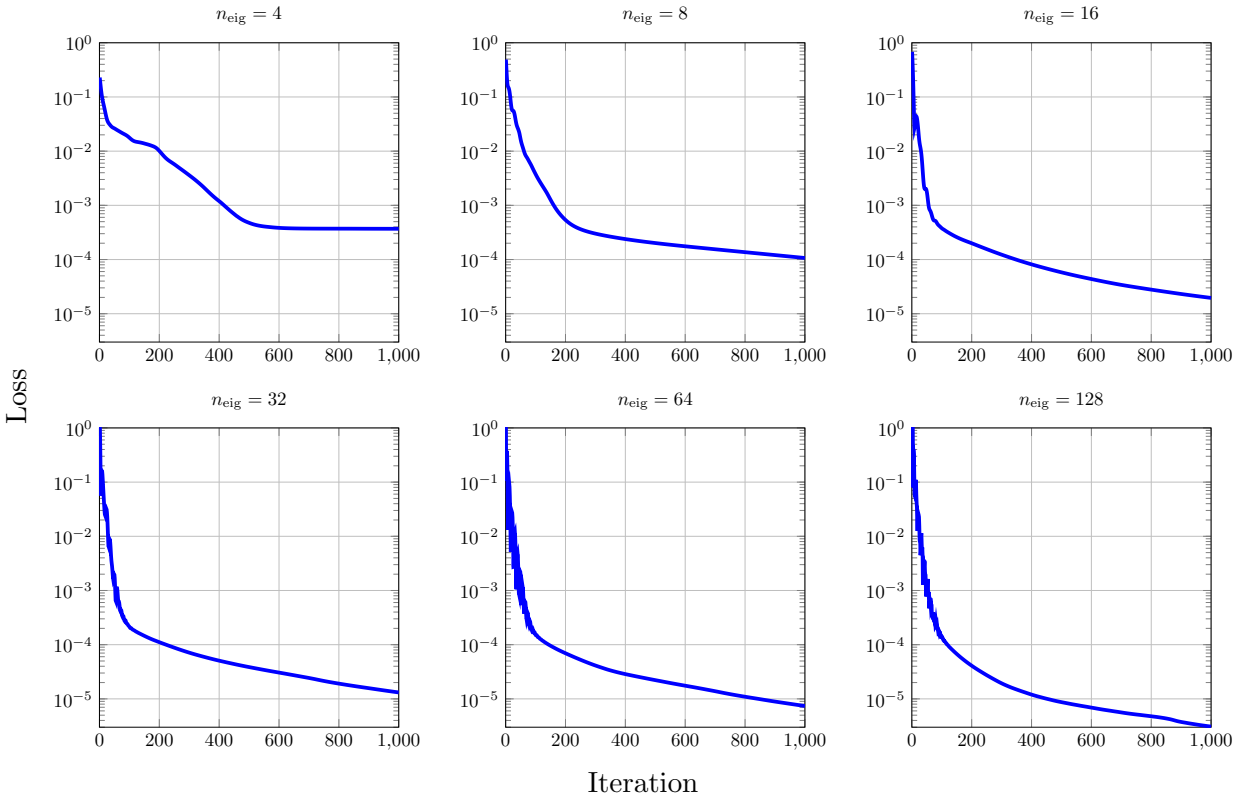

Figure 5.19: Training loss of the neural network for predicting crack length from different numbers of input eigenvalues n_{eig}.

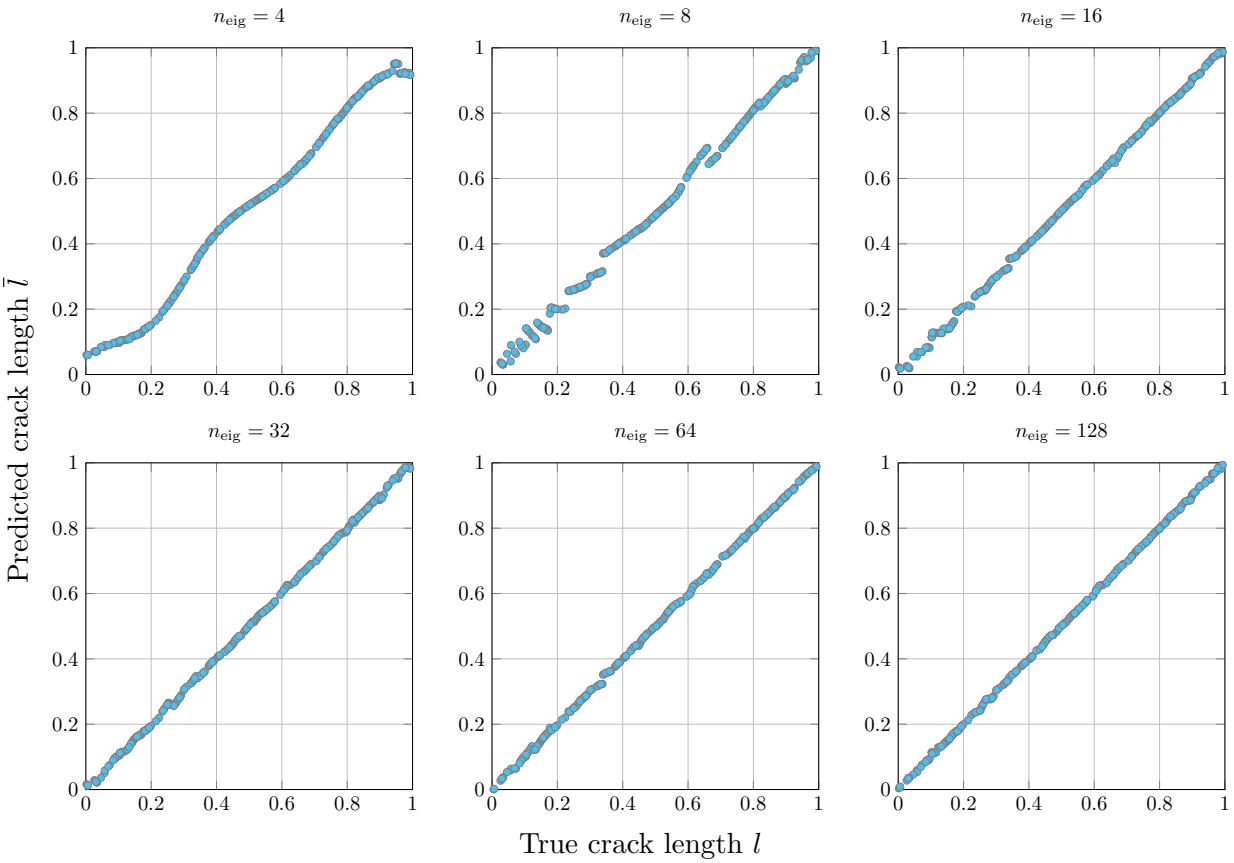

Figure 5.20: Prediction performance of the neural network based on n_{eig} input eigenvalues. The horizontal axis shows the true crack length, and the vertical axis shows the predicted value. The diagonal indicates perfect prediction.

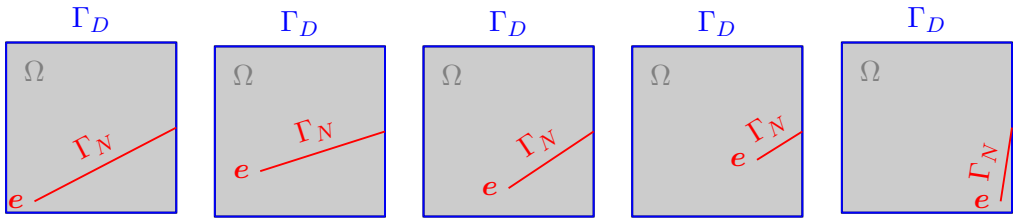

Figure 5.21: Examples of cracks in the unit square with fixed starting point and variable end point in the lower half.

Example 5.21. The second numerical experiment corresponds to the inverse problem described in Example 5.10. We again perform a series of simulations for the Laplace eigenvalue problem (5.23), but now with

$$\Gamma_c = \{\boldsymbol{x} \in \mathbb{R}^2 : \boldsymbol{x} = \boldsymbol{\gamma}_c(0) + z(\boldsymbol{e} - \boldsymbol{\gamma}_c(0)),\ z \in (0,1)\},$$

i.e., a straight outer crack with fixed starting point $\boldsymbol{\gamma}_c(0) = (1, 0.5)^T$ and variable endpoint $\boldsymbol{e} = (e_x, e_y)^T \in (0,1) \times (0, 0.5)$. The coordinates of the endpoint serve as parameters in this experiment. To ensure a unique solution of the inverse problem, we restrict the crack endpoints to the lower half of the domain; otherwise, symmetric reflections would yield identical spectra, as also observed in Example 5.10. Representative crack geometries are shown in Figure 5.21. We generate a dataset of 4950 simulations by varying e_x over the interval $(0.01, 0.99)$ and e_y over $(0.01, 0.5)$, both with a step size of 0.01. All remaining simulation parameters are identical to those used in Example 5.20. Since the interior vertex angles associated with the starting point of the crack differ from 90°, additional corner singularities may arise there. Nevertheless, the singularity at the crack tip remains dominant, so we retain the previous mesh grading strategy. Graded meshes in the vicinity of other corners can be incorporated as outlined in Remark 5.17.

The goal is to train a neural network to predict the crack endpoint $\boldsymbol{e} = (e_x, e_y)^T$ from the first n_{eig} simulated eigenvalues $\lambda_1, \ldots, \lambda_{n_{\text{eig}}}$. The network architecture, illustrated in Figure 5.22, is implemented in MATLAB using the Deep Learning Toolbox. The model consists of an input layer with n_{eig} neurons, which normalizes and rescales the input data to the interval $[-1, 1]$, followed by a fully connected hidden layer with $n_{\text{eig}}/2$ neurons. The output layer has two neurons representing the predicted coordinates of the crack endpoint. ReLU activation functions are applied between layers and after the final output to enforce non-negativity. We allocate 70% of the dataset for training and 30% for testing. The network is trained using MATLAB's `trainnet` routine, where the training parameters are chosen as in Experiment 5.20. The loss function is defined as the average of the mean squared errors for both coordinate components, $\text{MSE} = \frac{1}{2}(\text{MSE}_{e_x} + \text{MSE}_{e_y})$, and its evolution during training is plotted in Figure 5.23. Across all tested values of n_{eig}, the training loss converges to a small value, with accuracy improving as more eigenvalues are used. For larger n_{eig}, mild fluctuations appear in the loss curve, likely due to increased model complexity, but the overall trend remains favorable.

Next, we evaluate the accuracy on the test dataset. Figure 5.24 shows the predicted and true x-coordinates of the crack endpoints. For small n_{eig}, the predictions are less reliable for cracks with endpoints close to $x = 1$, i.e., for very short cracks, likely due to their weak spectral signatures. Yet, as n_{eig} increases, all cracks are predicted accurately. A similar pattern can be observed in Figure 5.25, where the predicted versus true y-coordinates are displayed. In addition, the data points are color-coded according to the absolute prediction error in e_x. A strong correlation between errors

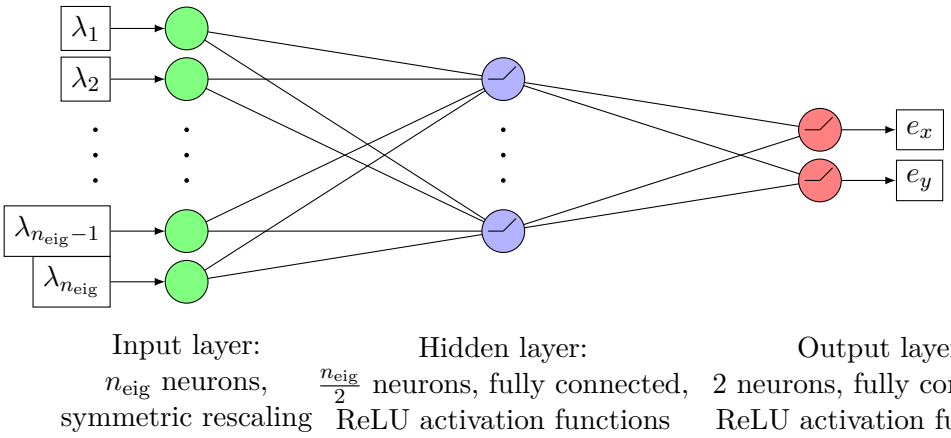

Figure 5.22: Neural network architecture used for predicting the crack endpoint.

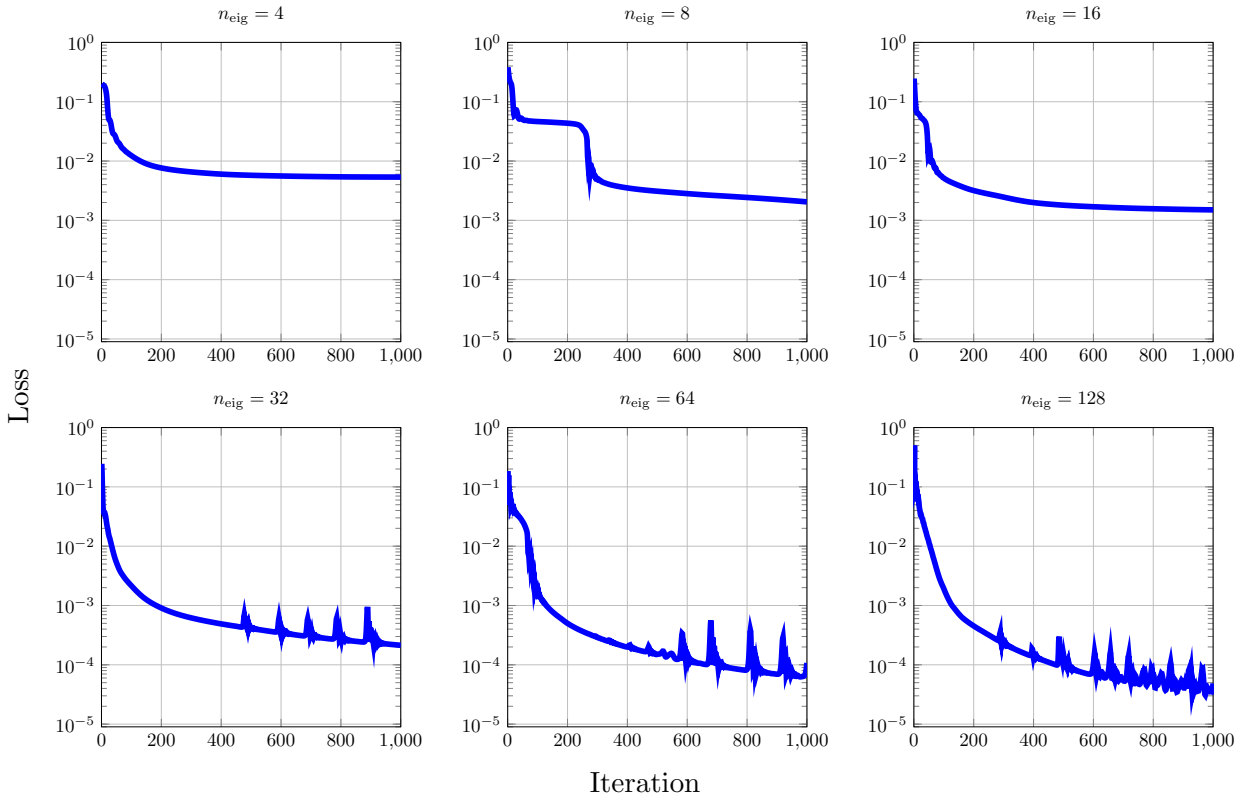

Figure 5.23: Training loss of the neural network for predicting the crack endpoint from different numbers of input eigenvalues n_{eig}.

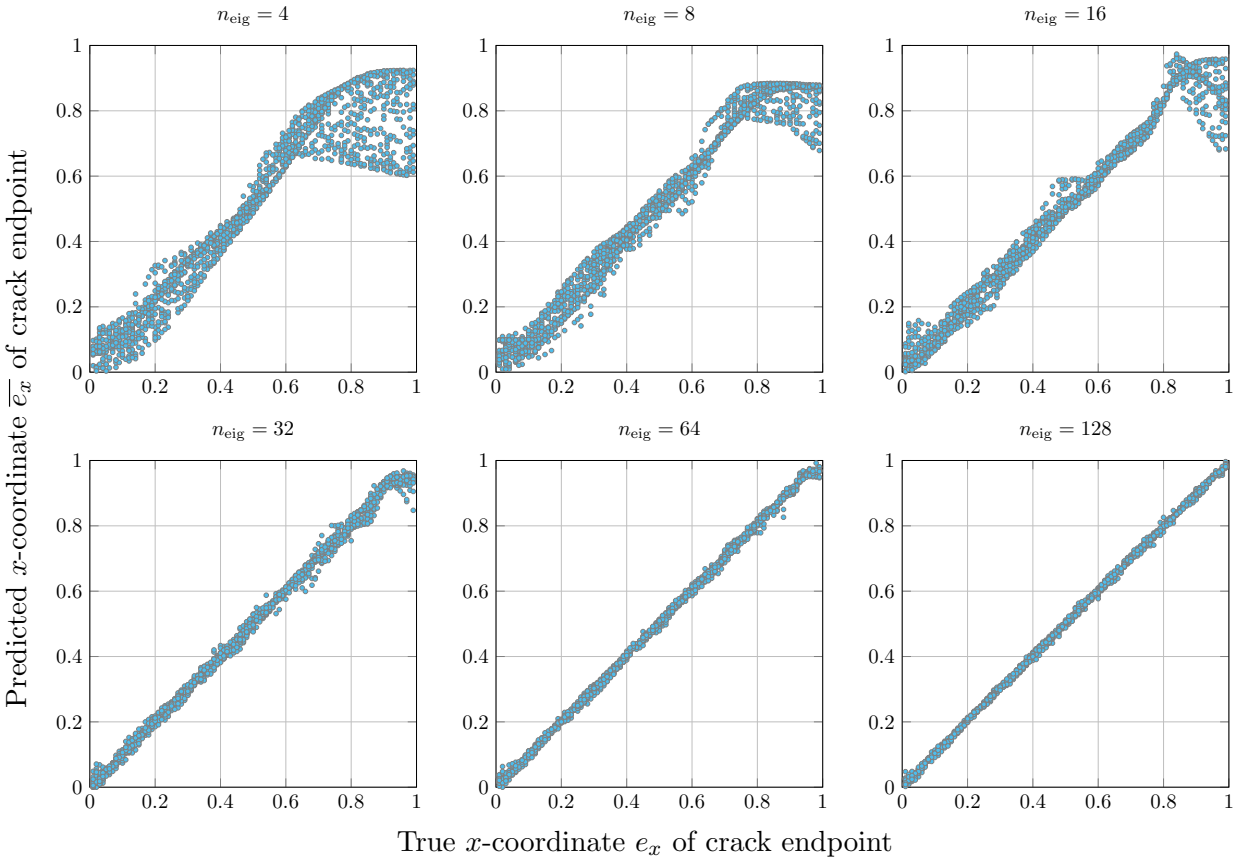

Figure 5.24: Prediction performance of the neural network for the x-coordinate of the crack endpoint based on n_{eig} input eigenvalues. The horizontal axis shows the true value, and the vertical axis shows the predicted value. The diagonal indicates perfect prediction.

in the two coordinates is visible, indicating that cracks which are difficult to resolve in one direction tend to be poorly predicted in the other as well. In particular, the most significant errors occur for cracks located near the bottom-right corner of the domain, that is, $e_x \approx 1$ and $e_y \approx 0$, as illustrated in the rightmost column of Figure 5.21. These outliers gradually disappear if more eigenvalues are taken into account. This observation is reinforced by Figure 5.26, where both predicted and true endpoints are shown in the (x, y)-plane and connected by black lines. The length of each line indicates the prediction error. Longer lines, which correspond to larger errors, are concentrated near the boundaries for small values of n_{eig}, but progressively disappear as n_{eig} increases, confirming the benefit of including more spectral input. Finally, we evaluate the prediction performance using the accuracy metrics defined in Table 5.2. The results are summarized in Table 5.4, where all metrics show consistent improvement for an increasing number input eigenvalues. In particular, the mean absolute error drops below 10^{-2} for both e_x and e_y, which matches the step size used for generating the data. This demonstrates that the network accurately resolves crack endpoints at the same resolution as the dataset itself.

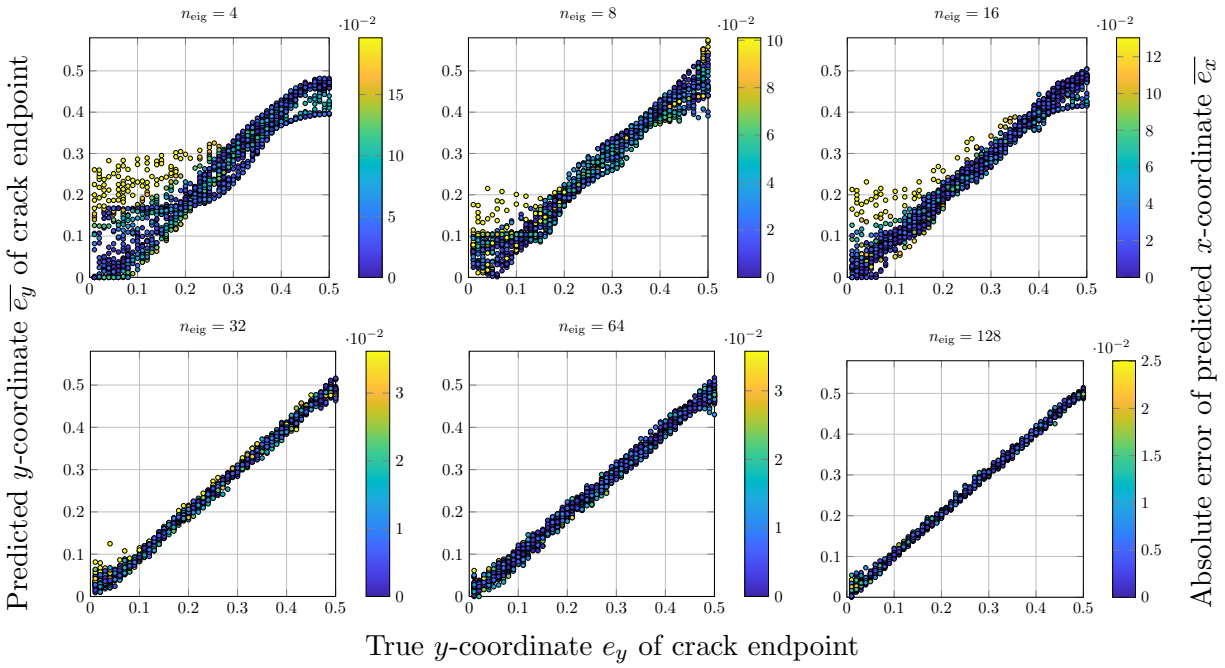

Figure 5.25: Predicted versus true y-coordinates of crack endpoints for varying values of n_{eig}. The diagonal indicates perfect prediction. In addition, the points are color-coded by the corresponding absolute x-coordinate prediction error.

n_{eig}	MSE_{e_x}	MSE_{e_y}	MAE_{e_x}	MAE_{e_y}	MaxE_{e_x}	MaxE_{e_y}	$R^2_{e_x}$	$R^2_{e_y}$
4	$7.9e-03$	$2.7e-03$	$6.2e-02$	$3.6e-02$	$3.8e-01$	$2.5e-01$	$9.0e-01$	$8.7e-01$
8	$3.1e-03$	$9.6e-04$	$4.0e-02$	$2.3e-02$	$3.1e-01$	$1.8e-01$	$9.6e-01$	$9.5e-01$
16	$2.2e-03$	$8.1e-04$	$2.8e-02$	$1.8e-02$	$3.1e-01$	$2.0e-01$	$9.7e-01$	$9.6e-01$
32	$2.8e-04$	$1.2e-04$	$1.2e-02$	$7.9e-03$	$1.4e-01$	$8.5e-02$	$1.0e+00$	$9.9e-01$
64	$9.0e-05$	$1.8e-04$	$7.2e-03$	$1.1e-02$	$5.4e-02$	$7.0e-02$	$1.0e+00$	$9.9e-01$
128	$4.8e-05$	$6.8e-05$	$5.5e-03$	$6.3e-03$	$3.8e-02$	$4.4e-02$	$1.0e+00$	$1.0e+00$

Table 5.4: Accuracy metrics for predicting the x- and y-coordinate of crack endpoints using a neural network trained on n_{eig} input eigenvalues.

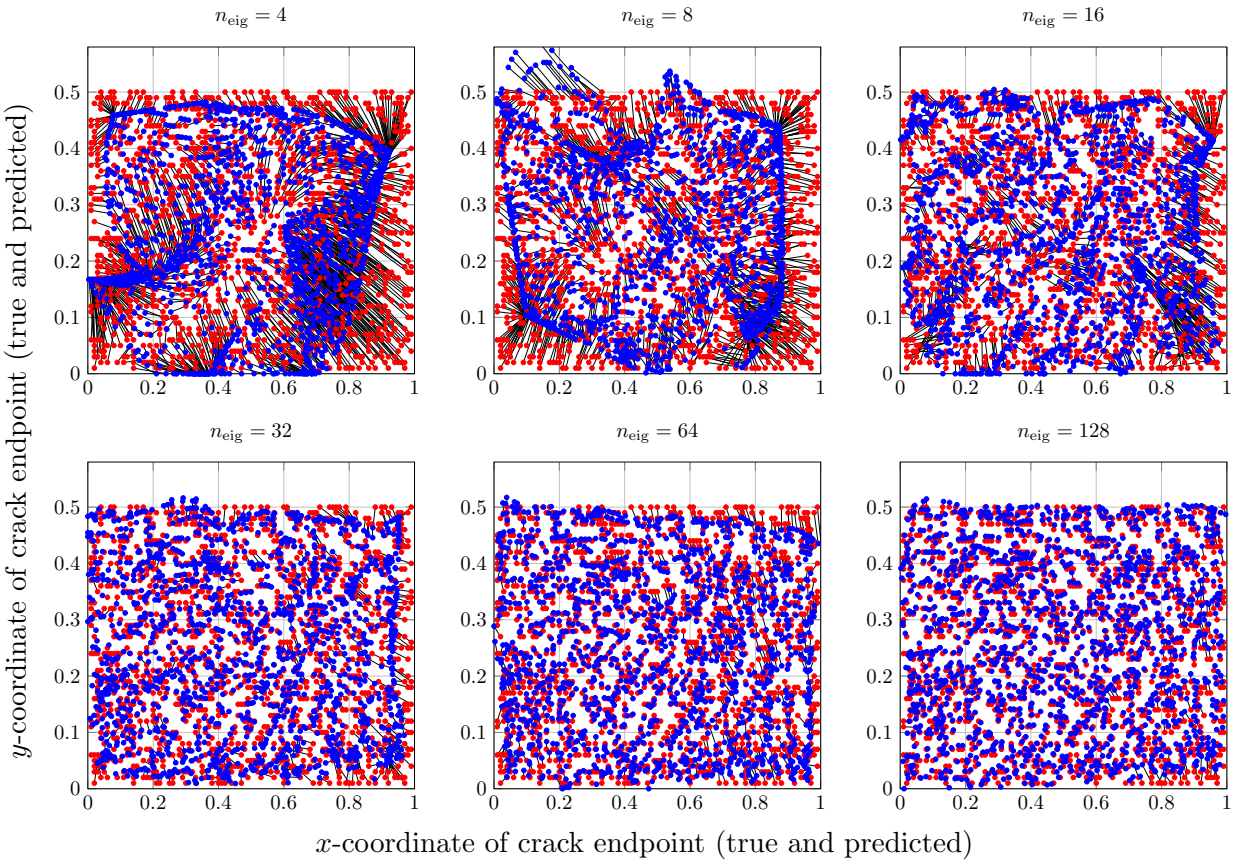

Figure 5.26: Predicted and true crack endpoints in the (x, y)-plane for varying values of n_{eig}. Predictions (blue) are connected to ground truth (red) by black lines indicating the magnitude of the error.

CHAPTER 6

Conclusion and Outlook

This thesis investigates isogeometric analysis on domains with corners and shows a related application in the context of crack identification. The work is motivated by the observation that, although IGA combines exact geometric representations with high-order approximation spaces, these features cannot be fully exploited in a straightforward manner on domains with non-smooth boundaries, for instance due to the occurrence of PDE solutions with corner singularities or singular geometry mappings. These limitations are also reflected in the state-of-the-art mathematical theory of IGA, which does not account for reduced solution regularity and does not cover singular geometry parameterizations, such as polar mappings with a collapsed edge. At the same time, both phenomena arise naturally in many applications and are closely connected, since domains with corners or cracks can be represented naturally by polar parameterizations. The central objective of this thesis is therefore to build a mathematical and computational framework that preserves the advantages of IGA in the presence of both a polar point in the geometry mapping and reduced solution regularity at that point, and to exploit the resulting methodology in the inverse problem of crack identification.

Chapter 3 of the dissertation contains two fundamental contributions in pursuit of this objective. First, we introduce a novel refinement approach for IGA on polar domains with corners that enables locally refined physical meshes in the vicinity of polar corners by grading the parametric mesh toward the collapsing edge. Second, we develop a numerical analysis framework tailored to polar parameterizations, which provides the theoretical foundation for the proposed method. This analysis requires tools beyond the scope of standard isogeometric approximation theory and represents an important step toward the development of parameterization-aware error estimates in IGA. Building on the concept of weighted function spaces, we introduce polar Sobolev spaces on the parametric domain and, by means of explicit derivative transformation formulas, we show that they capture the regularity of pull-backs of PDE solutions under polar parameterizations. The emerging approximation theory explicitly accounts for the singular character of the polar mapping and also covers PDE solutions with corner singularities at the polar point by incorporating graded meshes and weighted Sobolev spaces on the physical domain. Within this framework, error estimates and explicit conditions on the grading parameter are derived to guarantee optimal approximation properties of graded polar splines. These results show that polar parameterizations do not constitute an inherent obstacle to high-order isogeometric approximation and that the loss of convergence caused by solution singularities near polar corners can be effectively remedied.

The proposed grading strategy is particularly attractive because it is boundary-fitted, simple to implement, and computationally efficient. Finally, its successful transfer to the collocation setting further demonstrates that the approach is not limited to Galerkin formulations.

Building on this foundation, Chapter 4 studies the Laplace eigenvalue problem on circular sectors, which is a natural next step for several reasons: circular sectors are classical benchmark domains with corners, can be represented by polar NURBS parameterizations, and possess exact eigenpairs, thereby enabling a detailed investigation of spectral accuracy. The thesis provides a regularity analysis of the exact eigenfunctions and clarifies the distribution of smooth and singular eigenmodes. On this basis, the error estimates developed for boundary value problems are extended to the eigenvalue setting. It is shown both theoretically and numerically that graded polar refinement restores optimal convergence for eigenvalues and eigenfunctions in the presence of corner singularities. Beyond these results, the thesis also contributes to the study of spectral approximation properties of splines. In particular, it shows that smooth spline spaces yield a better approximation constant than their C^0-continuous counterparts, at least for the lower part of the Laplace spectrum. This extends earlier observations from rectangular domains to singularly parameterized circular sectors and thereby broadens the known range of favorable spectral behavior of smooth isogeometric function spaces. The numerical experiments further show that graded meshes lead to a balanced distribution of approximation errors across the computed eigenvalues and are especially effective when only a limited portion of the spectrum is of interest. In addition, a hierarchical refinement strategy is introduced in combination with mesh grading in order to avoid anisotropic elements in the physical domain and to omit redundant degrees of freedom near the conical point, leading to different approximation behavior for smooth eigenfunctions.

Finally, Chapter 5 turns to the application of the preceding investigations to the inverse problem announced in the title, namely crack identification from spectral data. By analyzing the short-time asymptotic expansion of the heat trace, it is first shown from an analytical perspective that cracks leave distinct fingerprints in the Laplace spectrum of the underlying domain and that this information allows one to recover certain crack characteristics. These results provide a partial answer to the question of whether one can hear a crack in a drum. The thesis then complements these analytical findings with a computational, data-driven proof of concept. A neural network is trained on simulated spectral data to approximate the inverse mapping from eigenfrequencies to crack parameters. This part of the thesis relies decisively on the numerical analysis developed in the preceding chapters: crack tips generate singular eigenfunctions, and accurate simulation therefore requires precisely the kind of graded isogeometric discretization introduced earlier. To guarantee the reliability of the spectral training data, corresponding error estimates for domains with cracks are derived. Owing to the high fidelity of the resulting data set, the neural network is able to recover crack parameters from a finite set of eigenfrequencies of the underlying domain with high accuracy.

Overall, the thesis advances three interrelated areas of research. First, it extends the mathematical foundations of IGA to the important class of polar parameterizations that is highly relevant from the CAD viewpoint. Second, it shows that graded refinement toward polar points provides a simple and robust mechanism for recovering optimal approximation of PDE solutions with corner singularities, both for boundary value and eigenvalue problems. Third, it demonstrates that these advances are not only of theoretical interest but also provide the foundation for tackling inverse spectral problems such as crack identification. A central message of the thesis is therefore that corners, polar points, and crack tips should not be viewed solely as obstructions to isogeometric analysis. Rather, once their structure is properly incorporated into the analysis and discretization, they become tractable features that can be handled accurately and efficiently.

The results of this dissertation open several avenues for future research along the three directions outlined above. In the first direction, a natural next step is to strengthen and generalize the approximation theory for polar parameterizations. In particular, it remains an open question whether a result analogous to Theorem 3.21 also holds for weighted H-spaces as introduced in Definition 2.1. Such an extension would prove the optimal approximation of functions that are smooth in the classical Sobolev sense on uniform polar tensor product meshes, as seen for the polynomial in Example 3.38 and the smooth eigenfunction in Example 4.12. For higher-order approximation, these cases are not covered by the error estimate in Corollary 3.22. This generalization would also allow one to establish optimal convergence under graded refinement in the case of Neumann boundary conditions at the corner, as discussed at the end of Section 2.1.2. In this context, it is of particular interest to investigate the approximation properties of the hierarchically structured meshes introduced in Chapter 4. In contrast to the tensor product construction, these meshes yield suboptimal convergence for PDE solutions that are smooth in the classical Sobolev sense when no grading is used; see Example 4.17 and [Tak25, Section 5.1]. Corresponding error estimates and a deeper theoretical understanding would be especially valuable in view of the practical advantages of such meshes. They could also help clarify whether the approximation result on uniform meshes stated in Corollary 3.22 is sharp for hierarchically structured meshes, as it does not appear to be for polar tensor product meshes.

Another natural continuation is the extension of our framework to polar domains without corners, such as the unit disk, which arise in many practical applications, for example in mathematical biology [Ape+26; CHB09]. Beyond this, the methodology should be applied to other model equations and boundary conditions, including inhomogeneous Dirichlet conditions and higher-order problems. The transition to more complex settings also opens up further research questions connected with the second direction. For higher-order PDEs such as the biharmonic equation, the systematic use of C^k-smooth polar spline spaces with $k \geq 1$ is required, and thus also a generalization of the grading approach to such spline constructions [ST21; TSHH17]. In the same spirit, the application of Tchebycheffian splines to construct polar parameterizations [RMS23; Spe22; Spe25] appears to be a promising direction, as it may overcome the limitation imposed by existing C^0-lines in the domain representation highlighted in Remark 3.9. In particular, this could broaden the scope of our graded collocation approach, which is currently restricted to smoothly parameterized domains with corners. Extensions to more complex two-dimensional geometries, multi-patch formulations, and ultimately three-dimensional domains with corner and edge singularities constitute further important challenges. Concerning eigenvalue problems, several questions likewise remain open. The circular sector analysis provides a first step, but a more complete investigation of the impact of mesh grading and non-smooth parameterizations on spectral properties of spline spaces is still needed, in particular regarding the approximation of high frequencies and the appearance of spectral branches.

Finally, in the third direction, the crack identification problem is far from exhausted. From an analytical perspective, the heat trace provides only limited geometric information. The present results show that certain crack parameters can be recovered, but they also indicate that the heat trace alone does not suffice for reconstructing completely arbitrary crack geometries or for localizing entirely unknown cracks. In this context, the analysis of other spectral invariants, and in particular the wave trace, may provide a natural next tool. On the computational side, the proposed data-driven framework admits many possible generalizations, including more advanced neural-network architectures or pre-trained models, physics-based or physics-informed approaches, improved training strategies, and larger, more diverse datasets covering a broader range of crack parameters and geometries. Such extensions are especially relevant for practically motivated scenarios that go beyond the class of analytically tractable isospectral problems.

In summary, this thesis provides a mathematical foundation for isogeometric mesh grading on

polar domains with corners and demonstrates how the approach can be applied to identify cracks in membranes. It thereby establishes a clear line from the development of a numerical method and the corresponding approximation theory to applications in spectral and inverse problems. The results show that careful numerical analysis is not only of independent mathematical interest, but also a key prerequisite for reliable computational methods and for the meaningful deployment of AI-based approaches in practical, real-world scenarios.

Declaration of generative AI and AI-assisted technologies in the writing process

During the preparation of this thesis, the author used ChatGPT and DeepL Write to fix writing errors and to improve readability and language throughout the manuscript. After using these tools, the author reviewed and edited the content and takes full responsibility for the content of the dissertation.

References

[ASR88] M. Abramowitz, I. A. Stegun, and R. H. Romer. "Handbook of Mathematical Functions with Formulas, Graphs, and Mathematical Tables". *American Journal of Physics* 56 (1988), 958–958. DOI: 10.1119/1.15378 (cit. on pp. 89, 90).

[AF03] R. A. Adams and J. J. F. Fournier. *Sobolev spaces*. Second. Vol. 140. Pure and Applied Mathematics (Amsterdam). Elsevier/Academic Press, Amsterdam, 2003, xiv+305 (cit. on pp. 7, 8, 63).

[AH94] T. Apel and B. Heinrich. "Mesh Refinement and Windowing Near Edges for Some Elliptic Problem". *SIAM J. Numer. Anal.* 31.3 (1994), 695–708. DOI: 10.1137/0731037 (cit. on p. 65).

[Ape99] T. Apel. *Anisotropic finite elements: local estimates and applications*. Advances in Numerical Mathematics. B. G. Teubner, Stuttgart, 1999, 261 (cit. on p. 36).

[Ape+26] T. Apel, K. Fellner, V. Kempf, R. Salcedo Lagunero, and P. Zilk. "Lipolysis on Lipid Droplets: Mathematical Modelling and Numerical Discretisations". *Results Math.* 81 (2026), 77. DOI: 10.1007/s00025-026-02639-y (cit. on p. 151).

[AM17] T. Apel and J. M. Melenk. "Interpolation and Quasi-Interpolation in h- and hp-Version Finite Element Spaces". In: *Encyclopedia of Computational Mechanics Second Edition (eds E. Stein, R. Borst and T.J.R. Hughes)*. John Wiley & Sons, Ltd., Chichester, 2017, 1–33. DOI: 10.1002/9781119176817.ecm2002m (cit. on pp. 51, 100).

[AN98] T. Apel and S. Nicaise. "The finite element method with anisotropic mesh grading for elliptic problems in domains with corners and edges". *Math. Methods Appl. Sci.* 21.6 (1998), 519–549. DOI: 10.1002/(SICI)1099-1476(199804)21:6<519::AID-MMA962>3.0.CO;2-R (cit. on pp. 22, 30).

[ANZ25] T. Apel, S. Nicaise, and P. Zilk. *Can one hear the shape of a crack in a drum? Spectral fingerprints and a data-driven perspective*. Preprint. 2025. HAL: https://hal.science/hal-05415870 (cit. on pp. 4, 93, 95, 100, 113, 117, 119, 129, 137–139).

[AP05] T. Apel and C. Pester. "Clement-type interpolation on spherical domains—interpolation error estimates and application to a posteriori error estimation". *IMA J. Numer. Anal.* 25.2 (2005), 310–336. DOI: 10.1093/imanum/drh024 (cit. on p. 108).

[ASS02] T. Apel, A.-M. Sändig, and S. I. Solov'ëv. "Computation of 3D vertex singularities for linear elasticity: error estimates for a finite element method on graded meshes". *Math. Model. Numer. Anal.* 36.6 (2002), 1043–1070 (2003). DOI: 10.1051/m2an:2003005 (cit. on p. 56).

[ASW96] T. Apel, A.-M. Sändig, and J. R. Whiteman. "Graded mesh refinement and error estimates for finite element solutions of elliptic boundary value problems in non-smooth domains". *Math. Methods Appl. Sci.* 19.1 (1996), 63–85. DOI: 10.1002/(SICI)1099-1476(19960110)19:1<63::AID-MMA764>3.0.CO;2-S (cit. on pp. 9, 22, 30, 65).

[AZ24a] T. Apel and P. Zilk. "Isogeometric analysis of the Laplace eigenvalue problem on circular sectors: Regularity properties and graded meshes". *Comput. Math. Appl.* 175 (2024), 236–254. DOI: 10.1016/j.camwa.2024.09.018 (cit. on pp. 4, 28, 30, 33, 51, 85, 87, 95, 99, 101).

[AZ24b] T. Apel and P. Zilk. *Isogeometric analysis of the Laplace eigenvalue problem on circular sectors: Regularity properties, graded meshes & variational crimes*. arXiv preprint. 2024. arXiv: 2402.16589 (cit. on p. 69).

[AZ26] T. Apel and P. Zilk. "Error estimates and graded mesh refinement for isogeometric analysis in the vicinity of polar corners". *Comput. Methods Appl. Mech. Engrg.* 452 (2026), 118695. DOI: 10.1016/j.cma.2025.118695 (cit. on pp. 4, 21, 24, 36, 49, 68, 133).

[ARKS23] J. Arf, M. Reichle, S. Klinkel, and B. Simeon. "Scaled boundary isogeometric analysis with C^1 coupling for Kirchhoff plate theory". *Comput. Methods Appl. Mech. Engrg.* 415 (2023), Paper No. 116198, 26. DOI: 10.1016/j.cma.2023.116198 (cit. on p. 22).

[ASKS19] C. Arioli, A. Shamanskiy, S. Klinkel, and B. Simeon. "Scaled boundary parametrizations in isogeometric analysis". *Comput. Methods Appl. Mech. Engrg.* 349 (2019), 576–594. DOI: 10.1016/j.cma.2019.02.022 (cit. on p. 22).

[AS84] D. N. Arnold and J. Saranen. "On the asymptotic convergence of spline collocation methods for partial differential equations". *SIAM J. Numer. Anal.* 21.3 (1984), 459–472. DOI: 10.1137/0721034 (cit. on p. 13).

[ASC11] M. Aubry, U. Schlickewei, and D. Cremers. "The wave kernel signature: A quantum mechanical approach to shape analysis". In: *2011 IEEE International Conference on Computer Vision Workshops (ICCV Workshops)*. 2011, 1626–1633. DOI: 10.1109/ICCVW.2011.6130444 (cit. on p. 116).

[Aur+10] F. Auricchio, L. Beirão da Veiga, T. J. R. Hughes, A. Reali, and G. Sangalli. "Isogeometric collocation methods". *Math. Models Methods Appl. Sci.* 20.11 (2010), 2075–2107. DOI: 10.1142/S0218202510004878 (cit. on pp. 13, 78–80).

[BO91] I. Babuška and J. Osborn. "Eigenvalue problems". In: *Finite Element Methods (Part 1)*. Vol. 2. Handbook of Numerical Analysis. Amsterdam: North-Holland, 1991, 641–787. DOI: 10.1016/S1570-8659(05)80042-0 (cit. on pp. 85, 96–98, 117).

[Bab70] I. Babuška. "Finite element method for domains with corners". *Computing* 6 (1970), 264–273. DOI: 10.1007/bf02238811 (cit. on pp. 22, 30).

[BDQ15] A. Bartezzaghi, L. Dedè, and A. Quarteroni. "Isogeometric analysis of high order partial differential equations on surfaces". *Comput. Methods Appl. Mech. Engrg.* 295 (2015), 446–469. DOI: 10.1016/j.cma.2015.07.018 (cit. on p. 105).

[Baz+06] Y. Bazilevs, L. Beirão da Veiga, J. A. Cottrell, T. J. R. Hughes, and G. Sangalli. "Isogeometric analysis: approximation, stability and error estimates for h-refined meshes". *Math. Models Methods Appl. Sci.* 16.7 (2006), 1031–1090. DOI: 10.1142/S0218202506001455 (cit. on pp. 1, 14, 17, 22, 29, 33, 38, 40, 44, 46, 99).

[BBSV14] L. Beirão da Veiga, A. Buffa, G. Sangalli, and R. Vázquez. "Mathematical analysis of variational isogeometric methods". *Acta Numer.* 23 (2014), 157–287. DOI: 10.1017/S096249291400004X (cit. on pp. 1, 14, 17, 18, 20, 22, 24, 33, 38–41, 44, 47, 48, 52, 54, 60, 62, 99).

[BCS12] L. Beirão da Veiga, D. Cho, and G. Sangalli. "Anisotropic NURBS approximation in isogeometric analysis". *Comput. Methods Appl. Mech. Engrg.* 209/212 (2012), 1–11. DOI: 10.1016/j.cma.2011.10.016 (cit. on pp. 1, 14, 17, 22, 25, 27, 30, 31, 33, 38–41, 44, 52, 53).

[Boo01] C. de Boor. *A practical guide to splines*. Revised. Vol. 27. Applied Mathematical Sciences. New York: Springer-Verlag, 2001, xviii+346 (cit. on pp. 19, 20).

[BGKV20] C. Bracco, C. Giannelli, M. Kapl, and R. Vázquez. "Isogeometric analysis with C^1 hierarchical functions on planar two-patch geometries". *Comput. Math. Appl.* 80.11 (2020), 2538–2562. DOI: 10.1016/j.camwa.2020.03.018 (cit. on p. 73).

[Bra97] D. Braess. *Finite elements*. Theory, fast solvers, and applications in solid mechanics, Translated from the 1992 German original by Larry L. Schumaker. Cambridge: Cambridge University Press, 1997, xvi+323. DOI: 10.1007/978-3-662-07233-2 (cit. on p. 12).

[BS08] S. C. Brenner and L. R. Scott. *The mathematical theory of finite element methods*. Third. Vol. 15. Texts in Applied Mathematics. New York: Springer, 2008, xviii+397. DOI: 10.1007/978-0-387-75934-0 (cit. on p. 12).

[BBGO11] A. M. Bronstein, M. M. Bronstein, L. J. Guibas, and M. Ovsjanikov. "Shape google: Geometric words and expressions for invariant shape retrieval". *ACM Trans. Graph.* 30.1 (2011). DOI: 10.1145/1899404.1899405 (cit. on p. 116).

[BSMM01] I. N. Bronstein, K. A. Semendjajew, G. Musiol, and H. Mühlig. *Taschenbuch der Mathematik*. Thun: Verlag Harri Deutsch, 2001, xxxviii+1196 (cit. on p. 92).

[Buf+22] A. Buffa, G. Gantner, C. Giannelli, D. Praetorius, and R. Vázquez. "Mathematical foundations of adaptive isogeometric analysis". *Arch. Comput. Methods Eng.* 29.7 (2022), 4479–4555. DOI: 10.1007/s11831-022-09752-5 (cit. on p. 22).

[Cle62] A. Clebsch. *Theorie der Elasticität fester Körper*. Leipzig: Teubner, 1862 (cit. on pp. 85, 87).

[Cos+19] L. Cosmo, M. Panine, A. Rampini, M. Ovsjanikov, M. M. Bronstein, and E. Rodola. "Isospectralization, or How to Hear Shape, Style, and Correspondence". In: *Proceedings of the IEEE/CVF Conference on Computer Vision and Pattern Recognition (CVPR)*. 2019 (cit. on p. 116).

[CDN12] M. Costabel, M. Dauge, and S. Nicaise. "Analytic regularity for linear elliptic systems in polygons and polyhedra". *Math. Models Methods Appl. Sci.* 22.8 (2012), 1250015. DOI: 10.1142/S0218202512500157 (cit. on pp. 11, 138).

[CHR07] J. A. Cottrell, T. J. R. Hughes, and A. Reali. "Studies of refinement and continuity in isogeometric structural analysis". *Comput. Methods Appl. Mech. Engrg.* 196.41 (2007), 4160–4183. DOI: 10.1016/j.cma.2007.04.007 (cit. on p. 86).

[CRBH06] J. A. Cottrell, A. Reali, Y. Bazilevs, and T. J. R. Hughes. "Isogeometric analysis of structural vibrations". *Comput. Methods Appl. Mech. Engrg.* 195.41-43 (2006), 5257–5296. DOI: 10.1016/j.cma.2005.09.027 (cit. on p. 86).

[CHB09] J. A. Cottrell, T. J. R. Hughes, and Y. Bazilevs. *Isogeometric analysis. Toward integration of CAD and FEA*. Chichester: John Wiley & Sons, Ltd., 2009. DOI: 10.1002/9780470749081 (cit. on pp. 14, 19, 22, 24, 27, 86, 105, 151).

[Dau88] M. Dauge. *Elliptic boundary value problems on corner domains*. Vol. 1341. Lecture Notes in Mathematics. Berlin: Springer-Verlag, 1988, viii+259. DOI: 10.1007/BFb0086682 (cit. on pp. 9, 11, 130, 137).

[Dur88] C. Durso. "On the inverse spectral problem for polygonal domains". PhD thesis. Massachusetts Institute of Technology, 1988 (cit. on p. 115).

[Elb01] Á. Elbert. "Some recent results on the zeros of Bessel functions and orthogonal polynomials". *J. Comput. Appl. Math.* 133.1 (2001), 65–83. DOI: 10.1016/S0377-0427(00)00635-X (cit. on p. 89).

[FRV11] C. de Falco, A. Reali, and R. Vázquez. "GeoPDEs: A research tool for Isogeometric Analysis of PDEs". *Adv. Eng. Softw.* 42.12 (2011), 1020–1034. DOI: 10.1016/j.advengsoft.2011.06.010 (cit. on pp. 68, 101).

[Fal+19] A. Falini, C. Giannelli, T. Kanduč, M. L. Sampoli, and A. Sestini. "An adaptive IgA-BEM with hierarchical B-splines based on quasi-interpolation quadrature schemes". *Internat. J. Numer. Methods Engrg.* 117.10 (2019), 1038–1058. DOI: 10.1002/nme.5990 (cit. on p. 22).

[Far95] G. E. Farin. *NURB curves and surfaces: from projective geometry to practical use*. Wellesley, MA: A. K. Peters, Ltd., 1995, xii+229 (cit. on p. 19).

[FGHP16] M. Feischl, G. Gantner, A. Haberl, and D. Praetorius. "Adaptive 2D IGA boundary element methods". *Eng. Anal. Bound. Elem.* 62 (2016), 141–153. DOI: 10.1016/j.enganabound.2015.10.003 (cit. on p. 22).

[GV18] E. M. Garau and R. Vázquez. "Algorithms for the implementation of adaptive isogeometric methods using hierarchical B-splines". *Appl. Numer. Math.* 123 (2018), 58–87. DOI: 10.1016/j.apnum.2017.08.006 (cit. on pp. 24, 73, 108).

[Gar+19] C. Garoni, H. Speleers, S.-E. Ekström, A. Reali, S. Serra-Capizzano, and T. J. R. Hughes. "Symbol-based analysis of finite element and isogeometric B-spline discretizations of eigenvalue problems: exposition and review". *Arch. Comput. Methods Eng.* 26.5 (2019), 1639–1690. DOI: 10.1007/s11831-018-9295-y (cit. on p. 86).

[GGHO21] S. Giani, L. Grubišić, H. Hakula, and J. S. Ovall. "A posteriori error estimates for elliptic eigenvalue problems using auxiliary subspace techniques". *J. Sci. Comput.* 88.3 (2021), 55. DOI: 10.1007/s10915-021-01572-2 (cit. on p. 106).

[GWW92] C. Gordon, D. L. Webb, and S. Wolpert. "One cannot hear the shape of a drum". *Bull. Amer. Math. Soc. (N.S.)* 27.1 (1992), 134–138. DOI: 10.1090/S0273-0979-1992-00289-6 (cit. on p. 114).

[GN13] D. S. Grebenkov and B.-T. Nguyen. "Geometrical structure of Laplacian eigenfunctions". *SIAM Rev.* 55.4 (2013), 601–667. DOI: 10.1137/120880173 (cit. on pp. 87, 89, 116).

[GM13] D. Grieser and S. Maronna. "Hearing the shape of a triangle". *Notices Amer. Math. Soc.* 60.11 (2013), 1440–1447. DOI: 10.1090/noti1063 (cit. on p. 115).

[Gri85] P. Grisvard. *Elliptic problems in nonsmooth domains*. Vol. 24. Monographs and Studies in Mathematics. Boston, MA: Pitman (Advanced Publishing Program), 1985, xiv+410 (cit. on p. 9).

[HLR21] H. Hezari, Z. Lu, and J. Rowlett. "The Dirichlet isospectral problem for trapezoids". *J. Math. Phys.* 62.5 (2021), Paper No. 051511, 13. DOI: 10.1063/5.0036384 (cit. on p. 115).

[HLR17] H. Hezari, Z. Lu, and J. Rowlett. "The Neumann isospectral problem for trapezoids". *Ann. Henri Poincaré* 18.12 (2017), 3759–3792. DOI: 10.1007/s00023-017-0617-7 (cit. on p. 115).

[HZ22] H. Hezari and S. Zelditch. "One can hear the shape of ellipses of small eccentricity". *Ann. of Math.* 196.3 (2022), 1083–1134. DOI: 10.4007/annals.2022.196.3.4 (cit. on p. 115).

[HHRS21] R. R. Hiemstra, T. J. R. Hughes, A. Reali, and D. Schillinger. "Removal of spurious outlier frequencies and modes from isogeometric discretizations of second- and fourth-order problems in one, two, and three dimensions". *Comput. Methods Appl. Mech. Engrg.* 387 (2021), 114115. DOI: 10.1016/j.cma.2021.114115 (cit. on pp. 86, 105, 106).

[HCB05] T. J. R. Hughes, J. A. Cottrell, and Y. Bazilevs. "Isogeometric analysis: CAD, finite elements, NURBS, exact geometry and mesh refinement". *Comput. Methods Appl. Mech. Engrg.* 194.39-41 (2005), 4135–4195. DOI: 10.1016/j.cma.2004.10.008 (cit. on pp. 16, 86).

[HRS08] T. J. R. Hughes, A. Reali, and G. Sangalli. "Duality and unified analysis of discrete approximations in structural dynamics and wave propagation: comparison of p-method finite elements with k-method NURBS". *Comput. Methods Appl. Mech. Engrg.* 197.49-50 (2008), 4104–4124. DOI: 10.1016/j.cma.2008.04.006 (cit. on pp. 2, 86, 106).

[HER14] T. J. R. Hughes, J. A. Evans, and A. Reali. "Finite element and NURBS approximations of eigenvalue, boundary-value, and initial-value problems". *Comput. Methods Appl. Mech. Engrg.* 272 (2014), 290–320. DOI: 10.1016/j.cma.2013.11.012 (cit. on pp. 2, 86).

[HS17] T. J. R. Hughes and G. Sangalli. "Mathematics of Isogeometric Analysis: A Conspectus". In: *Encyclopedia of Computational Mechanics Second Edition*. John Wiley & Sons, Ltd., 2017, 1–40. DOI: 10.1002/9781119176817.ecm2100 (cit. on pp. 1, 24).

[Hug12] T. J. Hughes. *The finite element method: linear static and dynamic finite element analysis*. Mineola, NY: Dover publications, 2012 (cit. on p. 106).

[JOKK13] J. W. Jeong, H.-S. Oh, S. Kang, and H. Kim. "Mapping techniques for isogeometric analysis of elliptic boundary value problems containing singularities". *Comput. Methods Appl. Mech. Engrg.* 254 (2013), 334–352. DOI: 10.1016/j.cma.2012.09.009 (cit. on p. 22).

[JLL19] T. Jonsson, M. G. Larson, and K. Larsson. "Graded parametric CutFEM and CutIGA for elliptic boundary value problems in domains with corners". *Comput. Methods Appl. Mech. Engrg.* 354 (2019), 331–350. DOI: 10.1016/j.cma.2019.05.024 (cit. on pp. 22, 30–32).

[Kac66] M. Kac. "Can one hear the shape of a drum?" *Amer. Math. Monthly* 73.4, part II (1966), 1–23. DOI: 10.2307/2313748 (cit. on pp. 3, 85, 113–115).

[KS84] J. R. Kuttler and V. G. Sigillito. "Eigenvalues of the Laplacian in two dimensions". *SIAM Rev.* 26.2 (1984), 163–193. DOI: 10.1137/1026033 (cit. on p. 87).

[LMMT15] U. Langer, A. Mantzaflaris, S. E. Moore, and I. Toulopoulos. "Mesh grading in isogeometric analysis". *Comput. Math. Appl.* 70.7 (2015), 1685–1700. DOI: 10.1016/j.camwa.2015.03.011 (cit. on pp. 22, 30, 31, 98, 99).

[LLM01] B.-G. Lee, T. Lyche, and K. Mørken. "Some examples of quasi-interpolants constructed from local spline projectors". In: *Mathematical methods for curves and surfaces (Oslo, 2000)*. Innov. Appl. Math. Vanderbilt Univ. Press, Nashville, TN, 2001, 243–252 (cit. on p. 17).

[Lev06] B. Levy. "Laplace-Beltrami Eigenfunctions Towards an Algorithm That "Understands" Geometry". In: *IEEE International Conference on Shape Modeling and Applications 2006 (SMI'06)*. 2006, 13–13. DOI: 10.1109/SMI.2006.21 (cit. on p. 116).

[LL00] Z. C. Li and T. T. Lu. "Singularities and treatments of elliptic boundary value problems". *Math. Comput. Modelling* 31.8-9 (2000), 97–145. DOI: 10.1016/S0895-7177(00)00062-5 (cit. on p. 22).

[Lu09] J. Lu. "Circular element: isogeometric elements of smooth boundary". *Comput. Methods Appl. Mech. Engrg.* 198.30-32 (2009), 2391–2402. DOI: 10.1016/j.cma.2009.02.029 (cit. on pp. 27, 86).

[LZ11] J. Lu and X. Zhou. "Cylindrical element: isogeometric model of continuum rod". *Comput. Methods Appl. Mech. Engrg.* 200.1-4 (2011), 233–241. DOI: 10.1016/j.cma.2010.08.007 (cit. on p. 22).

[LR15] Z. Lu and J. Rowlett. "The sound of symmetry". *Amer. Math. Monthly* 122.9 (2015), 815–835. DOI: 10.4169/amer.math.monthly.122.9.815 (cit. on p. 115).

[LR16] Z. Lu and J. M. Rowlett. "One can hear the corners of a drum". *Bull. Lond. Math. Soc.* 48.1 (2016), 85–93. DOI: 10.1112/blms/bdv094 (cit. on p. 115).

[LMS18] T. Lyche, C. Manni, and H. Speleers. "Foundations of spline theory: B-splines, spline approximation, and hierarchical refinement". In: *Splines and PDEs: from approximation theory to numerical linear algebra*. Vol. 2219. Lecture Notes in Math. Springer, Cham, 2018, 1–76 (cit. on pp. 14, 66).

[MSS22] C. Manni, E. Sande, and H. Speleers. "Application of optimal spline subspaces for the removal of spurious outliers in isogeometric discretizations". *Comput. Methods Appl. Mech. Engrg.* 389 (2022), 114260. DOI: 10.1016/j.cma.2021.114260 (cit. on pp. 2, 86, 105, 106).

[MH18] B. Marussig and T. J. R. Hughes. "A review of trimming in isogeometric analysis: challenges, data exchange and simulation aspects". *Arch. Comput. Methods Eng.* 25.4 (2018), 1059–1127. DOI: 10.1007/s11831-017-9220-9 (cit. on p. 22).

[MP78] V. G. Maz'ya and B. A. Plamenevskiĭ. "L^p-estimates of solutions of elliptic boundary value problems in domains with ribs". *Trudy Moskov. Mat. Obshch.* 37 (1978), 49–93, 270 (cit. on p. 9).

[MS67] H. P. McKean Jr. and I. M. Singer. "Curvature and the eigenvalues of the Laplacian". *J. Differential Geom.* 1.1 (1967), 43–69. DOI: 10.4310/jdg/1214427880 (cit. on pp. 114, 115).

[MR82] B. Mercier and G. Raugel. "Résolution d'un problème aux limites dans un ouvert axisymétrique par éléments finis en r, z et séries de Fourier en θ". *RAIRO Anal. Numér.* 16.4 (1982), 405–461 (cit. on pp. 9, 22, 58, 60–62).

[Mil64] J. Milnor. "Eigenvalues of the Laplace operator on certain manifolds". *Proc. Natl. Acad. Sci. USA* 51 (1964), 542. DOI: 10.1073/pnas.51.4.542 (cit. on p. 114).

[MST17] M. Montardini, G. Sangalli, and L. Tamellini. "Optimal-order isogeometric collocation at Galerkin superconvergent points". *Comput. Methods Appl. Mech. Engrg.* 316 (2017), 741–757. DOI: 10.1016/j.cma.2016.09.043 (cit. on pp. 13, 78, 79).

[NP94] S. A. Nazarov and B. A. Plamenevsky. *Elliptic problems in domains with piecewise smooth boundaries*. Vol. 13. De Gruyter Expositions in Mathematics. Berlin: Walter de Gruyter & Co., 1994, viii+525. DOI: 10.1515/9783110848915.525 (cit. on pp. 11, 138).

[NKP14] T. Nguyen, K. Karčiauskas, and J. Peters. "A Comparative Study of Several Classical, Discrete Differential and Isogeometric Methods for Solving Poisson's Equation on the Disk". *Axioms* 3.2 (2014), 280–299. DOI: 10.3390/axioms3020280 (cit. on p. 30).

[Nic93] S. Nicaise. *Polygonal Interface Problems*. Vol. 39. Methoden und Verfahren der mathematischen Physik. Frankfurt am Main: P. Lang, 1993 (cit. on p. 76).

[Nie+07] M. Niethammer, M. Reuter, F.-E. Wolter, S. Bouix, N. Peinecke, M.-S. Koo, and M. E. Shenton. "Global Medical Shape Analysis Using the Laplace-Beltrami Spectrum". In: *Medical Image Computing and Computer-Assisted Intervention – MICCAI 2007*. Ed. by N. Ayache, S. Ourselin, and A. Maeder. Berlin, Heidelberg: Springer, 2007, 850–857. DOI: 10.1007/978-3-540-75757-3_103 (cit. on p. 116).

[NRR23] E. Nilsson, J. Rowlett, and F. Rydell. "The isospectral problem for flat tori from three perspectives". *Bull. Amer. Math. Soc. (N.S.)* 60.1 (2023), 39–83. DOI: 10.1090/bull/1770 (cit. on p. 115).

[NRS19] M. Nursultanov, J. Rowlett, and D. Sher. "How to Hear the Corners of a Drum". In: *2017 MATRIX Annals*. Ed. by J. de Gier, C. E. Praeger, and T. Tao. Cham: Springer International Publishing, 2019, 243–278. DOI: 10.1007/978-3-030-04161-8_18 (cit. on p. 115).

[NRS24] M. Nursultanov, J. Rowlett, and D. Sher. "The heat kernel on curvilinear polygonal domains in surfaces". *Ann. math. Qué.* 49 (2024), 1–61. DOI: 10.1007/s40316-024-00237-4 (cit. on pp. 10, 115, 117, 118).

[OR68] L. A. Oganesjan and L. A. Rukhovets. "Variational-difference schemes for linear second-order elliptic equations in a two-dimensional region with piecewise smooth boundary". *Ž. Vyčisl. Mat i Mat. Fiz.* 8 (1968). In Russian. English translation in USSR Computational Mathematics and Mathematical Physics 8 (1968) 129-152., 97–114 (cit. on pp. 22, 30).

[OKJ14] H.-S. Oh, H. Kim, and J. W. Jeong. "Enriched isogeometric analysis of elliptic boundary value problems in domains with cracks and/or corners". *Int. J. Numer. Methods Eng.* 97.3 (2014), 149–180. DOI: 10.1002/nme.4580 (cit. on p. 22).

[Olv51] F. W. J. Olver. "A further method for the evaluation of zeros of Bessel functions and some new asymptotic expansions for zeros of functions of large order". *Proc. Cambridge Philos. Soc.* 47 (1951), 699–712. DOI: 10.1017/S0305004100027158 (cit. on p. 89).

[Olv52] F. W. J. Olver. "Some new asymptotic expansions for Bessel functions of large orders". *Proc. Cambridge Philos. Soc.* 48 (1952), 414–427. DOI: 10.1017/S030500410002781X (cit. on p. 89).

[Pfe14] J. Pfefferer. “Numerical analysis for elliptic Neumann boundary control problems on polygonal domains”. Dissertation. Neubiberg: Universität der Bundeswehr München, Fakultät für Bauingenieurwesen und Umweltwissenschaften, 2014. URL: https://athene-forschung.unibw.de/node?id=92055 (cit. on pp. 11, 63).

[PT95] L. Piegl and W. Tiller. *The NURBS Book*. Heidelberg: Springer Berlin, 1995. DOI: 10.1007/978-3-642-97385-7 (cit. on pp. 15, 19).

[Ple54] Å. Pleijel. “A study of certain Green’s functions with applications in the theory of vibrating membranes”. *Ark. Mat.* 2 (1954), 553–569. DOI: 10.1007/BF02591229 (cit. on p. 114).

[Pre89] P. M. Prenter. *Splines and variational methods*. Wiley Classics Library. New York: John Wiley & Sons, Inc., 1989, xii+323 (cit. on p. 13).

[RMS23] K. Raval, C. Manni, and H. Speleers. “Tchebycheffian B-splines in isogeometric Galerkin methods”. *Comput. Methods Appl. Mech. Engrg.* 403 (2023), Paper No. 115648, 31. DOI: 10.1016/j.cma.2022.115648 (cit. on pp. 84, 151).

[Ray45] Rayleigh, Lord (J. W. Strutt). *The Theory of Sound*. second. New York: Dover Publications, 1945, Vol. I, xlii+480 pp., vol. II, xii+504 (cit. on pp. 85, 87).

[RASK23] M. Reichle, J. Arf, B. Simeon, and S. Klinkel. “Smooth multi-patch scaled boundary isogeometric analysis for Kirchhoff-Love shells”. *Meccanica* 58.8 (2023), 1693–1716. DOI: 10.1007/s11012-023-01692-z (cit. on p. 22).

[RKLK24] M. Reichle, M. Klassen, J. Li, and S. Klinkel. “A modified approach for a scaled boundary shell formulation in structural isogeometric analysis”. *Eng. Anal. Bound. Elem.* 159 (2024), 81–94. DOI: 10.1016/j.enganabound.2023.11.017 (cit. on p. 22).

[Reu+09] M. Reuter, S. Biasotti, D. Giorgi, G. Patanè, and M. Spagnuolo. “Discrete Laplace–Beltrami operators for shape analysis and segmentation”. *Comput. Graph.* 33.3 (2009), 381–390. DOI: 10.1016/j.cag.2009.03.005 (cit. on p. 116).

[RWP06] M. Reuter, F.-E. Wolter, and N. Peinecke. “Laplace-Beltrami spectra as ‘Shape-DNA’ of surfaces and solids”. *Comput.-Aided Des.* 38.4 (2006), 342–366. DOI: 10.1016/j.cad.2005.10.011 (cit. on pp. 85, 115).

[RWSN09] M. Reuter, F.-E. Wolter, M. Shenton, and M. Niethammer. “Laplace–Beltrami eigenvalues and topological features of eigenfunctions for statistical shape analysis”. *Comput.-Aided Des.* 41.10 (2009), 739–755. DOI: 10.1016/j.cad.2009.02.007 (cit. on p. 116).

[Ros92] J. Rossmann. “On two classes of weighted Sobolev-Slobodetskiĭ spaces in a dihedral angle”. In: *Partial differential equations, Part 1, 2 (Warsaw, 1990)*. Vol. 27, Part 1, 2. Banach Center Publ. Polish Acad. Sci. Inst. Math., Warsaw, 1992, 399–424 (cit. on pp. 39, 63).

[SMS19] E. Sande, C. Manni, and H. Speleers. “Sharp error estimates for spline approximation: explicit constants, n-widths, and eigenfunction convergence”. *Math. Models Methods Appl. Sci.* 29.6 (2019), 1175–1205. DOI: 10.1142/S0218202519500192 (cit. on pp. 2, 86, 105).

[SMS20] E. Sande, C. Manni, and H. Speleers. “Explicit error estimates for spline approximation of arbitrary smoothness in isogeometric analysis”. *Numer. Math.* 144.4 (2020), 889–929. DOI: 10.1007/s00211-019-01097-9 (cit. on pp. 2, 86).

[Sch07] L. L. Schumaker. *Spline functions: basic theory*. Third. Cambridge Mathematical Library. Cambridge: Cambridge University Press, 2007, xvi+582. DOI: 10.1017/CBO9780511618994 (cit. on pp. 14, 17, 18, 58).

[Spe22] H. Speleers. "Algorithm 1020: computation of multi-degree Tchebycheffian B-splines". *ACM Trans. Math. Software* 48.1 (2022), Art. 12, 31. DOI: 10.1145/3478686 (cit. on pp. 84, 151).

[Spe25] H. Speleers. *On the normalization of trigonometric and hyperbolic B-splines*. arXiv preprint. 2025. arXiv: 2508.01817 [math.NA] (cit. on pp. 84, 151).

[ST21] H. Speleers and D. Toshniwal. "A general class of C^1 smooth rational splines: application to construction of exact ellipses and ellipsoids". *Comput.-Aided Des.* 132 (2021), Paper No. 102982, 14. DOI: 10.1016/j.cad.2020.102982 (cit. on pp. 22, 24, 25, 30, 36, 37, 84, 151).

[SF08] G. Strang and G. Fix. *An analysis of the finite element method*. Second. Wellesley, MA: Wellesley-Cambridge Press, 2008, x+402 (cit. on pp. 12, 106).

[Str08] W. A. Strauss. *Partial Differential Equations: An Introduction*. second. Chichester: John Wiley & Sons, Ltd., 2008 (cit. on pp. 85, 87, 88, 90, 95).

[SOG09] J. Sun, M. Ovsjanikov, and L. Guibas. "A Concise and Provably Informative Multi-Scale Signature Based on Heat Diffusion". *Comput. Graph. Forum* 28.5 (2009), 1383–1392. DOI: 10.1111/j.1467-8659.2009.01515.x (cit. on p. 116).

[Tak12] T. Takacs. "Singularities in isogeometric analysis". *Civil-Comp Proceedings* 100 (2012) (cit. on p. 108).

[TJ11] T. Takacs and B. Jüttler. "Existence of stiffness matrix integrals for singularly parameterized domains in isogeometric analysis". *Comput. Methods Appl. Mech. Engrg.* 200.49-52 (2011), 3568–3582. DOI: 10.1016/j.cma.2011.08.023 (cit. on pp. 22, 24, 25, 36, 37, 40, 98).

[TJ12] T. Takacs and B. Jüttler. "H^2 regularity properties of singular parameterizations in isogeometric analysis". *Graph. Models* 74.6 (2012), 361–372. DOI: 10.1016/j.gmod.2012.05.006 (cit. on pp. 22, 24, 25, 36, 37, 40).

[Tak15a] T. Takacs. *Approximation properties of isogeometric function spaces on singularly parameterized domains*. arXiv preprint. 2015. arXiv: 1507.08095 (cit. on pp. 23, 29).

[Tak15b] T. Takacs. "Construction of smooth isogeometric function spaces on singularly parameterized domains". In: *Curves and surfaces*. Vol. 9213. Lecture Notes in Comput. Sci. Springer, Cham, 2015, 433–451. DOI: 10.1007/978-3-319-22804-4_30 (cit. on p. 29).

[Tak25] T. Takacs. "Approximation properties over self-similar meshes of curved finite elements and applications to subdivision based isogeometric analysis". *Comput. Aided Geom. Des.* 116 (2025), 102413. DOI: 10.1016/j.cagd.2025.102413 (cit. on pp. 23, 30, 69, 108, 112, 151).

[TT23] T. Takacs and D. Toshniwal. "Almost-C^1 splines: biquadratic splines on unstructured quadrilateral meshes and their application to fourth order problems". *Comput. Methods Appl. Mech. Engrg.* 403 (2023), Paper No. 115640, 34. DOI: 10.1016/j.cma.2022.115640 (cit. on p. 30).

[TSHH17] D. Toshniwal, H. Speleers, R. R. Hiemstra, and T. J. R. Hughes. "Multi-degree smooth polar splines: A framework for geometric modeling and isogeometric analysis". *Comput. Methods Appl. Mech. Engrg.* 316 (2017), 1005–1061. DOI: 10.1016/j.cma.2016.11.009 (cit. on pp. 22, 24, 25, 30, 36, 37, 69, 84, 151).

[Váz16] R. Vázquez. "A new design for the implementation of isogeometric analysis in Octave and Matlab: GeoPDEs 3.0". *Comput. Math. Appl.* 72.3 (2016), 523–554. DOI: 10.1016/j.camwa.2016.05.010 (cit. on pp. 25, 68, 101, 133).

[WR16] C. Wachinger and M. Reuter. "Domain adaptation for Alzheimer's disease diagnostics". *NeuroImage* 139 (2016), 470–479. DOI: 10.1016/j.neuroimage.2016.05.053 (cit. on p. 116).

[Wat95] G. N. Watson. *A treatise on the theory of Bessel functions*. second. Cambridge Mathematical Library. Cambridge: Cambridge University Press, 1995, viii+804 (cit. on p. 89).

[Wey12] H. Weyl. "Das asymptotische Verteilungsgesetz der Eigenwerte linearer partieller Differentialgleichungen (mit einer Anwendung auf die Theorie der Hohlraumstrahlung)". *Math. Ann.* 71.4 (1912), 441–479. DOI: 10.1007/BF01456804 (cit. on pp. 114, 117, 118).

[Wie+24] M. Wiesheu, T. Komann, M. Merkel, S. Schöps, S. Ulbrich, and I. Cortes Garcia. "Combined parameter and shape optimization of electric machines with isogeometric analysis". *Optim Eng.* (2024). DOI: 10.1007/s11081-024-09925-0 (cit. on p. 22).

[Wil63] J. H. Wilkinson. *Rounding errors in algebraic processes*. Englewood Cliffs, NJ: Prentice-Hall, Inc., 1963, vi+161 (cit. on p. 83).

[Win15] M. Winkler. "Finite Element Error Analysis for Neumann Boundary Control Problems on Polygonal and Polyhedral Domains". Dissertation. Neubiberg: Universität der Bundeswehr München, Fakultät für Bauingenieurwesen und Umweltwissenschaften, 2015. URL: https://https://athene-forschung.unibw.de/102641 (cit. on p. 11).

[Xue+20] Y. Xue, G. Jin, T. Ye, K. Shi, S. Zhong, and C. Yang. "Isogeometric analysis for geometric modelling and acoustic attenuation performances of reactive mufflers". *Comput. Math. Appl.* 79.12 (2020), 3447–3461. DOI: 10.1016/j.camwa.2020.02.004 (cit. on p. 22).

[Zel00] S. Zelditch. "Spectral determination of analytic bi-axisymmetric plane domains". *Geom. Funct. Anal.* 10.3 (2000), 628–677. DOI: 10.1007/PL00001633 (cit. on p. 115).

[Zel04] S. Zelditch. "Inverse spectral problem for analytic domains. I. Balian-Bloch trace formula". *Comm. Math. Phys.* 248.2 (2004), 357–407. DOI: 10.1007/s00220-004-1074-y (cit. on p. 115).

[Zel09] S. Zelditch. "Inverse spectral problem for analytic domains. II. $\mathbb{Z}_2$-symmetric domains". *Ann. of Math. (2)* 170.1 (2009), 205–269. DOI: 10.4007/annals.2009.170.205 (cit. on p. 115).

[Zha+07] Y. Zhang, Y. Bazilevs, S. Goswami, C. L. Bajaj, and T. J. R. Hughes. "Patient-specific vascular NURBS modeling for isogeometric analysis of blood flow". *Comput. Methods Appl. Mech. Engrg.* 196.29-30 (2007), 2943–2959. DOI: 10.1016/j.cma.2007.02.009 (cit. on p. 22).

[Zho+20] S. Zhong, G. Jin, T. Ye, J. Zhang, Y. Xue, and M. Chen. "Isogeometric vibration analysis of multi-directional functionally gradient circular, elliptical and sector plates with variable thickness". *Compos. Struct.* 250 (2020), 112470. DOI: 10.1016/j.compstruct.2020.112470 (cit. on p. 22).